Nanomaterial Sensing: Integrating MEMS Technology and Self-Assembled Monolayers

by

Abduljabbar Ibrahim Rasheed Rushdi

A thesis submitted to

The University of Birmingham

For the degree of

DOCTOR OF PHILOSOPHY

School of Chemistry

University of Birmingham

College of Engineering and Physical Sciences

March 2018

This thesis is dedicated to the memory of my parents who they spent their

efforts and life to guide me to be what I am now

ABSTRACT

The integration of self-assembled monolayer (SAM) into microelectromechanical system (MEMS) devices is introduced in ***Chapter 1***. SAM formation and characterization is described, *via* the spontaneous assembly of surfactants to surfaces providing monolayer coverage, the so called *bottom-up* approach, and hence modifying the chemical and physical surface properties. Examples of SAMs which can be used for analyte sensing, via the recognition motifs incorporated into the SAM will be described. In addition, an overview of MEMS, which are fabricated by the so called *top-down* approaches, and their applications is provided.

Chapter 2 is concerned with the specific immobilization of NeutrAvidin on pure and mixed SAMs of biotinylated tri(ethylene glycol) thiol, undecanethiol (BUT, biotin containing sensor element for Neutravidin) and (11-mercaptoundecyl) tetra(ethylene glycol) (TEG, spacer) which were deposited on Au surfaces. Contact angle, ellipsometry and X-ray photoelectron spectroscopy (XPS) were used to characterize the composition of these SAMs. Surface plasmon resonance (SPR) and a quartz crystal microbalance (QCM) were used to study the adsorption behavior of NeutrAvidin to the pure and mixed SAMs.

Chapter 3 describes the optimum conditions in details of how to obtain the monolayer of 11-amino-1-undecanethiol hydrochloride (Alk-amine) and 4-aminothiophenol (Ar-amine) SAM, which were deposited on an Au surface by using an ethanolic solution of Triethylamine (TEA) and how to reduce the contamination which are combined with the deposition of the two amines. Finally, ellipsometry, contact angle and XPS were used to characterise the monolayer of two amine SAMs.

Chapter 4 describes the optimum conditions of gold nanoparticles (G-NPs) deposition on a monolayer of Alk and Ar-amine terminated SAMs, which were described in chapter 3, at different pHs. AFM and QCM confirm that the optimum deposition of G-NPs was at pH 5 for the two amine SAMs and the deposition on Alk-amine SAM is much higher than on Ar-amine SAM. Thus, Alk-amine SAM was chosen for chemically modifying the surface of a micro paddle. After the modification the paddle was used to detect the deposited mass of G-NPs and SEM was used to confirm dispersity of the monolayer of G-NPs.

Acknowledgements

Many people I would like to thank for their help and support during my PhD (Lab. work and writing up)

Firstly, I would like to thank Prof. Jon A. Preece and Prof. Paula Mendes, my supervisors, for giving me the opportunity to study for my PhD. Their help, advice and supervision have been invaluable.

I would also like to thank the Iraqi Cultural Attaché in London and the Ministry of higher education and Scientific Research and Mustansiriyah University in Baghdad/Iraq for funding my research. Thanks, must also go to Dr Parvez Iqbal and Dr James Bowen for their friendship and advice with my studies.

Also, thanks to JAP group, Greg, Dennis, Toni, Owen and Mariana for their friendship and advice within the period of my study.

I thank the staff members in the School of Chemistry, who helped me to characterize some compounds that have been synthesized: Dr Chi Tsang and Mr Peter Ashton (mass spectrometry), Dr Cecille Le Duff (NMR), Mrs Lianne Hill (Elemental Analysis) and Dr Alan Bowden (Chromatography).

My thanks also go to my collaborator Nasim Mahmoodi and her supervisor Dr Carl Anthony from the Department of Mechanical Engineering in relation to the MEM sensor side of the mass sensor project.

Also, I would also like to give thanks to my wife and my daughters, and also for my brothers and sisters for their morale support during my studies.

Finally, my thankful to Allah.

Contents

Chapter 1 1

1 Self-Assembled Monolayer (SAM) and Microelectromechanical ..... Systems (MEMS) 1

1.1. Introduction 2

1.2. Types of SAMs prepared 4

1.2.1. SAMs formed from organosilane. 4

1.2.2. SAMs formed from organosulfur 5

1.3. Characterisation of Surfaces – SAMs and Analytes Binding to SAMs 8

1.3.1. SAM Characterisation 9

1.3.1.1. Contact angle measurements 9

1.3.1.2. Ellipsometry measurements 11

1.3.1.3. X-ray photoelectron spectroscopy (XPS) measurements 12

1.3.2. Characterisation of the specific analytes deposited on SAM 14

1.3.2.1. Surface Plasmon Resonance (SPR) measurements 14

1.3.2.2. Quartz Crystal Microbalance (QCM) measurements 15

1.3.2.3. Atomic Force Microscopy (AFM) 18

1.3.2.4. Transmission Electron Microscopy (TEM) 19

1.3.2.5. Scanning Electron Microscopy (SEM) 20

1.4. Applications of SAMs 21

1.4.1. Microelectromechanical systems (MEMS) 23

1.4.1.1. Focused ion beam (FIB) 24

1.5. Hypothesis/Objectives of This Thesis 26

1.6. References 27

Chapter 2 38

2. Formation of Binary Biotin Containing SAMs to Study .....

NeutrAvidin Binding Using SPR and QCM 38

2.1. Introduction 40

2.2. Aim of the study in this chapter 43

2.3. Results and discussion 45

2.3.1. Contact Angle and Ellipsometry: Formation, Stability and Characterization of pure BUT SAM 45

2.4. Formation and Characterization of Pure BUT & TEG and Their Binary SAMs..... 48

2.4.1. Water Contact Angle 50

2.4.2. Ellipsometry 52

2.5. XPS Surface Characterisation of BUT, TEG and various BUT:TEG SAMs 54

2.5.1. Distribution of BUT, TEG and eight BUT:TEG SAMs on Au surface 54

2.5.2. XPS: Determination of the position of biotin moiety in the SAM 57

2.6. Adsorption of NeutrAvidin to the BUT/TEG SAMs 62

2.6.1. SPR measurements 62

2.6.2. QCM measurements 64

2.6.2.1. AFM Measurements: 68

2.7. Determination of the coverage of NeutrAvidin on BUT:TEG SAM 72

2.8. Conclusion 76

2.9. Future work 78

2.10. Experimental 80

2.10.1. a. Chemicals Supplied 80

2.10.2. b. Au Substrates Supplied 81

2.10.3. SAM Formation 82

2.10.3.1. Cleaning Au substrates for CA, Ellipsometry, SPR, XPS and QCM ..... Prior to SAM formation with TEG, BUT or Mixture 82

2.10.3.2. Preparation of BUT Self-Assembled Monolayers 83
2.10.3.3. Preparation of TEG Self-Assembled Monolayers 83
2.10.3.4. Preparation of mixed BUT and TEG Self-Assembled Monolayers 83
2.11. Surface characterisation 84
2.11.1. Contact angle (CA) measurements 84
2.11.2. Ellipsometry measurements 84
2.11.3. Surface Plasmon Resonance (SPR) measurements 85
2.11.4. Quartz Crystal Microbalance (QCM) measurements 86
2.11.5. AFM measurements 86
2.11.6. X-ray Photoelectron Spectroscopy (XPS) 87
2.12. References 88

Chapter 3 97

3. Experimental Optimization for the Formation of Alkyl and Aryl Amine-Terminated SAM on Au Surface 97

3.1. Introduction 99
3.2. Formation of a monolayer of Alk-amine and Ar-amine 99
3.3. Aim of the study in this chapter 102
3.4. Results and discussion 104
3.4.1. Formation and Characterisation of Alk-amine and Ar-amine terminated SAM with and without TEA to study the bilayer inhibiting effects of TEA 104
3.4.1.1. Contact Angle (CA) measurements 105
3.4.1.2. Ellipsometry measurements 108
3.4.2. Orientation of the two amines SAM from CA and Ellipsometry 109
3.4.3. XPS characterisation of SAMs formed under Alk-d and Ar-d Experimental..... Conditions (1mM TEA) 110

3.4.3.1. XPS characterisation of SAMs from Alk-a to Alk-d ..... Experimental Conditions: Examining the Sulfur Oxidation 113

3.4.3.2. Adsorption of CO_2 on Alk-d and Ar-d SAM surfaces..... 115

3.4.3.3. Effect of the TEA concentration on the monolayer formation ..... of the two SAMs 117

3.4.3.4. XPS Thickness of Alk and Ar-amine SAM on Au surface ..... (Alk-d and Ar-d Conditions) 119

3.4.3.5. Difference between the coverage and orientation of Alk-d and ..... Ar-d SAM on Au surface 120

3.5. Conclusion..... 123

3.6. Future work..... 123

3.7. Experimental..... 124

3.7.1. a. Chemicals Supplied..... 124

3.7.2. b. Au Substrates Supplied..... 124

3.7.3. SAM Formation..... 125

3.7.3.1. Cleaning Au substrate for CA, Ellip and XPS Prior to SAM ..... formation with Alk-amine or Ar-amine..... 125

3.7.3.2. Preparation of Alk and Ar-amine SAMs..... 125

3.8. Surface characterisation 126

3.8.1. Contact angle (CA) measurements..... 126

3.8.2. Ellipsometry measurements..... 127

3.8.3. X-ray Photoelectron Spectroscopy (XPS)..... 128

3.9. References 129

Chapter 4 134

4 Characterisation and Deposition of Gold Nanoparticles on Aliphatic ..... and Aromatic Amine Terminated SAMs as Function ..... of pH on a MicroElectroMechanical System Micropaddle 134

4.1. Introduction 136

4.2. Aim of the study in this chapter 139

4.3. Results and Discussion 140

4.3.1. Synthesis of G-NPs colloidal solution 140

4.3.1.1. Synthesis of G-NPs 140

4.3.2. Characterisation of G-NPs colloidal solution 141

4.3.2.1. UV-Vis Spectrophotometer measurements 141

4.3.2.2. Transmission Electron Microscopy (TEM) 141

4.3.2.3. Investigation of Room Temperature G-NP Stability as a Function of pH and time: A Dynamic Light Scattering (DLS), Zeta Potentiometry (ZP) and UV-Vis Study on the Colloidal G-NPs Solution 142

4.3.3. Characterization of the deposition of G-NPs on Alk and Ar-amine SAM at different pHs: Atomic Force Microscopy and QCM Analysis 150

4.3.3.1. Atomic Force Microscopy (AFM) Analysis 150

4.3.3.1.1 Deposition of G-NPs on Alk-amine and Ar-amine SAM at pHs 3–7 (2 h Immersion) 152

4.3.3.1.2 Recyclability of the Alk-amine and the Ar-Amine SAMs 158

4.3.3.2. Quartz Crystal Microbalance (QCM) measurements 160

4.3.3.2.2 QCM frequencies of G-NPs deposited on Alk-amine and Ar-amine SAM at different pHs 163

4.3.3.3. Translating the SAMs Technology to the MEMS Micro-Paddle: Laser Vibrometer measurements 169

4.4. Conclusion 171

4.5. Future work 172

4.6. Experimental 173

4.6.1. a. Chemicals Supplied 173

4.6.2. b. Au Substrates Supplied 173

4.6.3. SAM formation 174

4.6.3.1. Cleaning Au substrate for AFM and QCM Prior to SAM formation of the two amines 174

4.6.3.2. Preparation of Alk and Ar-amine Self-Assembled Monolayers 174

4.6.3.3. Preparation of gold Nanoparticles passivated with citrate 174

4.6.3.4. Deposition of G-NPs on Alk and Ar-amine SAMs at different pH..... 175
4.7. Surface characterisation 176
4.7.1. Atomic Force Microscopy (AFM) measurements..... 176
4.7.2. Quartz Crystal Microbalance (QCM) measurements 177
4.8. G-NPs colloidal solution characterization 178
4.8.1. Transmission Electron Microscopy (TEM) 178
4.8.2. UV-Vis spectrophotometer measurements 178
4.8.3. Dynamic Light Scattering (DLC) measurements 178
4.8.4. Zeta Potential (ZP) measurements..... 179
4.9. References 180
4.10. Published Paper (Nasim Mahmoodi, Abduljabbar I. Rushdi, James Bowen, ... Aydin Sabouri, Carl J. Anthony, Paula M. Mendes, and Jon A. Preece..... 186

Chapter 5 192

Appendices..... 192

Appendix A..... 193

Appendix B..... 202

List of Figures

Chapter 1

Figure 1.1: Illustrates the three molecular components of SAM…….
chemosorbed on gold substrate..... 3
Figure 1.2: Schematic representation of the Stages of alkanethiol SAM formation…….
on a Au surface 7
Figure 1.3: Illustrates the water advancing contact angle on a) hydrophilic SAM…….
(wetted surface) and b) hydrophobic SAM at room temperature..... 10
Figure 1.4: Schematic representation of a) ellipsometry measuring the thickness of SAM and b)..
tilt angle of the SAM deposited on a Au surface..... 12
Figure 1.5: Schematic diagram of the XPS process, illustrating the ejection of…….
a core electron by XPS photon 13
Figure 1.6: Schematic diagram of SPR measurements a) before, and b) during and after……..
deposition of an analyte by following the changes in the incident angle..... 15
Figure 1.7: Cartoon represents an AT-cut QCM-sensor two sided sensor……..
(same top and bottom views) 17
Figure 1.8: Schematic diagram of quartz crystal microbalance measuring……
the frequency in liquid..... 17
Figure 1.9: Schematic of AFM measurements 19
Figure 1.10: Schematic representation of TEM analytes measurements 20

Figure 1.11: Schematic representation of SEM operation 21

Figure 1.12: Example of a MEMS consisting of the mechanical structure.....

and electrical systems (ref [148])..... 23

Figure 1.13: Cartoon of micro paddle fabrication using FIB..... 24

Figure 1.14:Cartoon of depositing precursors on metal surfaces using FIB 25

Chapter 2

Figure 2.1: a) represents the helical conformation of OEG on an Au substrate, and b).....

non-helical conformation of OEG on an Ag substrate 42

Figure 2.2: Illustrates the chemical structures of a) BUT and b) hydrophilic spacer (TEG),.....

and the fully extended lengths calculated using ChemDraw, the difference between c).....

mixed BUT/TEG, and d) NeutrAvidin immobilized on mixed SAM BUT/TEG 44

Figure 2.3: Shows the difference between the mol% of a) BUT in the SAM and b) TEG SAM.....

relative to the mol% of BUT and TEG in the SAM forming solution, as deduced.....

by the Cassie equation 51

Figure 2.4: Illustrates the advancing angle, receding angle and hysteresis of pure and eight.....

different mixtures of BUT SAM and TEG SAM on Au surface 52

Figure 2.5: Illustrates the ellipsometric thickness of pure BUT SAM and TEG SAM and eight.....

different mixtures of them on surface of Au at R. T. 53

Figure 2.6: Depicts the biotin moieties of BUT SAM lay on the surface of TEG SAM.....

deposited on an Au surface at room temperature 54

Figure 2.7: XPS survey spectra, Au 4f, O 1s, C 1s, N 1s and S 2p peaks of $X^{\%BUT}$ in the……
SAM (numbers on left hand side of each spectra) 55
Figure 2.8: Graph shows N 1s/Au 4f ratio of TEG and BUT SAMs (pure and mixed) deposited……..
on Au surface at R.T vs. mole fraction of $X^{\%BUT}$ on the Au surface..... 58
Figure 2.9: Shows some of Biotin moieties exposed to the surface of 100 $X^{\%BUT}$ and other……..
biotin moieties exist in the depth of the BUT film 59
Figure 2.10: XPS spectra of S 2p peaks of a) 0 $X^{\% BUT}$ (100 $X^{\% TEG}$), b) 66 $X^{\% BUT}$, and c) 100 $X^{\% BUT}$……
SAM deposited on Au surface at R.T and d) the area calculated for S 2p 61
Figure 2.11: The SPR responses for $X^{\%BUT}$ SAM and $X^{\%TEG}$ SAM pure and eight different……
mixtures of them on Au surface at room temperature 63
Figure 2.12: a) The responses of SPR according to the $X^{\% BUT}$ on surface at room temperature,…..
and b) data inset..... 64
Figure 2.13: The responses of QCM for the 66 $X^{\%BUT}$ on the surface at room temperature……..
and summary final adsorption data (inset) 67
Figure 2.14: The topographic AFM images of a) Height-Trace for 66 $X^{\% BUT}$ SAM/Au, b)……..
Height-Trace for NeutrAvidin immobilized on 66 $X^{\% BUT}$ on Au surface of the QCM-sensor……
crystal at room temperature, c) Phase-Trace, and d) 3D..... 70
Figure 2.15: The Scheme of the total thickness of NeutrAvidin deposited on 66 $X^{\% BUT}$ ……..
and TEG SAMs on Au surface QCM-sensor crystal..... 71
Figure 2.16: Coverage of Neu (left axis) and XPS intensity ratio of N(1s)/Au(4f) at……
takeoff angle of 90^{o} (right axis) vs $X^{\%BUT}$ on surface..... 73

Figure 2.17: Coverage of BUT/Neu (left axis) and coverage of BUT/TEG (right axis)……..
vs % mole fraction of BUT on the surface of Au 75
Figure 2.18: Ratio of BUT/Neu (lift axis) and XPS intensity ratio of N(1s)/Au(4f) at a takeoff angle
of 90^{o} (right axis) vs $X^{\%BUT}$ on the surface of Au 76

Chapter 3

Figure 3.1: a) Formation of a bilayer, and b) improved method of a monolayer……
formation of Alk-amine on Au surface @ R.T. 102
Figure 3.2: Illustrates the chemical structures and theoretical length of a)……..
Alk-amine, and b) Ar-amine..... 103
Figure 3.3: Shows the preparation of Alk-c and Alk-d SAM on Au surface at R.T. 105
Figure 3.4: Illustrates the difference in the contact angle and ellipsometric determined……
thickness between a) Alk-a: bilayer formation (without adding 215 mM TEA and washed with……
HPLC EtOH), b and c) with adding 215 mM TEA for Alk-b: washed with CH_3COOH and……
for Alk-c: immersed in HCl, and d) adding 1 mM TEA for Alk-d: immersed in HCl..... 107
Figure 3.5: a) upright orientation of Ar-amine SAM and b) tilted Ar-amine ……
SAM on Au surface 110
Figure 3.6: XPS spectra of SAMS formed under Alk-d and Ar-d conditions……
(Table 3.1, Figure 3.3) a) survey spectra, b) Au 4p and O 1s of Alk-d and Ar-d amine……..
SAM deposited on Au surface at room temperature, and c) inset chemical……
structure of Alk and Ar-amine 111

Figure 3.7: The XPS attenuation of Au 4f with a) Alk-d (thick SAM) and b) Ar-d (thin SAM)..... 112

Figure 3.8: XPS data for S 2p spectra of Alk-amine SAM Across Alk-a to.....

Alk-e Experimental Formation Conditions 114

Figure 3.9: Schematic of carbamate formation after the.....

reaction between Ar-d SAM 115

Figure 3.10: XPS Spectra recorded of SAMs formed under Alk-d and Ar-d conditions.....

(1mM TEA and 500 mM HCl immersion for 1 h): a) N 1s spectrum of Alk-d SAM, b).....

N 1s spectrum of Ar-d SAM, c) C 1s spectrum of Alk-d, and d) C 1s spectrum.....

of Ar-d SAM on Au surface at R.T. 117

Figure 3.11: CO_2 reacted with free amine formed by adding a) 215 mM, and b) 1 mM TEA..... 120

Figure 3.12: Orientation of Alk-d SAM on Au Surface Via a).....

S atom, and b) N atom (upright orientation) 122

Chapter 4

Figure 4.1: Cartoon representation of a) Alk-amine SAM deposited on the Au surface.....

of a micro paddle, b) G-NPs deposited on an Alk-amine SAM/Au-micro paddle, and c).....

magnification of the deposited G-NPs on an Alk-amine SAM/Au-paddle 139

Figure 4.2: Schematic procedure of 14.5 ± 0.95 nm G-NPs synthesis and purification..... 140

Figure 4.3: UV-Vis spectra of G-NPs colloidal solution at R.T..... 141

Figure 4.4: A TEM image of the G-NPs passivated with citrate and the histogram showing the.....

size distribution of G-NPs passivated with citrate at pH 4.5..... 142

Figure 4.5: DLS of relative a) number, b) volume, c) intensity distribution, and d)…….
Zeta Potential of synthesised G-NPs at pH 4.5 and room temperature 143
Figure 4.6: Schematic showing the charges present on citrate-passivated G-NPs……
deposition on the amine and ammonium-terminated SAM surfaces at five…….
different pHs (low, intermediate and high pH) at room temperature..... 144
Figure 4.7: a) Zeta Potential, b) Dynamic Light Scattering and c) poly dispersity for…….
G-NPssolution at different pHs and time 146
Figure 4.8: a) Absorption maximum change of surface plasmon band (~520 nm)……
of the G-NPs as a function of pH and time, and b) UV-Vis at pHs 3, 4, 4.5, 5, 6 & 7,……..
at t = 0 h, c) t = 1 h, d) t = 2 h and, e) t = 6 h 148
Figure 4.9: The Zeta Potential and Particle Size measurements for G-NPs……
solution after 2 h of changing the pH at different values 149
Figure 4.10: Deposition of G-NPs on bare Au at pH 3, pH 4 and pH 5, and…….
2 h immersion (control experiments)..... 152
Figure 4.11: 5 × 5 µm AFM images for G-NPs deposited onto Alk-amine…….
SAM at different pHs (2 h)..... 153
Figure 4.12: Expanded AFM images from Figure 4.11 at pH 3, 4, and 5 on……
Alk-amine SAM. At pHs 3 and 4 one can observe G-NPs on top of each other,……
presumably because of particle aggregation in the dispersion prior to…….
deposition/self-assembly on the surface, whereas at pH 5 the particles are not aggregated... 154

Figure 4.13: 5 × 5μm AFM images for G-NPs deposited onto Ar-amine SAM……
at different pHs (2 h) 155
Figure 4.14: A histogram showing the difference between the number of G-NPs……
deposited on Alk and Ar-amine at different pHs (using AFM), 2 h) 157
Figure 4.15: 5 × 5 μm AFM images of deactivation of Alk-amine SAM……..
for new deposition of G-NPs at pH 5 159
Figure 4.16: 5 × 5 μm AFM images of deactivation of Ar-amine SAM……
for new deposition of G-NPs at pH 5 160
Figure 4.17: QCM Response of G-NPs adsorption on Alk--amine SAM ……..
by QCM at pH 5 and room temperature, together with a schematic……..
highlighting the methodology 162
Figure 4.18: 5 × 5 μm AFM images of a control experiment a) bear Au, and b)…….
of depositing G-NPs at pH 5 on bare Au of a QCM-sensor 163
Figure 4.19: a) Measured frequencies by QCM, and b) combined 5 × 5 μm AFM images……..
of G-NPs deposition on Alk-amine SAM at different pHs 165
Figure 4.20: a) Measured frequencies by QCM, and b) combined 5 × 5 μm AFM images……
of G-NPs deposition on Ar-amine SAM at different pHs 167
Figure 4.21: (a) Change in frequencies upon G-NPs deposition on the Alk and Ar-amine……
SAM (1 cm^2) as function of pH on the QCM, and (b) number of G-NPs deposited……
on the Alk and Ar-amine SAM (25 μm^2) as function of pH on the QCM (calculated via……
the Sauerbrey equation and scaled from 1cm^2 to 25 μm^2) 168

Figure 4.22: a) SEM image of micro paddle, and b) laser vibrometer signals of……

a micro paddle before and after G-NPs deposition on Alk-amine SAM at pH 5 170

Figure 4.23: SEM image of a) before, and b) after G-NPs deposited on an……

Alk-amine SAM functionalized surface of a micro paddle 171

Figure 4.24: Deposition of G-NPs on Alk-amine SAM for 2 h at room temperature 176

Figure 4.25: Schematic of QCM system for G-NPs deposition on Alk and……..

Ar-amine SAM at different pHs 177

List of tables

Chapter 2

Table 2.1: Contact angle and ellipsometry measurements……

(twenty seven measurements performed for each experiment) of the BUT SAM……

deposited on Au surface under degassed and non-degassed N_2 conditions……

and characterized immediately and after 7 days in air. 46

Table 2.2: Mixing volumes of ethanolic solutions of 0.1 mM of BUT and TEG 48

Table 2.3: The contact angles and ellipsometric thickness of the pure……

.and binary BUT and TEG SAMs 49

Chapter 3

Table 3.1: Contact angle, ellipsometric and XPS data for Alk-amine and Ar-amine……

SAM on an Au surface without and with TEA (215 mM) addition and washing……..

the SAMs with CH_3COOH (1748 mM) or immersing in HCl. Note: the grey……..

boxes indicate which variable has changed relative to previous experimental condition,……

e.g TEA concentration changed or post SAM modification with CH_3COOH or HCl..... 106

Table 3.2: XPS results of atomic percent ratios C 1s, N 1s, S 2p and O 1s normalized……

with Au 4f for Alk-d and Ar-d SAM at takeoff angle 90^o. 121

Chapter 4

Table 4.1: The number of G-NPs deposited on Alk-amine and Ar-amine SAM……

at pH 3–7 obtained by AFM (Figure 4.11 and Figure 4.13) 153

Table 4.2: Electrostatic force between citrate passivated G-NPs and Alk-amine……..

SAM deposited on Au surface (5 nm as separated distance) in solution at various…….

pH ranging from 3-7 and at room temperature. Assuming pK_a values of citrate……

(3.13, 4.76 and 6.40), and pK_a = ~7.5 for Alk-amine SAM 158

List of abbreviations and acronyms

Alkanethiol	AT
Advancing contact angle	θ_a
Average	Av.
Atomic force microscopy	AFM
11-amino-1-undecanethiol hydrochloride	Alk-amine
4-amino-thiophenol	Ar-amine
Atomic weight	Aw
Attogram	ag
Association constant	K_a
biotinylated tri (ethylene glycol) undecane thiol	BUT
biotinylated Bovine Serum Albumin	b-BSA
biotinylated Hyaluranon	b-HA
Bovine Serum Albumin	BSA
Binding energy	BE
Contact Angle	CA
Change in the fundemental frequency	Δf
Cosin of the advancing angle of pure BUT SAM	$cos\ \Theta_1$
Cosin of the advancing angle of pure TEG SAM	$cos\ \Theta_2$
Coulomb's constant	k_e
Charge of the ion	q_1
Dynamic light scattering	DLS
Dalton	Da
Density	ρ
Distance between two charges	r
Dissociation constant	K_d
Energy of the X-ray sources	$h\upsilon$
Focused Ion Beam	FIB
Fundamental resonance frequency of analyte	FRF
Frequency of the analyte	f_a
Force of the interaction between the charges	F
Femtogram	fg
gold	Au
gold nanoparticles	G-NPs

Hysteresis	$\Delta\theta$
Hour	h
Hartz	Hz
Kinetic energy	KE
Mole frection of BUT thiolate on the surface	f_1
Mole frection of TEG thiolate on the surface	f_2
Mass sensitivity constant	C
Microelectromechanical Systems	MEMS
Molar percent of BUT thiol in solution	Mol $\%^{BUT}$
Molar percent of BUT thiol on surface	$X^{\%BUT}$
Mass of micropaddle	m_p
Mass of analyte on a micro paddle	m_d
Mass sensitivity of micro paddle	S
Milli Molar	mM
Micro meter	µm
Minute	min
Molecular weight	Mwt
11-(mercaptoundecyl) tetra(ethylene glycol)	TEG
Mass of analyte	m
Nano meter	nm
NeutrAvidin	Neu
Newton	N
Pico gram	pg
Quartz crystal Micro balance	QCM
Refractive Index	n_f
Receding contact angle	θr
Root mean square	RMS
Response unit	RU
Scanning electron microscopy	SEM
Silicon Nitride	Si_3N_4
Surface plasmon resonance	SPR
Self-Assembled Monolayer	SAM
Theoretical Calculation	T. C.
Transmission electron microscopy	TEM
Two dimensions	2-D
Triethylamine	TEA
Thickness	d
Ultra High Vacuum	UHV

Ultra High Quality Water	UHQW
Volume	V
Volume of BUT thiol	V^{TEG}
Volume of TEG thiol	V^{BUT}
X-ray Photoelectron Spectroscopy	XPS
Zeta potential	ZP

Chapter 1

Self-Assembled Monolayer (SAM) and Microelectromechanical Systems (MEMS)

Abstract

Self-assembled monolayers (SAMs) open a new approach for applications in nanotechnology *via* the surface functionalisation of resonating microelectromechanical systems (MEMS) for the detection of analytes. The sensing is by virtue of changes in resonance frequency upon deposition of an analyte to the chemically tuned MEMS surface through the SAMs. So, the resonator needs specific SAMs (pure or mixed), which contain recognition motifs for complementarity analytes. This PhD chapter is concerned with chemically derivatising MEMS to fabricate sensors based on this approach. Pure or mixed SAMs are deposited on the surface of a resonator and an analyte can be recognised by these SAMs.

1.1. Introduction

The specific organization of nanomaterials into two and three-dimensional nanostructures represents a new direction in nanotechnology for the production of new functional devices.[1–3] This approach opens up new applications in nanomaterials such as optics,[4] and electronics[5] as well as sensing,[6,7] bringing together chemists, engineers, physicists and biologists to fabricate novel nanomaterials and devices.[8,9] There are two distinct approaches to build or fabricate nanoscale devices. One of them is *top-down*[10] and the other is *bottom-up*.[11] Focused ion beam and lithographic processes work *via* a top-down approach by etching away a solid substrate to obtain nanostructures.[10] Whereas the bottom-up approach self-assembles and self-organises atoms/ions/molecules into larger structure with nanoscale dimensions (and potentially function), *e.g.* self-assembled monolayers (SAMs).[11] SAMs form by spontaneous chemisorption of organic

surfactant molecules from solutions, for example the adsorption of alkanethiols on Au, Ag, Si, Pt and Cu surfaces to form an immobilized and a well-ordered monolayer in two-dimensions.[12,13] The composition of these surfactants (the adsorbate) consists of three important molecular components: the headgroup, backbone and terminal (functional) group as shown in Figure 1.1.

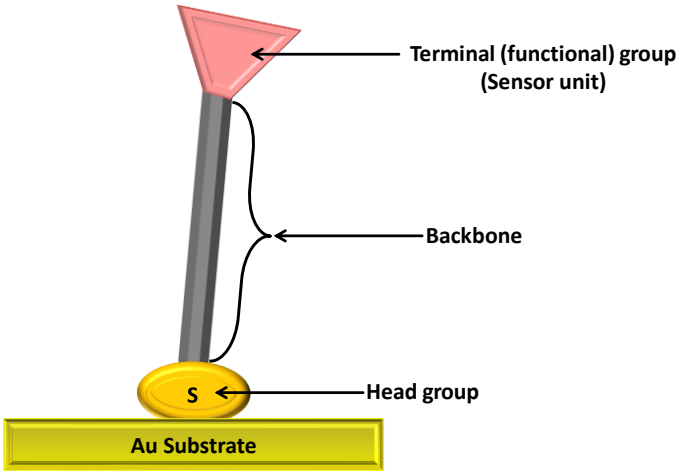

Figure 1.1: Illustrates the three molecular components of SAM chemosorbed on gold substrate

- ***The headgroup***: represents the chemical anchor to the surface. The selection of the headgroup depends upon the type of substrate. Thiols (-SH)[13–15] and silanes[16,17] are the most common headgroups which bind to gold and the silica surfaces, respectively.
- ***The backbone***: the backbone is usually an aliphatic[18] or an aromatic component.[19] The backbone plays a very important role to control the long-range structural packing of the SAM, and hence the stability and ordering of the SAMs, where every molecule of the SAM interacts with its neighbour through the backbone. This interaction comes from van der Waals forces[20] and/or π-π interactions,[19] and will lead to a quasi-ordered or well-ordered

layer in the SAM depending on the nature of the substrate and length of backbone in chain.[21,22]

- ***The terminal (functional) group (sensor unit)***: The terminal group determines the chemical and physical properties of the interface. Thus, if a terminal group is a hydrophobic methyl group and the surface of the clean substrate had hydrophilic properties such as Au, then the new surface properties become hydrophobic upon SAM formation.[23] Thus, this feature enables surface properties to be modified through SAM formation, and modulating corrosion and wettability.[24–26] One of the application of SAMs is to use them to modify the surface of resonators of microelectromechanical systems (MEMS), in order to fabricate a sensor. MEMS represent excellent devices, which integrate electrical and mechanical components in microscale system for sub-ng mass detection.[27–31]

1.2. Types of SAMs prepared

SAMS are generally formed by surfactants either adsorbing to oxide or metal surfaces and can best be represented by the two main types that have been studied, namely SAMs formed from silanes and thiols on silica and gold surfaces, respectively.[13,32]

1.2.1. SAMs formed from organosilane.

Organosilane derivatives have been used to prepare SAMs by adsorbing them onto suitable hydrophilic substrates, such as silica and glass by the wet chemical method[33] or the dry method.[34] The headgroup of the organosilane surfactants are of the general composition $–SiX_3$,

where X represents OR or Cl. Thus, a covalent bond Si-O will arise between a headgroup of organosilane and a hydroxylated surface (as well as extensive cross-linking between the adsorbed surfactant molecules) *via* the substitution of the X group.[35–37] As a result of these new multiple strong Si-O bonds anchoring the organic component to the surface, SAMs formed by organosilane are more robust than SAMs produced by organosulfur surfactants on Au.[38] The mechanism of formation of these silane SAMs requires some surface adsorbed water to initiate the surface chemistry,[35] which can affect the quality of the SAMs formed, depending on the amount of water present. An excess of water leads to polymerization of the silane, rather than monolayer formation, whilst an absence of water leads to an incomplete monolayer. So SAM formation from organosilane is technically more challenging than SAM formation from thiols on Au.[39,40]

1.2.2. SAMs formed from organosulfur

Organosulfur compounds are well known as good surfactants, which are used to prepare SAMs on different metal surfaces such as Au,[41] Ag,[42,43] Hg,[12] Cu,[44] Ni[45] and Pt.[46] However, most commonly the Au surface is used for two main reasons. Firstly, the surface is easy to activate *via* removal of a thin oxide layer, and secondly Au has a good affinity for sulfur.[47,48]

Alkanethiols (R-SH),[22,49] dialkyl disulfides (R-S-S-R),[50,51] dialkyl sulfides (R-S-R)[52,53] and thiophenes[54,55] are four types of organosulfur that have been used to form self-assembled monolayers (SAMs) on Au. Most studies have focused on R-SH surfactants due to the good understanding of the binding and ordering between the S atom of the thiol and surface Au atoms of the substrate to form the Au-thiolates,[13,42,56] as well as detailed understanding of the packing of the alkyl chains in the monolayer.[54]

The mechanism of R-SH/Au SAM formation proceeds *via* four stages (Figure 1.2):

Stage 1: involves the R-SH being physisorbed on to the Au substrate.[56]

Stage 2: the physisorption enables the SH headgroup to chemisorb onto the Au substrate by forming a S-Au bond**.**[13]

Stage 3: Subsequently, increasing the number of surfactants bound to the Au substrate leads to independent, sub monolayer, island formation, as the van der Waals interactions between the organics backbone units prevails over the organic backbone-surface interaction. The reorganisation of adsorbates in the Stage 3 reduces the free energy of the adsorbate molecules, although it is still high.[56]

Stage 4: The final stage is relatively slow as the islands grow and coalesce through further surfactant adsorbing to the increasingly crowded surface, as well as tilting of the surfactant between the adsorbed surfactants. The tilting optimizes the intermolecular interactions, such as van der Waals interaction and trans conformation in the chain-chain (backbone) between the alkanethiolates.[20,57,58]

The kinetics of Stages 1 and 2 are well studied, and it has been observed that the rates corresponding to these stages are relatively high and take only a few minutes to complete and the coverage of SAM approaches 80–90 % of the full coverage of the Au surface. Stages 3 and 4 are much slower and are dependent on backbone chain length. Increasing the chain length results in stronger van der Waals interactions, thus a thermodynamically more stable structure, but they have more non-trans C-C conformers in the backbone which need to anneal to trans C-C conformers in order to give good packing, and hence slow the final SAM formation.[59]

Kinetically, the rates of ordering and tilting of SAMs are slow and take several hours to complete.[58]

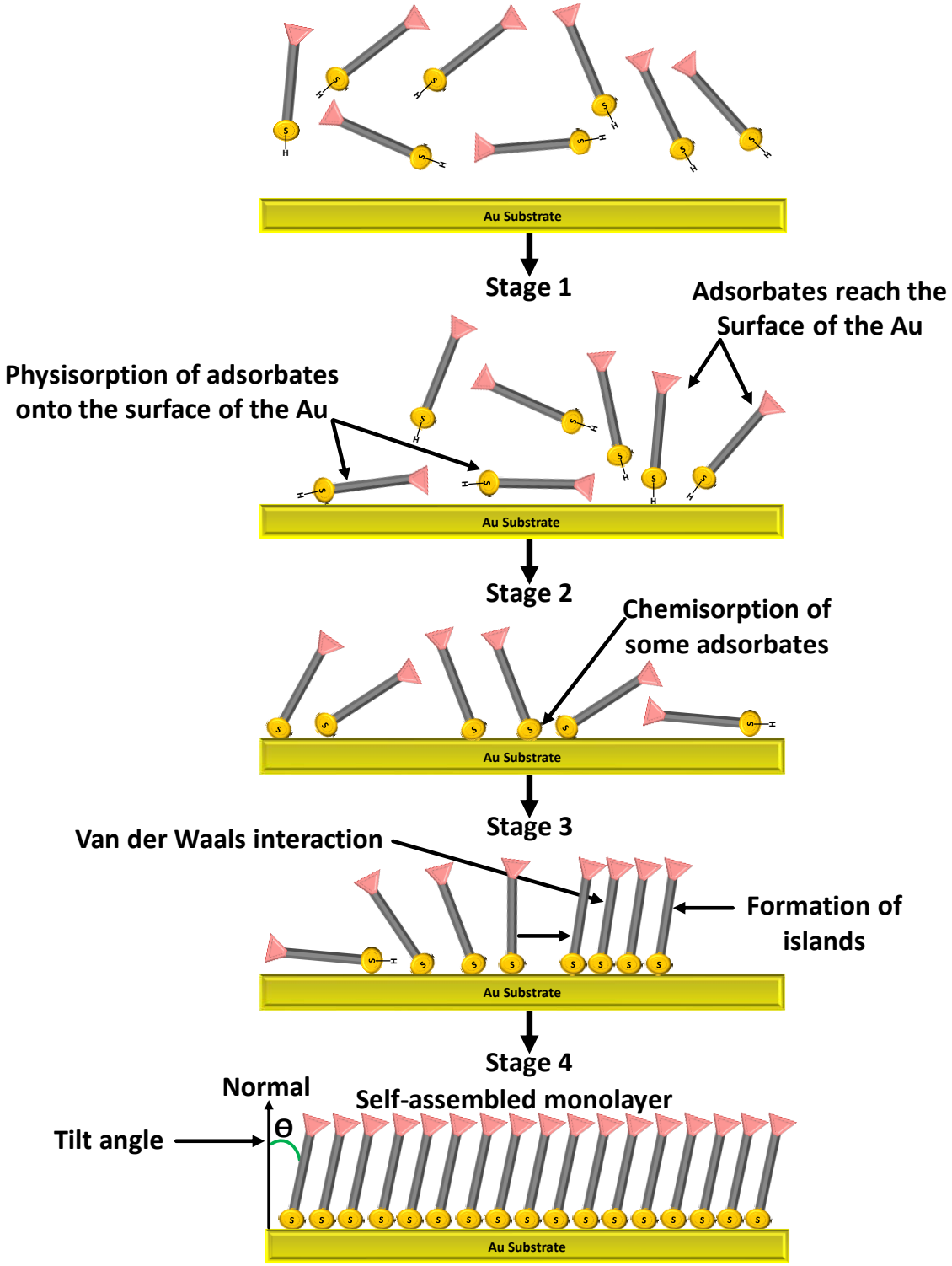

Figure 1.2: Schematic representation of the Stages of alkanethiol SAM formation on a Au surface

1.3. Characterisation of Surfaces – SAMs and Analytes Binding to SAMs

There are several types of techniques used to characterise surfaces. The characterisation of surfaces is important to firstly establish the composition of a SAM, but if the SAM is designed to have a Surface Functional Group that can recognise an analyte, then detection of the analyte adsorbed to the SAM surface is required. Thus, usually one thinks of these as two processes that need to be characterised sequentially, and one would use the following techniques for each process:

A. SAM characterisation

1. Surface type (hydrophilic or hydrophobic): contact angle.[60]

2. Thickness: ellipsometry[61]

3. Elemental composition: X-ray photoelectron spectroscopy (XPS).[62]

B. Adsorption of analytes to the SAM

1. Rate and amount of analyte adsorption:

    a. Surface plasmon resonance (SPR).[43,63]

    b. Quartz crystal microbalance (QCM).[64]

2. Surface structure after analyte adsorption: AFM,[10] TEM & SEM.[2]

However, that is not to say that techniques from A might be used in B and *vice versa*, *e.g*. if the analyte is large (1 nm or more) then ellipsometry could be used to monitor an increase in

thickness of the surface, or SPR can be used to monitor the kinetics of SAM formation. The next two sections (1.3.1 and 1.3.2) detail the techniques highlighted above.

1.3.1. SAM Characterisation

1.3.1.1. Contact angle measurements

Contact angle analysis gives information about the wettability[56] and energy[65,66] of the surface before and after the deposition of SAMs, which will be determined by the surface functional group, *e.g.* hydroxyl/amine/carboxyl groups give low water-contact angle whilst aryl and alkyl give high water-contact angle.[20,23] The principle of this technique measures the equilibrium forces between a liquid droplet on a solid substrate. These equilibrium forces arise from the intermolecular forces at the three phases boundary (solid, liquid and gas phase **(**Figure 1.3)), namely

(i) solid/liquid,

(ii) solid/gas, and

(ii) liquid/gas.

Thus, the angle which arises from the liquid droplet which is in contact with the solid substrate is referred to as the contact angle (CA).[67] There are three ways to measure the contact angle: (i) tilting plate,[68] (ii) dynamic,[69] and (iii) sessile drop.[70] In this chapter, the dynamic contact angle method will be discussed in detail (Figure 1.3).

Dynamic contact angle measurement involves a droplet of solvent being placed on a horizontal sample *via* a needle. Two limiting contact angles can be measured:

1. ***Advancing contact angle*** **(Θ_a)** is determined as the droplet increases in volume (as more water is injected into the droplet) without the footprint of the droplet changing, whilst the angle formed by the tangent of the water droplet and the solid interface increases. The advancing angle is the angle directly before the droplet increases its footprint.
2. ***Receding contact angle*** **Θ_r** is obtained when water is removed from the droplet to the point at which the footprint decreases.

Thus, the advancing contact angle (Θ_a) is always greater than the receding contact angle (Θ_r). The magnitude of the contact angle reflects the hydrophobicity of the terminal groups in the SAM, *i.e.* if the terminal group is hydrophilic a small contact angle is observed and *vice versa* for a hydrophobic group. Figure 1.3a, shows a small water contact angle on a hydrophilic SAM, whereas, Figure 1.3b shows a large water contact angle on a hydrophobic SAM. Thus, the hydrophilic surface is wetted whilst the hydrophobic surface is not, *i.e.* the water does not spread across the hydrophobic surface.

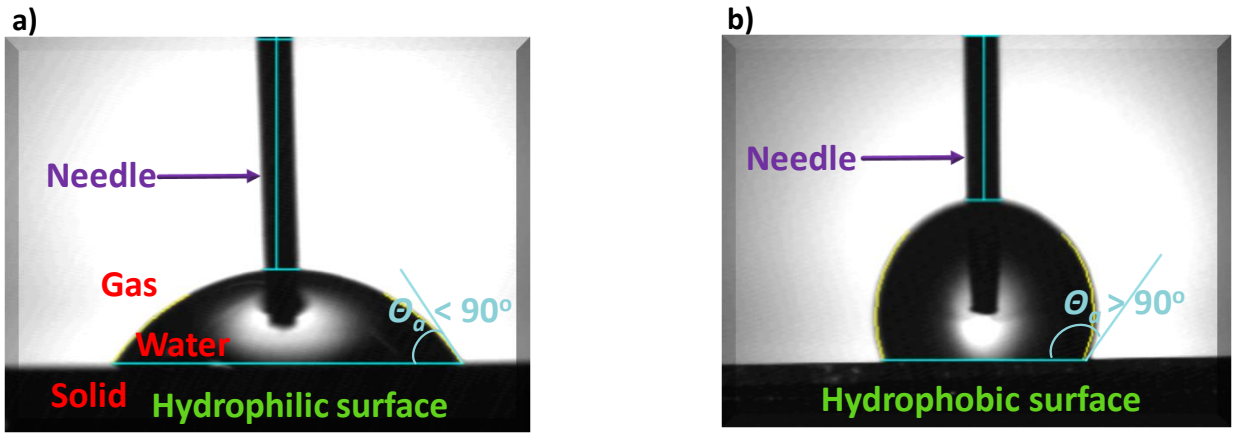

Figure 1.3: Illustrates the water advancing contact angle on a) hydrophilic SAM (wetted surface) and b) hydrophobic SAM at room temperature

The difference between Θ_a and Θ_r is known as the contact angle hysteresis (Equation 1.1).[20,69] When the surface is rough the difference between Θ_a and Θ_r is high, so the value of contact angle hysteresis ($\Delta\Theta$) is also high. In contrast on a smooth surface the $\Delta\Theta$ is low.[68]

$$\Delta\Theta = \Theta_a - \Theta_r \qquad \text{Where } \Delta\Theta \neq 0 \qquad \textbf{(Equation 1.1)}$$

1.3.1.2. Ellipsometry measurements

Ellipsometry is an optical, non-destructive technique, which is used to determine the thickness of SAMs by measuring the change in reflected elliptical polarised light from surfaces, after it has interacted with the surface (SAM), which by its very nature is anisotropically ordered, giving rise to birefringence of light interacting with it. The change in polarisation of the p and s wave components of the incident light (amplitude and phase), with the reflected light after it has interacted with the SAM allows calculation of the thickness of the monolayer, after approximating the refractive index of the SAM and applying a complex mathematical expression (Figure 1.4a).[71]

The ellipsometer can also aid in approximating the tilt angle (tilt angle is the angle formed between the molecular axis of the SAM forming molecules and the normal and the surface, **(**see Figure 1.4b) of the SAM by comparing the ellipsometric thickness with a theoretical molecular length of the molecular structure forming the SAM.[61]

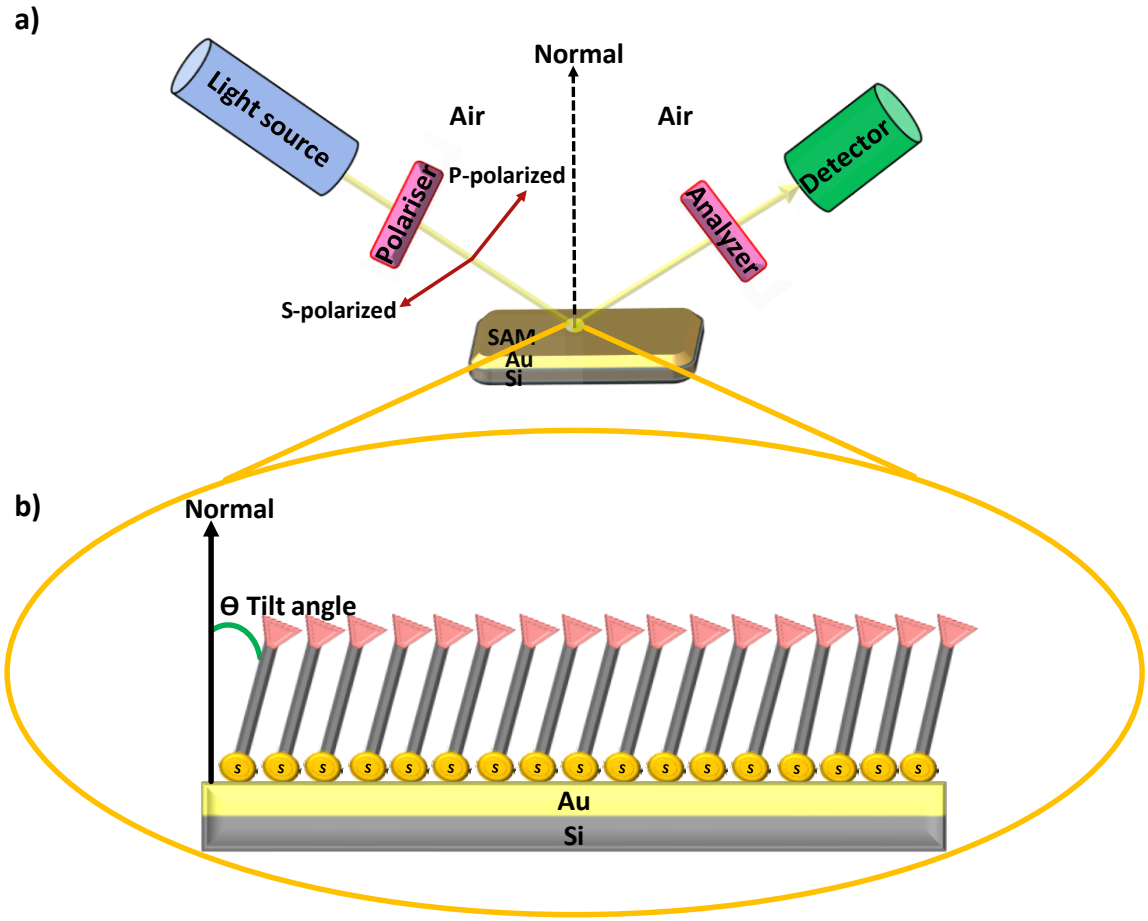

Figure 1.4: Schematic representation of a) ellipsometry measuring the thickness of SAM and b) tilt angle of the SAM deposited on a Au surface

1.3.1.3. X-ray photoelectron spectroscopy (XPS) measurements

X-ray photoelectron spectroscopy (XPS) is a technique to analyse the elemental composition of a sample. When a beam of X-rays impinges upon a surface (two common energy sources (Mg K_α: $h\upsilon$ = 1253.6 eV or Al K_α: $h\upsilon$ = 1486.6 eV) core electrons are excited in the atoms. If the X-ray energy is enough to overcome the electron binding energy (BE) of the atomic orbital then the electron can escape the atom, and form a photoelectron (Figure 1.5).

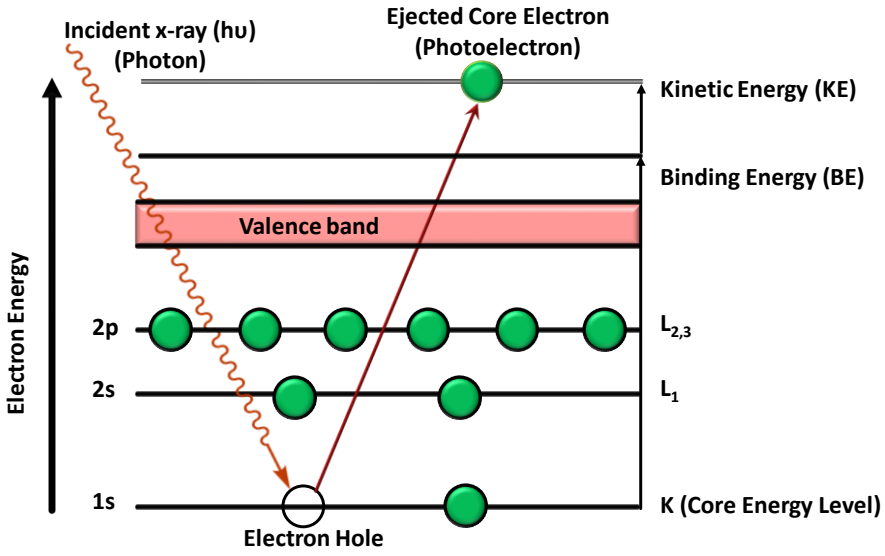

Figure 1.5: Schematic diagram of the XPS process, illustrating the ejection of a core electron by XPS photon

The binding energies (BE) of the ejected photoelectrons are specific to an element, thus allowing elemental composition to be determined. The binding energy of each element can be determined after applying equation 1.2.[72]

$$KE = h\upsilon - BE \qquad \textbf{(Equation 1.2)}$$

Where *hυ* represents the energy of the X-ray sources, and KE represents the kinetic energy of the photoelectrons detected from the XPS. The spectrum in the XPS technique of any element represents the plot of the number of ejected electrons (Y-axis) against the BE or KE of the ejected electrons (x-axis).[73]

1.3.2. Characterisation of the specific analytes deposited on SAM

When considering the binding of an analyte to a surface one is interested in two processes. Firstly, the binding event to the surface as a function of time, *i.e.* the rate of adsorption, and secondly the final state of the surface after analyte binding is complete. Techniques such SPR and QCM are able to monitor the rate of adsorption, whilst techniques such as AFM, and electron microscopy allow one to observe the final surface structure after the analyte has been adsorbed.

1.3.2.1. Surface Plasmon Resonance (SPR) measurements

SPR can measure adsorption kinetics in real time by following the change in the surface plasmon of a surface as the surface dielectric changes as a result of the analyte binding. Surface Plasmon Resonance (SPR) is an optical technique,[74,75] which has been used to detect the binding between a thin film on the SPR sensor and analytes in a subphase (Figure 1.6).[76] The term Surface Plasmon Resonance comes from the part of the energy of the incident light which will combine between a conductive metal and a dielectric material (organic material adsorbed on the metal). The SPR sensor consists of a glass substrate coated with a thin film of Au (~50 nm) (conducting metal) on to which a thin film or SAM can be deposited. The incident light passes through SPR sensor and reflects at the metal surface of the sensor. When the light reaches the metal surface at specific angle (Θ), part of it will be adsorbed to promote an electronic transition, called the surface plasmon, which is detected. If the SAM has recognition motifs on its surface, the dielectric (refractive index) of the material will change as analytes bind to the recognition motifs, and as a result the surface plasmon energy will change. This change in surface plasmon is therefore

related to the adsorption of the analyte to the surface. [63,76,77] As the changes in surface plasmon can be monitored in real time, kinetics of adsorption can be monitored.

The interaction (binding) causes in the change in the refractive index, which depends upon the concentration of the analytes at the film surface, and the binding constant. The angle of the reflected light in SPR will be shifted proportionally with change of refractive index.[63,76,77]

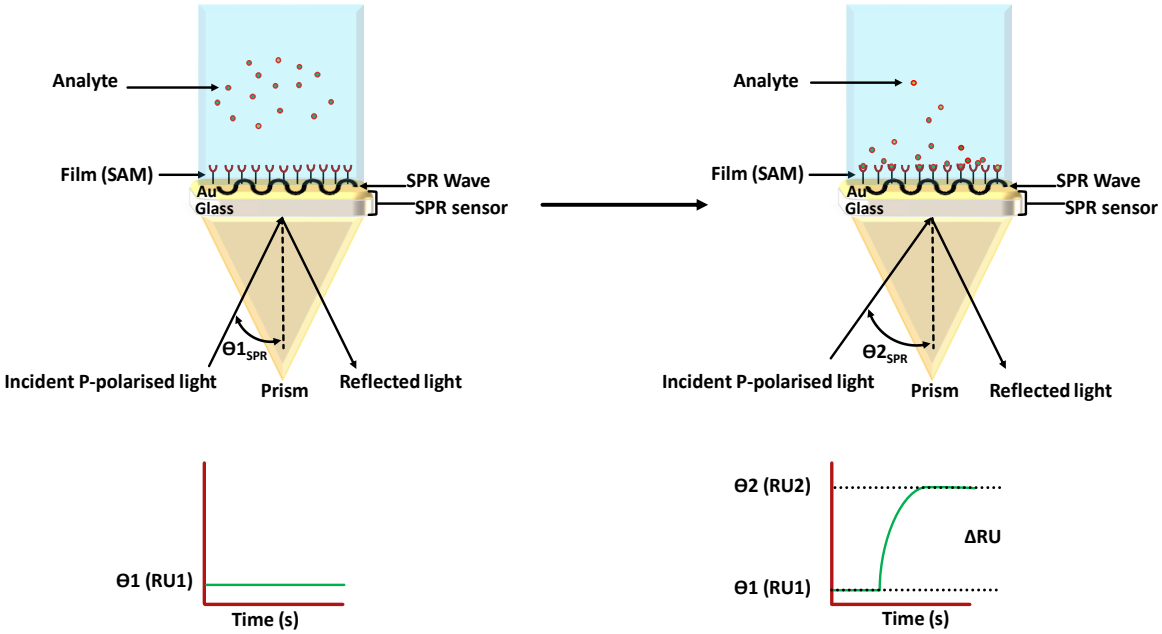

Figure 1.6: Schematic diagram of SPR measurements a) before, and b) during and after deposition of an analyte by following the changes in the incident angle

1.3.2.2. Quartz Crystal Microbalance (QCM) measurements

A QCM is a microbalance with nanogram mass sensitivity, which can measure adsorption kinetics in real time by following the change in the fundamental resonance frequency (FRF) of a

piezoelectric material as an analyte adsorbs to the surface. Using the Sauerbrey equation (Equation 1.3)[78] the change in the FRF can be converted to the adsorbed mass (*m*) of the analyte.[79–81]

$$\Delta m = -C\Delta f \qquad \textbf{(Equation 1.3)}$$

Where *C* represents the mass sensitivity constant of QCM-sensor and the value of *C* depends upon the FRF of QCM-sensor. For example, *C* is equal to 17.8 ng. Hz^{-1} cm^{-2} for a QCM-sensor with a FRF of 5MHz,[80,82–84] while *C* is equal to 4.5 ng. Hz^{-1} cm^{-2} for a QCM-sensor with a FRF of 10 MHz,[85–87] f_0 is the FRF, and Δf represent the frequency change ($f_a - f_0$), where f_a represents the frequency upon analyte binding. The highest sensitivity of the sensor is ~ 1 ng.cm^{-2}, where this sensitivity depends upon the stability of the oscillator and the resolution of the signal, which is ~1Hz.[88–92]

The circular QCM-sensor is made from AT-cut (35°) or BT-cut (49°) quartz crystal[80,82,85,90,93] [79] with varying thicknesses of quartz to tailor the FRF. An Au electrode is deposited on each side of the crystal quartz, and an electric potential drives the quartz to resonate at its FRF.

Figure 1.7 shows a QCM-sensor (AT-cut) which is made with same views. Figure 1.7 shows that the top electrode view which in contact with liquid is similar to the bottom one which is in contact with air.[92,94,95]

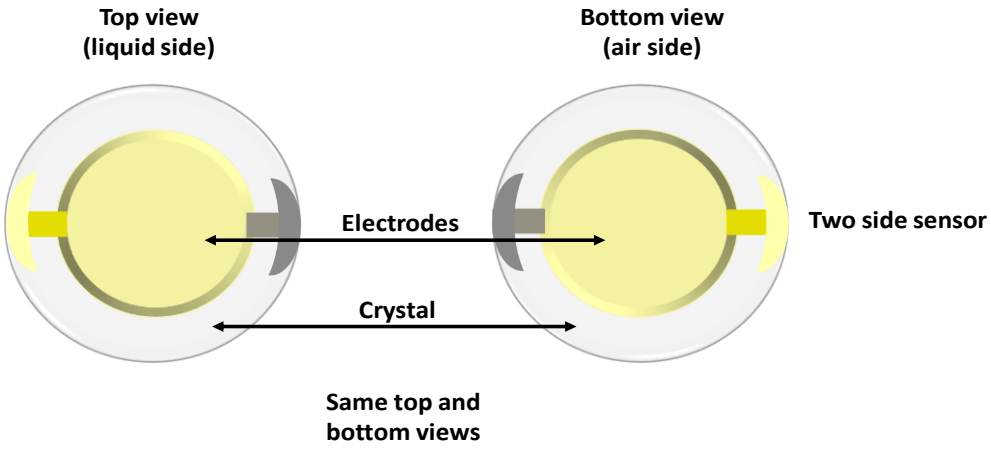

Figure 1.7: Cartoon represents an AT-cut QCM-sensor two sided sensor (same top and bottom views)

The QCM has been used to detect the mass of gas, when it is performed under vacuum[96] as well as to detect the mass of the analytes in liquid environments[85,97] (Figure 1.8) such as DNA,[98,99] proteins,[84,100,101] lipids,[80,102] antibodies[91,103,104] and nanoparticles.[105–108] The drawback of using QCM for liquid applications is that the liquid viscosity limits the sensitivity.[80,90,109]

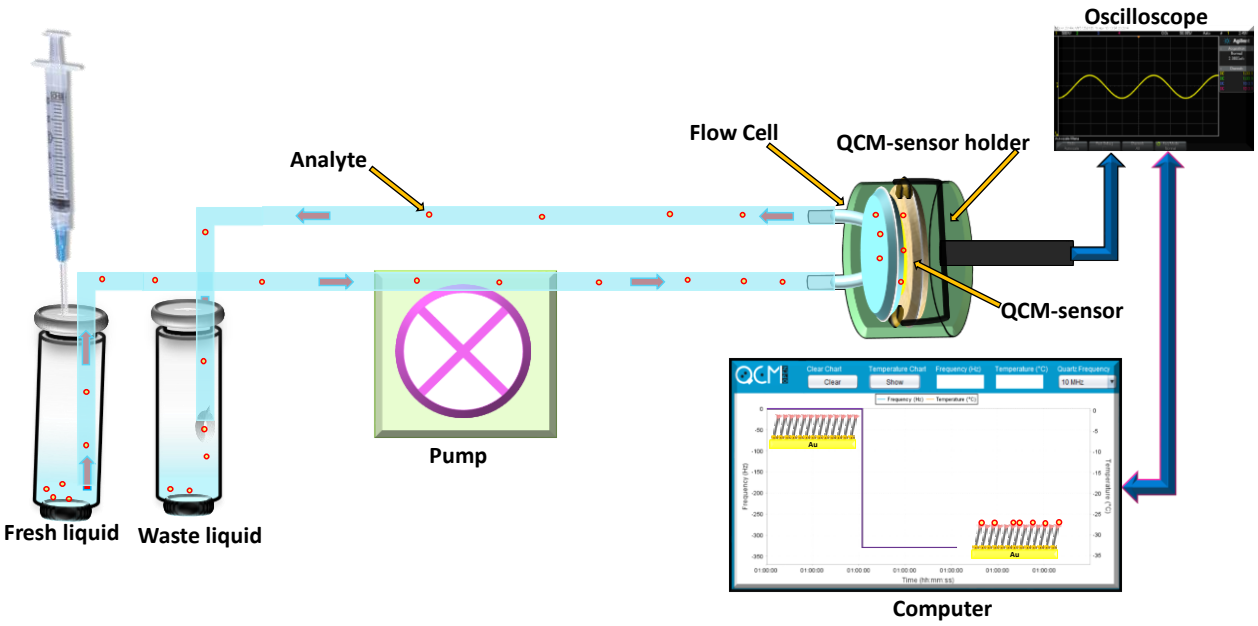

Figure 1.8: Schematic diagram of quartz crystal microbalance measuring the frequency in liquid

Plotting the change in the frequency as a function of time (Figure 1.8) enables the kinetics of analyte adsorption to be followed.[86,87]

1.3.2.3. Atomic Force Microscopy (AFM)

The invention of AFM in 1986 by Binnig *et al.*,[110] built upon on their Nobel prize winning the invention of the STM.[110] The AFM allowed not only nanometre topographical resolution imaging on conducting surfaces (as was the limit for STM), but also on insulating surfaces. An AFM consists (Figure 1.9) of a microfabricated flexible cantilever (silicon or silicon nitride), on which a tip is fabricated at one end, with a reflective surface on the opposite side of the cantilever from the tip, from which laser light is reflected onto a 4-sector photo-diode.[110] The tip is brought close to (or touching) a surface, such that a force between tip and surface causes a deflection of the cantilever, which is concomitantly transduced by the movement of the reflected laser light on the photodiode. Thus, as the tip is rastered across a surface a feedback mechanism can be transduced to give a topographical image of the surface. Depending on the sharpness of the tip and the roughness of the substrate sub-nanometer resolution can be attained. Thus, with a single atom at the end of a tip on an atomically smooth surface, atomic features are discernible.

Contact mode and tapping mode[111] are the two common approaches of collecting AFM topography images. In the contact mode, the tip which is hard, should be in direct contact with the surface, whilst in the tapping mode, the cantilever should vibrate close to it is resonance frequency and the tip is held a short distance from the substrate.[110]

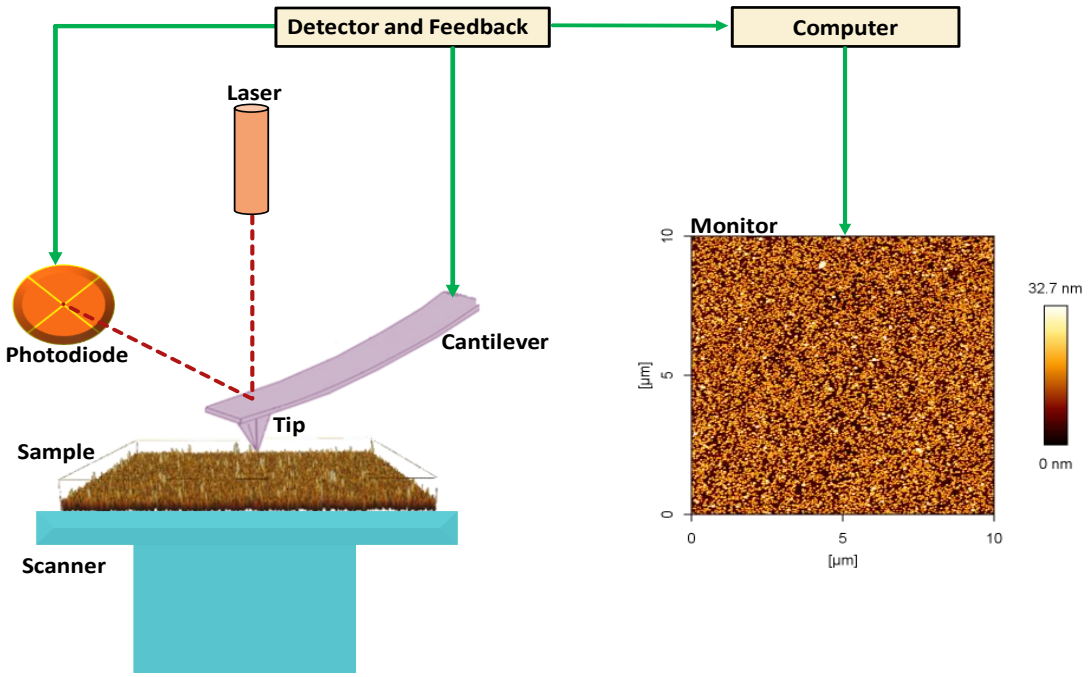

Figure 1.9: Schematic of AFM measurements

1.3.2.4. Transmission Electron Microscopy (TEM)

Images from this technique are obtained from the transmission of a collimated beam of electrons, which are passed through a thin film (thickness around 30 nm) of the sample.[56] The sample can be covered with a thin carbon or gold coating to ensure that the incident electron beam will not cause charging of the sample. The imaged features in the film by TEM represents the differences in the scattering or diffraction of the electron beam which is produced due to defects on surface structure (Figure 1.10), or chemical element variation.

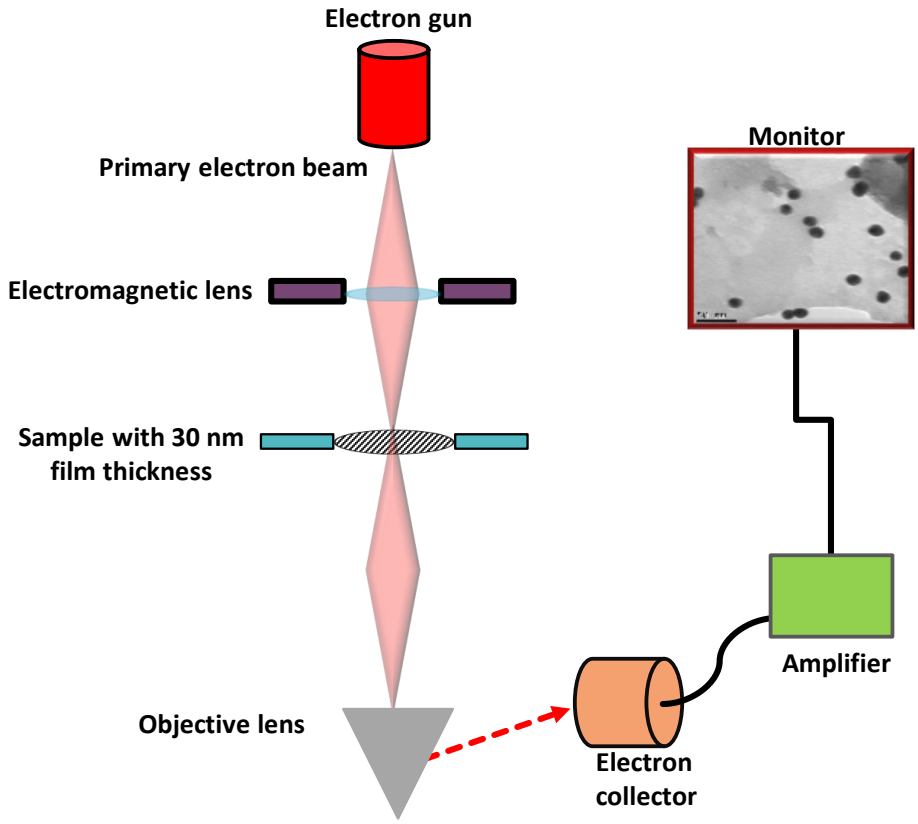

Figure 1.10: Schematic representation of TEM analytes measurements

1.3.2.5. Scanning Electron Microscopy (SEM)

Bombarding the surface of a sample with high energy primary electrons produces two types of emitted electrons:

a. backscattered electrons: these are primary incident electrons which are elastically scattered from the atoms of the sample and hence maintain a relatively high energy), and

b. secondary electrons: these arise from the primary incident beam inelastically hitting electrons in the atoms of the sample, resulting in the core electrons being ejected from the atoms.

The detection of backscattered and secondary electrons leads to the topography of the sample being revealed. Also, absorption of high energy primary electrons induces X-rays to be produced from the sample. These X-ray can be used for chemical analysis of the sample (Figure 1.11).[20,112]

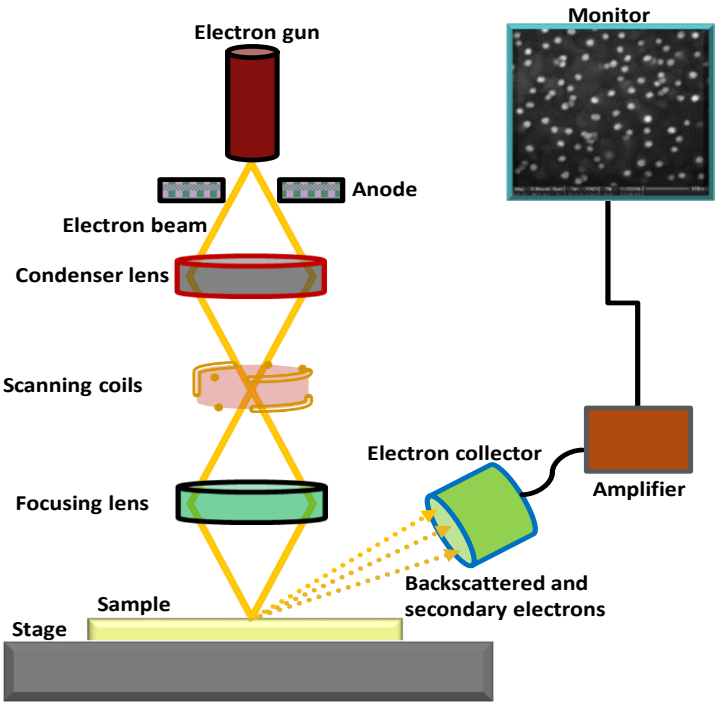

Figure 1.11: Schematic representation of SEM operation

1.4. Applications of SAMs

SAMs offer a facile way to change and manipulate the physical and chemical properties of a surface. This feature has led to potential applications such as (i) sensing nanoparticles,[113] nanotubes,[114] and biomolecules[115,116] to SAM surfaces tailored with recognition motifs, (ii) development of gold nanoparticles that can be used for drug delivery,[117,118] (iii) protection of metal surfaces from corrosion[24] and (v) chemical and biochemical sensors.[31,119] However, the

studies have been focused on (i) alkanethiols**,** because of the high affinity to modify metals surfaces,[58] and (ii) organosilane owing to excellent ability to alter silica surfaces, making them ideal for integration into silicon based electronics.[120] In recent years, many studies[113,121–124] have shown SAMs being formed on silicon nitride,[31,125,126]

A particularly interesting application of SAMs is integrating them in microelectromechanical systems (MEMS), which contain a sensing component (functionalised SAM) and an actuator (MEMS component covered with the SAM).[127] The actuator works *via* an electric potential driving a vibrational resonance proportional to the mass of the actuator, similar in principle to the QCM described previously but on the micron scale rather than the 1 cm scale.[128] Thus, as mass binds to the actuator there is a change in its resonant frequency which is proportional to the mass being bound to the sensing component.[129,130] A hydrophobic SAM (octadecanethiolate) deposited on Au/micro cantilever was used for the mass detection of bovine serum albumin (BSA), which were non-specifically immobilized on this SAM by Butt[129] In another example, the mass of DNA was detected by the use of a micro cantilever modified with a layer of Au onto which a SAM of gluteraldehyde-terminated cysteamine was deposited.[131] Gold nanoparticles (G-NPs) mass have been sensed using a Si_3N_4 micro-paddle coated with an amine-terminated silane SAM.[132] The purpose of utilizing amine (aliphatic or aromatic) as the functional group is that amine groups are protonated at low pH, and these protonated amino groups will electrostatically bind to the citrate stabilised G-NPs which are negatively charged. After electrostatically binding, the frequency of the resonator will change according to the increase in the deposited mass.[113,133,134]

1.4.1. Microelectromechanical systems (MEMS)

The term MEMS devices comes from the integration and fabrication of micromechanical and microelectronic components to afford functional micron scale devices.[135] Monocrystalline Si is the main material which is used for fabrication of MEMS[136] as Si is a flexible material with good fatigue properties, making it ideal for moving mechanical parts, whilst its semiconductive properties enable it to be integrated into electronic circuits.[137]

The chemical and physical detection of the types of MEMS devices such as switches, sensors and actuators[12,28,29,138–143] have been extensively researched focussed on the integration and fabrication of functional (sub)micron scale devices[144–147] (Figure 1.12).[148]

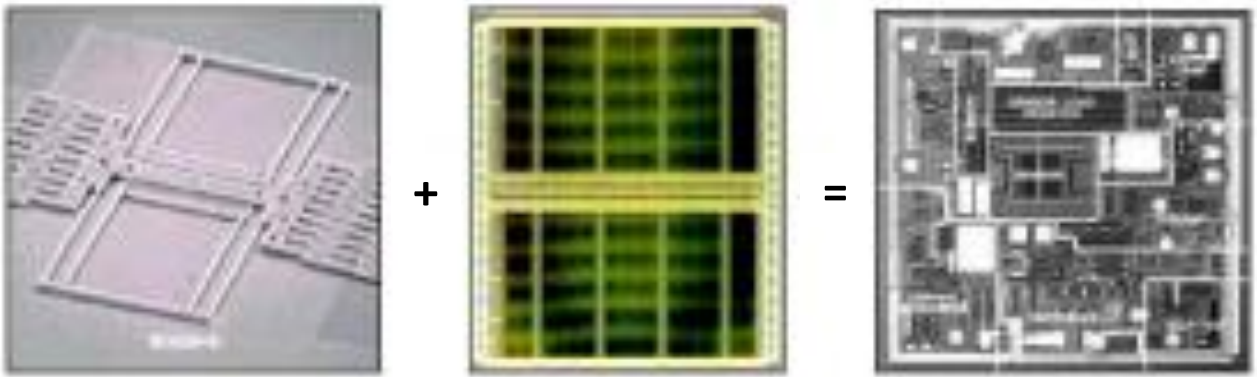

Figure 1.12: Example of a MEMS consisting of the mechanical structure and electrical systems (ref [148])

MEMS devices are fabricated using micro-machining techniques for example focused ion beam-milling[136] and bulk or surface micromachining[149,150] *i.e*. top-down approaches. These two methods are typically used to fabricate the MEMS devices and FIB will be discussed below.

1.4.1.1. Focused ion beam (FIB)

The principle of FIB is to create a focussed beam of gallium ions (Ga^+), ~10 nm diameter under UHV, which is directed to a surface (usually made from silicon nitride)[151,152] to ablate atoms from it (Figure 1.13),[136,153,154] to create microstructures such as paddles, which are the resonating component in the MEMS device.

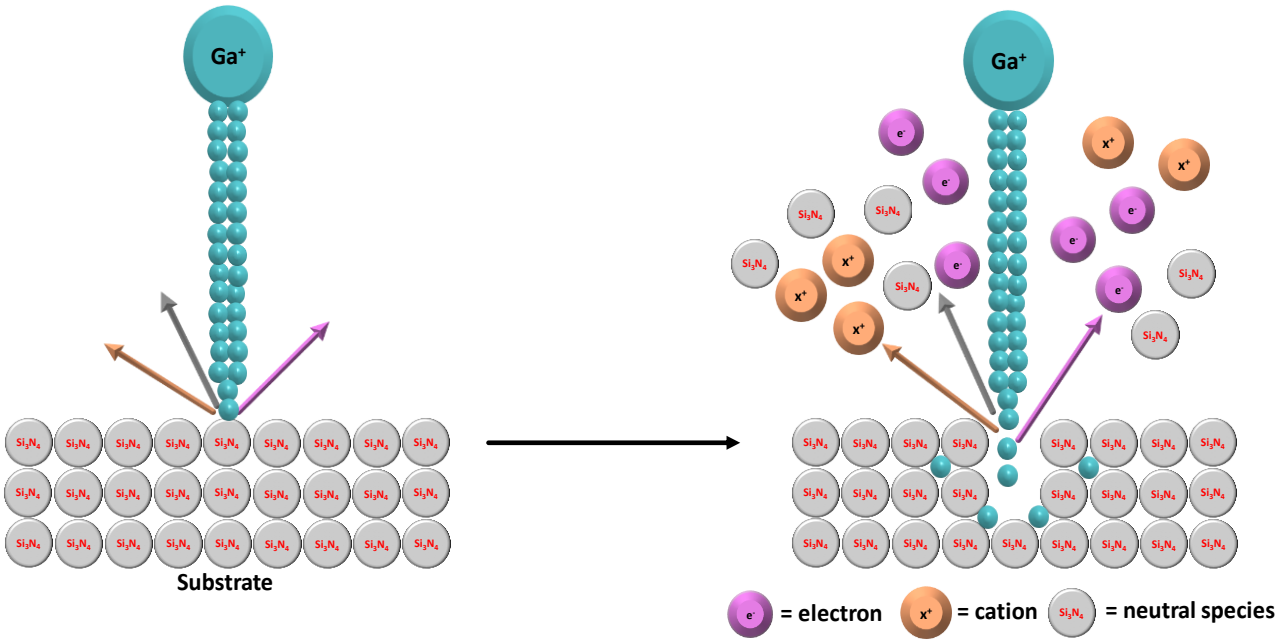

Figure 1.13: Cartoon of micro paddle fabrication using FIB

Another application of FIB is to use the Ga ions to induce a chemical decomposition reaction in organometallic species which have been deposited on the substrate surface.[155] As the decomposition reaction proceeds the organic component volatilises into the UHV chamber and the metal atoms aggregate to form metal nano/micron structures on the surface. The

disadvantage of this process is that the surfaces can be contaminated by carbonaceous material which come from the precursor molecules, in addition to the Ga ions (Figure 1.14).[156]

An example of such an application is using the precursor tungsten hexacarbonyl and trimethyl(methylcyclopentadienyl) platinum to create tungsten and platinum structures.[157]

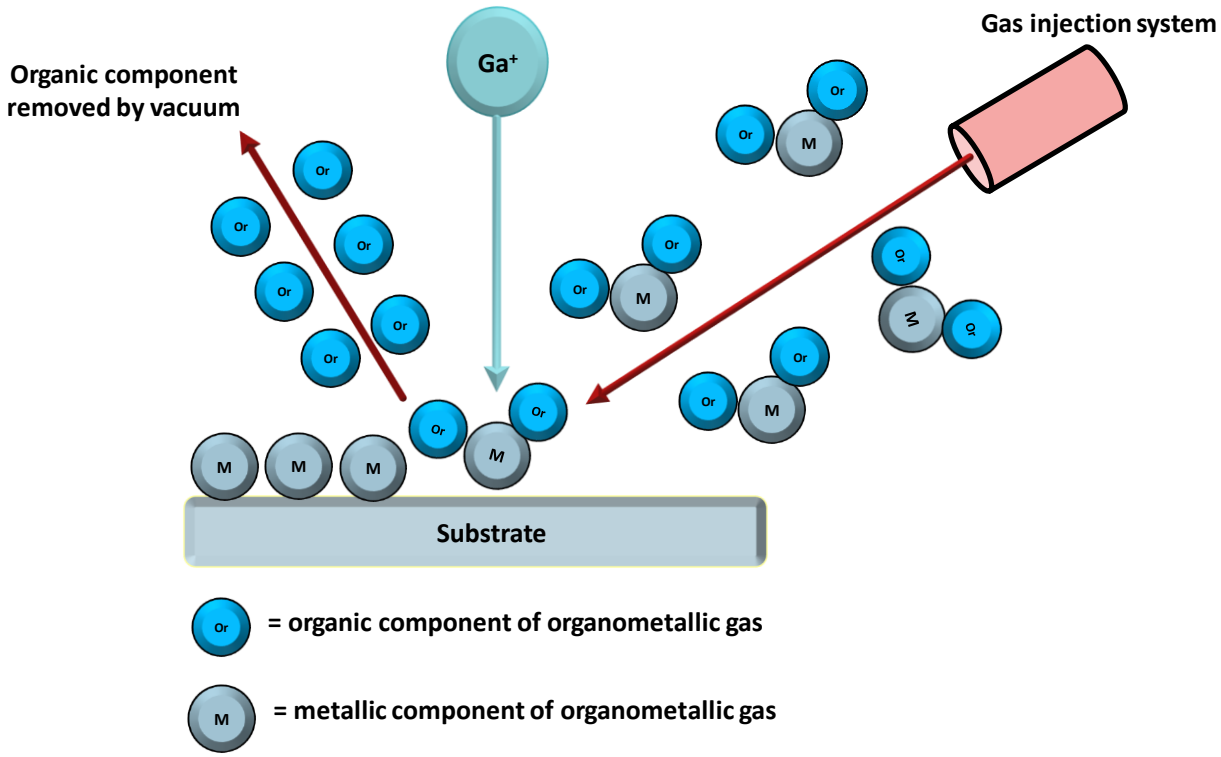

Figure 1.14:Cartoon of depositing precursors on metal surfaces using FIB

1.5. Hypothesis/Objectives of This Thesis

The purpose of the research described in this thesis is to produce sensors for specifically sensing different types of analytes, in a liquid environment, by integrating SAMs onto MEMS device.

Chapter 2 System 1 [binary SAMs consisting of biotinylated tri(ethylene glycol) thiol, undecanethiol (BUT) and (11-mercaptoundecyl) tetra(ethylene glycol) (TEG) for NeutrAvidin immobilisation], investigates the optimum concentration of biotin moieties in the binary SAM on an Au substrate required for the optimum immobilisation of the protein (NeutrAvidin). The necessary conditions required for optimum immobilisation of NeutrAvidin should be achieved with the aid of techniques such as SPR, QCM, AFM and XPS techniques.

Chapter 3 System 2, investigates the optimum conditions required for the monolayer formation of aliphatic (Alk) and aromatic (Ar) amine terminated SAMs on an Au substrate. The monolayer formation can be studied using CA, ellipsometry and XPS techniques.

Chapter 4 System 3, investigates the optimum conditions for the G-NPs deposition on a monolayer of Alk and Ar-amine-terminated SAMs at different pHs.

The purpose behind system 1 and 3 is to apply the optimum conditions for binding of the specific analyte to the SAM onto Au coated micro paddles so that the mass change caused by analyte deposition could be detected on the micro paddle and hence providing a practical example of a MEMS device.

1.6. References

[1] M. Kang, H. Kim, B. Han, J. Suh, J. Park and M. Choi, *Microelectron. Eng.*, 2004, **71**, 229–236.

[2] S. Carrara, D. Ricci, E. di Zitti, E. Di Fabrizio, M. Altissimo and M. Tormen, *Mater. Lett.*, 2006, **60**, 3682–3685.

[3] F. Hua, J. Shi, Y. Lvov and T. Cui, *Nano Lett.*, 2002, **2**, 1219–1222.

[4] S. C. Wu, C. F. Chen and W. C. Chao, *Microelectron. Eng.*, 2005, **77**, 277–284.

[5] J. Huang, A. R. Tao, S. Connor, R. He and P. Yang, *Nano Lett.*, 2006, **6**, 524–9.

[6] M. Yang, Y. Yang, Y. Liu, G. Shen and R. Yu, *Biosens. Bioelectron.*, 2006, **21**, 1125–31.

[7] J. Riu, A. Maroto and F. X. Rius, *Talanta*, 2006, **69**, 288–301.

[8] J. J. Gooding, F. Mearns, W. Yang and J. Liu, *Electroanalysis*, 2003.

[9] T. Hasobe, H. Imahori, P. V Kamat, T. K. Ahn, S. K. Kim, D. Kim, A. Fujimoto, T. Hirakawa and S. Fukuzumi, *J. Am. Chem. Soc.*, 2005, **127**, 1216–28.

[10] M. Geissler, H. Wolf, R. Stutz, E. Delamarche, U. W. Grummt, B. Michel and A. Bietsch, *Langmuir*, 2003, **19**, 6301–6311.

[11] A. S. G. Khalil, D. Konjhodzic and F. Marlow, *Adv. Mater.*, 2006, **18**, 1055–1058.

[12] M. Cohen-Atiya and D. Mandler, *J. Electroanal. Chem.*, 2003, **550**–**551**, 267–276.

[13] A. Ulman, *Chem. Rev.*, 1996, **96**, 1533–1554.

[14] L. Yan, C. Marzolin, A. Terfort and G. M. Whitesides, *Langmuir*, 1997, **13**, 6704–6712.

[15] G. Yang and G. Liu, *J. Phys. Chem. B*, 2003, **107**, 8746–8759.

[16] M. Wang, K. M. Liechti, Q. Wang and J. M. White, *Langmuir*, 2005, **21**, 1848–1857.

[17] L. Chrisey, *Nucleic Acids Res.*, 1996, **24**, 3031–3039.

[18] P. Laibinis, M. Fox, J. Folkers and G. Whitesides, *Langmuir*, 1991, **7**, 3167–3173.

[19] S. Frey, V. Stadler, K. Heister, W. Eck, M. Zharnikov, M. Grunze, B. Zeysing and a. Terfort, *Langmuir*, 2001, **17**, 2408–2415.

[20] A. Ulman, *An introduction to ULTRATHIN ORGANIC FILMS From Langmuir-Blodgett to Self-Assembly, Part-2: Langmuir-Blodgett Films*, Academic Press (San Diego), 1991, pp. 101–132.

[21] H. Sellers, A. Ulman, Y. Shnidman and J. E. Eilers, *J. Am. Chem. Soc.*, 1993, **115**, 9389–9401.

[22] N. Tillman, A. Ulman and J. F. Elman, *Langmuir*, 1989, **5**, 1020–1026.

[23] N. Mahmoodi, A. I. Rushdi, J. Bowen, A. Sabouri, C. J. Anthony, P. M. Mendes and J. A. Preece, *J. Vac. Sci. Technol. A Vacuum, Surfaces, Film.*, 2017, **35**, 041514.

[24] J. Scherer, M. R. Vogt, O. M. Magnussen and R. J. Behm, *Langmuir*, 1997, **13**, 7045–7051.

[25] N. Tillman, A. Ulman, J. S. Schildkraut and T. L. Penner, *J. Am. Chem. Soc.*, 1988, **110**, 6136–6144.

[26] L. Vroman, *Nature*, 1962, **196**, 476–477.

[27] P. M. Mendes and J. A. Preece, *Curr. Opin. Colloid Interface Sci.*, 2004, **9**, 236–248.

[28] N. J. Choi, Y. S. Lee, J. H. Kwak, J. S. Park, K. B. Park, K. S. Shin, H. D. Park, J. C. Kim, J. S. Huh and D. D. Lee, *Sensors Actuators, B Chem.*, 2005, **108**, 177–183.

[29] D. C. Meier, C. J. Taylor, R. E. Cavicchi, M. W. Ellzy, K. B. Sumpter and S. Semancik, *IEEE Sens. J.*, 2005, **5**, 712–725.

[30] B. Boonliang, P. D. Prewett, J. Hedley, J. Preece and C. A. Hamlett, *J. Micromechanics*

Microengineering, 2008, **18**, 1–4.

[31] S. C. Charandabi, P. D. Prewett, C. A. Hamlett, C. J. Anthony and J. A. Preece, *Microelectron. Eng.*, 2011, **88**, 2229–2232.

[32] J. C. Love, L. a Estroff, J. K. Kriebel, R. G. Nuzzo and G. M. Whitesides, *Chem. Rev.*, 2005, **105**, 1103–1169.

[33] S. Petitdidier, V. Bertagna, N. Rochat, D. Rouchon, P. Besson, R. Erre and M. Chemla, *Thin Solid Films*, 2005, **476**, 51–58.

[34] J. Sagiv, *J. Am. Chem. Soc.*, 1980, **399**, 92–98.

[35] P. Silberzan, L. Leger, D. Ausserre, J. J. Benattar and J. J. Silberzan, P. Léger, L. Ausserré, D. Benattar, *Langmuir*, 1991, **7**, 1647–1651.

[36] S. R. Wasserman, Y. T. Tao and G. M. Whitesides, *Langmuir*, 1989, **5**, 1074–1087.

[37] R. Maoz and J. Sagiv, *J. Colloid Interface Sci.*, 1984, **100**, 465–496.

[38] E. Cortés, G. Benitez, P. Carro, M. E. Vela and R. C. Salvarezza, *Langmuir*, 2009, **25**, 5661–6.

[39] J. D. Grange, J. L. Markham and C. R. Kurkjian, *Langmuir*, 1993, **7**, 1749–1753.

[40] B. C. Bunker, R. W. Carpick, R. A. Assink, M. L. Thomas, M. G. Hankins, J. A. Voigt, D. Sipola, M. P. de Boer and G. L. Gulley, *Langmuir*, 2000, **16**, 7742–7751.

[41] M. Tominaga, A. Ohira, Y. Yamaguchi and M. Kunitake, *J. Electroanal. Chem.*, 2004, **566**, 323–329.

[42] J. C. Love, J. K. Kriebel, R. G. Nuzzo and G. M. Whitesides, *Chem. Rev.*, 2005, **105**, 1103–69.

[43] T. T. Ehler, N. Malmberg and L. J. Noe, *J. Phys. Chem. B*, 1997, **101**, 1268–1272.

[44] M. M. Sung and Y. Kim, *Bull. Korean Chem. Soc.*, 2001, **22**, 748–752.

[45] S. Bengió, M. Fonticelli, G. Benítez, A. H. Creus, P. Carro, H. Ascolani, G. Zampieri, B. Blum and R. C. Salvarezza, *J. Phys. Chem. B*, 2005, **109**, 23450–23460.

[46] D. Y. Petrovykh, H. Kimura-Suda, A. Opdahl, L. J. Richter, M. J. Tarlov and L. J. Whitman, *Langmuir*, 2006, **22**, 2578–2587.

[47] D. Li, S. Chen, S. Zhao and H. Ma, *Colloids Surfaces A Physicochem. Eng. Asp.*, 2006, **273**, 16–23.

[48] T. Shimura and K. Aramaki, *Corros. Sci.*, 2008, **50**, 2407–2414.

[49] Y. Xue, X. Li, H. Li and W. Zhang, *Nat. Commun.*, 2014, **5**, 1–9.

[50] C. Jung, C. Jung, O. Dannenberger, O. Dannenberger, Y. Xu, Y. Xu, M. Buck, M. Buck, M. Grunze and M. Grunze, *Langmuir*, 1998, **14**, 1103–1107.

[51] H. Grönbeck, A. Curioni and W. Andreoni, *J. Am. Chem. Soc.*, 2000, **122**, 3839–3842.

[52] E. Sabatani, J. Cohen-boulakia, M. Bruening and I. Rubinstein, *Langmuir*, 1993.

[53] M. W. J. Beulen, B.-H. Huisman, P. A. van der Heijden, F. C. J. M. van Veggel, M. G. Simons, E. M. E. F. Biemond, P. J. de Lange and D. N. Reinhoudt, *Langmuir*, 1996, **12**, 6170–6172.

[54] M. Zharnikov, S. Frey, H. Rong, Y. Yang, K. Heister, M. Buck and M. Grunze, *Phys. Chem. Chem. Phys.*, 2000, **2**, 3359–3362.

[55] M. Haran, J. E. Goose, N. P. Clote and P. Clancy, *Langmuir*, 2007, **23**, 4897–4909.

[56] A. Ulman, *An introduction to ULTRATHIN ORGANIC FILMS From Langmuir-Blodgett to Self-Assembly, Part-3: Langmuir-Blodgett Films,* 1991.

[57] M. Himmelhaus, F. Eisert, M. Buck and M. Grunze, *J. Phys. chem. B*, 2000, **104**, 576–584.

[58] F. Schreiber, *Prog. Surf. Sci.*, 2000, **65**, 151–256.

[59] C. D. Bain, J. Evall and G. M. Whitesides, *J. Am. Chem. Soc.*, 1989, **111**, 7155–7164.

[60] S. D. EVANS, R. SHARMA and A. ULMAN, *Langmuir*, 1991, **7**, 156–161.

[61] H. Fujiwara, *Spectroscopic Ellipsometry Principles and Applications*, John Wiley and sons, Ltd (Japan), 2007.

[62] C. L. A. Lamont and J. Wilkes, *Langmuir*, 1999, **15**, 2037–2042.

[63] J. Homola, *Surface Plasmon Resonance Based Sensors*, Springer Berlin Heidelberg, Berlin, Heidelberg, 2006, vol. 4.

[64] T. W. Schneider and D. A. Buttry ', *J . Am. Chem. SOC*, 1993, **115**, 12391–12397.

[65] M. K. Chaudhury, *Mater. Sci. Eng. R Reports*, 1996, **R16**, 97–159 pp.

[66] J. A. Callow, M. E. Callow, L. K. Ista, G. Lopez and M. K. Chaudhury, *J. R. Soc. Interface*, 2005, **2**, 319–325.

[67] A. W. Adamson, in *Physical Chemistry of Surfaces*, Wiley Interscience (Chichester), 5th edn., 1990, p. 270.

[68] A. W. Adamson, in *Physical Chemistry of Surfaces*, Wiley Interscience (Chichester), 5th edn., 1990, p. 269.

[69] J. Lyklema, in *Fundamentals of Interface and Colloid Science Volume 3: Liquid-fluid Interface*, Acamdemic Press (London), 2000, p. 539.

[70] A. W. Adamson, in *Physical Chemistry of Surfcaes*, Wiley Interscience (Chichester), 5th edn., 1990, p. 265.

[71] H. Frey and H. R. Khan, *Handbook of Thin-Film Technology*, Springer Berlin Heidelberg, Berlin, Heidelberg, 2015.

[72] A. Zangwill, *Physics at surfaces*, Cambridge University Press, Cambridge, 1996.

[73] G. Attard and C. Barnes, *Surfaces*, Oxford University Press, Oxford, 1998.

[74] J. Spinke, M. Liley, H. G. L. Angermaierj and W. Knoll, *Langmuir*, 1993, **9**, 1821–1825.

[75] L. Häussling, H. Ringsdorf, F. Schmitt and W. Knoll, *Langmuir*, 1991, **7**, 1837–1840.

[76] L. S. Jung, C. T. Campbell, T. M. Chinowsky, M. N. Mar and S. S. Yee, *Langmuir*, 1998, **14**, 5636–5648.

[77] J. Lahiri, L. Isaacs, J. Tien and G. M. Whitesides, *Anal. Chem.*, 1999, **71**, 777–790.

[78] G. Sauerbrey, *Zeitschrift für Phys.*, 1959, **155**, 206–222.

[79] H. Anderson, M. Jönsson, L. Vestling, U. Lindberg and T. Aastrup, *Sensors Actuators, B Chem.*, 2007, **123**, 27–34.

[80] M. C. Dixon, *J. Biomol. Tech.*, 2008, **19**, 151–158.

[81] A. Baba, F. Kaneko and R. C. Advincula, *Colloids Surfaces A Physicochem. Eng. Asp.*, 2000, **173**, 39–49.

[82] S. H. Kristensen, G. A. Pedersen, L. N. Nejsum and D. S. Sutherland, 2013.

[83] B. D. Spangler and B. J. Tyler, *Anal. Chim. Acta*, 1999, **399**, 51–62.

[84] S. H. Kristensen, G. A. Pedersen, L. N. Nejsum and D. S. Sutherland, *Phys. Chem. B*, 2013, **117**, 10376.

[85] Z. A. Talib, Z. Baba, Z. Kurosawa, H. A. A. Sidek, A. Kassim and W. M. M. Yunus, *Am. J. Appl. Sci.*, 2006, **3**, 1853–1858.

[86] C. M. A. Brett, S. Kresak, T. Hianik and A. M. Oliveira Brett, *Electroanalysis*, 2003, **15**, 557–565.

[87] J. Li and Y. J. Yuan, *Langmuir*, 2014, **30**, 9637–9642.

[88] S. Kurosawa, E. Tawara, N. Kamo and Y. Kobatake, *Anal. Chim. Acta*, 1990, **230**, 41–49.

[89] L. Lin, H. qiu Zhao, J. ru Li, J. an Tang, M. xing Duan and L. Jiang, *Biochem. Biophys. Res. Commun.*, 2000, **274**, 817–820.

[90] C. K. O'Sullivan and G. G. Guilbault, *Biosens. Bioelectron.*, 1999, **14**, 663–670.

[91] M. M. Kamel, M. K., El Nimr, S. T., Assar, and A. S. Atlam, *Instrumention Sci. Technol.*, 2013, **41**, 473–489.

[92] S. J. Martin, G. C. Frye and K. O. Wessendorf, *Sensors Actuators A. Phys.*, 1994, **44**, 209–218.

[93] K. H. Choi, J. M. Friedt, F. Frederix, A. Campitelli and G. Borghs, *Appl. Phys. Lett.*, 2002, **81**, 1335–1337.

[94] M. Thompson, C. L. Arthur and G. K. Dhaliwal, *Anal. Chem.*, 1986, **58**, 1206–1209.

[95] G. V. Cimpoca, I. V. Popescu, I. D. Dulama, C. Radulescu, I. Bancuta, M. Cimpoca, I. Cernica, V. Schiopu, M. Danila and R. Gavrila, *Proc. Int. Semicond. Conf. CAS*, 2009, **1**, 135–138.

[96] W. H. King, *Anal. Chem.*, 1964, **36**, 1735–1739.

[97] M. Rodahl, F. Hook and B. Kasemo, *Doktorsavhandlingar vid Chalmers Tek. Hogsk.*, 1997, **68**, 2219–2227.

[98] W. Y. X. Peh, E. Reimhult, F. T. Huey, J. S. Thomsen and X. Su, *Biophys. J.*, 2007, **92**, 4415–4423.

[99] T. H. Nguyen and M. Elimelech, *Langmuir*, 2007, **23**, 3273–3279.

[100] M. M. Ouberai, K. Xu and M. E. Welland, *Biomaterials*, 2014, **35**, 6157–6163.

[101] F. Hk, M. Rodahl, P. Brzezinski and B. Kasemo, *Langmuir*, 1998, **7463**, 729–734.

[102] C. A. Keller and B. Kasemo, 1998, **75**, 1397–1402.

[103] M. V Voino, M. Jonson and B. Kasemo, *Biosens. Bioelectron.*, 2002, **17**, 835–841.

[104] S. Heydari and G. H. Haghayegh, *J. Sens. Technol.*, 2014, **4**, 81–100.

[105] M. J. Santos-Martinez, I. Inkielewicz-Stepniak, C. Medina, K. Rahme, D. Arcy, D. Fox, J. D. Holmes, H. Zhang and M. W. Radomski, *Int. J. Nanomedicine*, 2012, **7**, 243–255.

[106] A. A. Feiler, P. T. Davies and B. Vincent, *Soft Matter*, 2011, **7**, 6660–6670.

[107] K. Kubiak, Z. Adamczyk, J. Maciejewska and M. Oćwieja, *J. Phys. Chem. C*, 2016, **120**, 11807–11819.

[108] C. Grunewald, M. Schmudde, C. N. Noufele, C. Graf and T. Risse, *Anal. Chem.*, 2015, **87**, 10642–10649.

[109] M. Rodahl, F. Höök, C. Fredriksson, C. A. Keller, A. Krozer, P. Brzezinski, M. Voinova and B. Kasemo, *Faraday Discuss.*, 1997, **107**, 229–246.

[110] G. Binnig, C. F. Quate and C. Gerber, *Phys. Rev. Lett.*, 1986, **56**, 930–933.

[111] M. S. I. M. V. Digital Instruments Veeco Metrology Group and U. 4.31ce, Digital Instruments Veeco Metrology Group (Santa Barbara, USA), 1999, 2–7.

[112] M. Ohring, *The Materials Science of thin films*, Academic Press (Boston), 1992.

[113] C. A. E. Hamlett, P. T. Docker, M. C. L. Ward, P. D. Prewett, K. Critchley, S. D. Evans and J. A. Preece, *J. Exp. Nanosci.*, 2009, **4**, 147–157.

[114] M. M. Rahman, *Nat. Sci.*, 2011, **03**, 208–217.

[115] C. L. Yeung, P. Iqbal, M. Allan, M. Lashkor, J. A. Preece and P. M. Mendes, *Adv. Funct.*

Mater., 2010, **20**, 2657–2663.

[116] W. Shu, D. Liu, M. Watari, C. K. Riener, T. Strunz, M. E. Welland, S. Balasubramanian and R. A. McKendry, *J. Am. Chem. Soc.*, 2005, **127**, 17054–17060.

[117] C. Gonçalves, P. Pereira and M. Gama, *Materials*, 2010, **3**, 1420–1460.

[118] G. Zhu, J. Zheng, E. Song, M. Donovan, K. Zhang, C. Liu and W. Tan, *Proc. Natl. Acad. Sci. U. S. A.*, 2013, **110**, 7998–8003.

[119] B. Manning, S. J. Leigh, R. Ramos, J. a. Preece and R. Eritja, *J. Exp. Nanosci.*, 2010, **5**, 26–39.

[120] B. Gao, K. Sarveswaran, G. H. Bernstein and M. Lieberman, *Langmuir*, 2010, **26**, 12680–12683.

[121] R. Maboudian, W. R. Ashurst and C. Carraro, *Sensors Actuators, A Phys.*, 2000, **82**, 219–223.

[122] J.-J. Gau, E. H. Lan, B. Dunn, C.-M. Ho and J. C. S. Woo, *Biosens. Bioelectron.*, 2001, **16**, 745–755.

[123] N. Satyanarayana and S. K. Sinha, *J. Phys. D. Appl. Phys.*, 2005, **38**, 3512–3522.

[124] Y. Song, R. P. Nair, M. Zou and Y. Wang, *Nano Res.*, 2009, **2**, 143–150.

[125] T. Ito, M. Namba, P. Bühlmann and Y. Umezawa, *Langmuir*, 1997, **7463**, 4323.

[126] X. M. Lin, H. M. Jaeger, C. M. Sorensen and K. J. Klabunde, *J. Phys. Chem. B*, 2001, **105**, 3353–3357.

[127] N. K. Chaki and K. Vijayamohanan, *Biosens. Bioelectron.*, 2002, **17**, 1–12.

[128] L. L. Norman and A. Badia, *J. Am. Chem. Soc.*, 2009, **131**, 2328–2337.

[129] H.-J. Rgen Butt, *J. Colloid Interface Sci.*, 1996, **180**, 251–260.

[130] D. Fariña, M. Álvarez, S. Márquez, C. Dominguez and L. M. Lechuga, *J. Phys. D. Appl. Phys.*,

2015, **48**.

[131] D. A. Raorane, M. D. Lim, F. F. Chen, C. S. Craik and A. Majumdar, *Nano Lett.*, 2008, **8**, 2968–2974.

[132] J. A. Preece, C. A. E. Hamlett, P. T. Docker, M. C. L. Ward, P. D. Prewett, K. Critchley and S. D. Evans, *J. Exp. Nanosci.*, 2009, **4**, 147–157.

[133] T. Zhu, X. Fu, T. Mu, J. Wang and Z. Liu, *Langmuir*, 1999, **15**, 5197–5199.

[134] C. A. E. Hamlett, K. Critchley, M. Gorzny, S. D. Evans, P. D. Prewett and J. A. Preece, *Surf. Sci.*, 2008, **602**, 2724–2733.

[135] R. Maboudian, *Surf. Sci. Rep.*, 1998, **30**, 207–269.

[136] A. A. Tseng, *J. Micromechanics Microengineering*, 2004, **14**.

[137] W. Lang, *Mater. Sci. Eng. R Reports*, 1996, **17**, 1–55.

[138] J. Gong, Q. Chen, W. Fei and S. Seal, *Sensors Actuators, B Chem.*, 2004, **102**, 117–125.

[139] N. V. Lavrik, M. J. Sepaniak and P. G. Datskos, *Rev. Sci. Instrum.*, 2004, **75**, 2229–2253.

[140] T. E. Mlsna, S. Cemalovic, M. Warburton, S. T. Hobson, D. A. Mlsna and S. V. Patel, *Sensors Actuators, B Chem.*, 2006, **116**, 192–201.

[141] V. K. Varadan and V. V. Varadan, *Smart Mater. Struct.*, 2000, **9**, 953–972.

[142] F. Zee and J. W. Judy, *Sensors Actuators, B Chem.*, 2001, **72**, 120–128.

[143] W. Zhou, A. Khaliq, Y. Tang, H. Ji and R. R. Selmic, *Sensors Actuators, A Phys.*, 2005, **125**, 69–75.

[144] T. Akiyama, D. Collard and H. Fujita, *J. Microelectromechanical Syst.*, 1997, **6**, 10–17.

[145] J. M. Sallese and D. Bouvet, *Sensors Actuators, A Phys.*, 2007, **133**, 173–179.

[146] Y. hua Zhang, G. Ding, X. Shun, D. Gu, B. Cai and Z. Lai, *Sensors Actuators, A Phys.*, 2007, **134**, 532–537.

[147] M. T. a. Saif and T. A. Saif, *J. Microelectromechanical Syst.*, 2000, **9**, 157–170.

[148] P. F. Partnership, *Prime Faraday Technol. Watch*, 2002, 1–51.

[149] J. Oberhammer and N. Somjit, *IET Microwaves, Antennas Propag.*, 2013, **7**, 291–298.

[150] M. T. Stickel, P. C. Kremer and G. V. Eleftheriades, *IEE Proc. - Microwaves, Antennas Propag.*, 2004, **151**, 450.

[151] A. Peltonen, H. Q. Nguyen, J. T. Muhonen and J. P. Pekola, *J. Vac. Sci. Technol. B, Nanotechnol. Microelectron. Mater. Process. Meas. Phenom.*, 2016, **34**, 062201.

[152] M. Pettersson, M. Bryant, S. Schmidt, H. Engqvist, R. M. Hall, A. Neville and C. Persson, *Mater. Sci. Eng. C*, 2016, **62**, 497–505.

[153] B. Li, X. Tang, H. Xie and X. Zhang, *Sensors Actuators, A Phys.*, 2004, **111**, 57–62.

[154] D. Guo, X. Wu, J. Lei, B. Xu, R. Kometani and F. Luo, *Procedia CIRP*, 2016, **42**, 733–736.

[155] T. Morita, R. Kometani, K. Watanabe, K. Kanda, Y. Haruyama, T. Hoshino, K. Kondo, T. Kaito, T. Ichihashi, J. Fujita, M. Ishida, Y. Ochiai, T. Tajima and S. Matsui, *J. Vac. Sci. Technol. B Microelectron. Nanom. Struct.*, 2003, **21**, 2737.

[156] R. Puers and S. Reyntjens, *Sensors Actuators, A Phys.*, 2001, **92**, 249–256.

[157] S. Reyntjens and R. Puers, *J. Micromechanics Microengineering*, 2001, **11**, 287–300.

Chapter 2

Formation of Binary Biotin Containing SAMs to Study NeutrAvidin Binding Using SPR and QCM

Abstract

The integration of self-assembled monolayers (SAMs) with microelectromechanical systems (MEMS) opens a new approach for applications in nanotechnology *via* the surface functionalisation of the MEMS resonator for the detection of analytes. The sensing is a result of changes in resonance frequency upon deposition of the analyte to the chemically tuned MEMS surface. Thus, this chapter is concerned with chemically derivatising a MEMS surface to fabricate highly specific and sensitive sensors, making use of the recognition between surface mounted biotin and neutravidin as the analyte.

The model system that will be studied is a mixed binary SAM formed from a biotinylated tri(ethylene glycol) thiol, undecanethiol (BUT) and (11-mercaptoundecyl) tetra(ethylene glycol) (TEG) which acts as hydrophilic spacer (diluent), to which the protein NeutrAvidin is exposed to as the analyte. Eight different binary SAM compositions of BUT and TEG were studied to investigate the optimum NeutrAvidin binding, using the Surface Plasmon Resonance (SPR) technique. The characterisation of the 8 binary SAMs was achieved through multiple techniques (contact angle (CA), change in surface hydrophobicity), ellipsometry (SAM thickness), and X-ray Photoelectron Spectroscopy (XPS, SAM elemental composition)). A quartz crystal microbalance (QCM) was used to monitor the absorption of NeutrAvidin, which is immobilized on 2:1 of mixed SAMs on Au surface, also the results of QCM and Atomic Force Microscopy (AFM) reveal that the distribution of NeutrAvidin is as a monolayer on the biotin surface.

2.1. Introduction

Self-assembled monolayers (SAMs) of terminally functionalised alkyl and aryl thiols have been extensively used because of their spontaneous adsorption to Au and Ag surfaces, and their ability to modulate the physical and chemical properties of these surfaces by their terminal functionality.[1,2] The terminal group plays an important role in determining the wetting properties of solid surfaces,[3,4] and how the surfaces binds analytes.[5] Thus, SAMs have been employed for surface molecular recognition for use as potential sensor platforms.[6] This type of affinity[7] opens up many biological applications for molecular recognition on solid surfaces such as diagnostic assays,[8] delivery of therapeutics,[9] and biosensors.[10] For this purpose, biotin-terminated alkanethiols have been used for molecular recognition of proteins,[11–13] such as Streptavidin[14] or NeutrAvidin[15] (the difference between the Streptavidin and NeutrAvidin is that NeutrAvidin is free from carbohydrate which results in less lectin binding biotin. Thus, decreases the non-specific binding of NeutrAvidin with biotin),[16–18] which have a high affinity for the biotin moiety. These types of proteins are tetrameric, having four molecular pockets for biotin binding ($K_a = 10^{13}$ M or $K_d = 10^{-15}$ M). Where K_a and K_d, represent the association and dissociation constants for NeutrAvidin binding biotin respectively.,[11,13,19–21]

Chapter 1 (section 1.2.2) described the formation and properties of alkanethiolate self-assembled monolayer (SAM) on an Au substrate,[22–28] and how the surface chemical functionality of the Au substrate can be manipulated by the functional group of the alkanethiolate.[29–32] Therefore, the selection of the head group plays an important role when considering using such SAM surfaces as sensors for specific binding towards an analyte. However, the head

group/analyte binding cannot be considered in isolation when the headgroup is attached to a surface, because the approach trajectory of the analyte needs to be considered, as well as accessibility of the head group to the analyte. Thus, the spatial positioning and orientation of the head group on the surface needs to be considered as well, such that the analyte can approach and bind to the head group unhindered.

Overcoming this challenge is achieved by adding a spacer thiol (diluent) into the SAM which can spread out the functional headgroups, as well as provide orientational mobility for the head group.[33–36]

11-Mercaptoundecanol has been used as a spacer molecule in SAMs that have been co-adsorbed with thiols that have a functional group such as the biotin moiety, in order to create space around the biotin moiety so it can bind to avidin proteins,[37] as well as preventing non-specific protein adsorption, by virtue of the hydrophilic properties of the hydroxyl moiety.[38] For example, previously, 11-mercaptoundecanol was co-adsorbed with a biotin-terminated thiol to form a mixed SAM that was used for molecular recognition of the protein Streptavidin.[39] Although 11-mercaptoundecanol inhibits binding of protein to surfaces, Prime and Whitesides[40] reported mixed SAMs of 11-mercaptoundecanol adsorbs more proteins to their surface than mixed SAMs in which 11-mercaptoundecanol was replaced with thiols that presented oligoethylene glycols (OEG) to a protein containing subphase. Also, they found that simple methoxy-terminated SAMs have enhanced protein resistance relative to 11-mercaptoundecanol. Another study immobilized bovine serum albumin (BSA) which reduced the non-specific binding of NeutrAvidin.[41] In addition Catherine *et al.*[42] have reported that $HS(CH_2)_{11}(OEG)_mOH$ is soluble in ethanol and stable in air,

and can forms SAMs on Au rapidly and reproducible, as well as resisting protein absorption.

The ability of the OEG SAMs to resist protein adsorption is thought to correlate with the molecular conformation that the ethylene glycol units adopt in the SAMs deposited on Au or Ag surfaces, where all-gauche (helical) and all-trans (linear) conformations in the OEG moiety are formed, respectively (Figure 2.1). The helical conformation dominates on a Au surface due to the monolayers being less densely packed, relative to the Ag surface, which in turn encourages the more expanded helical conformation to dominate in Au monolayer.[43–47]

Both OEG conformations ability to resist surface protein adsorption have been extensively studied, revealing that the helical conformation on Au provides higher resistance to protein adsorption than the all-trans conformation on Ag surfaces.[40,43,48,49] Wang and Kreuzer[43,44] and Harder *et. al.*[45] rationalised that the resistance of protein adsorption on to the helical conformation on Au is due to its increased capacity to hydrogen bond to the water subphase, relative to the all-*trans* conformation on Ag.

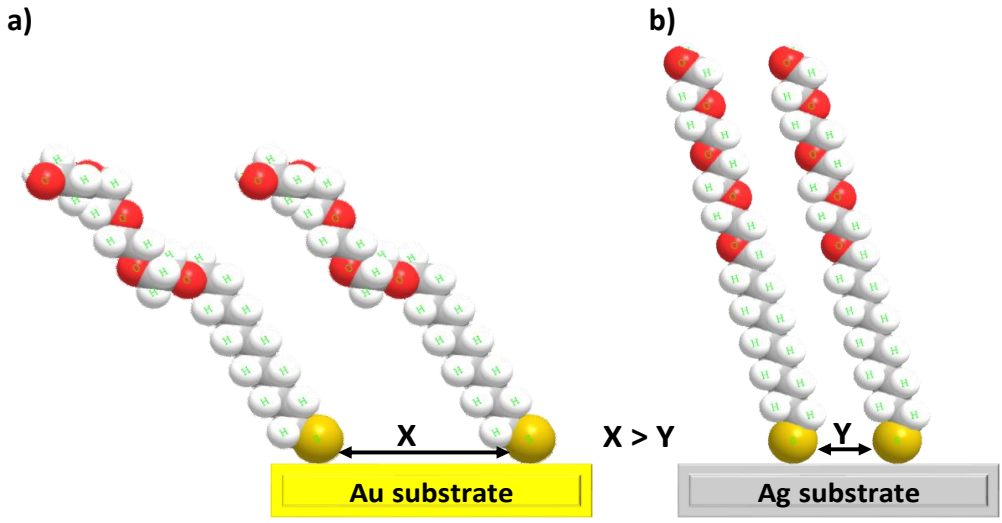

Figure 2.1: a) represents the helical conformation of OEG on an Au substrate, and b) non-helical conformation of OEG on an Ag substrate

The increased hydrogen bonding of the helical conformation arises due to the greater exposure of the ethylene oxy 'O' atoms to the subphase. This increased propensity to hydrogen bond to water molecules results in the helical conformation SAM having a thin hydrogen bonded layer of water molecules across the surface, which act as barrier to non-specific interactions with the proteins in the subphase.

2.2. Aim of the study in this chapter

This chapter investigates the chemical modification of the surface of a MEMS device (microresonator) with a binary SAM that can bind to NeutrAvidin in the subphase, and thus acting as a biological sensor. The MEMS surface is chemically modified through coating the surface with a layer of Au onto which a binary SAM of BUT and TEG is formed (Figure 2.2a,b). The BUT provides the binding moiety for Neutravidin *via* the presence of a biotin headgroup, whilst the TEG acts as a spacer for the biotin moieties (Figure 2.2c), in order to maximise the binding to the Neutravidin macromolecules (Figure 2.2d). TEG was specifically selected as the spacer for several reasons:

the theoretical difference in the chain length between the BUT molecule (Figure 2.2a) and the TEG molecule (Figure 2.2b) is 1.40 nm. This difference in chain length is the same as the size of biotin moiety reported in literature, which is around 1.40 nm.[50,51] This implies that the biotin moieties will be completely accessible for good insertion inside the pocket of a protein.

TEG is an excellent repellent to proteins due to presence of the ethoxy glycol moieties, as discussed earlier.[47]

the TEG coadsorbant has been utilised to space out biotin in SAMs, in previous studies, which have subsequently shown that the biotin binds Streptavidin or NeutrAvidin with greater efficiency when coadsorbed with the TEG spacer.[14,15,48]

SPR and QCM were used to study the optimum immobilization of NeutrAvidin on the mixed SAMs.

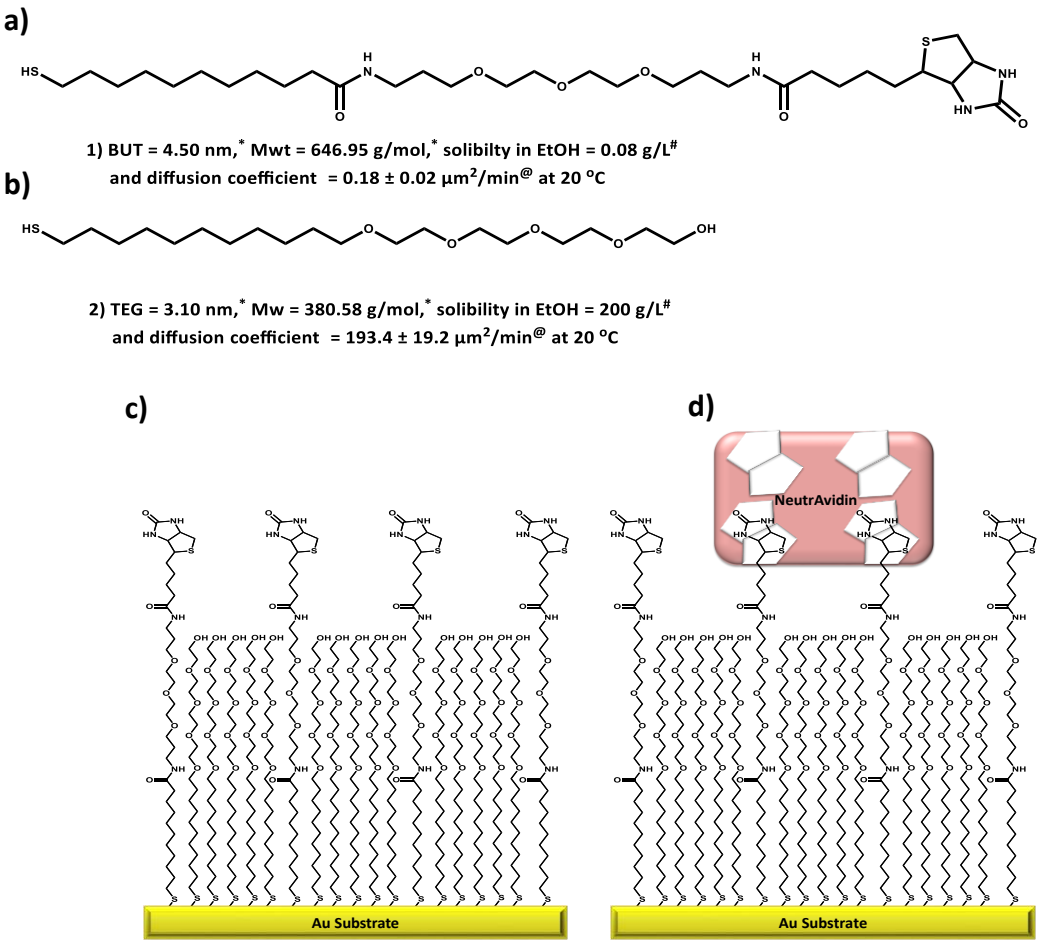

Figure 2.2: Illustrates the chemical structures of a) BUT and b) hydrophilic spacer (TEG), and the fully extended lengths calculated using ChemDraw, the difference between c) mixed BUT/TEG, and d) NeutrAvidin immobilized on mixed SAM BUT/TEG

** The data calculated from ChemBio Draw 3D Ultra.*

 # The data calculated practically in the lab.

@ The data collected from the literature.[52,53]

2.3. Results and discussion

2.3.1. Contact Angle and Ellipsometry: Formation, Stability and Characterization of pure BUT SAM

The literature suggests that the oxidation of the thiol moiety can be problematic both *during* SAM formation and *after* they have been formed when left dry and in air.[54] The former oxidation is a result of dissolved oxygen in the solution from which the SAM is formed, and the latter by atmospheric oxidation of the dry SAM.

Thus, in order to evaluate the propensity of the BUT system to oxidise in these two scenarios, three experiments were designed:

Experiment 1: The SAM forming solution was not degassed with N_2 gas, and the SAMs were characterised immediately after their formation by contact angle and ellipsometry

Experiment 2a: SAM forming solution was degassed with N_2 gas, and the SAMs were characterised immediately after their formation by contact angle and ellipsometry, and

Experiment 2b: a continuation of Experiment 2a where the SAM characterisation was repeated after 7 days (stored in a closed vial, inside a fume hood at 20 ^oC).

Thus, a comparison of the SAMs formed under the conditions relating to Experiments 1 and 2a will allow an assessment of the oxidation *during* SAM formation, whereas comparing Experiments 2a and 2b will allow an assessment of oxidation *after* 7 days of SAM aging in air. Contact angle and ellipsometry were used to establish any differences in the SAMs under these three experi-

mental conditions (Table 2.1).

Table 2.1: Contact angle and ellipsometry measurements (twenty seven measurements performed for each experiment) of the BUT SAM deposited on Au surface under degassed and non-degassed N_2 conditions and characterized immediately and after 7 days in air.

		Experiment		
		1	***2a***	***2b***
Experimental Parameters Varied	**SAM[a] Solution degassed with N_2**	No	Yes	Yes
	Aging prior to characterisation	Immediate	Immediate	7 Days
Characterisation				
Contact Angle	**Θ_a(^{O})**	77 ± 0.86	67 ± 0.78	67 ± 1.14
	Θ_r(^{O})	52 ± 1.2	40 ± 1.05	42 ± 0.97
Ellipsometry[b]	**SAM Thickness (nm)**	3.30 ± 0.15	2.92 ± 0.20	2.83 ± 0.40
	Tilt angle[c](^{O})	43	50	51

[a] BUT SAMs were formed over 24 h, by immersion of a cleaned Au substrate in HPLC ethanolic (degassed with N_2 gas or not) solution of BUT (0.1 mM) for 24 h, followed by rinsing with HPLC ethanol and drying with N_2 gas.
[b] refractive index of 1.475 used for ellipsometric SAM thickness determination.
[c] tilt angle was calculated according to cos Θ = SAM thickness (nm)/theoretical length (4.50 nm)[d].
[d] 4.50 nm for BUT, calculated by using ChemBio Draw 3D Ultra.

Examination of the data in Table 2.1 reveals:

1. a significant difference between Experiments 1 and 2a in that the contact angles and ellipsometric thickness are significantly smaller in the degassed SAM formation conditions, but
2. no significant difference between Experiments 2a and 2b, where the contact angles and SAM thickness are similar.

On the basis of evidence in Table 2.1, it is reasonable to conclude that oxidation is occurring *during* the formation of the SAM and not *after* formation, and literature showing

oxidation of thiols in SAMs.[54,55]Further work to elucidate the exact mechanism of degradation in oxygenated solvent, such as spectroscopy, would advantageous in future work. Thus, for all experiments in this Thesis SAMs will all be formed in degassed solvents, and will be stored for no longer than 7 days before further manipulation.

It is clear to see that the ellipsometric SAM thickness of BUT (~2.9 nm, Table 2.1) is shorter than the modelled thickness (~4.5 nm, Figure 2.2a). To understand the discrepancy in detail for such a complex surfactant as BUT would require a detailed structural study, which is not conducted here. However, it is known that conformational preferences to maximise van der Waal interactions between adjacent molecules are important,[29,56] as is the number of atoms in an alkyl chain that determine the tilt of the surfactant in the monolayer, once again to maximise interactions between adjacent molecules.[57–62] Thus, undoubtedly a complex interplay of a number of factors results in the discrepancy, which is not that unexpected, given the bulky nature of biotin relative to the alkyl chain linking it to the surface. Recent studies[57–62] have attributed the main reason for the high difference between theoretical and experimental thickness is related to the tilt of the terminal group and this arises from the odd and even effect of atoms in the backbone. Thus, the tilt angle of the terminal group of an alkyl chain consisting of an even number of methylene units is 0^{o} from the normal to the surface, whereas, the tilt angle of terminal group of the alkyl chain containing an odd-number of methylene units is oriented at 60^{o} from the normal to the Au surface. Thus, it could be assumed that the marked discrepancy between theoretical and experimental thickness of this type of BUT SAM which consists of eleven methylene moieties

suffers from the even and odd-numbered effect. Hence, the tilt angle for the terminal group biotin will be 60^{o} from the normal to the Au surface. [63,64]

2.4. Formation and Characterization of Pure BUT & TEG and Their Binary SAMs

Three Au slides were immersed for 24 h in:

i) Degassed 0.1 mM ethanolic solution of BUT,

ii) Degassed 0.1 mM ethanolic solution of TEG, and

iii) Eight degassed ethanolic binary solutions comprised of BUT (0.1 mM) and TEG (0.1 mM) combined in volumes as detailed in Table 2.2. The molar percentage of BUT in solution was calculated using equation 2.1.

Each SAM was then rinsed with HPLC ethanol and dried under a stream of N_2.

$$Mol\ \%^{BUT} = V^{BUT} / (V^{BUT} + V^{TEG}) \qquad \textit{(Equation 2.1)}$$

Table 2.2: Mixing volumes of ethanolic solutions of 0.1 mM of BUT and TEG

0.1 mM V^{BUT}	0.1 mM V^{TEG}	Mol $\%^{BUT}$ in solution
0.5	5.0	9.1
1.0	5.0	16.6
2.0	5.0	28.5
3.0	5.0	37.5
4.0	5.0	44.4
5.0	5.0	50.0
7.5	2.5	75.0
8.5	1.5	85.0

The contact angle and ellipsometric characterisation data for the pure and mixed SAMs are summarised in Table 2.3. Each data point is the average of nine measurements being made on each of the three SAMs, *i.e.* the average of twenty seven measurements.

Table 2.3: The contact angles and ellipsometric thickness of the pure and binary BUT and TEG SAMs

Theoretical Calculations ChemBio Draw 3D Ultra (nm)	**Molar % of BUT in *Solution* with TEG**	**Θ_a (H_2O) (^{o})**	**Θ_r (H_2O) (^{o})**	**$\Delta\Theta$ (^{o})**	**Molar % of BUT on *Surface* with TEG from Cassie eq. (see section 2.4.1)**	**Average Experimental Thickness of three fresh samples (nm)**
TEG = 3.10	**0.0**	**36 ± 0.50**	**28 ± 0.62**	**8 ± 0.78**	**0.0**	**2.21 ± 0.10**
	9.0	44 ± 0.70	34 ± 0.92	10 ± 0.91	27.0 ± 2.0	2.18 ± 0.16
	16.6	46 ± 1.27	34 ± 0.94	12 ± 1.36	29.0 ± 0.6	2.13 ± 0.01
	28.5	52 ± 0.82	38 ± 0.86	14 ± 1.06	47.0 ± 2.0	2.05 ± 0.06
	37.5	56 ± 0.63	38 ± 0.75	17 ± 0.95	58.6 ± 1.0	2.14 ± 0.04
	44.4	57 ± 0.68	39 ± 0.50	18 ± 0.82	62.9 ± 1.0	2.15 ± 0.05
	50.0	58 ± 0.90	39 ± 1.33	19 ± 1.38	66.0 ± 0.5	2.16 ± 0.10
	75.0	60 ± 0.85	37 ± 0.93	23 ± 0.75	74.7 ± 3.0	2.04 ± 0.03
	85.0	63 ± 1.30	38 ± 0.95	25 ± 1.43	84.6 ± 2.0	2.02 ± 0.06
BUT = 4.50	**100.0**	**67 ± 0.78**	**40 ± 1.05**	**27 ± 0.96**	**100.0**	**2.92 ± 0.20**

2.4.1. Water Contact Angle

The advancing and receding contact angle for TEG and BUT were similar to what have been reported in the literature for polyethylene glycol (PEG) and other biotin terminated SAMs, respectively.[42,65] As one might expect, as the mole fraction of BUT increases in the solution forming the SAM, the contact angle approaches the pure BUT contact angle (reflecting the increasing amount of BUT in the SAM). Indeed, sixty years ago, Cassie reported an equation to describe the composition of a surface by using its wetting properties, as determined by the contact angle. The mole fraction of BUT and TEG in the SAM formed on the Au surfaces were calculated according to the Cassie equation.[66]

$$\cos \Theta^C = f_1 \cos \Theta_1 + f_2 \cos \Theta_2 \qquad \textit{(Equation 2.2)}$$

Where $\cos \Theta^C$ represents the cosine of the advancing CA of each of the eight mixed BUT and TEG SAM; $\cos \Theta_1$ and $\cos \Theta_2$ are the cosine of the CA of pure BUT SAM (67°) and pure TEG SAM (36°); f_1 represents the mole fraction of BUT on Au surface in mixed SAM, and f_2 represent the mole fraction of TEG on Au surface in the mixed SAM, and because of $f_1 + f_2 = 1$, thus $f_2 = 1 - f_1$. After applying the Cassie equation to the CA data shown in Table 2.3, the mole fraction of BUT (f_1) and TEG (f_2) on the surface of the Au can be determined. Figure 2.3 shows the correlation between the mole fraction of BUT and TEG in the mixed solution and on the Au surface. Interestingly, it can be observed that the deposition ratio of BUT molecules (for 50% in solution is about 65% adsorbed into the SAM (Figure 2.3a) on the clean Au surface, which is higher than the (TEG) molecules which is about 35%) (Figure 2.3b) on the Au surface. There is not a clear explanation for the deviation of the deposition ratios 75% and 85% from the other data points (Figure 2.3a).

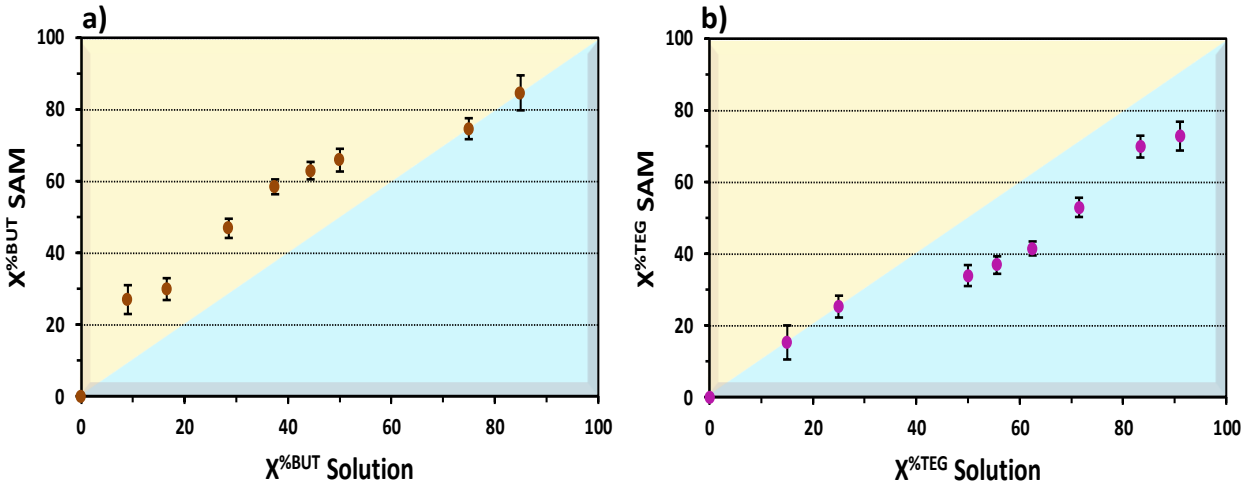

Figure 2.3: Shows the difference between the mol% of a) BUT in the SAM and b) TEG SAM relative to the mol% of BUT and TEG in the SAM forming solution, as deduced by the Cassie equation

Previously, Laibinis and Whitesides[67] studied the effect of the polar solvent ethanol on the deposition ratio of long chain (less polar) and short chain (more polar) alkanethiols. From these experiments, it was observed that the deposition rate of long chains was higher than the short chains on the Au surface. It was postulated that this was due to the dipole-dipole interaction between the solvent and the solute. This interaction increased with the shorter and relatively more polar chains. For example, ethanol is a polar solvent and thus, will have a higher solubility for polar alkanethiols than nonpolar alkanethiols. Therefore, TEG will prefer to remain solubilised more than BUT, and hence BUT will deposit more rapidly than TEG onto the Au (Figure 2.3).

The contact angle data of the mixed surface SAMs decreases with increasing the percentage of BUT in the mixed surface (Figure 2.4), as expected as the pure BUT SAM is more hydrophobic than the pure TEG SAM, and is in agreement with literature for CA measurements of biotin-terminated alkanethiolate.[12,68,69]

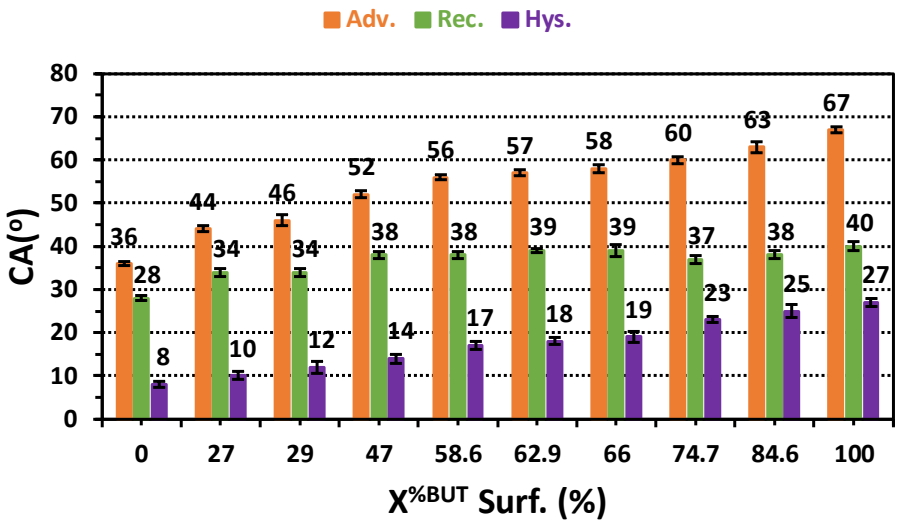

Figure 2.4: Illustrates the advancing angle, receding angle and hysteresis of pure and eight different mixtures of BUT SAM and TEG SAM on Au surface

2.4.2. Ellipsometry

The ellipsometric thickness for TEG SAM was observed as 2.21 ± 0.10 nm, which is ~1 nm shorter than the extended length (Figure 2.2b). This reduction is presumably a result of molecular tilt and the helical conformation of the oligoethylene glycol (OEG).[58,61,62,64] Moreover, unlike the contact angle trend, the ellipsometric thickness of pure TEG and all binary BUT:TEG SAMs are the same within experimental error in the range of 2.1–2.2 nm (Figure 2.5), whilst a pure BUT SAM is significantly longer at ~2.9 nm.

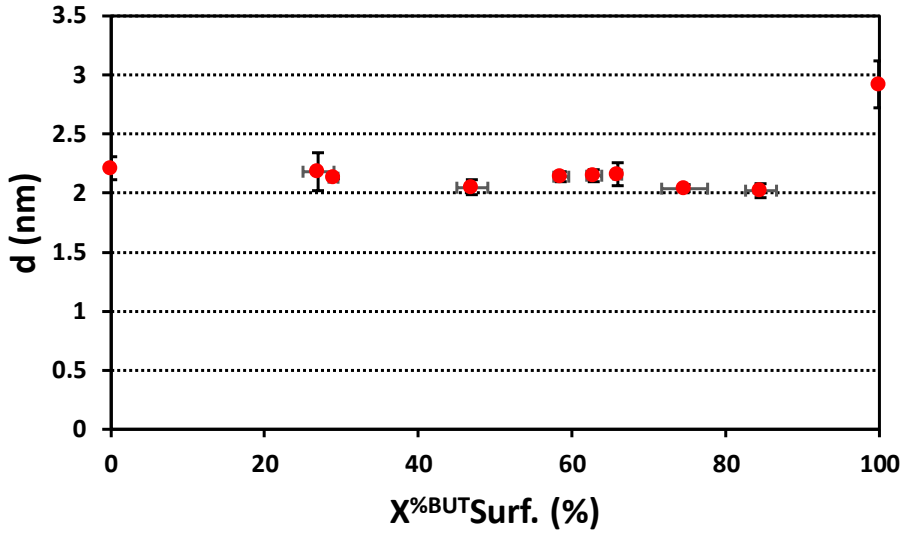

Figure 2.5: Illustrates the ellipsometric thickness of pure BUT SAM and TEG SAM and eight different mixtures of them on surface of Au at R. T.

This observation suggests that the biotin moiety in the binary SAMS is lying on the TEG surface rather than being in the upright orientation (Figure 2.6). This observation is supported by the results of CA and hysteresis, and in agreement with previous observations made on BUT SAMs, which have shown that BUT molecules are poorly packed and poorly ordered in the monolayer.[12,69] Moreover, the poor packing and ordering in the monolayer may provide the required space around the biotin moiety for the NeutrAvidin to bind to the biotin.

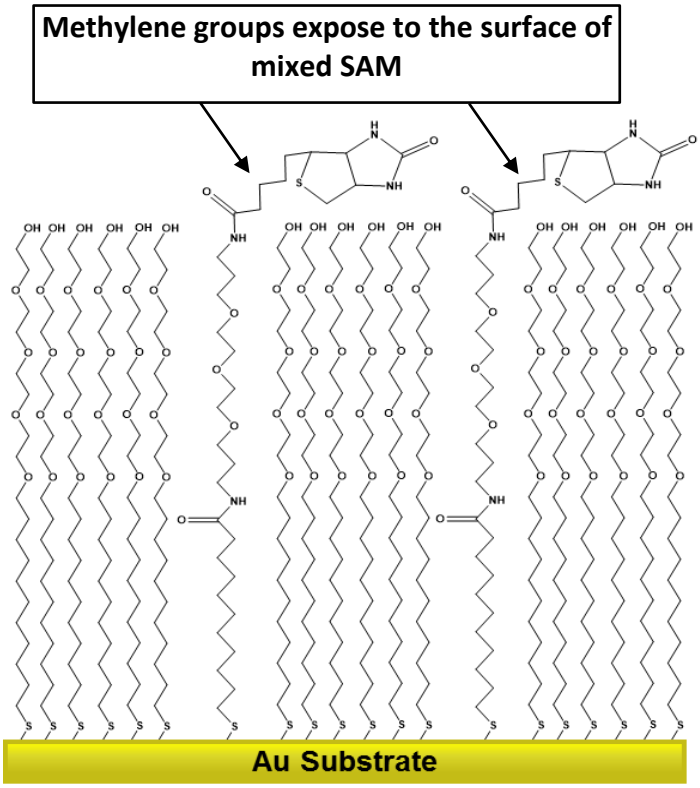

Figure 2.6: Depicts the biotin moieties of BUT SAM lay on the surface of TEG SAM deposited on an Au surface at room temperature

2.5. XPS Surface Characterisation of BUT, TEG and various BUT:TEG SAMs

2.5.1. Distribution of BUT, TEG and eight BUT:TEG SAMs on Au surface

XPS was used to characterize pure BUT and TEG and the eight different binary SAMs, and survey spectra are shown in Figure 2.7. XPS data collection was performed on three SAM surfaces for each of the pure and mixed SAMs, and three XPS spectra were recorded on each of the three SAMs, such that nine XPS data sets for each SAM (BUT, TEG and 8 binary BUT/TEG SAMs) were recorded. Figure 2.7 shows one representative XPS spectra of the three for each $X^{\%BUT}$.

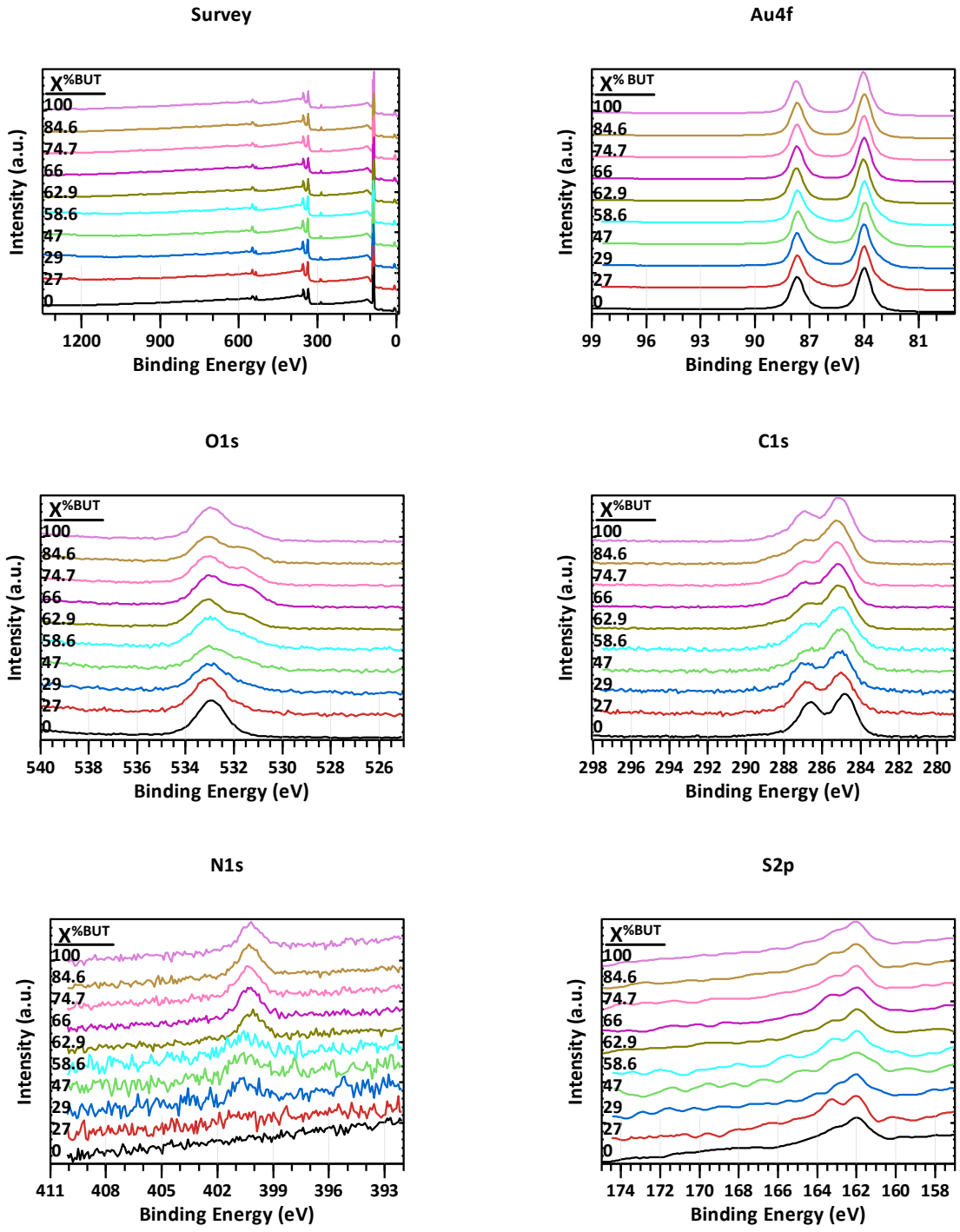

Figure 2.7: XPS survey spectra, Au 4f, O 1s, C 1s, N 1s and S 2p peaks of $X^{\%BUT}$ in the SAM (numbers on left hand side of each spectra)

For each elemental survey spectra in Figure 2.7, the ten stacked spectra go from pure TEG (bottom spectra) to pure BUT (top spectra) with the numbers on the left hand side of each spectra indicating the $X^{\%BUT}$ on the surface, relative to TEG, and derived from the Cassie equation (Table 2.3). The following can be noted:

i) The C 1s spectra shows clearly the difference between 0 $X^{\%BUT}$ (100 $X^{\%TEG}$) and the binary SAMs through the increasing area of C 1s peak, which is in agreement with the increase in the number of carbon atoms per unit area that have increased proportionally with increasing the mole fraction of BUT on the Au surface.

ii) The O 1s spectra shows a reduction in the -**O**-CH_2CH_2- oxygen atom peak (533 eV) and a new peak has appeared at 531.5 eV which is the O from the amide group (NH**O**=C).[6,14,70,71]

iii) The N 1s spectra of TEG has no peak at 392–410 eV corresponding to the nitrogen, as would be expected. However, when BUT is co-deposited the N 1s peak centered at 400.4 eV[15,71–74] is observed from the amide group.

iv) The S 2p spectrum reveals an emergence of a second peak at 164 eV which is from the thioether sulfur atom in biotin moiety of BUT, alongside the sulfur from the Au-thiolates in both TEG and BUT at 162 eV

2.5.2. XPS: Determination of the position of biotin moiety in the SAM

The XPS intensity ratio of N(1s)/Au(4f) (Figure 2.8), Appendix A1, Table A1.1) goes through three stages with increasing the fraction of BUT on the surface:

1. from 27–66 $X^{\%BUT}$ the N/Au ratio in the film increases, as it would expect,
2. from 66–85 $X^{\%BUT}$ the N/Au ratio remains constant, and
3. at 100 $X^{\%BUT}$ the N/Au ratio drops

The same observations have been reported by Linda *et al.*[75] and Kjell *et al.*[14] where they followed the changes of mixed SAMs by plotting the ratios N(1s)/C(1s). They attributed the reduction in the ratio of N(1s)/C(1s) with 100% biotinylated alkanethiol (BAT) to be due the position of biotin moiety. Their studies confirm that some of the biotin moieties are *exposed* to the surface in the binary SAMs and some of them are *trapped* in the monolayer and hence are not *exposed* at the surface for binding (Figure 2.8). Therefore, a lower N 1s signal is observed from XPS due to attenuation experienced by the trapped biotin moieties with 100 $X^{\%BUT}$.

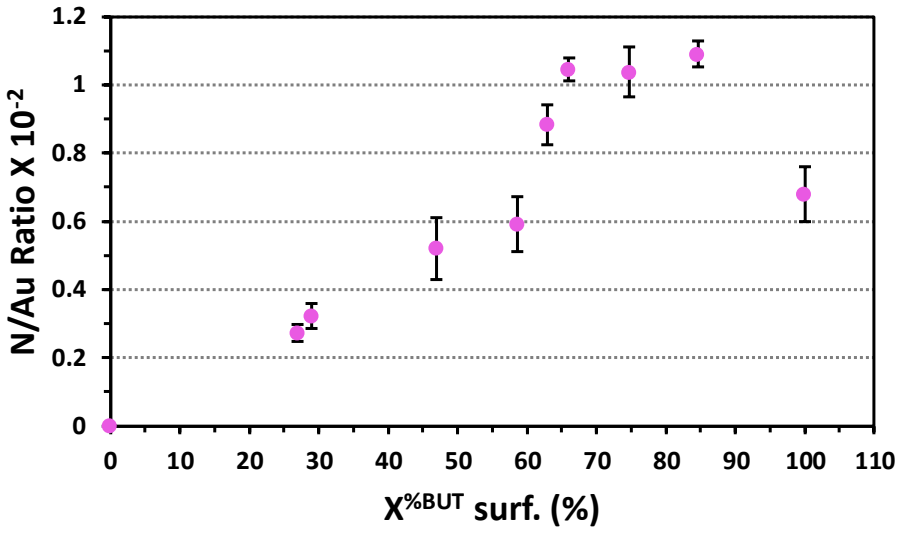

Figure 2.8: Graph shows N 1s/Au 4f ratio of TEG and BUT SAMs (pure and mixed) deposited on Au surface at R.T vs. mole fraction of $X^{\%BUT}$ on the Au surface

Therefore, in this study, N 1s has been chosen in addition to the above reason, to determine the position of biotin moieties where two N atoms are allocated in the biotin moiety (near the surface of binary SAMs) and with an XPS take-off angle of 90°, the changes in the area of N 1s can be followed. The reduction in the area of N 1s spectra is clearly attributed to increase in the attenuation of N 1s due to the orientation of biotin moieties. This attenuation increases when the biotin moieties are in limiting positions (Figure 2.9), such that they are:

(ii) *Exposed* to the subphase, and

(iii) *Trapped* within the Biotin SAM and this is an indication that the film of 100 $X^{\%BUT}$ is not densely packed and accordingly some of the biotin moieties find spaces to be filled. These spaces are filled by the spacer TEG with mixed SAMs and improving the packing of biotin moieties especially with 66 $X^{\%BUT}$.

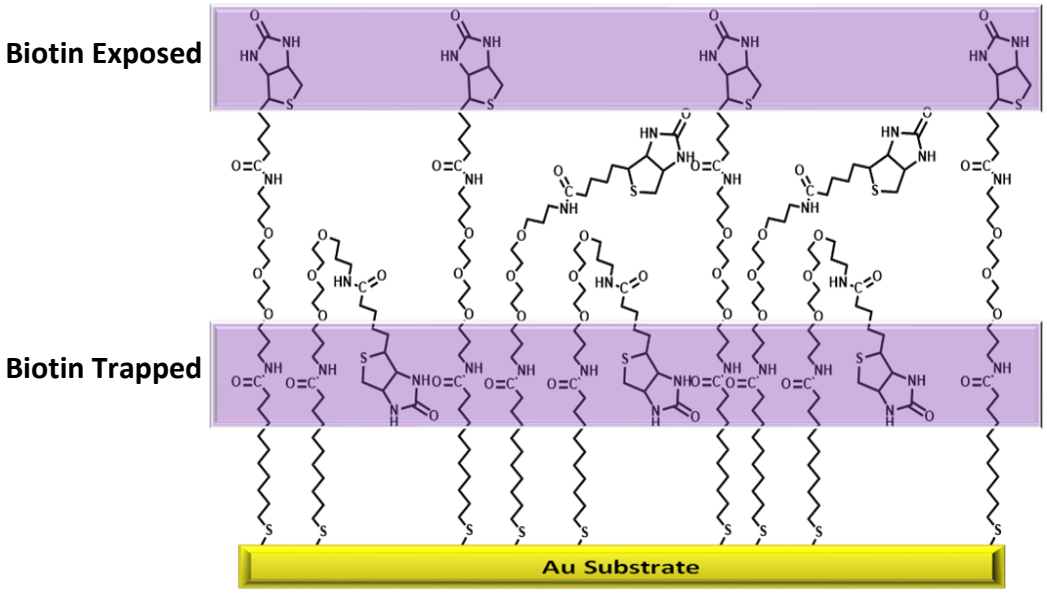

Figure 2.9: Shows some of Biotin moieties exposed to the surface of 100 $X^{\%BUT}$ and other biotin moieties exist in the depth of the BUT film

In this study, the orientation of biotin moieties has also been confirmed by calculating the area of the S 2p doublet ($2p_{3/2}$ and $2p_{1/2}$) for 0 $X^{\%BUT}$ (100 $X^{\%TEG}$) (Figure 2.10a), 66 $X^{\%BUT}$ (Figure 2.10b) and 100 $X^{\%BUT}$ (Figure 2.10c). As 100 $X^{\%TEG}$ has one sulfur[14,75] binding to the Au surface [BE of 162.16 eV ($2p_{3/2}$)] as a thiolate **(S-Au)**,[47,76] so it will be used as an indication of monolayer formation (not bilayer formation) and as a base line for the 66 and 100 $X^{\%BUT}$ SAMs, in addition the BUT has unbound thiol which is located in the biotin moiety so cannot be used as a reference.

The difference between the bound and unbound thiol has been observed by plotting the area of the S 2p against the mole fraction of BUT on surface (Figure 2.10d). The plot shows that the area of unbound thiol [BE of 164 eV ($2p_{3/2}$)][71] increases with increasing the BUT mole fraction and interestingly the unbound thiol area of 100 $X^{\%\ BUT}$ is smaller than 66 $X^{\%BUT}$, which is similar to

N 1s. This discrepancy is attributed to the attenuation of unbound thiol which is located in the biotin moiety and underneath the N atom (Figure 2.2a), and this is further evidence that the boitin moiety is surface exposed as illustrated in (Figure 2.9). This explanation raises two questions:

1. why is the ellipsometric thickness of the mixed SAMs lower than the pure BUT SAM see Table 2.3? and
2. why is the immobilization of Neutravidin (by SPR) with 100 $X^{\%\ BUT}$ similar to 66 $X^{\%\ BUT}$?

The two questions can be answered as follows. The results from CA confirm that the 100 $X^{\%BUT}$ is more hydrophobic than the mixed SAMs (Figure 2.2) and from the difference in the hysteresis of 66 $X^{\%BUT}$ (hysteresis = 19) and 100 $X^{\%BUT}$ (hysteresis = 27), it confirms that pure BUT SAM is less densely packed than 66 $X^{\%BUT}$ SAM, where the improvement of packing with the 66 $X^{\%BUT}$ is attributable to the TEG spacer. Accordingly, more methylene groups are exposed to the surface of the 100 $X^{\%BUT}$ and this enhances the non-specific binding of NeutrAvidin, while with the 66 $X^{\%BUT}$ SAM not enough space is available for non-specific binding due to the spacer (TEG) increases the packing of BUT. This result has been confirmed by XPS spectra peaks of N 1s and S 2p where the attenuation is less for 66 $X^{\%BUT}$ than for 100 $X^{\%BUT}$. The observations from XPS measurements confirm that the biotin moieties with 66 $X^{\%BUT}$ are exposed to the surface and the lower thickness confirms that the biotin moieties lay on the surface of the mixed SAMs with high free volume. The free volume around the biotin and the packing of the 66 $X^{\%\ BUT}$ enables the biotin moiety to specifically bind NeutrAvidin.

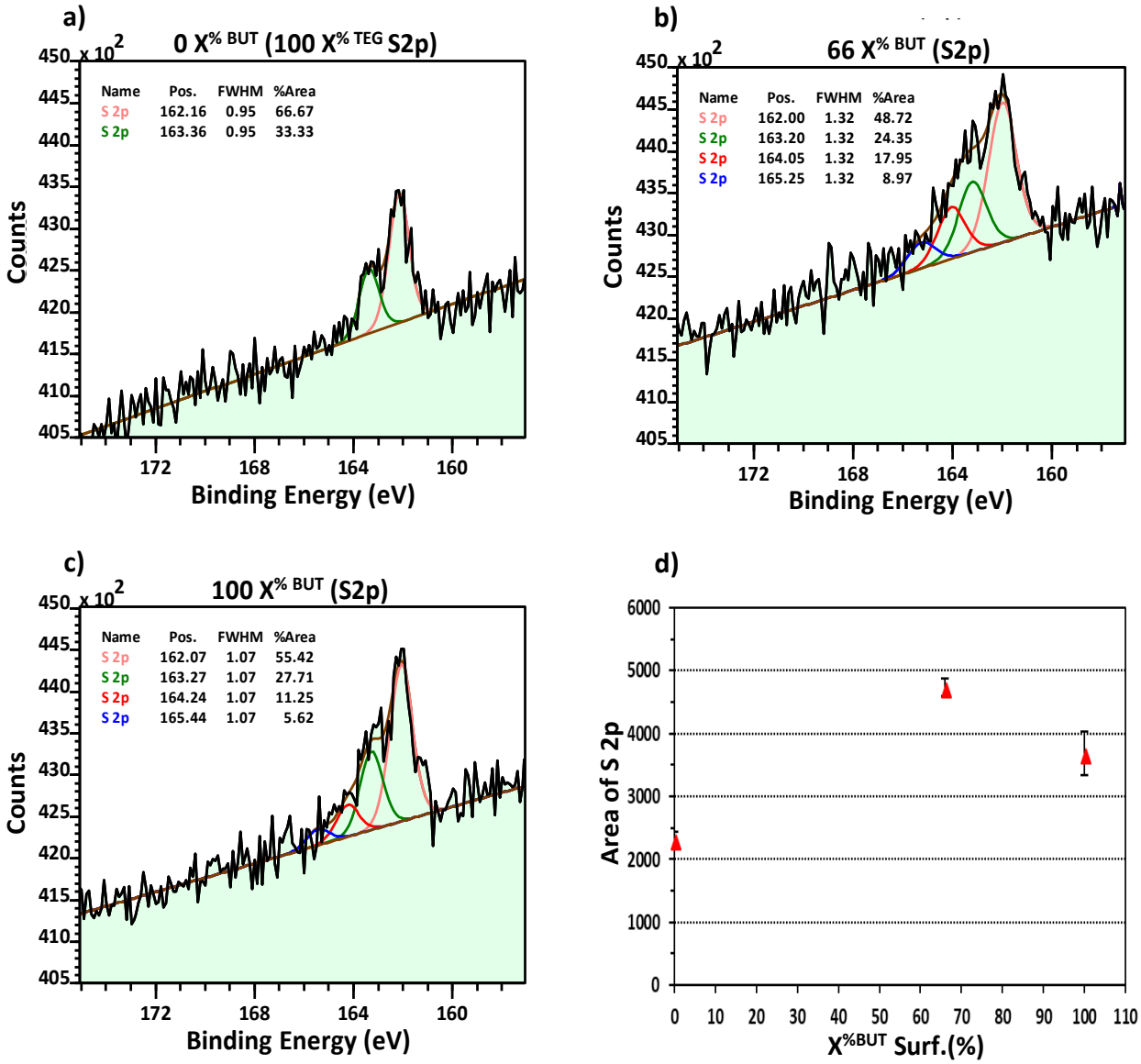

Figure 2.10: XPS spectra of S 2p peaks of a) 0 $X^{\%\ BUT}$ (100 $X^{\%\ TEG}$), b) 66 $X^{\%\ BUT}$, and c) 100 $X^{\%\ BUT}$ SAM deposited on Au surface at R.T and d) the area calculated for S 2p

2.6. Adsorption of NeutrAvidin to the BUT/TEG SAMs

2.6.1. SPR measurements

SPR is an optical technique,[77] which is used to follow the immobilisation of analytes such as proteins (Streptavidin and NeutrAvidin)[48,78] on the biotin-terminated SAM, which is deposited on the Au surface, by following the changes in the refractive index due to the immobilisation (see Chapter 1, Figure 1.6). The changes in the refractive index can be interpreted to calculate the concentration and the thickness of the immobilised protein.[38,78–80]

Herein, phosphate-buffered saline (PBS, 10 mM, pH=7.4) was used to enhance the binding between the biotin moiety and the NeutrAvidin. At pH=7.4, the protein is immobilized onto the functionalized SAM by hydrogen bonding between the biotin functionalized SAM and NeutrAvidin.[81]

The SPR responses to each binary surface are shown in Figure 2.11. Initially, a stable baseline was obtained by flowing through PBS solution for 15 min, followed by injection of NeutrAvidin solution 5 µg/mL at 10 µL/min for 50 min, and finally the surface is washed with pure PBS solution for ~20 min to remove any physisorbed NeutrAvidin. After washing, the final SPR response from the baseline is assigned to the specifically chemisorbed NeutrAvidin on the TEG/BUT SAM (Figure 2.11).

In addition, longer time responses were investigated to check whether the saturation of the surface (66 $X^{\%BUT}$) with NeutrAvidin was reached (see Appendix A2, Figure A2.1).

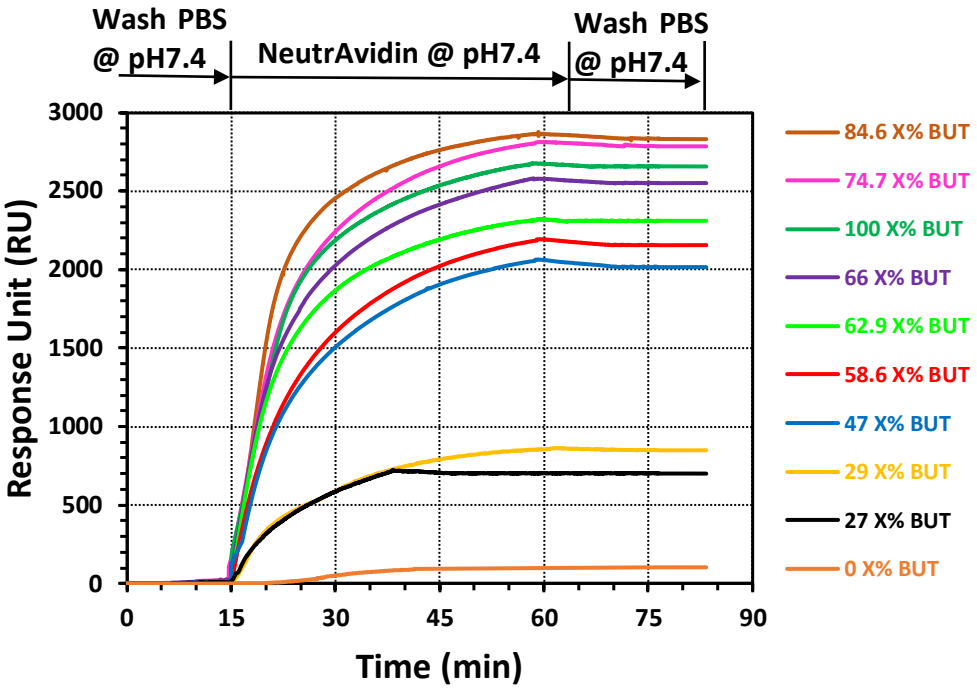

Figure 2.11: The SPR responses for $X^{\%BUT}$ SAM and $X^{\%TEG}$ SAM pure and eight different mixtures of them on Au surface at room temperature

The plot of maximum SPR response vs $X^{\%BUT}$ on the Au surface (Figure 2.12a), clearly shows an increase in SPR response upto 66 $X^{\%BUT}$, and then a plateauing. The SPR response observed on pure TEG SAM was 103 ± 25 suggesting only a weak affinity of NeutrAvidin towards TEG, presumably because of the helical conformation of TEG leading to the thin layer of hydrogen bonded water, inhibiting the adsorption of NeutrAvidin to the surface of TEG (Figure 2.12a).[43–45] The increase in NeutrAvidin binding as the surface moves from a low to high density of biotin moieties is clearly expected, and is observed upto 66 $X^{\%\ BUT}$, where after the binding plateaus. Thus, it can be concluded that the optimum binding between biotin and NeutrAvidin is ~ 66 $X^{\%BUT}$ mixed SAM of BUT and TEG, and in line with the positional analysis of the biotin moieties discussed in the previous section and illustrated in (Figure 2.12a).

The mass of NeutrAvidin deposited on the surface of BUT with the 66 $X^{\%BUT}$ was calculated according to the sensitivity of SPR which was used herein, where 1000 ΔRU (ΔRU was calculated by representing that the stabilized signal is equal to zero, which was deleted from the final SPR response for each experiment) is equal to 100 ng/cm^2,[15,48,71] which gives the mass of NeutrAvidin deposited equal to 255 ± 15 ng/cm^2.

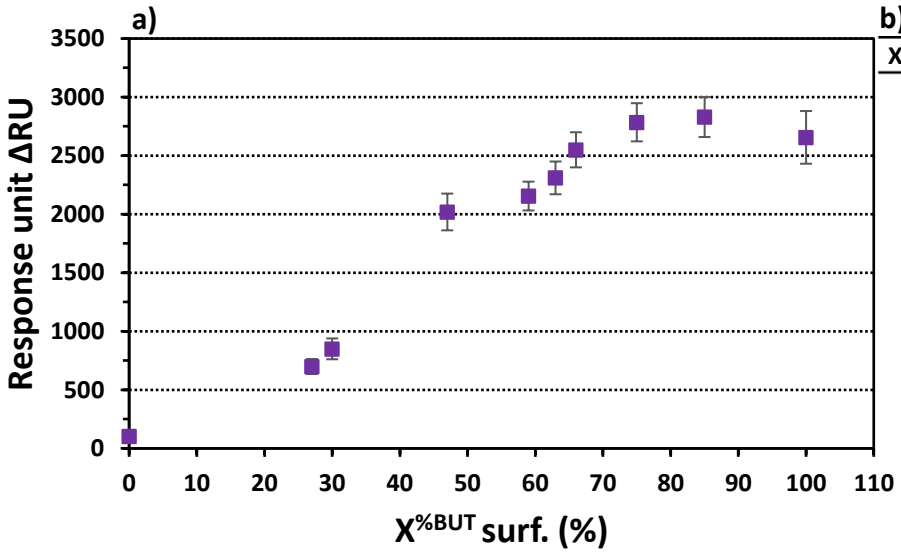

b)

$X^{\%BUT}$ Surf.	ΔRU	± Error
0	103	25
27.0	699	64
29.0	850	89
47.0	2019	157
58.6	2155	123
62.9	2310	140
66.0	2550	150
74.7	2785	163
84.6	2830	171
100	2656	225

Figure 2.12: a) The responses of SPR according to the $X^{\%\ BUT}$ on surface at room temperature, and b) data inset

2.6.2. QCM measurements

QCM was also used to follow the binding between biotin moiety with ratio a 66 $X^{\%BUT}$ surf. (as optimum conditions concluded from the SPR results, see above section) and NeutrAvidin, in a similar fashion to the SPR measurements. PBS solution was injected first to obtain a stabilized signal as a baseline for 15 min. After stabilization, NeutrAvidin of 5µg/mL in concentration was injected with a flow rate of 40 µL/min at room temperature until a stable signal was observed,

followed by 30 min washing the surface with PBS again to remove the physisorbed layer from the surface (Figure 2.13). The final response from QCM obtained is Δf = -121.5 Hz, and the Sauerbrey[82] equation was applied to calculate the mass (m) of NeutrAvidin which is immobilized on biotin surface of mixed SAMs.

$$\Delta m = -C\Delta f \qquad \textbf{(Equation 2.3)}$$

Where C represents the mass sensitivity constant of quartz crystal sensor (4.5 ng. Hz/cm^2), f_0 is the fundamental frequency (10 MHz), and Δf represents the frequency change ($f_a - f_0$), where f_a represents the frequency upon analyte binding.

The plot in (Figure 2.13) is an average of four experiments and reveals that 80 mins is the time required to complete the binding between BUT and NeutrAvidin and to reach the plateau where the frequency change Δf is -121.5 Hz. Wolny *et al.*[13] calculated the acoustic thickness of Streptavidin, Avidin and NeutrAvidin immobilized on biotinylated supported lipid bilayers (b-SLBs) and according to the calculated thickness, it is possible to know the thickness of protein deposited on b-SLBs by applying the following equation.[83]

$$d = \Delta m/\rho H_2O \qquad \textbf{(Equation 2.4)}$$

Where d represents the acoustic thickness of biomolecules (protein), m represents the mass of protein, and ρ represents the density of the proteins (~1.35g/cm^3)[84–86]. It is well known that water contributes to the deposition of proteins, where water molecules are trapped inside the protein,[87] which amounts to more than 50% of the total mass of the protein film after coupling of water molecules, and accordingly, the change in the frequency corresponds to the deposition of protein, as well as water molecules in the protein film.[87,88] The calculation to determine the

thickness of the proteins is shown in equation 2.4. The equation neglects the density of protein due to the difference between the density of water and protein being small and hence, the density of water will be used in equation 2.4. By applying equation 2.4, the acoustic thickness of NeutrAvidin here in which binds to BUT is determined to be d = 5.5 nm. Wolny *et al*. also reported the thickness from equation 2.4 and observed the dispersity of protein on the surface being a monolayer or a multilayer (if a protein agglomerates on the surface) after knowing the dimensions or the shape of the protein, for example the flattened ellipsoid of Bovine Serum Albumin (BSA) in shape is (3 nm × 4 nm × 8 nm)[89], which binds biotin and the obtained thickness was d = 2.4 nm. This thickness suggests that BSA deposits with the long axis parallel to the surface. Also, they demonstrated that the thickness of Streptavidin, Avidin and NeutrAvidin, which were immobilized on biotinylated supported lipid bilayers, are 5.1, 4.7 and 5.8 nm, respectively, confirming the formation of a dense monolayer of these proteins[13]. Based on these studies, the calculated thickness of NeutrAvidin in this study is d = 5.5 nm and indicates the formation of a monolayer,[21,90] see inset (Figure 2.13).

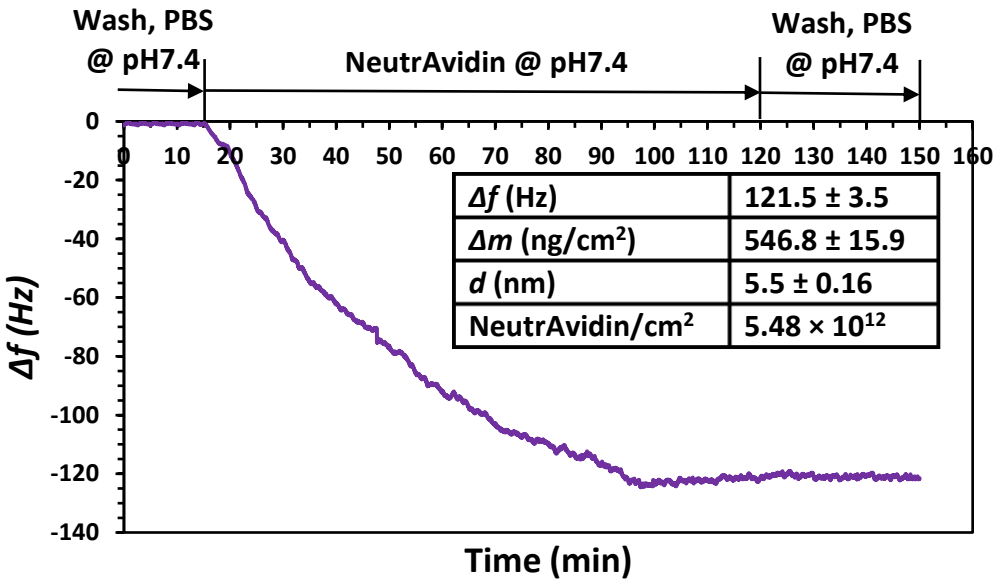

Figure 2.13: The responses of QCM for the 66 $X^{\%BUT}$ on the surface at room temperature and summary final adsorption data (inset)

A comparison has been made for calculating the mass of NeutrAvidin by SPR and the mass by QCM-equation 2.3. It is worth noting that the mass of NeutrAvidin which is deposited on 66 $X^{\%BUT}$ of binary SAMs, calculated by QCM-equation 2.3 (Δm_{QCM} = 546.8 ± 15.9 ng/cm^2) is ~double the mass which was calculated by SPR (Δm_{SPR} = 255 ± 15.0 ng/cm^2).[15,48,71]

The same observation was reported by Hook and Kasemo[88] and they attributed this increase to the water molecules which are trapped between the protein molecules when they deposit on the surface of QCM-sensor crystal. Their observations were confirmed by adding $NaIO_4$ to the deposited protein and cross-linking between $NaIO_4$ and the deposited protein which contains the water molecules, where the idea is to release the water molecules leading to the protein film being more compact which causes additional decrease in the mass of the surface by QCM-sensor. The results of cross-linking have been obtained as an increase in the frequency and

decrease in the mass of Neutravidin film. This increase has been followed by many researchers and they related this increase to the principle of sensing of mass by QCM, which is different from the SPR. The SPR signal represents an average of the change in the refractive index, and the refractive index of the trapped or coupled water molecules with deposited protein is already neglected, due to the refractive index of water was pre-detected during the base line of the SPR measurements. Whilst by QCM the signal is due to the change in the frequency and the base line represents the stabilized frequency, and accordingly the coupled water is going to be detected as a mass included with the mass of protein.[13,88,89,91–93] In this study, the increase in the mass (mass ratio $\Delta m_{SPR}/\Delta m_{QCM}$) by QCM is ~47% higher than SPR and according to the literature the difference between the masses observed for the two techniques is related to an increase of water coupled NeutrAvidin film.[94,95]

The immobilization of NeutrAvidin on 66% (2:1) binary SAMs of BUT and TEG was imaged by (AFM) Atomic Force Microscopy[96] (Figure 2.14).

2.6.2.1. AFM Measurements:

The QCM-sensor crystal for the 66 $X^{\%BUT}$/NeutrAvidin film described above was imaged (Figure 2.14) immediately with the AFM in topography mode, after monitoring the changes in the frequency, in order to see the distribution of the NeutrAvidin on the 66 $X^{\%BUT}$ surface. It is noteworthy to see that NeutrAvidin is dispersed on the surface with the semi spherical shape (blobs). These blobs are due to the convolution between the tip and the surface.[97,98] The convolution effects the resolution of the AFM image which leads to difficulty in distinguishing between the agglomeration of the protein[99] or the protein deposited on the surface as a

strand.[87,100] According to the NeutrAvidin thickness which was calculated as d = 5.5 nm in this study, it can be inferred that Neutravidin is distributed as a monolayer. In addition to the convolution effects, coupling of water with the protein also causes changes in the diameter or the size of the protein. Andreas *et al*.[94] reported that the effective thickness of the deposited Neutravidin on a biotin-terminated SAM is 7 nm, which is higher than the diameter of the protein (around 5 nm). The difference was attributed to the increase in the thickness due to the swelling caused by water molecules within the NeutrAvidin film. Jiang *et al*.[101] measured that the thickness of the layer, which consists of biotinylated hyaluronan immobilized (b-HA) on NeutrAvidin (where initially this NeutrAvidin is immobilized first on b-BSA), to be 20 nm taking into consideration the composition of the layer containing the three components; b-BSA/NeutrAvidin/b-HA. Indeed, the thickness was observed to be 19.6 nm *via* measuring the height of the layer by AFM. Taking into consideration the same principles that Jiang *et al.*[84] used to predict the layer thickness, it would be expected that the total thickness prepared herein should be ˜7 nm, based on the thickness of the binary SAMs 66 $X^{\%BUT}$ which is 2.16 ± 0.10 nm (see Table 2.3), and the thickness of protein is ˜5 nm[38,51,94,99,101] (Figure 2.15).

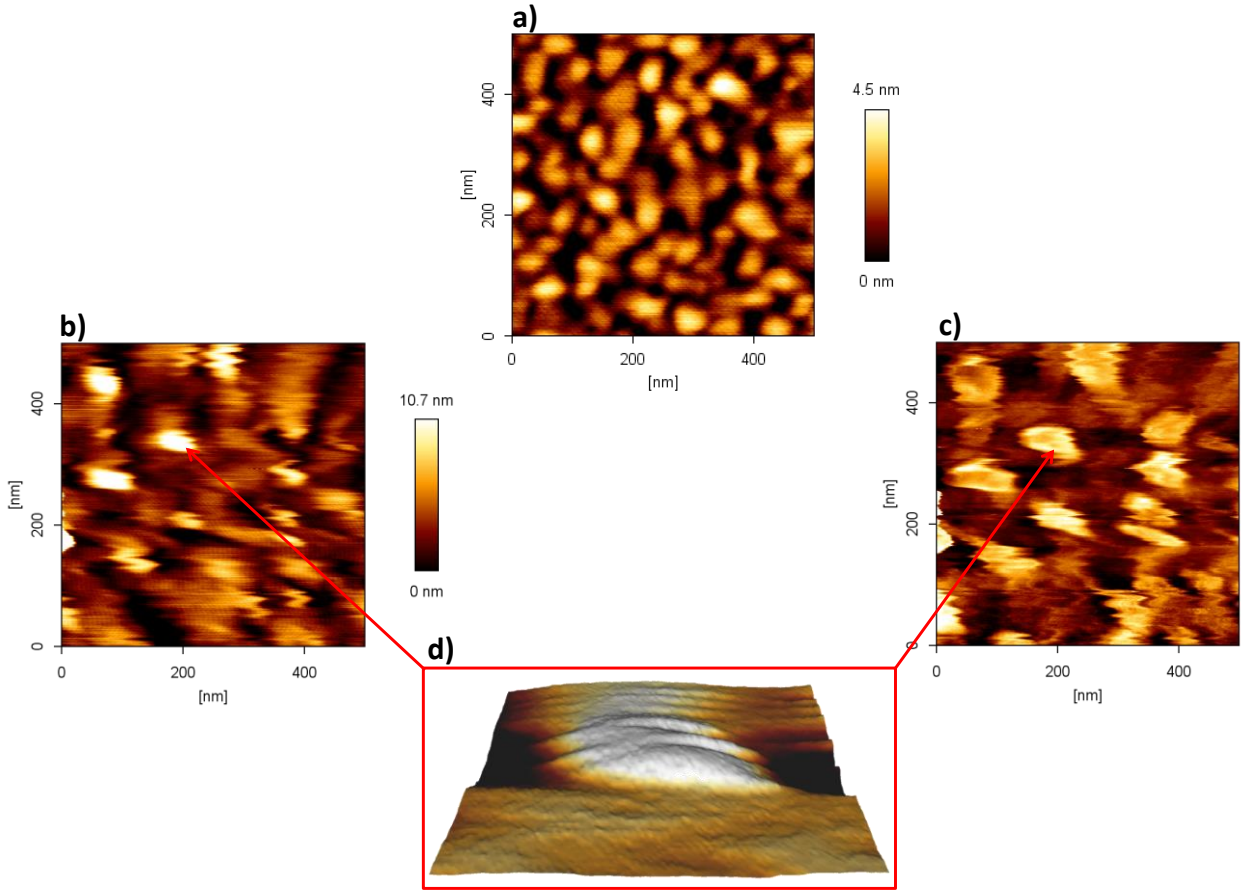

Figure 2.14: The topographic AFM images of a) Height-Trace for 66 $X^{\%\ BUT}$ SAM/Au, b) Height-Trace for NeutrAvidin immobilized on 66 $X^{\%\ BUT}$ on Au surface of the QCM-sensor crystal at room temperature, c) Phase-Trace, and d) 3D

From the AFM images in Figure 2.14, it can be observed the structures are around 6 nm in height which are in good agreement to what was expected. Finally, based on the QCM response of 66 $X^{\%BUT}$ the coverage or the number of NeutrAvidin adsorbed on BUT surface is determined to be (5.48×10^{12} Neu/cm^2) which is within the same range of coverage observed for similar proteins on binary SAMs consisting of biotin functionalized thiolates as one of the components in the SAM. Dahlin *et al.*[94] observed coverage of NeutrAvidin to be 6.85×10^{12} Neu/cm^2 on a mixture of biotinylated poly(ethylene glycol) and poly(L-lysine)-graft-poly(ethylene glycol). Whereas Seifert

et al.[102] calculated the bulk coverage of Streptavidin to be 2.50 × 10^{12} SA/cm^2 on similar biotin functionalized binary SAMs. The big differences in the surface coverage for the different proteins are related to the shape and the dimensions of the proteins,[38,103] or the experimental conditions in which the protein immobilization has been carried out, for example for NeutrAvidin. The calculated coverage of immobilised NeutrAvidin is (9.84 × 10^{12} Neu/cm^2)[99] which is close to NeutrAvidin immobilized in this study. The small difference between the coverage is related to the amount of water molecules within the protein film, which vary from one to another and depends upon the nature of protein.[86,102]

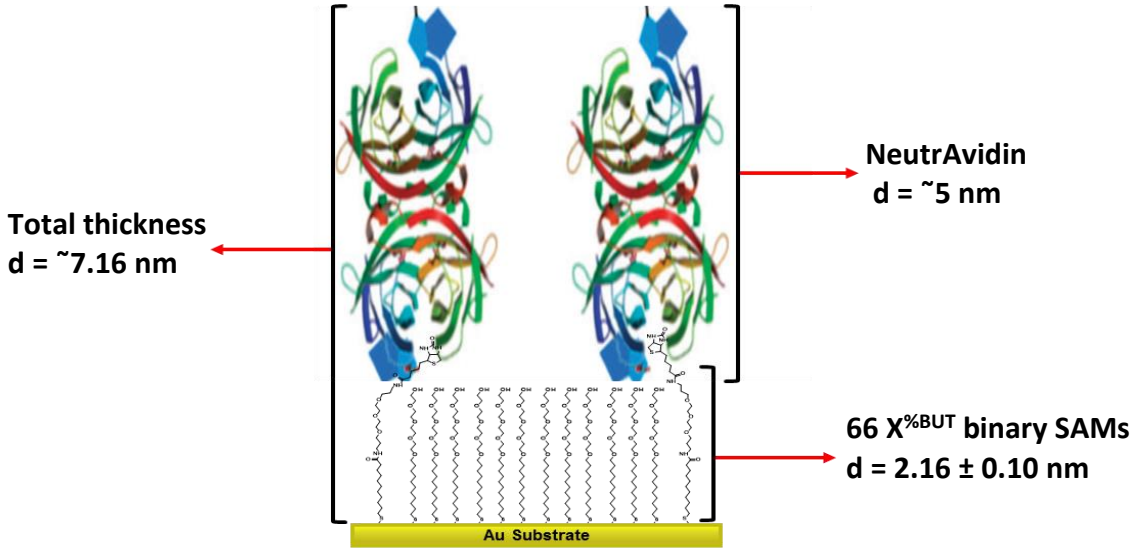

Figure 2.15: The Scheme of the total thickness of NeutrAvidin deposited on 66 $X^{\%\,BUT}$ and TEG SAMs on Au surface QCM-sensor crystal

2.7. Determination of the coverage of NeutrAvidin on BUT:TEG SAM

The SPR response for the immobilization of NeutrAvidin on the surfaces of pure and 8 mixed SAMs (Figure 2.11), can be converted to the coverage of NeutrAvidin as the number of NeutrAvidin molecules per unit area (Neu/cm^2) (see Appendix A3, Table A3.4).

Figure 2.16 shows the coverage of NeutrAvidin and N (1s)/Au(4f) XPS intensity ratio for pure and mixed SAMs at the takeoff angle of 90^o as a function of mole fraction of BUT on surface ($X^{\%BUT}$ surface). Interestingly, the trend of NeutrAvidin coverage matchs the trend of N (1s)/Au(4f) ratio where this ratio represents the concentration of biotin moeities on the surface of BUT film. It is clear to see that the coverage of NeutrAvidin on the surface of 0 $X^{\%BUT}$ surface or 0 ratio of N(1s)/Au(4f) [100 $X^{\%TEG}$ surface] is 0.10 × 10^{12} Neu/cm^2 where this is attributed to the repulsion of the TEG towards the proteins and as mentioned above in section 2.6.1. The coverage increases dramatically with increasing ratio of N(1s)/Au(4f) within the range of 27–66 $X^{\%BUT}$ surface in line with the range of coverage of the NeutrAvidin (0.70–2.56 × 10^{12} Neu/cm^2) and then plateaus for the range of (66–85) $X^{\%BUT}$ surface. After this plateau a noticeable decrease in the N(1s)/Au(4f) intensity ratio is seen with 100 $X^{\%BUT}$ surface, although the NeutrAvidin coverage on 100 $X^{\%BUT}$ surface (2.67 × 10^{12} Neu/cm^2) is relatively similar to the coverage observed on 66 $X^{\%BUT}$ surface. The increase with 100 $X^{\%BUT}$ surface is an evidence of non-specific immobilization of NeutrAvidn on the surface of BUT film and confirms that the oreintation of some biotin moeities are within the depth of BUT and more methylene groups are exposed to the surface.

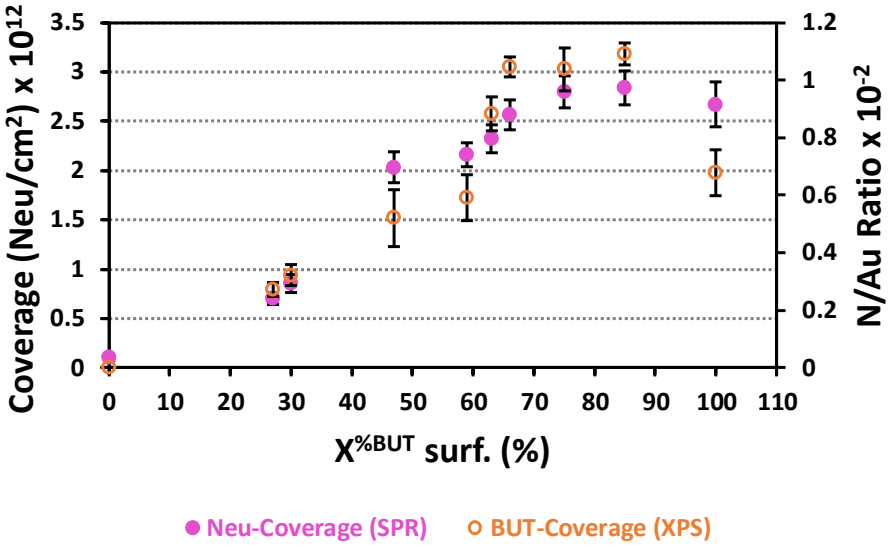

Figure 2.16: Coverage of Neu (left axis) and XPS intensity ratio of N(1s)/Au(4f) at takeoff angle of 90° (right axis) vs $X^{\%BUT}$ on surface

The number of BUT molecules which are required to immobilize the NeutrAvidin molecules was calculated *via* plotting the ratio of (BUT/Neu)/cm^2 (left axis) and (BUT/TEG)/cm^2 (right axis) (see Appendix A3 Tables A3.4 and A3.5) versus percent mole fraction of BUT ($X^{\%BUT}$ surface) SAM which is deposited on the surface of the Au (Figure 2.17). The plot shows that the ratio of BUT/Neu decreases dramatically until 47 $X^{\%BUT}$ surface is reached, and thereafter plateaus until 75 $X^{\%BUT}$ (within error), followed by an increase until 100 $X^{\%BUT}$ BUT/Neu. The increase observed between 75-100 $X^{\%BUT}$ is related to the increase in the number of BUT molecules, hence increasing the number of binding sites for NeutrAvidin to immobilize on. This observation is further supported by the ratio of BUT/TEG (right axis), where the trend shows clearly that the BUT/TEG ratio increases with increasing coverage of BUT molecules on the surface of Au. As the optimum NeutrAvidin coverage is observed on surfaces with $X^{\%BUT}$ between 47-66, the BUT to NeutrAvidin ratio ranges between 69-77:1. This BUT to NeutrAvidin ratio is higher than what was

expected. In theory there are two binding pockets on each side of the NeutrAvidin molecule which the biotin moieties can bind to. As two of the binding pockets will be at the periphery when bound to the SAM, thus these will be unable to bind to other biotin moieties on the monolayer (see Figure 2.2c&d), hence only two biotin molecules can possibly bind to one NeutrAvidin *via* the accessible binding pockets.[75,104] Therefore, a minimum of 75 (BUT:NeutrAvidin ratio of 77:1) of the 77 biotin moieties are not bound to the NeutrAvidin molecule. Moreover, as the ratio between biotin and NeutrAvidin is greater than 2 on the 66 $X^{\%BUT}$ surface SAM this confirms the biotin most likely binds specifically to NeutrAvidin and the non-specific binding is inhibited dramatically on this binary surface. An explanation to the nonbinding of 75 biotins could be due to poor orientation of these biotins, which do not have enough mobility to achieve a good insertion of biotin moiety inside the NeutrAvidin pocket. As previous studies have confirmed that the complete insertion of the biotin moiety inside the pocket of protein is required for successful binding, and as the size of

biotin moiety is ~1.40 nm in length[50,51] (similar to the difference in length between TEG and BUT (see Figure 2.2a,b), it is highly likely some of the biotin moieties will be sterically hindered on the surface of the monolayer of the binary SAM. The same observation has been reported previously by Victor *et al.*[19] and Linda *et al.*[48] and they attributed the difference between the number of biotin moieties and Streptavidin to the protruding of biotin moieties on the surface of the pure and mixed SAMs, and also it depends upon the mobility of the biotin moieties which enables for a complete insertion inside the pocket of Streptavidin when they approach the surface of BUT SAM. In addition to the above reasons, Seifert *et al.*[102] reported that the 2-D crystal of Streptavidin

offer two binding sides with biotin moieties where each side has two pockets. The low full coverage of NeutrAvidin in this study was confirmed by AFM (Figure 2.14).

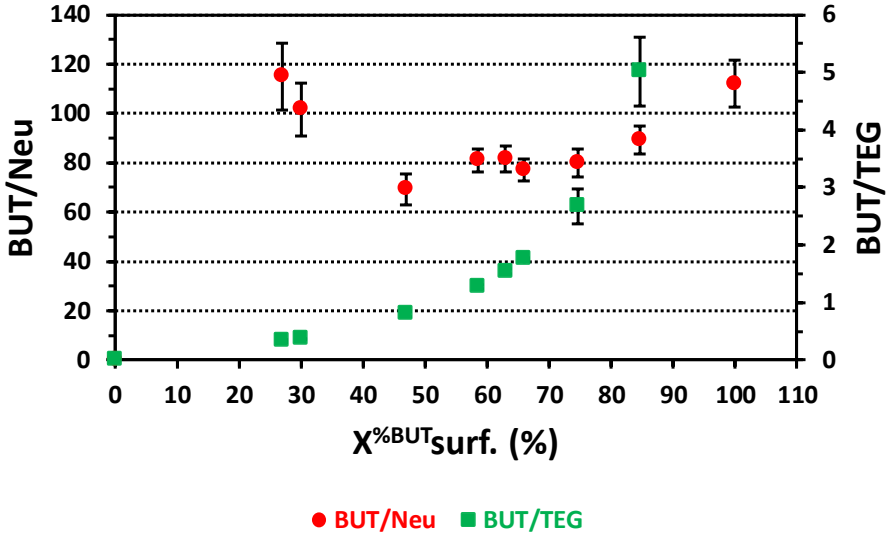

Figure 2.17: Coverage of BUT/Neu (left axis) and coverage of BUT/TEG (right axis) vs % mole fraction of BUT on the surface of Au

Linda *et al.*[75] were reported that the optimum binding between biotin moieties and Streptavidin is reached at 65 $X^{\%BAT}$ of biotin-terminated alkanethiol (BAT) on the surface of Au, and from their calculations they observed that the number of biotin moieties is three fold higher than the number of Streptavidin molecules. They attributed this difference to the possibility of the formation of islands of BAT on the surface in addition to the above two reasons.

The trend of the ratio BUT/Neu (left axis) matches the trend which was observed by the XPS intensity ratio of N(1s)/Au(4f) (right axis) (Figure 2.18). The ratio of N(1s)/Au(4f) is an indication of BUT molecules which are deposited on the surface of the Au, and this ratio increases with increasing $X^{\%BUT}$ surface. This increase matches the dropping in the ratio of BUT/Neu where the two trends indicate that the concetration of the BUT is low until the 63 $X^{\%BUT}$ surface and

thereafter a slight increase in the conc. of BUT surface is observed until 58.6 $X^{\%BUT}$ surface. after which an increase is observed in both ratios until 100 $X^{\%BUT}$ surface when a decrease is observed for the N(1s)/Au(4f) ratio. However, the BUT/Neu ratio is increased, and this is an indication that biotin moieties are poorly oriented and some of them protrude into the depth of the 100% BUT SAM film (Figure 2.18).

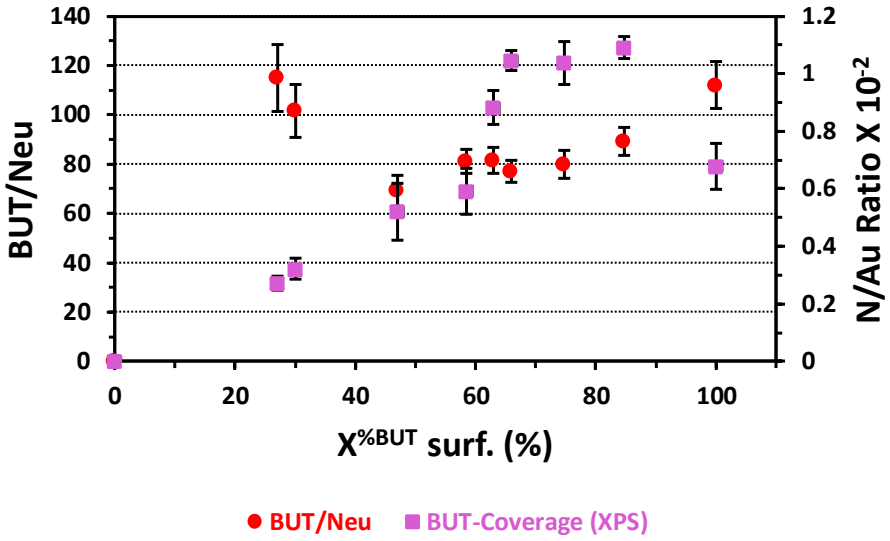

Figure 2.18: Ratio of BUT/Neu (lift axis) and XPS intensity ratio of N(1s)/Au(4f) at a takeoff angle of 90° (right axis) vs $X^{\%BUT}$ on the surface of Au

2.8. Conclusion

Self-assembled monolayers (SAMs) have been prepared by chemisorption of two organic thiol surfactants, BUT and TEG, in various ratios, to produce monolayers of a pure and binary SAMs on Au surfaces. The contact angle, ellipsometry and XPS measurements have confirmed that SAMs have been formed, and the SPR measurements reveal the TEG spacer plays an

important role to space out the biotin moieties and enable efficient binding of NeutrAvidin to the surface. XPS analysis reveals that the high nitrogen signal at 400.4 eV is observed with 66 $X^{\%BUT}$ in the binary SAM, which indicates that the terminal biotin is exposed to the surface of the binary SAMs while with 100 $X^{\%BUT}$, the high SPR response (coverage of NeutrAvidin) is attributed to the non-specific binding of NeutrAvidin with methylene groups which are protruded to the surface, with some of the biotin moieties trapped in the BUT SAM, and unavailable for binding to the NeutrAvidin. Accordingly, the ratio 66 $X^{\%BUT}$ SAM will be used to functionalize the surface of MEMS.

The low SPR response (ΔRU = 103) for the pure TEG SAM confirms this SAM has low non-specific binding for proteins, presumably because a helical OEG conformation is adopted. Furthermore, the SPR confirms that the optimum immobilization of NeutrAvidin (coverage = 2.56 × 10^{12} Neu/cm^2) is observed on the binary SAM formed from a 2:1 molar surface of BUT:TEG SAM on the Au surface.

The frequency change of a QCM upon immobilization of NeutrAvidin, which is 121.5 Hz, on the 66 $X^{\%BUT}$ SAM equals to a coverage of 5.49 × 10^{12} Neu/cm^2, which is ~double the coverage of NeutrAvidin measured by SPR. This increase is attributed to the coupling of water with the NeutrAvidin film, which is confirmed by AFM. Additionally, AFM shows that the NeutrAvidin film is dispersed as a monolayer with a thickness of ~5nm in height and this matches the thickness of 5.5 nm that is calculated from QCM data. The calculated ratio of BUT/Neu confirms the specific binding between biotin moieties and NeutrAvidin.

2.9. Future work

The objective of the prepared system in chapter 2 is to chemically modify the surface of a MEMS micro-paddle with an optimum concentration of mixed SAMs BUT and TEG in order to specifically immobilise the NeutrAvidin. This system was applied to the micro paddle, but no result was obtained due to the limitation of the sensitivity of the vibrometer, which was not able to detect the light masses such as NeutrAvidin. Therefore, the next step was to use G-NPs to increase the mass of NeutrAvidin in order to be detectable. This work was carried out by replacing the citrate passivated G-NPs with NeutrAvidin and the new system tested by QCM first and then applied on a micro-paddle, as discussed in Chapters 3 and 4.

In order to detect the mass of the deposited NeutrAvidin on binary SAM without G-NPs, another micro paddle should be designed which has more mass sensitivity than the one that was used before. From previous study by Boonliang,[105] the mass sensitivity (*S*) of a micro paddle was improved to be 55 ag/Hz, which was calculated practically after adding 1000 fg mass of platinum to a micro paddle with the total area of ˜80 μm^2 (˜8 × ˜10 µm) with support beams (each measuring 1 × 2.5 µm), and the thickness of Si_3N_4 membrane of the micro paddle is 200 nm.

After addition of the platinum mass a shift in the resonance frequency was measured to be 18.1 KHz from a fundamental frequency of ~1.3 MHz. This micro paddle is planned to be used for the purpose of detecting the deposited mass of protein (NeutrAvidin) on binary SAM BUT/TEG. To measure the change in the frequency before and after deposition of NeutrAvidin, the following equations should be applied.[105,106]

$$f_0 = B(m_p)^{-1/2} \qquad \textbf{(Equation 2.5)}$$

$$f_a = B(m_p + m_d)^{-1/2} \qquad \textbf{(Equation 2.6)}$$

Where B represents a constant and it was calculated from the previous study to be 1.768 Hz/g$^{-1/2}$,[107] f_0 is the fundamental frequency (1.3 MHz), and f_a represents the frequency change upon analyte binding. m_p and m_d represent the mass of the paddle and the analyte respectively. Therefore Δf represents the frequency change ($f_0 - f_a$). After combining equation 2.5 and 2.6, equation 2.7 will be as follows:

$$m_d = B^2/(f_a^2 - f_0^2) \qquad \textbf{(Equation 2.7)}$$

Thus, if it is assumed that the change in the fundamental frequency is 1 Hz, then m_d will be equal to 2.845 ag, and if the change in the fundamental frequency is 1000 Hz due to the deposition of analyte, then m_d will be equal to 2.845 fg.

This can be related to the coverage of NeutrAvidin on this Micropaddle through the following calculations:

M_w of NeutrAvidin is 60000 Da which is equal to 9.96×10^{-23} kg/NeutrAvidin, where 1 Da is equal to 1.66×10^{-27} kg.

The total area of the micro paddle is 80×10^{-8} cm^2.

Area of NeutrAvidin (2D) is 5 nm × 5 nm = 25.00×10^{-14} cm^2, and by dividing the total area of the micro paddle with the area of NeutrAvidin, then the total number (complete coverage) of NeutrAvidin on this micro paddle is 3.20×10^6 molecule.

Maximum mass of deposited NeutrAvidin for a complete coverage of a micro paddle

= 3.20×10^6 molecule × 9.96×10^{-20} g/molecule

Maximum mass = 3.18×10^{-13} g.

The mass sensitivity of this micro paddle as mentioned above is 55 ag/Hz.

Thus, the frequency required to detect the deposited mass of NeutrAvidin was calculate according to the following equation.[108]

$$\Delta f = \Delta m / S \qquad \textit{(Equation 2.8)}$$

$= 3.18 \times 10^{-13}$ g $/ 5.50 \times 10^{-18}$ g/Hz

= 5.8 kHz is the frequency shift when there is a complete coverage of NeutrAvidin which is equivalent to of 3.99×10^{12} Neutravidin/cm^2 as a maximum number of NeutrAvidin. Typically, this type of sensors might be expected to have 1 Hz frequency resolution,[109,110] if the fundamental frequency shifts 1 Hz then a minimum mass of deposited NeutrAvidin on micro paddle = 1 Hz × 5.50×10^{-18} g/Hz to be 6.90×10^{7} Neutravidin/cm^2 as a minimum number of NeutrAvidin.

2.10. Experimental

2.10.1. a. Chemicals Supplied

- BUT [biotinylated tri(ethylene glycol) undecanethiol] was purchased from Nanoscience Instruments, USA.
- TEG [(11-Mercaptoundecyl) Tetra(ethylene Glycol)] was synthesised by Dr Parvez Iqbal with purity >99%, analysed by elemental analysis (Appendix A4).
- NeutrAvidin was purchased from Life Technologies, USA.

- H_2SO_4 98% (w/w) was purchased from Fischer scientific.
- H_2O_2 30% (w/w) in H_2O was purchased from Fischer scientific.
- HPLC ethanol was purchased from Fischer scientific with purity of 99.9%.
- UHQ water was collected from an Ultra High-Quality Purification System Unit (UHQ-PS), which was purchased from the USFELGA Company. The UHQ-PS was filled with de-ionized water to get Ultra High-Quality water (18 μΩ.cm).

2.10.2. b. Au Substrates Supplied

1. ***The polycrystalline Au substrates for contact angle and ellipsometry*** were purchased from George Albert PVD, Germany. This Au substrate consisted of a 100 nm layer of Au, on top of a 5 nm adhesion layer of titanium between the Au and the 4 inch-silicon wafer, and had lateral dimensions of 10 mm × 10 mm. This type of Au substrate was used to characterize the SAM by CA and ellipsometry. Three substrates of Au were used for every experiment to deposit the SAM on.
2. ***The Au substrate for SPR*** was purchased from George Albert PVD, Germany. This Au substrate consisted of a 50 nm layer of Au layer, on top of a 5 nm adhesion layer of Cr between the Au and the 4 inch-glass substrate. It had lateral dimensions of 125 mm x 125 mm. This type of Au substrate was used to deposit pure BUT, TEG and the eight BUT:TEG mixed SAMs on, and to characterize the immobilization of NeutrAvidin on these SAMs, by Surface

Plasmon Resonance. Three of the Au substrates were used for each experiment to deposit the SAM on.

3. ***The Au substrate for QCM*** was purchased from Novaetech, Italy. This Au substrate consisted of a 200 nm layer of Au, on top of a 10 nm adhesion layer of titanium between the Au and the 160 µm thickness quartz crystal, with a fundamental frequency of 10 MHz. The QCM had a blank diameter of 13.9 mm with an electrode diameter of 6 mm for both sides. $4.5 \times 10^{-9} g/Hz^1.cm^2$ is the nominal sensitivity of this QCM-sensor with a resistance of ~10 ohm. This type of Au substrate was used as a sensor to characterize the immobilization of NeutrAvidin on optimum mixing of BUT: TEG mixed SAM which is 2:1 (from SPR), by Quartz Crystal Microbalance. 3–4 QCM-sensor crystals were used for each experiment to deposit the SAM on.

2.10.3. SAM Formation

2.10.3.1. Cleaning Au substrates for CA, Ellipsometry, SPR, XPS and QCM Prior to SAM formation with TEG, BUT or Mixture

Prior to SAM formation the Au substrates listed above (section 2.10.2b) were immersed in Piranha solution (5 ml, 7:3, concentrated 70% H_2SO_4: 30% H_2O_2) in a glass vial (7 mL) for ~10 min at room temperature, (Caution: Piranha solution is a strong oxidant and can violently react with organic compounds, thus keep organic solvents and solids away from this solution). The Au substrate was removed with tweezers and rinsed thoroughly with copious amounts of (UHQ) water for 1 min, then immersed in HPLC ethanol (5 mL) in a vial (7 mL) and (30 kHz) ultrasonicated

for 2 min, removed with tweezers and dried with stream of nitrogen immediately prior to being immersed in 0.1 mM of HPLC ethanolic solutions of BUT or TEG and their binary mixtures thereof.

2.10.3.2. Preparation of BUT Self-Assembled Monolayers

A freshly prepared HPLC ethanolic solution of BUT (2 mL, 0.1 mM) was purged with N_2 (3 mins) in a glass vial (3.5 mL). The gold substrate was immersed in the degassed solution, and immediately the vial was capped and sealed with parafilm, and covered in foil to exclude light. After 24 hours the gold substrate was removed carefully with clean tweezers, and rinsed with HPLC ethanol (10–15 seconds) followed by sonication in a clean vial (3.5 mL) containing HPLC ethanol (3 mL) for 10 mins. The Au substrate was removed from the vial and the sonication procedure carried out again in fresh HPLC ethanol. The Au substrate was removed with tweezers from the HPLC ethanol and dried under a stream of N_2 gas, and then stored for characterisation immediately as a fresh sample in a clean dry vial which was capped and sealed with parafilm, and covered in foil.

2.10.3.3. Preparation of TEG Self-Assembled Monolayers

The TEG SAM formation on Au substrates was identical to BUT SAM formation as detailed above using a HPLC ethanol solution of 0.1 mM of TEG (experimental section 2.10.3.2).

2.10.3.4. Preparation of mixed BUT and TEG Self-Assembled Monolayers

Eight different binary solutions were prepared from the stock BUT (0.1 mM) and TEG (0.1 mM) solutions by combining various volumes of each together as detailed in Table 2.2. These

solutions were then used to form SAMs on Au surfaces as was the case for pure BUT and TEG SAMS detailed above (section 2.10.3.2).

2.11. Surface characterisation

2.11.1. Contact angle (CA) measurements

Dynamic contact angle (CA) analysis was utilised to determine the advancing and receding contact angles for pure and mixed SAMs of TEG and BUT. The measurements were performed using a Theta Lite instrument (KSV Ltd., Helsinki, Finland) which was equipped with automatic water dispensing system at 17 ^{o}C and camera. The analysis of the CA of a droplet of ultrahigh Quality (UHQ) water at the connection of the three phases was made by using the OneAttension software at 17 ^{o}C and the sessile drop technique was used. The left-hand and right-hand side contact angle of the droplet when advancing and receding was determined using the Young-Laplace equation around the water droplet, and the average value was used for comparison between different samples. Averages and standard errors for the CA values were calculated by making each SAM on three Au substrates, and taking five measurements from each substrate.

2.11.2. Ellipsometry measurements

A Jobin-Yvon UVISEL ellipsometer with a xenon light source was used as spectroscopic method to observe the thickness of the SAMs on Au substrates. The calculations were built on a model of three-phase (ambient/SAM/Au model) using the software DeltaPsi, and assuming that the SAM was homogeneous. A 70^{o} angle was fixed as the angle of incident light in all subsequent

measurements. The wavelength range was 250–800 nm. Averages and standard errors for the ellipsometric thickness were derived from three SAMS on which nine measurements, at different places on the substrate, on each were made, *i.e.* twenty seven individual measurement for each SAM. The errors reported are standard errors for each thickness and are reported in Table 2.3. All results of ellipsometry observed for BUT SAM on gold coated silicon substrates are in good agreement with the length of biotin calculated theoretically by ChemBio Draw 3D Ultra 14.0 which was determined as 4.50 nm, (see Figure 2.2). The refractive index used in this type of BUT SAM was $n_f = 1.475$ according to the refractive index of the TEG spacer.[30]

2.11.3. Surface Plasmon Resonance (SPR) measurements

All SPR measurements were performed on a Reichert SR7000DC Dual Channel Spectrometer (Buffalo, NY, USA) at 25 °C. A two-channel flow cell with two independent parallel flow channels was used to carry out the NeutrAvidin binding experiments. A gold-coated SPR substrate, derivatised with the SAMs, as described earlier (section 2.10.3), was placed on the base of the SPR prism using a refractive index-matching oil. Ten different SAMs were analysed (i) pure BUT, and (ii) pure TEG, and (iii) the eight binary BUT:TEG SAMs (Table 2.2). A solution of phosphate-buffered saline (10 mM PBS; 11.9 mM Phosphates, 137 mM NaCl, and 2.7 mM KCl, pH 7.4) was flowed (10 µl/min) over the SAM for 15 min to obtain a baseline, followed by a NeutrAvidin solution (5 µg/mL), (10 µl/min) for 50 min, followed finally by the phosphate-buffered saline solution (10 µl/min) for 20 min to wash any non-specifically adsorbed Neutravidin from the surface. The results were obtained from SPR are an average of 3–4 experiments for each SAM.

2.11.4. Quartz Crystal Microbalance (QCM) measurements

All QCM were performed on an OpenQCM (Novaetech, Italy). A one flow cell with two independent parallel flow channels was used to carry out the NeutrAvidin binding experiments. A gold-coated AT-cut QCM-sensor, covered with a 66 $X^{\%\,BUT}$ SAMs was installed on the QCM holder (HC-48/u). All experiments were performed at a flow rate of 40 µl/min by using a peristaltic pump with a regulator to adjust the flow rate. A solution of phosphate-buffered saline (10 mM PBS; 11.9 mM Phosphates, 137 mM NaCl, and 2.7 mM KCl, pH 7.4) was flowed (40 µl/min) over one side of QCM-sensor (coated with the SAM) for 15 min to obtain a baseline, followed by a NeutrAvidin solution (5 µg/mL), 40 µl/min) for 105 min, followed finally by the phosphate-buffered saline solution (40 µl/min) for 30 min to wash any non-specifically adsorbed NeutrAvidin from the surface. This experiment was repeated four times for reproducibility of the QCM measurements.

2.11.5. AFM measurements

A NanoWizard II AFM (JPK Instruments, UK) was used to image the topography of the surfaces before and after immobilization of NeutrAvidin onto the 66 $X^{\%BUT}$ SAM, using a non-contact and tapping mode in air, using an uncoated Si cantilever (PPP-NCL, Windsor Scientific, UK, nominal length 225 ± 10 µm, width 38 ± 7.5 µm, thickness 7 ± 1 µm, tip height 10–15 µm, tip radius <10 nm and spring constant 21–98 N/m. The scan size was 500 nm × 500 nm, employing a pixel density of 512 × 512. Three Au substrates were analysed, with and without NeutrAvidin absorption, scanning six areas on each, in order to observe the uniformity, or not, of the distrib-

ution of the immobilised NeutrAvidin.

2.11.6. X-ray Photoelectron Spectroscopy (XPS)

XPS was performed using a K-Alpha instrument (Thermo Scientific, East Grinstead, UK) which is based at the Newcastle EPSRC Nanolab Nexus XPS Facility at the Newcastle University, UK. A monochromatic Al K_α 1486.68 eV radiation was used as the source of X-ray (Voltage/Current/Power: 12 kV/3 mA/36 W), with a zero-degree emission (take off angle 90^o) from the normal to the surface, and a rectangular spot size of 400 µm × 800 µm. The survey spectra were recoded with 200 eV pass energy, fifty scans, dwell time 0.01 s and step size 1 eV over a binding energy range of -9.92 eV to 1350.08 eV. The spectra of N (1s) and S (2p) were recorded with 40 eV pass energy, fifty scans, dwell time 0.025 s and step size 0.1 eV. Whereas, Au (4f), C (1s), O (1s) were recorded with 40 eV pass energy, ten scans, 0.1 s dwell time and step size 0.1 eV. CasaXPS software version 2.3.18PR1.0 was used for all spectral fitting of binding energies with linear background type and Gaussian/Lorentzian peaks fitting [G (70)/L (30)], and to calculate the area under the binding energies of each element.

2.12. References

[1] S. Maisch, F. Buckel and F. Effenberger, *J. Am. Chem. Soc.*, 2005, **127**, 17315–22.

[2] S. Frey, V. Stadler, K. Heister, W. Eck, M. Zharnikov, M. Grunze, B. Zeysing and A. Terfort, *Langmuir*, 2001, **17**, 2408–2415.

[3] C. D. Bain and G. M. Whitesides, *Angew Chem Adv Mater*, 1989, **4**, 522–528.

[4] G. K. Toworfe, S. Bhattacharyya, R. J. Composto, C. S. Adams, I. M. Shapiro and P. Ducheyne, *J. Tissue Eng. Regen. Med.*, 2009, **3**, 26–36.

[5] J. N. Herron, W. Muller and H. Ringsdorf, *Langmuir*, 1992, **8**, 1413–1416.

[6] M. Riepl, K. Enander, B. Liedberg, M. Schäferling, M. Kruschina and F. Ortigao, *Langmuir*, 2002, **18**, 7016–7023.

[7] P. H. Tan. and P. S. stayton and A. Chilkoti, *Biophysics (Oxf).*, 1995, **92**, 1754.

[8] E. P. Diamandis and T. K. Christopoulos, *Clin. Chem.*, 1991, **37**, 625–636.

[9] T. M. Alvarez-Diez, J. Polihronis and R. M. Reilly, *Nucl. Med. Biol.*, 1996, **23**, 459–466.

[10] J. Zhang, H. P. Lang, F. Battiston, N. Backmann, F. Huber and C. Gerber, *Sensors (Basel).*, 2013, **13**, 5273–85.

[11] N. M. Green, *Biochem. J.*, 1966, **101**, 774–780.

[12] B. L. Haussling, B. Michel and H. Ringsdorf, *Angew. Chem. Int. Ed. Engl.*, 1991, **30**, 3–6.

[13] P. M. Wolny, J. P. Spatz and R. P. Richter, *Langmuir*, 2010, **26**, 1029–34.

[14] K. E. Nelson, L. Gamble, L. S. Jung, M. S. Boeckl, E. Naeemi, S. L. Golledge, T. Sasaki, D. G.

Castner, C. T. Campbell and P. S. Stayton, *Langmuir*, 2001, **17**, 2807–2816.

[15] C. L. Yeung, P. Iqbal, M. Allan, M. Lashkor, J. A. Preece and P. M. Mendes, *Adv. Funct. Mater.*, 2010, **20**, 2657–2663.

[16] Y. Hiller, J. M. Gershoni, E. A. Bayer and M. Wilchek, *Biochem. J.*, 1987, **248**, 167–171.

[17] R. K. Clark, Y. Tani and I. Damjanov, *J. Histochem. Cytochem.*, 1986, **34**, 1509–1512.

[18] P. J. Brett, H. Tiwana, I. M. Feavers and B. M. Charalambous, *J. Biol. Chem.*, 2002, **277**, 20468–20476.

[19] V. H. Pérez-Luna, M. J. O'Brien, P. D. Hampton, G. P. López and P. S. Stayton, *J. Am. Chem. Soc.*, 1999, **121**, 6469–6478.

[20] N. M. Green, *Adv. Protein Chem.*, 1963, **29**, 85–133.

[21] C. Rosano, P. Arosio and M. Bolognesi, *Biomol. Eng.*, 1999, **16**, 5–12.

[22] G. E. Poirier and E. D. Pylant, *Science*, 1996, **272**, 1145–1148.

[23] G. Poirier and M. Tarlov, *Langmuir*, 1994, **10**, 2853–2856.

[24] B. Lüssem, L. Müller-Meskamp, S. Karthäuser and R. Waser, *Langmuir*, 2005, **21**, 5256–5258.

[25] G. M. Wang, W. C. Sandberg and S. D. Kenny, *Nanotechnology*, 2006, **17**, 4819–4824.

[26] H. Grönbeck, A. Curioni and W. Andreoni, *J. Am. Chem. Soc.*, 2000, **122**, 3839–3842.

[27] G. E. Poirier, *Langmuir*, 1997, **13**, 2019–2026.

[28] E. Torres, A. T. Blumenau and P. U. Biedermann, *Phys. Rev. B - Condens. Matter Mater.*

Phys., 2009, **79**, 1–6.

[29] A. Ulman, *Chem. Rev.*, 1996, **96**, 1533–1554.

[30] A. Ulman, *An introduction to ULTRATHIN ORGANIC FILMS From Langmuir-Blodgett to Self-Assembly, Part-3: Langmuir-Blodgett Films,* 1991.

[31] L. Houssiau, M. Graupe, R. Colorado, H. I. Kim, T. R. Lee, S. S. Perry and J. W. Rabalais, *J. Chem. Phys.*, 1998, **109**, 9134–9147.

[32] Y. Liu, M. Yang, Z. Zheng and B. Zhang, *Electrochem. commun.*, 2005, **7**, 344–348.

[33] S. E. Creager and J. Clarke, *Langmuir*, 1994, **10**, 3675–3683.

[34] C. D. Bain, J. Evall and G. M. Whitesides, *J. Am. Chem. Soc.*, 1989, **111**, 7155–7164.

[35] J. P. Folkers, P. E. Laibinis and G. M. Whitesides, *Langmuir*, 1992, **8**, 1330–1341.

[36] E. B. Troughton, C. D. Bain, G. M. Whitesides, R. G. Nuzzo, D. L. Allara and M. D. Porter, *Langmuir*, 1988, **4**, 365–385.

[37] P. Pollheimer, B. Taskinen, A. Scherfler, S. Gusenkov, M. Creus, P. Wiesauer, D. Zauner, W. Schöfberger, C. Schwarzinger, A. Ebner, R. Tampé, H. Stutz, V. P. Hytönen and H. J. Gruber, *Bioconjug. Chem.*, 2013, **24**, 1656–1668.

[38] J. Spinke, M. Liley, H. G. L. Angermaierj and W. Knoll, *Langmuir*, 1993, **9**, 1821–1825.

[39] Z. Yang, W. Frey, T. Oliver and A. Chilkoti, *Langmuir*, 2000, **16**, 1751–1758.

[40] K. L. Prime and G. M. Whitesides, *J. Am. Chem. Soc.*, 1993, **115**, 10714–10721.

[41] R. Maalouf, C. Fourneir-Wirth, J. Coste, H. Chebib, Y. Saikali, O. Vittori, J. Cloarec, C.

Martelet and N. Jaffrezic-Renault, *Anal. Chem.*, 2007, **79**, 4879–4886.

[42] C. Pale-Grosdemange, *J. Am. Chem. Soc.*, 1991.

[43] A. J. Pertsin, M. Grunze and I. A. Garbuzova, *J. Phys. Chem. B*, 1998, **102**, 4918–4926.

[44] R. L. C. Wang, H. J. Kreuzer and M. Grunze, *J. Phys. Chem. B*, 1997, **101**, 9767–9773.

[45] P. Harder, M. Grunze, R. Dahint, G. M. Whitesides and P. E. Laibinis, *J. Phys. Chem. B*, 1998, **102**, 426–436.

[46] Z. Yang, J. A. Galloway and H. Yu, *Langmuir*, 1999, **15**, 8405–8411.

[47] L. Li, S. Chen, J. Zheng, B. D. Ratner and S. Jiang, *J. Phys. Chem. B*, 2005, **109**, 2934–2941.

[48] L. S. Jung, K. E. Nelson, C. T. Campbell, P. S. Stayton, S. S. Yee, V. Pérez-Luna and G. P. López, *Sensors Actuators B Chem.*, 1999, **54**, 137–144.

[49] I. Zaccari, B. G. Catchpole, S. X. Laurenson, A. G. Davies and C. Wälti, *Langmuir*, 2014, **30**, 1321–1326.

[50] P. C. Weber, D. H. Ohlendorf, J. J. Wendoloski and F. R. Salemme, *Science*, 1989, **243**, 85–88.

[51] W. A. Hendrickson, A. Pähler, J. L. Smith, Y. Satow, E. A. Merritt and R. P. Phizackerley, *Proc. Natl. Acad. Sci. U. S. A.*, 1989, **86**, 2190–4.

[52] A. J. W. Hartel, M. Glogger, N. G. Jones, W. Abuillan, C. Batram, A. Hermann, S. F. Fenz, M. Tanaka and M. Engstler, *Nat. Commun.*, 2016, **7**, 1–9.

[53] X. Wang, Y. Liu, Z. Chen, Y. Li, K. Sun and X. Jiang, *J. Mater. Sci.*, 2014, **49**, 4394–4398.

[54] T. M. Willey, A. L. Vance, T. Van Buuren, C. Bostedt, L. J. Terminello and C. S. Fadley, *Surf. Sci.*, 2005, **576**, 188–196.

[55] J. Maciel, M. C. L. Martins and M. A. Barbosa, *J. Biomed. Mater. Res. Part A*, 2010, **9999A**, NA-NA.

[56] J. C. Love, J. K. Kriebel, R. G. Nuzzo and G. M. Whitesides, *Chem. Rev.*, 2005, **105**, 1103–69.

[57] C. T. Buscher, D. McBranch and D. Li, *J. Am. Chem. Soc.*, 1996, **118**, 2950–2953.

[58] R. Arnold, A. Terfort and C. Wöll, *Langmuir*, 2001, **17**, 4980–4989.

[59] Y. T. Long, H. T. Rong, M. Buck and M. Grunze, *J. Electroanal. Chem.*, 2002, **524**–**525**, 62–67.

[60] T. Pham, D. Lai, D. Ji, W. Tuntiwechapikul, J. M. Friedman and T. R. Lee, *Colloids Surfaces B Biointerfaces*, 2004, **34**, 191–196.

[61] P. Srivastava, W. G. Chapman and P. E. Laibinis, *Langmuir*, 2005, **21**, 12171–12178.

[62] F. Tao and S. L. Bernasek, *Chem. Rev.*, 2007, **107**, 1408–53.

[63] D. Kim and K. Koo, *J. Ind. Eng. Chem.*, 2004, **10**, 920–926.

[64] D. Kim, E. C. Cho and K. Koo, *NSTI-Nanotech*, 2005, **1**, 438–441.

[65] R. Valiokas, S. Svedhem, S. C. T. Svensson and B. Liedberg, *Langmuir*, 1999, **15**, 3390–3394.

[66] A. B. D. Cassie, *Dis. Fara. Soc.*, 1948, **3**, 11.

[67] P. E. Laibinis and G. M. Whitesides, *J. Am. Chem. Soc.*, 1992, **114**, 1990–1995.

[68] V. H. Pérez-Luna, M. J. O'Brien, K. A. Opperman, P. D. Hampton, G. P. López, L. A. Klumb

and P. S. Stayton, *J. Am. Chem. Soc.*, 1999, **121**, 6469–6478.

[69] J. Spinke, M. Liley, F.J. Schmitt, H.J. Guder, L. Angermaier and W. Knoll, *J. Chem. Phys.*, 1993, **99**, 7012.

[70] C.-M. Yam, C.-M. Pradier, M. Salmain, P. Marcus and G. Jaouen, *J. Colloid Interface Sci.*, 2001, **235**, 183–189.

[71] M. Lashkor, F. J. Rawson, J. A. Preece and P. M. Mendes, *Analyst*, 2014, **139**, 5400–5408.

[72] N. Graf, E. Yegen, T. Gross, A. Lippitz, W. Weigel, S. Krakert, A. Terfort and W. E. S. Unger, *Surf. Sci.*, 2009, **603**, 2849–2860.

[73] A. Stephenson-Brown, H.-C. Wang, P. Iqbal, J. a Preece, Y. Long, J. S. Fossey, T. D. James and P. M. Mendes, *Analyst*, 2013, **138**, 7140–5.

[74] M. Riepl, K. Enander, B. Liedberg, M. Schäferling, M. Kruschina and F. Ortigao, *Langmuir*, 2002, **18**, 7016–7023.

[75] L. S. Jung, K. E. Nelson, P. S. Stayton and C. T. Campbell, *Langmuir*, 2000, **16**, 9421–9432.

[76] K. Kummer, D. V. Vyalikh, G. Gavrila, A. Kade, M. Weigel-Jech, M. Mertig and S. L. Molodtsov, *J. Electron Spectros. Relat. Phenomena*, 2008, **163**, 59–64.

[77] B. Liedberg, I. Lundström and E. Stenberg, *Sensors Actuators B. Chem.*, 1993, **11**, 63–72.

[78] L. Häussling, H. Ringsdorf, F. Schmitt and W. Knoll, *Langmuir*, 1991, **7**, 1837–1840.

[79] L. S. Jung, C. T. Campbell, T. M. Chinowsky, M. N. Mar and S. S. Yee, *Langmuir*, 1998, **14**, 5636–5648.

[80] E. Stenberg, B. Persson, H. Roos and C. Urbaniczky, *J. Colloid Interface Sci.*, 1991, **143**, 513–526.

[81] I. Barinaga-Rementeria Ramírez, L. Ekblad and B. Jergil, *J. Chromatogr. B Biomed. Sci. Appl.*, 2000, **743**, 389–396.

[82] G. Sauerbrey, *Zeitschrift für Phys.*, 1959, **155**, 206–222.

[83] E. Reimhult, C. Larsson, B. Kasemo and F. Höök, *Anal. Chem.*, 2004, **76**, 7211–7220.

[84] M. L. Quillin and B. W. Matthews, *Acta Crystallogr. Sect. D Biol. Crystallogr.*, 2000, **56**, 791–794.

[85] C. Larsson, M. Rodahl and F. Höök, *Anal. Chem.*, 2003, **75**, 5080–5087.

[86] J. Vörös, *Biophys. J.*, 2004, **87**, 553–561.

[87] M. Rodahl, F. Höök, C. Fredriksson, C. A. Keller, A. Krozer, P. Brzezinski, M. Voinova and B. Kasemo, *Faraday Discuss.*, 1997, **107**, 229–246.

[88] F. Hook, B. Kasemo, T. Nylander, C. Fant, K. Sott and H. Elwing, *Anal. Chem.*, 2001, **73**, 5796–5804.

[89] F. Höök, M. Rodahl, P. Brezezinski and B. Kasemo, *Langmuir*, 1998, **14**, 729–734.

[90] P. Popov, Kent State University, PhD thesis, 2015.

[91] C. A. Keller and B. Kasemo, 1998, **75**, 1397–1402.

[92] S. H. Kristensen, G. A. Pedersen, L. N. Nejsum and D. S. Sutherland, *Phys. Chem. B*, 2013, **117**, 10376.

[93] P. Bingen, G. Wang, N. F. Steinmetz, M. Rodahl and R. P. Richter, *Anal. Chem.*, 2008, **80**, 8880–8890.

[94] A. B. Dahlin, P. Jönsson, M. P. Jonsson, E. Schmid, Y. Zhou and F. Höök, *ACS Nano*, 2008, **2**, 2174–2182.

[95] S. J. Fraser, X. Mulet, L. Martin, S. Praporski, A. Mechler, P. G. Hartley, A. Polyzos and F. Separovic, *Langmuir*, 2012, **28**, 620–627.

[96] A. Taninaka, O. Takeuchi and H. Shigekawa, *Int. J. Mol. Sci.*, 2010, **11**, 2135–2151.

[97] J. Canet-Ferrer, E. Coronado, A. Forment-Aliaga and E. Pinilla-Cienfuegos, *Nanotechnology*, 2014, **25**, 395703.

[98] A. T. Winzer, C. Kraft, S. Bhushan, V. Stepanenko and I. Tessmer, *Ultramicroscopy*, 2012, **121**, 8–15.

[99] S. Boujday, A. Bantegnie, E. Briand, P. Marnet, M. Salmain and C. Pradier, *J. Phys. Chem. B*, 2008, **112**, 6708–6715.

[100] H. P. Erickson, *Biol. Proced. Online*, 2009, **11**, 32–51.

[101] L. Jiang, J. Han, L. Yang, H. Ma and B. Huang, *Soft Matter*, 2015, **11**, 7276–7287.

[102] M. Seifert, M. T. Rinke and H. J. Galla, *Langmuir*, 2010, **26**, 6386–6393.

[103] E. D. Kaufman, J. Belyea, M. C. Johnson, Z. M. Nicholson, J. L. Ricks, P. K. Shah, M. Bayless, T. Pettersson, Z. Feldotö, E. Blomberg, P. Claesson and S. Franzen, *Langmuir*, 2007, **23**, 6053–6062.

[104] E. Araya, M. J. Kogan, A. G. Guell, C. A. Escobar and F. Sanz, *J. Chil. Chem. Soc.*, 2014, **59**, 2458–2463.

[105] B. Boonliang, P. D. Prewett, J. Hedley, J. Preece and C. A. Hamlett, *J. Micromechanics Microengineering*, 2008, **18**, 1–4.

[106] S. C. Charandabi, P. D. Prewett, C. A. Hamlett, C. J. Anthony and J. A. Preece, *Microelectron. Eng.*, 2011, **88**, 2229–2232.

[107] N. Mahmoodi, University of Birmingham, PhD thesis, 2017.

[108] A. Boisen, S. Dohn, S. S. Keller, S. Schmid and M. Tenje, *Reports Prog. Phys.*, 2011, **74**.

[109] A. N. Cleland, *New J. Phys.*, 2005, **7**, 235–235.

[110] G. A. Palasantzas, *J. Appl. Phys.*, 2007, **102**, 1–4.

Chapter 3

Experimental Optimization for the Formation of Alkyl and Aryl Amine-Terminated SAM on Au Surface

Abstract

Although the formation of aliphatic and aromatic amine-terminated SAMs on Au and SiO_2 surfaces are well known, the present challenge is to incorporate the benefits of these SAMs in the field of technological interest such as Microelectromechanical systems (MEMS). Thus, this chapter is dedicated towards investigating the optimal experimental conditions necessary for the formation of 11-amino-1-undecanethiol hydrochloride (Alk-amine) and 4-aminothiophenol (Ar-amine) SAM. Through contact angle, ellipsometry and XPS measurements the formation and uniformity of the SAMs are determined. Initially a bilayer formed through hydrogen bonding of the amino functionality. The conditions were modified to have the SAM forming solution acidic (HCl) and basic (triethylamine (TEA)) in order to disrupt the hydrogen bonding. The TEA was shown to be essential to stop the formation of a bilayer. Additionally, the concentration of the TEA solution was also shown to be crucial in limiting the amount of absorption of atmospheric CO_2(g) in the SAM. Two different TEA concentrations were investigated 215 mM and 1 mM. The use of lower concentration was observed to lead to lower amounts of CO_2(g) absorption compared to the higher TEA concentration. Furthermore, the immersion of both SAMs after preparation in 500 mM HCl(aq) was shown to be important to ensure the removal of oxidized sulfur from the SAM. In fact, 500 mM HCl(aq) solution was more effective than using weaker acids such as acetic acid[1] or lower concentration of HCl solutions[2] as used previously, which showed the persistent presence of oxidized sulfur.

3.1. Introduction

11-Amino-1-undecanethiol (Alk-amine)[3,4] and 4-amino thiophenol (Ar-amine)[5,6] SAMs have been widely used by many researchers due to their extensive applications,[7–9] for example as molecular adhesion agents on Au substrates.[6,8,10–12] Due to the basic nature of the amine and therefore the ease in controlling the protonation state *via* simply adjusting the pH of the solution[5] the SAM is in contact with, the subsequent ammonium surfaces can be used to electrostatically bind anionic analytes, such as double or single stands of DNA arrays,[13] proteins,[14] bacteria,[15] organic and inorganic phosphates,[16] and nanoparticulates of SiO_2,[17] zirconia,[18] silver,[19] Cu,[20] and (G-NPs)[21] and functionalized G-NPs.[22] Thus, there is immense interest among the scientific community in utilizing amine-terminated thiolate SAMs for application in biosensors and MEMS devices.[23,24]

3.2. Formation of a monolayer of Alk-amine and Ar-amine

Amine-terminated aliphatic[4] or aromatic-amine thiols[15] are well known to form bilayers when they form a SAM on the surface of Au from an ethanolic solution,[25] as a result of hydrogen bonding between the H of the amine moieties at the periphery of the SAM with the lone pair of amine of unbound thiol which are present in the bulk solution (Figure 3.1a). In order to prevent this bilayer formation Lingyan *et al.*[26] reported that adding a basic solution of 10% (v/v), 1480 mM NH_4OH to the ethanolic solution of the HS-Alk-amine, that was used to form a SAM on gold, followed by washing the SAM with 10% (v/v), 1748 mM CH_3COOH, inhibited the bilayer formation. In addition to inhibiting the bilayer formation, they observed by XPS that the oxidised sulfur was

greatly reduced, as the S 2p spectra showed a peak at a binding energy (BE) of 162 eV which is assigned to the bound thiolate, as well reductions in the BEs at 164 eV and 166 eV, which are characteristic for unbound thiol and oxidized sulfur, respectively. Furthermore, Wang *et al.*[1] also reported that the bilayer is formed as an interplane hydrogen bond between the NH_2 moiety of the deposited molecule of 11-amino-1-undecanethiolate (Alk-amine) SAM on the surface of Au with the NH_2 moiety from 11-amino-1-undecanethiol, which is in the bulk solution (Figure 3.1a). This bilayer phenomena is further encouraged if ethanol is used as the solvent.[25] Moreover, they also observed that the hydrogen bonding was suppressed after addition of triethylamine (TEA) as an organic base [3% (v/v), 215 mM] in HPLC ethanol to the ethanolic solution of the HS-Alk-amine (Figure 3.1b), followed by washing the SAM surface with a solution of CH_3COOH in ethanol [1748 mM] to remove excess TEA from the surface of the Alk-amine SAM. Their observations were confirmed by contact angle and XPS measurements. The CA for the Alk-amine SAM obtained by this improved method was reduced from $43^o \pm 5$ to $28^o \pm 2$ and the difference is attributed to the improvement in the packing density of deposited Alk-amine SAM on the Au surface (Figure 3.1b). Furthermore, this is an indication of the disruption in the interplane hydrogen bonds and hence the removal of the bilayer from the surface of the Alk-amine SAM. The XPS spectra indicated that the unbound thiol (*i.e.* the 11-amino-1-undcanethiol in the bulk solution) with binding energy centred at S $2p_{3/2}$ = 164 eV disappeared and only bound thiol with BE centred at S $2p_{3/2}$ = 162 eV was present, thus strongly suggesting no bilayer was formed. More interestingly, there was a noticeable reduction in the amount of oxidized sulfur (BE of S $2p_{3/2}$ = 166 eV), which was attributed to the addition of TEA which suppressed -$\mathbf{NH_3^+}$ groups formation, thus reducing the

oxidized sulfur which is associated with -$\mathbf{NH_3^+}$ group formation.[1] The thickness of Alk-amine SAMs obtained by Wang *et al.*[1] was 2.04 nm (by XPS) which further indicated a monolayer was formed, although, this thickness is still higher than the theoretical length of 1.80 nm, which was calculated by fully extending the hydrocarbon chain (*i.e.* all the carbons in the hydrocarbon are in trans conformation) in the molecule using ChemBioDraw Ultra 14.0. This increase in the thickness of the amine-terminated thiolate SAM was explained by Song *et al.*[12] who attributed the increased thickness to anions binding to the protonated amine present on the SAM surface, formed by the final acid wash of the SAM. Their explanation was supported by the results of XPS and NEXAFS measurements. According to the oxidised sulfur formation problems, this improved procedure by Wang *et al*[1] was modified by Chuang and Lin.[2] Chuang and Lin used an ethanolic solution of HCl [1% (v/v), 120 mM] rather than CH_3COOH, and observed a small concentration of unbound thiol by XPS, in addition to the oxidized sulfur. They attributed their observation as the result of washing the SAM surface with a weak acid. The weak acid used was an ethanolic solution of CH_3COOH (1748 mM), which was used to remove the excess of TEA as well as removing the unbound thiol and oxidized sulfur from the surface. Thus, an ethanolic solution of strong acid [1% (v/v), 120 mM HCl] was used for washing purposes and a noticeable reduction was obtained in the concentration of unbound thiol and a greater removal of oxidized sulfur from the SAM surface was observed by XPS. Moreover, the XPS spectra showed a small quantity of oxygen present within the SAM. This was attributed to the possibility of adsorption of the atmospheric CO_2 on the surface of the Alk-amine terminated SAM. The CA was measured after washing the surface with 120 mM HCl solution and was observed as $30^o \pm 0.1^o$ which indicates that the packing of the

Alk-amine SAM on the surface of Au had probably improved.

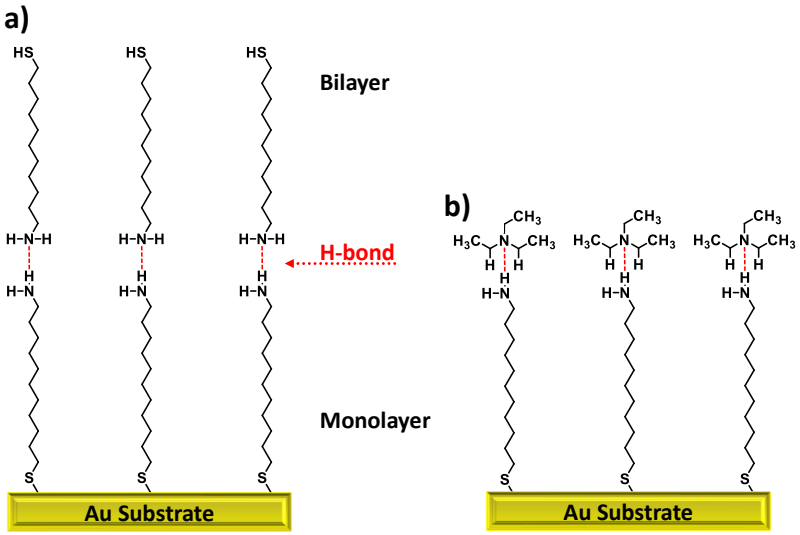

Figure 3.1: a) Formation of a bilayer, and b) improved method of a monolayer formation of Alk-amine on Au surface @ R.T.

According to the above explanation, the conditions for the monolayer formation of Alk-amine and Ar-amine deposited on the Au surface at room temperature were best achieved using Wang's *et al.*[1] procedure. Herein this procedure is used and modify it to further improve upon the SAM formation of Alk-amine and Ar-amine SAMs.

3.3. Aim of the study in this chapter

The aims of this chapter are to form high quality Alk-amine and Ar-Amine SAMs (Figure 3.2) on Au, as a prelude to these SAMs being formed on a MEMS device as detailed in Chapter 4, such that citrate passivated (anionic) gold nanoparticles (G-NPs) can be sensed on the MEMS device *via* modulatable (protonation state of the **-NH_3/-NH_4^+** SAM) electrostatic interactions and investigate the possibility of using a specifically chemically manipulated surface of MEMS

(microresonator) as a sensor for sensing nanoparticles gold nanoparticles (G-NPs), and ultimately smaller and lighter species to improve their limits of detection.

The Alk-amine and Ar-amine thiols used in this study to compare amine surfaces with different pK_as (**-NH_3^+/-NH_2** pK_a for the Alk-amine SAM is ~7.5[3,27–32], while for the Ar-amine SAM is ~5.9[5,33]) in order to see how the G-NP/SAM binding profile varies as function of pH varies, are shown in Figure 3.2.

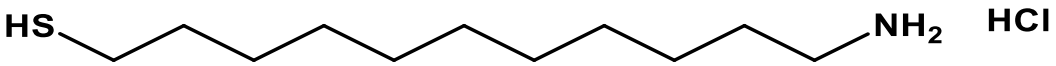

a) Alk-amine = 1.80 nm,* Mwt = 239.85 g/mol,* solibility in EtOH = 0.75 g/L# PK_a of terminal group (in solution) = (10-11) and PK_a on surface ~7.5@

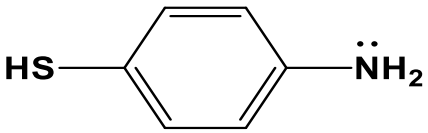

b) Ar-amine = 0.83 nm,* Mwt = 125.19 g/mol,* solibility in EtOH = 5.20 g/L,# PK_a of terminal group in solution = 10-11 and PK_a on surface ~5.9@

Figure 3.2: Illustrates the chemical structures and theoretical length of a) Alk-amine, and b) Ar-amine
** The data calculated from ChemBio Draw 3D Ultra.*
 # The data calculated practically in the lab.
@ The data collected from the literature which are referenced within the text.

Considering the previous literature on Alk-amine SAM formation described earlier, the conditions for the monolayer formation of the Alk-amine and Ar-amine deposited on an Au surface at room temperature were carried out in this chapter using Wang's *et al*.[1] procedure with a modification made by immersion of the amine SAMs in 500 mM $HCl_{(aq)}$ solution for 1h after SAM formation. In addition, a study is performed in this chapter on the effect of TEA concentration on the quality

of the two SAMs. The purpose of this study is to form a monolayer of an Alk-amine and an Ar-amine SAM in order to deposit gold nanoparticles (G-NPs) as a function of pH on to the two SAMs. Contact angle, ellipsometry and XPS are used to confirm the monolayer formation for these two amine SAMs.

3.4. Results and discussion

3.4.1. Formation and Characterisation of Alk-amine and Ar-amine terminated SAM with and without TEA to study the bilayer inhibiting effects of TEA

The SAMs were formed (Figure 3.3) by:

1. immersing for 24 hours three clean Au substrate in HPLC ethanolic (degassed) solution containing Alk-amine or Ar-amine (0.1 mM)
    a. without TEA (three substrates), or
    b. with TEA (215 mM or 1 mM) (three substrates)
2. washing the SAM surface with copious amount of HPLC EtOH and
3. followed by splitting the substrates and:
    a. washing three SAMs formed ***with*** TEA in ethanolic solution of CH_3COOH (1748 mM), and
    b. immersing three SAMs formed ***without*** TEA in $HCl_{(aq)}$ (500 mM) solution for 1 h (control Exp.), and
    c. immersing three SAMs formed ***with*** TEA in $HCl_{(aq)}$ (500 mM) solution for 1 h (Figure 3.3).

4. washed again with copious amount of HPLC ethanol followed by drying with N_2 gas.

The SAMs were characterized by contact angle, ellipsometry and XPS.

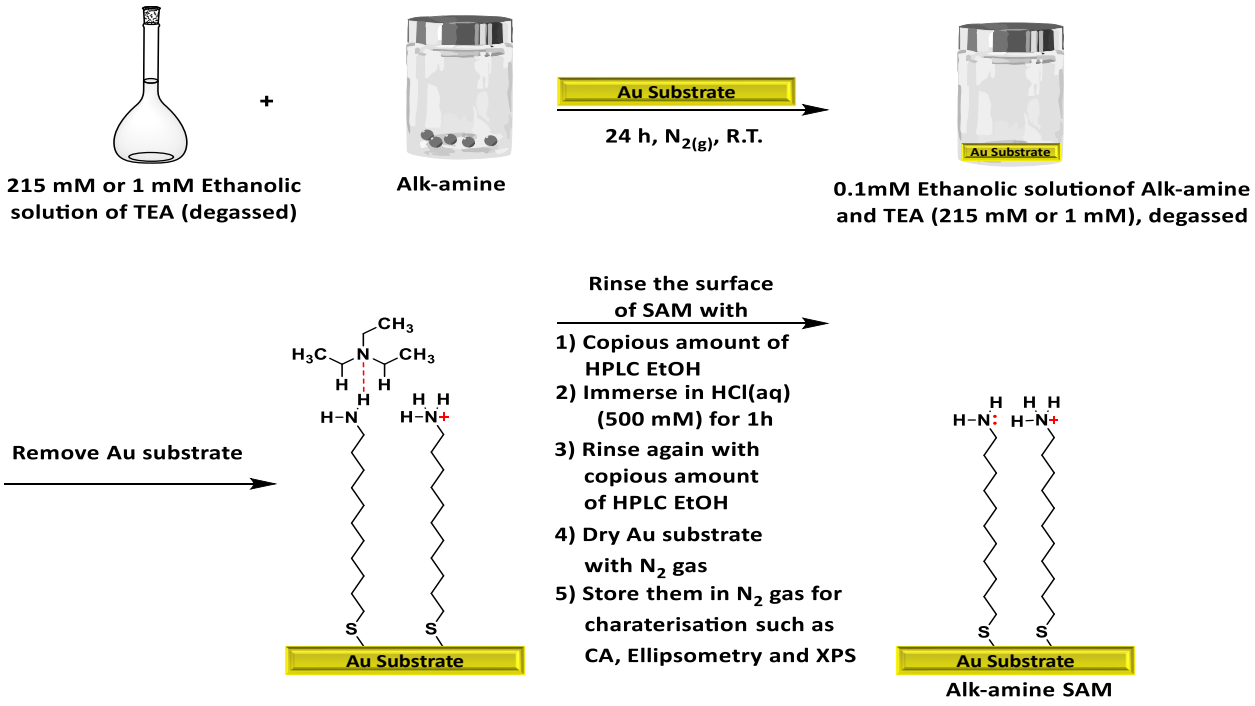

Figure 3.3: Shows the preparation of Alk-c and Alk-d SAM on Au surface at R.T.

3.4.1.1. Contact Angle (CA) measurements

To ensure reproducibility of the measurements, for each amine, three substrates were prepared for each variation in the experimental condition and three contact angle (Θ_a and Θ_r) measurements were recorded on each SAM formed. Each measurement is the average of nine. The contact angle and ellipsometry data are summarized in (Table 3.1)

Table 3.1: Contact angle, ellipsometric and XPS data for Alk-amine and Ar-amine SAM on an Au surface without and with TEA (215 mM) addition and washing the SAMs with CH_3COOH (1748 mM) or immersing in HCl. Note: the grey boxes indicate which variable has changed relative to previous experimental condition, e.g TEA concentration changed or post SAM modification with CH_3COOH or HCl

	Type of Amine (Theoretical Molecular Length)	**Alk-amine (1.80 nm)**					**Ar-amine (0.83 nm)**				
	Experiment Number	***Alk-a***	***Alk-b***	***Alk-c***	***Alk-d***	***Alk-e***	***Ar-a***	***Ar-b***	***Ar-c***	***Ar-d***	***Ar-e***
Technique	**TEA Concentration (mM)**	0	215	215	1	0	0	215	215	1	0
	Post SAM Process/Acid	Washing with EtOH	Washing with CH_3COOH	Immersing in HCl	Immersing in HCl	Immersing in HCl	Washing with EtOH	Washing with CH_3COOH	Immersing in HCl	Immersing in HCl	Immersing in HCl
	Experimental Question		Does TEA inhibit bilayer?	Does HCL remove oxidised S?	Is TEA being retained on SAM?	Control experiment		Does TEA inhibit bilayer?	Does HCL remove oxidised S?	Is TEA being retained on SAM?	Control experiment
CA	Θ_a (°)	72 ± 1	32 ± 3	39 ± 1	42 ± 1	74 ± 3	76 ± 3	59 ± 2	55 ± 2	56 ± 2	75 ± 2
	Θ_r (°)	48 ± 2	10 ± 1	16 ± 2	23 ± 2	51 ± 1	45 ± 2	26 ± 2	26 ± 2	31 ± 3	48 ± 1
	$\Delta\Theta$ (°)	24 ± 1	22 ± 1	23 ± 1	19 ± 1	23 ± 2	31 ± 2	32 ± 2	29 ± 2	25 ± 2	27 ± 2
Ellip	**Thickness (nm)**	2.65 ± 0.36	2.15 ± 0.10	1.90 ± 0.04	1.63 ± 0.07	2.39 ± 0.09	1.53 ± 0.17	0.95 ± 0.10	0.78 ± 0.05	0.55 ± 0.02	1.29 ± 0.13
	%age thicker than theory[a]	47	19	5	-10	33	84	14	-6	-34	55
	Tilt Angle (°)	b	b	b	25	b	b	b	b	48	b
XPS	**Thickness (nm)[c]**	2.16 ± 0.04	1.85 0.02	1.47 ± 0.06	1.69 ± 0.05	2.05 ± 0.03	0.91 ± 0.04	0.70 ± 0.01	0.44 ± 0.03	0.50 ± 0.03	0.87 ± 0.02
	%age diff from Ellip	18	14	23	4	14	41	26	44	9	33
	%age -NH_2	56 ± 3	76 ± 1	64 ± 3	50 ± 1	41 ± 2	87 ± 2	96 ± 4	95 ± 2	90 ± 1	81 ± 3
	%age -NH_3^+	44 ± 1	24 ± 2	36 ± 3	50. ± 1	59 ± 3	23 ± 1	4 ± 1	5 ± 2	10 ± 1	19 ± 3
	Au 4f	29.9 ± 0.8	32.7 ± 1.2	38.2 ± 1.5	35.5 ± 0.9	31.1 ± 0.8	50.3 ± 1.8	55.8 ± 1.7	66.0 ± 2.0	64.0 ± 2.5	51.5 ± 1.2
	C1s	61.0 ± 1.0	57.8 ± 2.0	54.0 ± 0.7	57.0 ± 0.9	60.0 ± 0.6	44.2 ± 1.3	37.3 ± 0.9	28 ± 1.7	30 ± 1.5	43.4 ± 0.9
	N 1s	3.5 ± 0.3	2.7 ± 0.3	2.2 ± 0.3	3.1 ± 0.1	3.7 ± 0.2	1.4 ± 0.2	1.8 ± 0.1	1.2 ± 0.5	1.8 ± 0.3	1.6 ± 0.2
	S $2p_{3/2}$	4.5 ± 0.5	2.6 ± 0.2	1.1 ± 0.2	2.2 ± 0.3	4.1 ± 0.1	2.1 ± 0.1	1.5 ± 0.2	0.6 ± 0.2	1.0 ± 0.1	1.7 ± 0.2

[a] %age the film is thicker relative to theoretical molecular length

[b] tilt angle not calculated as the models (Figure 3.4 a-c and e) are not monolayers, but monolayers with adsorbates on them

[c] Thickness was calculated according to [(C 1s) + (N 1s)]/Au 4f [34]

When comparing the SAM washes with the HPLC EtOH (**Alk-a**, **Ar-a**) or CH_3COOH (**Alk-b**, **Ar-b**) and the solution with and without TEA in the SAM forming solution, respectively, one can clearly see the advancing contact angle is much higher when TEA is not present (72° *vs* 32° for Alk; or 76° *vs* 59° for Ar). This result presumably reflects the moiety exposed to the surface is hydrophobic thiol (-SH),[35] which results from the hydrogen bonded bilayer, relative to a hydrophilic amine/ammonium ($-NH_2$) monolayer, when TEA is used to inhibit the bilayer, as illustrated in (Figure 3.4). Thus, using TEA to inhibit this bilayer is presumably working, and the TEA is subsequently being removed from the SAM surface by the CH_3COOH wash. See ellipsometry and XPS data in the next sections, as evidence for this assumption.

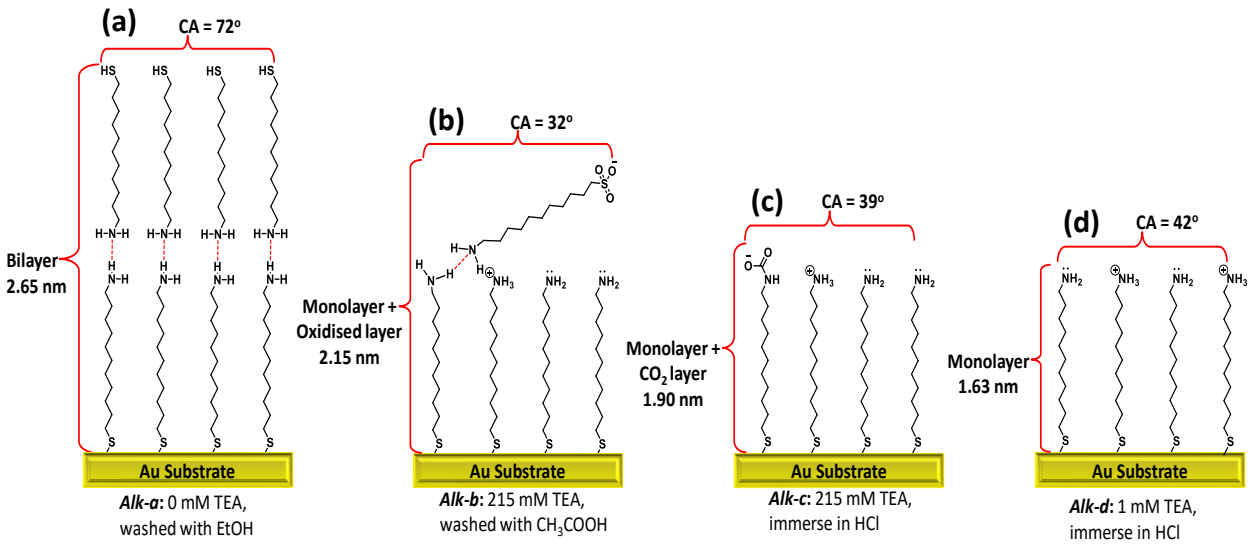

Figure 3.4: Illustrates the difference in the contact angle and ellipsometric determined thickness between a) Alk-a: bilayer formation (without adding 215 mM TEA and washed with HPLC EtOH), b and c) with adding 215 mM TEA for Alk-b: washed with CH_3COOH and for Alk-c: immersed in HCl, and d) adding 1 mM TEA for Alk-d: immersed in HCl

3.4.1.2. Ellipsometry measurements

Similar to the contact angle data, the ellipsometric thicknesses recorded in Table 3.1. are the average of nine measurements taken from 3 SAMs formed for each experimental condition (with and without 215 mM TEA).

As observed with the contact angle results, the ellipsometry data also suggests that the 215 mM TEA inhibits the bilayer formation. Thus, without TEA (**Alk-a**, **Ar-a**) the ellipsometric thickness is significantly greater than the fully extended length of the Alk-amine (47%) or Ar-amine (84%) Figure 3.4a, whilst with 215 mM TEA (**Alk-b**, **Ar-b**) the ellipsometric thickness is only 19% and 14% greater than the fully extended length of the Alk-amine or Ar-amine (Figure 3.4b). However, the thicknesses observed for the two amine SAMs when using TEA, and after washing with CH_3COOH solution, is still higher than the expected thickness. As stated above in (Section 3.2) the increase in the thickness is may be due to the Alk or Ar-amine in which the sulfur has been oxidized and is physisorbed onto the surface of the amine *via* H-bonding. Previously, it has been shown washing the surface with CH_3COOH was not sufficient to remove the oxidized sulfur species from the amine surface[1] (Figure 3.4b), and a stronger acid was required (HCl).[2] Thus, a comparison was made between using CH_3COOH (**Alk-b**, **Ar-b**) and HCl (**Alk-c**, **Ar-c**), for a TEA formed SAM and the data is reported in Table 3.1. Clearly after immersion in 500 mM HCl (**Alk-b**, **Ar-b**), relative to the CH_3COOH acetic acid (**Alk-c**, **Ar-c**) solution, there is a further reduction in the ellipsometric thickness to within less than 10% of the theoretical thickness. The reduction in thicknesses concurs with the improved results obtained for the advancing contact angle data, which is rationalised to be related to the reduction in the defects on the surface of amine SAM that results

from the removal of the oxidized sulfur species (Figure 3.4c).

However, one might suspect that the SAMs should be thinner than found so far, as the molecules are generally found to tilt when forming a SAM, thus reducing the SAM thickness to below the theoretical length. It is hypothesized that the additional thickness might be a result of the concentration of 215 mM for the TEA (**Alk-c**, **Ar-c**) was so high that some of the TEA molecules were still being retained at the SAM surface post the HCl acid immersion (Figure 3.4c). Thus, experiments were designed to reduce the concentration of TEA from 215 mM (**Alk-c**, **Ar-c**) to 1 mM (**Alk-d**, **Ar-d**). The observed thicknesses from ellipsometry for both Alk-amine and Ar-amine SAM have both reduced to less than the theoretical molecular length (1.63 nm (**Alk-d)**, 0.55 nm (**Ar-d)**), giving a tilt angle of 25^{o} (**Alk-d**) and 48^{o} (**Ar-d**), respectively. In addition, the SAM thicknesses calculated *via* XPS are in very good agreement (deviation of 4% and 9%, respectively) at 1 mM TEA, relative to 215 mM TEA (deviation of 23% and 44%, respectively), suggesting that now it should have a coherent monolayer of just the thiols under these final set of conditions (Table 3.1).

3.4.2. Orientation of the two amines SAM from CA and Ellipsometry

The orientation of a monolayer of the amine-terminated **Alk-d** and **Ar-d** SAM is indicated from the tilt angle of the two molecules to the surface in the monolayer. Interestingly, the 48^{o} tilt angle of **Ar-d** is greater than **Alk-d** which is 25^{o}.[3,36] This higher tilt angle of the **Ar-d** SAM/Au surface is similar to the observed tilt angles by Frey *et al*.[37] They attributed the higher tilt angle to the random molecular orientation of the thiolates within the SAM, as well as the thicker backbone

(i.e. the benzene ring), relative to an extended Alk chain. Tao *et al*.[38] and Szafranski *et al*.[39] suggested that the sulfur atom (Au-S-Ph) prefers sp^3 (bend angle of ~104°) (Figure 3.5a) over sp (angle of 180°) hybridization[40–43] (Figure 3.5b). The sp^3 orientation leads to a tilt from the surface normal and accordingly manifests in a higher tilt angle.[36,44] Also, the high tilt angle of **Ar-d** SAM explains why there is a larger difference between the theoretical length and the ellipsometric thickness of **Ar-d** SAM. In addition, the high tilt will expose more of the phenyl ring, which in turn will make the surface more hydrophobic (Figure 3.5b), hence, this explains why the contact angle was higher at 56° for **Ar-d** in comparison to the **Alk-d** SAM which was 42°.

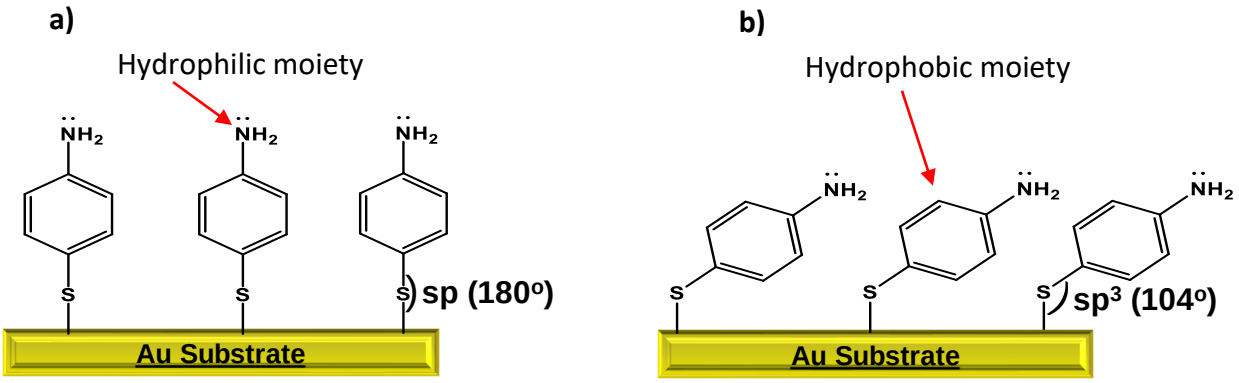

Figure 3.5: a) upright orientation of Ar-amine SAM and b) tilted Ar-amine SAM on Au surface

3.4.3. XPS characterisation of SAMs formed under Alk-d and Ar-d Experimental Conditions (1mM TEA)

XPS survey spectra of 0–800 eV were carried out for **Alk-d** or **Ar-d** SAMs to obtain the elemental composition of the two SAMs (Figure 3.6a). The XPS survey spectra for the two amines

SAMs confirm the presence of all of the XPS spectra peaks that are related to the chemical structure of each amine-terminated SAM which are C 1s, N 1s and S 2p.

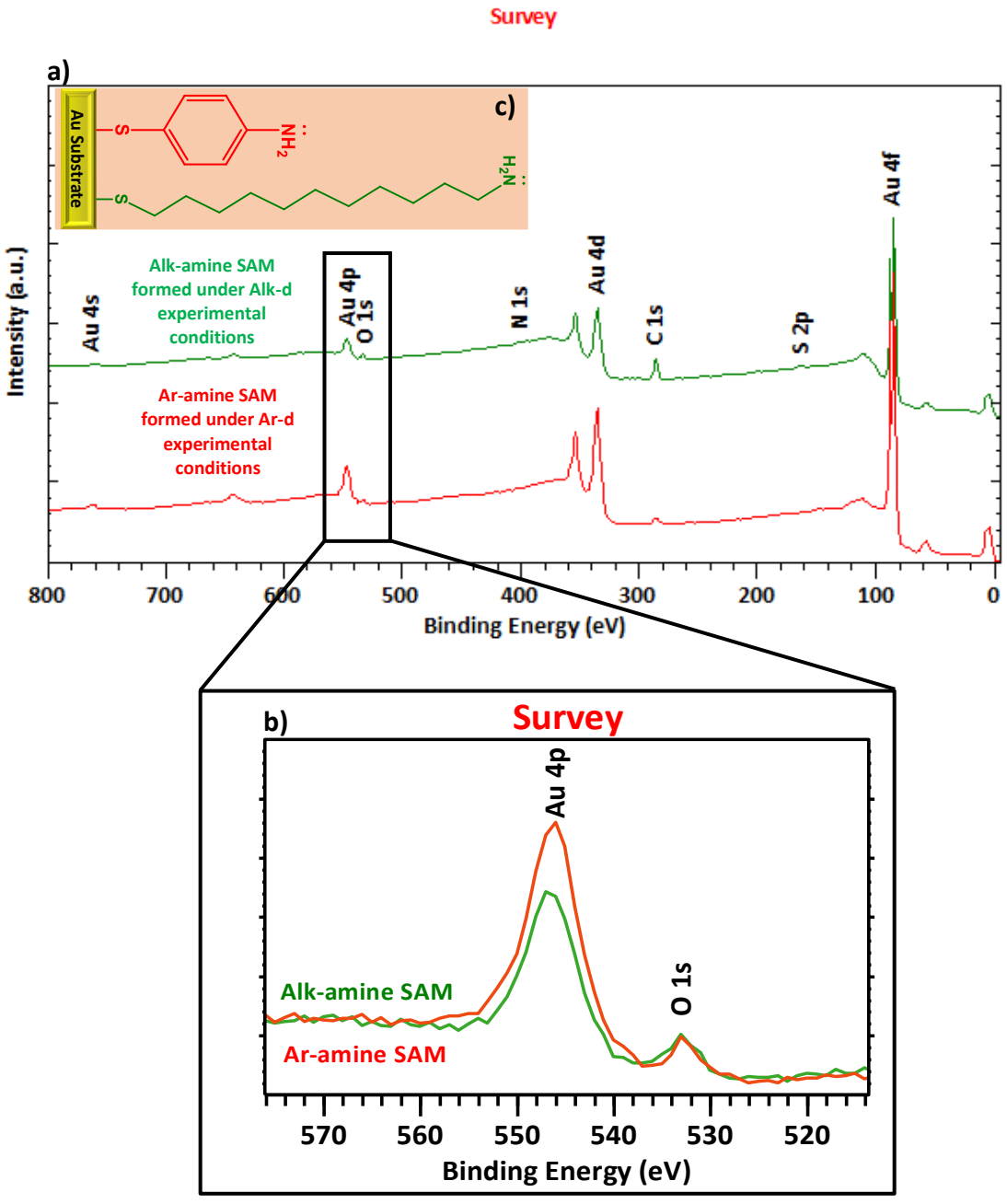

Figure 3.6: XPS spectra of SAMS formed under Alk-d and Ar-d conditions (Table 3.1, Figure 3.3) a) survey spectra, b) Au 4p and O 1s of Alk-d and Ar-d amine SAM deposited on Au surface at room temperature, and c) inset chemical structure of Alk and Ar-amine

It can be seen that the area under the C 1s signal for Alk-amine SAM is much higher than the area under the C 1s signal corresponding to Ar-amine SAM and this difference is related to the higher number of carbon atoms present in Alk-amine molecule (11 relative to 6) (Figure 3.6c). This difference in the number of carbon atoms explains why the intensity of Au 4f from the Alk-amine (Figure 3.7a) spectrum is lower than the intensity from Ar-amine SAM **(Figure 3.7b)**. The attenuation of Au 4f is enhanced by the increase of number of carbon atoms due to the thicker monolayer formed on top of the Au surface (Figure 3.7).[45] In addition, this attenuation could be attributed to the packing density in the **Alk-d** SAM which is more densely packed than the **Ar-d** SAM as confirmed from the ellipsometry results (Table 3.1).

Interestingly, in both the **Alk-d** and **Ar-d** SAM there is an extra XPS spectrum peak in the survey spectra which is related to O 1s spectrum at BE 533 eV (Figure 3.6a,b), this will be discussed in more detail in Section 3.4.3.2.

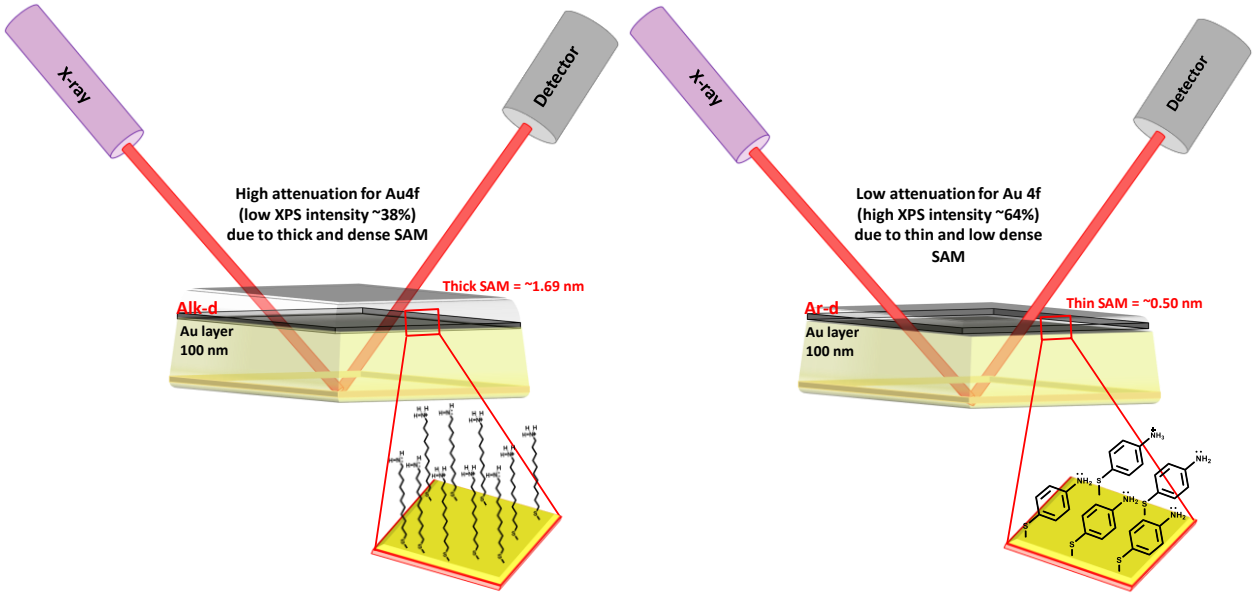

Figure 3.7: The XPS attenuation of Au 4f with a) Alk-d (thick SAM) and b) Ar-d (thin SAM)

3.4.3.1. XPS characterisation of SAMs from Alk-a to Alk-d Experimental Conditions:

Examining the Sulfur Oxidation

From the S 2p spectra one can gain greater insight in to the nature of the interaction between S and the Au surface. Figure 3.8a,e shows the S 2p spectra for a SAM formed without (0 mM TEA, **Alk-a and Alk-e**) and Figure 3.8b,c with 215 mM TEA (**Alk-b** and **Alk-c**), and Figure 3.8d with 1 mM TEA (**Alk-d**) for the Alk thiol. It is clear to see the effect of adding of TEA by following the XPS spectra of S 2p. The S 2p ($2p_{3/2}$ and $2p_{1/2}$) doublet spectrum for the bound thiol to Au surface (S-Au) is centred at BE of about S $2p_{3/2}$ = 162 eV, while the unbound thiols, the doublet is centred at BE of about S $2p_{3/2}$ = 164 eV and no oxidized sulfur was observed from these spectra, which should appear at the BE of about S $2p_{3/2}$ = 168 eV (Figure 3.8c,d,e).[37,46–48] The disappearance of oxidized sulfur in these experiments is due to use of 500 mM HCl solution instead of using ethanolic CH_3COOH (1748 mM) that was reported by Wang *et al*.[1] to wash the surfaces after immersion in thiol solution, as previously mentioned in section 3.2. Repeating Wang's procedure by washing the surfaces with ethanolic CH_3COOH (1748 mM), it is noticeable that the oxidized sulfur is still present on both SAMs (Figure 3.8a,b). This observation was also previously reported by Chuang and Lin and they replaced the CH_3COOH with $HCl_{(aq)}$ (120 mM) (see section 3.2). In this study, the two amine SAMs were immersed in more concentrated $HCl_{(aq)}$ (500 mM) solution to ensure the complete removal of oxidised sulfur. The XPS spectra for S2p (Figure 3.8c,d,e) shows no presence of the XPS peak corresponding to the oxidised sulfur (BE ~168 eV) and hence, the immersion of the SAMs in 500 mM HCl enhances the removal of the oxidized sulfur from the surface.

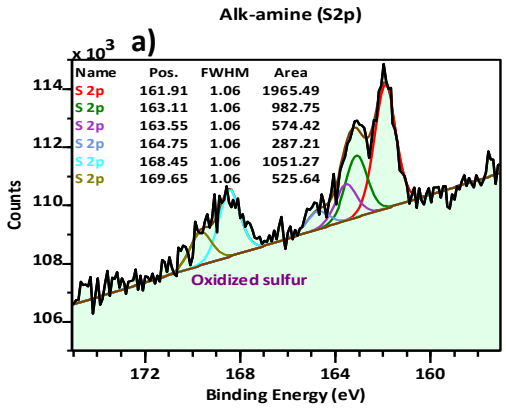

Alk-a: 0 mM TEA, washed with EtOH

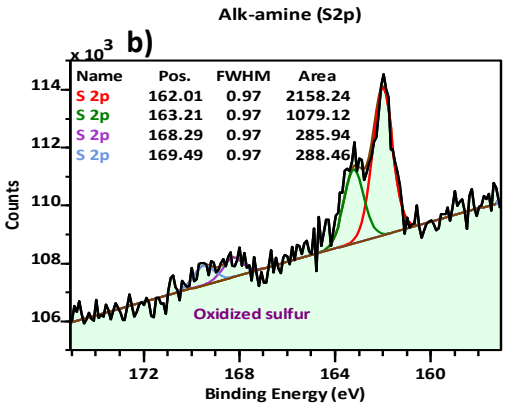

Alk-b: 215 mM TEA-, washed with CH_3COOH

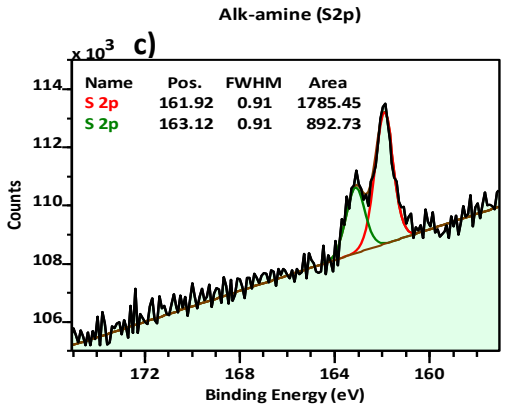

Alk-c: 215 mM TEA, immersed in HCl

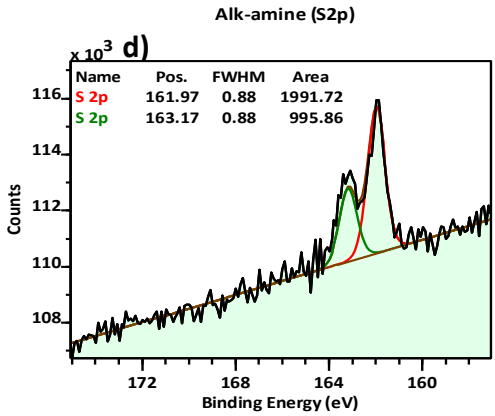

Alk-d: 1 mM TEA-, immersed in HCl

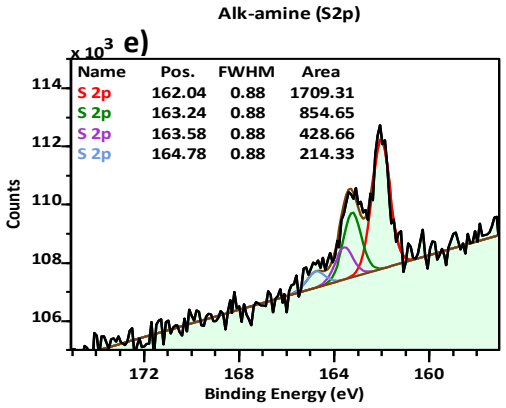

Alk-e (control Exp): 0 mM TEA, immersed in HCl

Figure 3.8: XPS data for S 2p spectra of Alk-amine SAM Across Alk-a to Alk-e Experimental Formation Conditions

3.4.3.2. Adsorption of CO_2 on Alk-d and Ar-d SAM surfaces

Although the oxidised sulfur has been removed from the SAM as described in section 3.4.1 under the **Alk-d** conditions, the oxygen peak can still be observed in the XPS spectra (Figure 3.6b). Hence, there must be another contaminate adsorbed on the surface, which is a contributor to the oxygen present. Previously such O 1s peaks at BE 532 eV[49,50] have been observed on similar SAMs and have been attributed to the presence of oxygen from one of two sources;

- Presence of water which binds to the terminal amine group tightly *via* H-bonding[16,51–53]
- Presence of ambient CO_2.[2,10,15,28,54,55] The CO_2 is either adsorbed from the atmosphere or absorbed in water *via* the formation of H-bond between amine-terminated SAM and CO_2 or *via* the reaction between amine-terminated SAM and CO_2, and forming carbamate as shown by the proposed mechanism (Figure 3.9).[1,10,28,51,56–58]

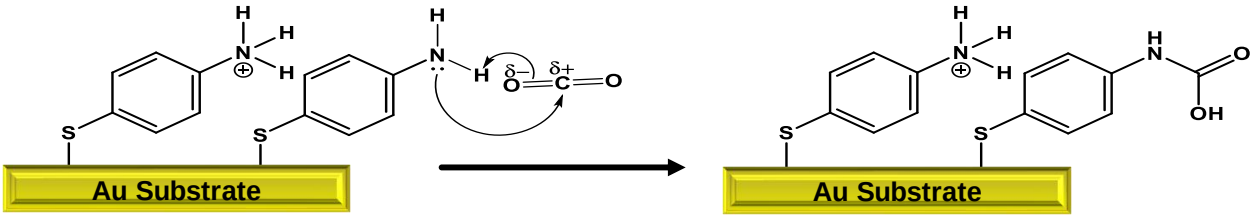

Figure 3.9: Schematic of carbamate formation after the reaction between CO_2 and Ar-d SAM

To determine which is the more plausible contaminant the high resolution spectra of C 1s can be analyzed, as the presence of CO_2 should lead to a peak being observed corresponding to the carbonyl moiety at a binding energy of 289 eV. Indeed, the C1s C=O peak is observed in both **Alk-d** and **Ar-d** SAM (Figure 3.10 c,d). Hence, the likely source of the O 1s peak centered at 533

eV[49] is the presence of absorbed CO_2 in the SAM. The absorption of CO_2 could be detrimental for the purpose of the application as this will reduce the concentration of free amine groups available on the surface for the specific sensing application.[4,49,56,59]

Interestingly, it is noticeable from the XPS data obtained for both amine SAMs that the amount of CO_2 present in the SAM surface is depended upon the concentration of free amine (-NH_2) present on the surface. The amount of free NH_2 can be quantified from the XPS spectra of N 1s (Figure 3.10 a,b). Free NH_2 has a characteristic BE peak at 399 eV, whereas protonated NH_2 has a characteristic BE peak at 401 eV.[15,16,28,46,49,51,56,60] Figure 3.10a shows the high resolution of N 1s spectra for the **Alk-d** SAM. From this spectrum it can be observed that there are two peaks with BE of 399 eV and 401 eV. After fitting the peaks, there is a 1:1 ratio between the two peaks which suggests that there is 50 % NH_2 present and 50 % protonated (Figure 3.10a), while for the Ar-d SAM, only ~10% of the free amine are protonated (Figure 3.10b).[15,28,46,56] The discrepancy between the ratio of free and protonated amine on both Alk- and Ar-NH_2 SAM was also reported by Dietrich *et al*.[46] They concluded the discrepancy was due to the pK_a difference between the Alk-d and Ar-d SAM, which are ~7.5[3,27–32] and ~5.9[5,33] respectively. Hence, it is easier to protonate the Alk-d SAM than the Ar-d SAM.

Furthermore, Table 3.1 shows that there is a clear difference between the free amine that forms from adding 215 and 1 mM TEA to form **Alk-c** and **Alk-d** SAM respectively, while there is a small difference of the free amine with **Ar-c** and **Ar-d** SAM after adding the two concentrations of TEA. The increase of the free amine with 215 mM TEA explains why the high concentration of CO_2 adsorbs on the surface of the two amine SAMs. Accordingly, the formation of the two amine

SAMs was optimized by adding 1 mM TEA.

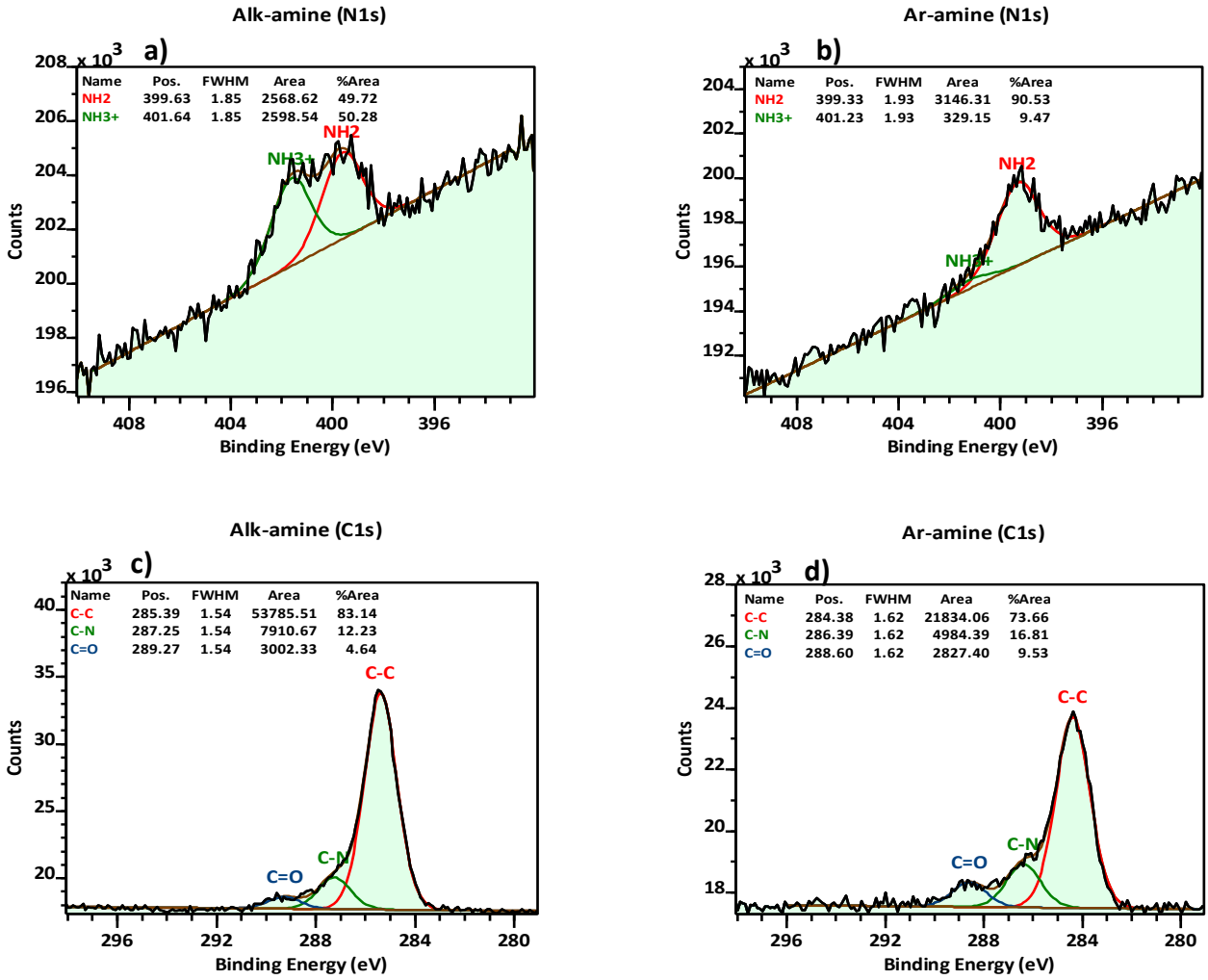

Figure 3.10: XPS Spectra recorded of SAMs formed under Alk-d and Ar-d conditions (1mM TEA and 500 mM HCl immersion for 1 h): a) N 1s spectrum of Alk-d SAM, b) N 1s spectrum of Ar-d SAM, c) C 1s spectrum of Alk-d, and d) C 1s spectrum of Ar-d SAM on Au surface at R.T.

3.4.3.3. Effect of the TEA concentration on the monolayer formation of the two SAMs

Wang *et al.*[1] reported that 3% v/v (215 mM) ethanolic solution of TEA should be used to prevent the bilayer formation. Furthermore, they confirmed that this concentration of TEA is effective to form free amine and suppress the formation of protonated amine (NH_3^+). As

mentioned above (see section 3.4.3.2), the 215 mM TEA generates high concentration of free amine where the later leads to adsorption of higher concentration of CO_2 (oxygen content). The XPS measurements, with takeoff angle 55°, by Wang revealed that the atomic percentage of oxygen content on the **Alk-c** SAM surface was about 5.5 ± 0.2%. Other studies have repeated the same procedure and used the same XPS takeoff angle. The obtained atomic percentage of oxygen content was higher than the one obtained by Wang.[2,28,46]

Herein, Wang's procedure was repeated with exception of the XPS spectra being obtained with a takeoff angle of 90°. Similar results were observed as reported by Wang such as the quantity of oxygen present in the monolayer. The atomic percentage of oxygen observed was 5.5 ± 0.7% which concurs with the reported figure by Wang *et al*.[1] Therefore, two experiments were devised for comparison purposes between the high concentration of **215 mM TEA** and the low concentration of **1 mM TEA** and as mentioned above, the two amine-SAMs were immersed in 500 mM HCl and the results are reported in Table 3.1.

Table 3.1 shows that there is no big difference between the two concentrations apart from atomic percentage of oxygen content especially with **Alk-d** SAM which is reduced to half and this is an indication that the monolayer formation is not affected by the concentration of TEA. In addition, the reduction of oxygen content decreases the attenuation of C 1s, N 1s and S 2p signals of the two amine SAMs and increases the attenuation of Au 4f signal. Thus, the packing density of the two amines were improved and accordingly the quality of the two amine-SAMs on Au surface was increased.

The atomic percentage of oxygen content on Ar-d SAM surface is not reduced as much as seen for the Alk-d where the oxygen content increases with the concentration of free Amine (Figure 3.10a,b).[15,28,46] Furthermore, from Table 3.2 the ratios of O 1s/N 1s for the two amines are ~0.67 and ~1.67 respectively, which means that CO_2 reacts and incorporates with ~33% (~0.67) of Alk-amine SAM and ~83% (~1.67) of Ar-amine SAM.

3.4.3.4. XPS Thickness of Alk and Ar-amine SAM on Au surface (Alk-d and Ar-d Conditions)

The film thickness can also be estimated using data observed by XPS. Graham and Ratner estimated the film thickness of alkanethiolate SAM according to the XPS intensity ratio of C 1s/Au 4f for dodecanethiolate SAM [$HS(CH_2)_{11}CH_3$] which consists of twelve C atoms and was used as a reference for the estimation of SAM film thickness of different alkanethiolates length. They found that this type of SAM follows a linear relationship as a function of the chain length of CH_3-SAM and their finding is based on the attenuation of Au 4f signal (underlying) by the C 1s of the backbone (overlying).[34] Alk-amine SAM consists of eleven carbon atoms + 1 N atom; thus, the total no. of Alk-amine SAM is equal to dodecanethiolate SAM which is 12 and a ratio of (C 1s +N 1s)/Au 4f should follow a linear relationship versus NH_2-SAM chain length. In this study, the same method was used to calculate the film thickness of the two amine SAMs and it can be seen that there is a noticeable difference in the thickness of Alk-a, Alk-b, Alk-c, Alk-d and Ar-a, Ar-b, Ar-c, Ar-d SAM (Table 3.1).

The thickness with 215 mM TEA (Alk-c and Ar-c) is lower than 1 mM TEA (Alk-d and Ar-d), which is due to the higher amount of oxygen (CO_2) adsorbed onto the surface of the amine SAM at higher TEA concentration that leads to stronger attenuation of C 1s signal (Figure 3.11).

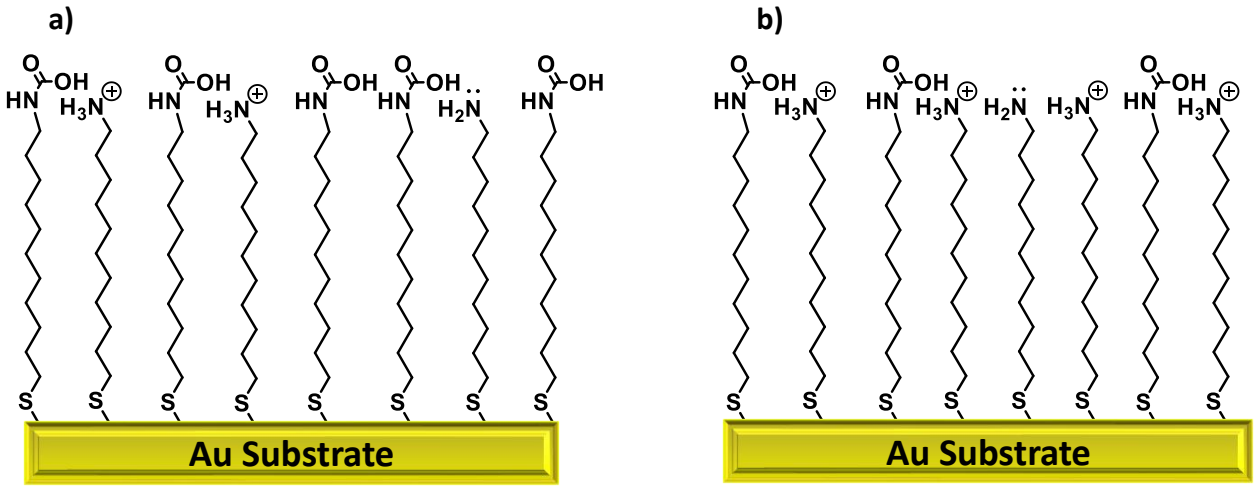

Figure 3.11: CO_2 reacted with free amine formed by adding a) 215 mM, and b) 1 mM TEA

The estimated **Alk-d** SAM film thickness by XPS measurements is somewhat higher than the thickness obtained by ellipsometry (Table 3.1). The small discrepancy in the thicknesses obtained from the two techniques for the SAMs prepared in a thiol solution containing 1 mM TEA can be neglected due to the experimental error and the difference in the principle of the two techniques.

3.4.3.5. Difference between the coverage and orientation of Alk-d and Ar-d SAM on Au surface

The difference in the quality and the coverage of the **Alk-d** and **Ar-d** SAM can be determined from the XPS measurements. Table 3.2 shows the ratios of atomic percentage of the elements C 1s, N 1s, S 2p and O 1s, which were normalized with Au 4f. Table 3.2 clearly reveals the difference between the coverage of **Alk-d** SAMs and **Ar-d** SAM by using the ratios of S/Au and N/Au.[25] The calculated values of S/Au and N/Au ratios suggest that the coverage of **Alk-d** SAM to be 0.060 ± 0.002 and 0.090 ± 0.004 respectively on Au surface is much higher than for **Ar-d** SAM

which is 0.016 ± 0.005 and 0.030 ± 0.009 respectively. [15,25,28,46,60] These findings are supported by the results obtained from contact angle and ellipsometry. (see Table 3.1) and confirms that the coverage of Ar-d SAM is lower than that of Alk-d SAM.

Furthermore, previous studies[2,4,15,16,25,28,34,37,46,49,51,56,58,60,61] have confirmed that the position of the C 1s peak corresponding to C-C moieties provide information on how well the alkanethiols have deposited and the packing density of alkanethiolate SAM on Au surface. Herein, the high resolution C 1s signal for **Alk-d** and **Ar-d** SAM are centred at ~285.4 eV and at 284.4 eV respectively (see Figure 3.10c,d). The shift observed in the position of the peak corresponding to the C-C moiety from 285.4 to 284.4 eV for **Ar-d** SAM suggests that the monolayer is less densely packed than the packing in **Alk-d** SAM where no shift was observed.

The film thickness, by XPS, of the **Alk-d** and **Ar-d** SAM is higher than the film thickness of the two amines SAM without the oxygen content (Table 3.2), and this is an indication that the

Table 3.2: XPS results of atomic percent ratios C 1s, N 1s, S 2p and O 1s normalized with Au 4f for Alk-d and Ar-d SAM at takeoff angle 90°

SAM	Alk-d	Ar-d
Conc. of TEA (mM)	1	1
C/Au	1.600 ± 0.080	0.470 ± 0.010
N/Au	0.090 ± 0.004	0.030 ± 0.009
S/Au	0.060 ± 0.002	0.016 ± 0.005
O/Au	0.060 ± 0.020	0.050 ± 0.001
Thickness (nm) [a]	**1.81 ± 0.08**	**0.57 ± 0.03**

[a] Thickness was calculated according to [(C 1s) + (N 1s) + (S 2p) + (O 1s)]/Au 4f

quality of the two amine SAM is improved and also confirms that the packing density are more

densely packed with less oxygen content (Figure 3.11b).[58] Based on that, the quality of **Alk-d** SAM is higher than **Ar-d** SAM as the oxygen content of the **Ar-d** SAM is higher than the **Alk-d** SAM. Moreover, further information on the orientation of the amine thiols, *i.e.* whether the molecule is bound via sulfur (Figure 3.12a) or nitrogen (Figure 3.12b) can be found by reference to the intensities of N 1s and S 2p peaks.

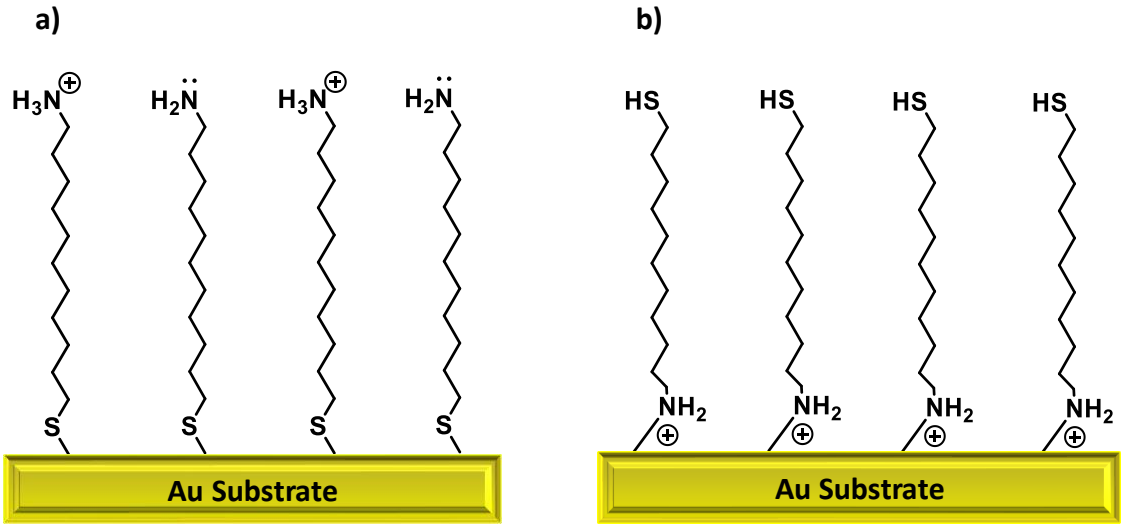

Figure 3.12: Orientation of Alk-d SAM on Au Surface Via a) S atom, and b) N atom (upright orientation)

In principle, the intensity of the N 1s peak should be equal to intensity of the S 2p peak (1:1 ratio), but according to the XPS results which are reported in Table 3.2, it is evident that the intensity of N 1s is higher than S 2p. This is due to stronger attenuation experienced by the sulfur, suggesting the sulfur is more embedded in the monolayer than the nitrogen, hence, suggesting that the sulfur atom is located at the end (underlying) of the backbone chain (overlying) of the **Alk-d** and **Ar-d** SAM **(see Figure 3.6c)**.[62] This, indicates that the **Alk-d** and **Ar-d** SAMs are attached to the Au surface *via* the sulfur atom (Figure 3.12a) not *via* the N atom (Figure 3.12b).

3.5. Conclusion

Contact angle, ellipsometry and XPS have confirmed that monolayers of **Alk-d** and **Ar-d** SAMs have been chemically formed on Au surface, with the addition of ethanolic solution of 1 mM TEA. Also, it was confirmed that TEA plays an important role in inhibiting the formation of a bilayer. In addition, no oxidized sulfur was observed after immersing the SAMs in 500 mM HCl. Furthermore, reducing the amount of adsorbed ambient CO_2 on the free amine surface improves the quality of the deposited SAM on Au for the two amines through the improvement in the thickness which is obtained from XPS and ellipsometry, as well as improving the reduction in the attenuation of the XPS intensities of C 1s, N 1s and S 2p. The ratios of N 1s/Au 4f and S 2p/Au 4f confirm that the attachment of the two amine SAMs are *via* the sulfur atom and the packing density of Alk-d SAM is higher than Ar-d SAM.

3.6. Future work

The objective of the above prepared system is to chemically modify the surface of a micro paddle with a monolayer of Alk or Ar-amine terminated SAM, and the next step is to use this micro paddle to detect the mass of G-NPs.

3.7. Experimental

3.7.1. a. Chemicals Supplied

- 11-amino-1-undecanethiol hydrochloride (99%), Alk-amine, was purchased from Sigma Aldrich, UK.
- 4-aminothiophenol (97%), Ar-Amine, was purchased from Alfa Aesar.
- HPLC ethanol was purchased from Fischer scientific (99.9%).
- HCl (37% w/w) was purchased from Acros organic.
- H_2SO_4 (98% w/w) was purchased from Fischer scientific.
- H_2O_2 30% (w/w) in H_2O was purchased from Fischer scientific.
- UHQ water was collected from Ultra High-Quality Purification System Unit (UHQ-PS) which was purchased from USFELGA Company. The UHQ-PS was filled with de-ionized water to get Ultra High-Quality water (18 μΩ.cm).

3.7.2. b. Au Substrates Supplied

The polycrystalline Au substrates for contact angle, ellipsometry and X-ray photoelectron spectroscopy were purchased from George Albert PVD, Germany. This Au substrate consisted of a 100 nm layer of Au layer, on top of a 5 nm adhesion layer of titanium bonded to the (10 mm × 10 mm) square silicon wafer. This type of Au substrate was used to characterize the SAM by contact angle, ellipsometry and XPS. Three Au substrates were used for each SAM formation, and three analyses were made on each substrate, such that nine measurement of contact angle and

ellipsometric thickness were made, in order to determine and average value and error.

3.7.3. SAM Formation

3.7.3.1. Cleaning Au substrate for CA, Ellip and XPS Prior to SAM formation with Alk-amine or Ar-amine

Prior to SAM formation the Au substrates listed above (section 3.7.2 b) were immersed in Piranha solution (5 ml, 7:3, concentrated 70% H_2SO_4: 30% H_2O_2) in a glass vial (7 mL) for ~10 min at room temperature, (Caution: Piranha solution is a strong oxidant and can violently react with organic compounds. Hence no organic solvents or materials should come into contact with Piranha solution, and should be stored away from Piranha solution). The Au substrate was removed with tweezers and rinsed thoroughly with copious amounts of (UHPQ) water for 1 min, then immersed in HPLC ethanol (5 mL) in a vial (7 mL) and ultrasonicated (30 KHz) for 2 min, before removal and drying with a stream of nitrogen. The clean Au substrates were then immediately immersed in 0.1 mM of HPLC ethanol solutions of the Alk-amine or Ar-amine.

3.7.3.2. Preparation of Alk and Ar-amine SAMs

All the SAM formation (Alk-a, Alk-b, Alk-c, Alk-d and Ar-a, Ar-b, Ar-c, Ar-d) were prepared within 0.1 mM by using HPLC EtOH as a solvent and same amount of Alk-amine or Ar-amine thiols was used for each preparation. This section focused on Alk-d and Ar-d due to the small differences between 'without' or with 'TEA' and washing the prepared SAM with HPLC EtOH, CH3COOH or immersing in HCl.

Thus, for preparing **Alk-d** and **Ar-d**, a 1 mM degassed solution of TEA (20 mL in HPLC EtOH) was added to a glass vial containing 11-amino-1-undecanethiol hydrochloride (the Alk-d) (0.5 mg, 0.002 mmol) or (40 mL in HPLC EtOH) was added in a glass vial of 4-aminothiophenol (Ar-d) (0.5 mg, 0.004 mmol) affording 0.1 mM solution of the two thiols.

The TEA/Thiol solutions were purged again with N_2 (3 mins) in a glass vial (3.5 mL). The gold substrate was immersed in the degassed solution, and immediately the vial was capped, and again was purged with N_2 (3 min) *via* a needle, sealed with parafilm, and covered in foil to exclude light. After 24 hours the gold substrate was removed and rinsed with copious amounts of HPLC EtOH followed by immersion in a clean vial (3.5 mL) containing 500 mM $HCl_{(aq)}$ (3 mL) for 1h. After immersion, the Au substrate was removed from the vial and was rinsed with copious amount of HPLC EtOH, dried under a stream of N_2 gas, and then stored for characterisation as a fresh sample in a clean dry vial, which was capped and sealed with parafilm, and covered in foil (see Figure 3.3).

3.8. Surface characterisation

3.8.1. Contact angle (CA) measurements

Dynamic contact angle (CA) analysis was utilised to determine the advancing and receding contact angles for the Alk-a, Alk-b, Alk-c, Alk-d and Ar-a, Ar-b, Ar-c, Ar-d SAMs. The measurements were performed using a Theta Lite instrument (KSV Ltd., Helsinki, Finland) which was equipped with automatic water dispensing system at 17 ^{o}C and camera. The analysis of the CA of a droplet of ultrahigh Quality (UHQ) water at the three phases was made using OneAttension software and

the sessile drop technique was optioned. The left-hand and right-hand side contact angle of the droplet when advancing and receding was determined using the Young-Laplace equation around the water droplet, and the average value was used for comparison between different samples. Averages and standard errors for the CA values were calculated by making each SAM on three Au substrate, and taking three measurements from each substrate were made, i.e. nine individual measurement for each SAM.

3.8.2. Ellipsometry measurements

A Jobin-Yvon UVISEL ellipsometer with a xenon light source was used as spectroscopic method to observe the thickness of the SAMs on Au substrate. The calculations were built on a model of three-phase ambient/SAM/Au using the software DeltaPsi, and assuming that the SAM was isotropic and homogeneous. A 70^{o} angle was fixed as the angle of incidence light in all measurements. The wavelength range was 250–800 nm. Averages and standard errors for the ellipsometric thickness were derived from three SAMS on which three measurements on each substrate were made, i.e. three individual measurement for each SAM. The errors reported are standard errors for each thickness and are reported in (Table 3.1). Only the results observed by ellipsometry for Alk-d and Ar-d SAMs on gold coated silicon substrate are in good agreement with the length of Alk-amine and Ar-amine calculated theoretically by ChemBio Draw 3D Ultra 14.0, which was determined as 1.80 nm and 0.83 nm respectively, (see Figure 3.2). The refractive index used in this type of Alk and Ar-amine SAM was *(n_f =1.45)*.[63]

3.8.3. X-ray Photoelectron Spectroscopy (XPS)

XPS was preformed using a K-Alpha instrument (Thermo Scientific, East Grinstead, UK), which is based at the Newcastle EPSRC Nanolab Nexus XPS Facility at the Newcastle University, UK. A monochromatic Al K_α 1486.68 eV radiation was used as the source of X-rays (Voltage/Current/Power: 12 kV/3 mA/36 W), with a zero-degree emission (take off angle 90^o) from the normal to the surface, and a rectangular spot size of 400 µm × 800 µm. The survey spectra were recorded with 200 eV pass energy, five scans, dwell time 0.01 s and step size 1 eV over a binding energy range of -9.92 eV to 1350.08 eV. The spectra of high resolution N (1s) and S (2p) were recorded with 40 eV pass energy, 100 scans, dwell time 0.025 s and step size 0.1 eV. Whereas, the high resolution of Au (4f), C (1s), O (1s) were recorded with 40 eV pass energy, twenty scans, 0.025 s dwell time and step size 0.1 eV. CasaXPS software version 2.3.18PR1.0 was used for all spectral fitting of binding energies with linear background type and Gaussian/Lorentzian peaks fitting [G (70) / L (30)], and to calculate the area under the binding energies of each element.

3.9. References

[1] H. Wang, S. Chen, Lingyan Li and S. Jiang, *Langmuir*, 2005, **21**, 2633.

[2] W.-H. Chuang and J.-C. Lin, *J. Biomed. Mater. Res. Part A*, 2007, **82A**, 820–830.

[3] J. M. Campiña, A. Martins and F. Silva, *J. Phys. Chem. C*, 2007, **111**, 5351–5362.

[4] R. R. Sahoo and A. Patnaik, *Appl. Surf. Sci.*, 2005, **245**, 26–38.

[5] M. A. Bryant and R. M. Crooks, *Langmuir*, 1993, **9**, 385–387.

[6] W. A. Hayes and C. Shannon, *Langmuir*, 1996, **12**, 3688–3694.

[7] Y. Chen, A. Nguyen, L. Niu and R. M. Corn, *Langmuir*, 2009, **25**, 5054–5060.

[8] Y. Q. Zhao, H. Q. Luo and N. B. Li, *Sensors Actuators, B Chem.*, 2009, **137**, 722–726.

[9] D. Peelen and L. M. Smith, *Langmuir*, 2005, **21**, 266–271.

[10] L. Liu, S. Song and P. Zhang, *Surf. Interface Anal.*, 2013, **45**, 993–997.

[11] L.-B. Zhao, M. Zhang, B. Ren, Z.-Q. Tian and D.-Y. Wu, *J. Phys. Chem. C*, 2014, **118**, 27113–27122.

[12] X. Song, Y. Ma, C. Wang, P. M. Dietrich, W. E. S. Unger and Y. Luo, *J. Phys. Chem. C*, 2012, **116**, 12649–12654.

[13] T. Strother, R. J. Hamers and L. M. Smith, *Nucleic Acids Res.*, 2000, **28**, 3535–3541.

[14] E. Araya, M. J. Kogan, A. G. Guell, C. A. Escobar and F. Sanz, *J. Chil. Chem. Soc.*, 2014, **59**, 2458–2463.

[15] A. E. Hooper, D. Werho, T. Hopson and O. Palmer, *Surf. Interface Anal.*, 2001, **31**, 809–814.

[16] W. A. Marmisolle, D. A. Capdevila, E. De Llave, F. J. Williams and D. H. Murgida, *Langmuir*, 2013, **29**, 351–359.

[17] J. Bowen, M. Manickam, S. D. Evans, K. Critchley, K. Kendall and J. A. Preece, *Thin Solid Films*, 2008, **516**, 2987–2999.

[18] Y. Tang and M. R. Guire, *J. Mater. Chem.*, 2004, **14**, 1173.

[19] N. Fukuda, N. Ishida, K. Nomura, T. Wang, K. Tamada and H. Ushijima, *Langmuir*, 2011, **27**, 12916–12922.

[20] Z. Z. Liu, Q. Wang, X. Liu and J. Q. Bao, *Thin Solid Films*, 2008, **517**, 635–640.

[21] P. M. Mendes, S. Jacke, K. Critchley, J. Plaza, Y. Chen, K. Nikitin, R. E. Palmer, J. A. Preece, S. D. Evans and D. Fitzmaurice, *Langmuir*, 2004, **20**, 3766–3768.

[22] S. D. Techane, L. J. Gamble and D. G. Castner, *Biointerphases*, 2011, **6**, 98–104.

[23] J. C. Love, J. K. Kriebel, R. G. Nuzzo and G. M. Whitesides, *Chem. Rev.*, 2005, **105**, 1103–69.

[24] P. R. Solanki, S. K. Arya, Y. Nishimura, M. Iwamoto and B. D. Malhotra, *Langmuir*, 2007, **23**, 7398–7403.

[25] J. Park, A. N. Vo, D. Barriet, Y. Shon and T. R. Lee, *Langmuir*, 2005, **21**, 2902–2911.

[26] L. Li, S. Chen and S. Jiang, *Langmuir*, 2003, **19**, 3266–3271.

[27] B. Wang, R. D. Oleschuk and J. H. Horton, *Langmuir*, 2005, **21**, 1290–1298.

[28] N. Graf, E. Yegen, T. Gross, A. Lippitz, W. Weigel, S. Krakert, A. Terfort and W. E. S. Unger, *Surf. Sci.*, 2009, **603**, 2849–2860.

[29] D. J. Garrett, B. S. Fiavel, J. G. Shapter, K. H. R. Baronian and A. J. Downard, *Langmuir*, 2010, **26**, 1848–1854.

[30] E. W. van der Vegte and G. Hadziioannou, *Langmuir*, 1997, **13**, 4357–4368.

[31] T. H. Degefa, P. Schön, D. Bongard and L. Walder, *J. Electroanal. Chem.*, 2004, **574**, 49–62.

[32] E. W. van der Vegte and G. Hadziioannou, *J. Phys. Chem. B*, 1997, **101**, 9563–9569.

[33] H. Zhang, H.-X. He, T. Mu and Z.-F. Liu, *Thin Solid Films*, 1998, **327**–**329**, 778–780.

[34] D. J. Graham and B. D. Ratner, *Langmuir*, 2002, **18**, 5861–5868.

[35] N. Balachander and C. N. Sukenik, *Langmuir*, 1990, **6**, 1621–1627.

[36] H. Sellers, A. Ulman, Y. Shnidman and J. E. Eilers, *J. Am. Chem. Soc.*, 1993, **115**, 9389–9401.

[37] S. Frey, V. Stadler, K. Heister, W. Eck, M. Zharnikov, M. Grunze, B. Zeysing and A. Terfort, *Langmuir*, 2001, **17**, 2408–2415.

[38] Y.-T. Tao, C.-C. Wu, J.-Y. Eu, W.-L. Lin, K.-C. Wu and C. Chen, *Langmuir*, 1997, **13**, 4018–4023.

[39] C. A. Szafranski, W. Tanner, P. E. Laibinis and R. L. Garrell, *Langmuir*, 1998, **14**, 3570–3579.

[40] H. Sellers, A. Ulman, Y. Shnidman and J. E. Eilers, *J. Am. Chem. Soc.*, 1993, **115**, 9389–9401.

[41] A. Ulman, *Chem. Rev.*, 1996, **96**, 1533–1554.

[42] M. Zharnikov, S. Frey, H. Rong, Y. Yang, K. Heister, M. Buck and M. Grunze, *Phys. Chem. Chem. Phys.*, 2000, **2**, 3359–3362.

[43] K. Heister, M. Zharnikov, M. Grunze and L. S. O. Johansson, *J. Phys. Chem. B*, 2001, **105**, 4058–4061.

[44] J. F. Kang, S. Liao, R. Jordan and A. Ulman, *J. Am. Chem. Soc.*, 1998, **120**, 9662–9667.

[45] D. Y. Petrovykh, H. Kimura-Suda, M. J. Tarlov and L. J. Whitman, *Langmuir*, 2004, **20**, 429–440.

[46] P. M. Dietrich, N. Graf, T. Gross, A. Lippitz, S. Krakert, B. Schüpbach, A. Terfort and W. E. S. Unger, *Surf. Interface Anal.*, 2010, **42**, 1184–1187.

[47] Y. W. Yang and L. J. Fan, *Langmuir*, 2002, **18**, 1157–1164.

[48] T. M. Willey, A. L. Vance, T. Van Buuren, C. Bostedt, L. J. Terminello and C. S. Fadley, *Surf. Sci.*, 2005, **576**, 188–196.

[49] S. H. Lee, W. C. Lin, C. H. Kuo, M. Karakachian, Y. C. Lin, B. Y. Yu and J. J. Shyue, *J. Phys. Chem. C*, 2010, **114**, 10512–10519.

[50] K. Kummer, D. V. Vyalikh, G. Gavrila, A. Kade, M. Weigel-Jech, M. Mertig and S. L. Molodtsov, *J. Electron Spectros. Relat. Phenomena*, 2008, **163**, 59–64.

[51] J. E. Baio, T. Weidner, J. Brison, D. J. Graham, L. J. Gamble and D. G. Castner, *J. Electron Spectros. Relat. Phenomena*, 2009, **172**, 2–8.

[52] A. A. Shestopalov, R. L. Clark and E. J. Toone, *J. Am. Chem. Soc.*, 2007, **129**, 13818–13819.

[53] Y. Zubavichus, M. Zharnikov, Y. J. Yang, O. Fuchs, E. Umbach, C. Heske, A. Ulman and M. Grunze, *Langmuir*, 2004, **20**, 11022–11029.

[54] P. Harder, M. Grunze, R. Dahint, G. M. Whitesides and P. E. Laibinis, *J. Phys. Chem. B*, 1998, **102**, 426–436.

[55] P. Harder, P. Harder, K. Bierbaum, K. Bierbaum, C. Woell, C. Woell, M. Grunze, M. Grunze, S. Heid, S. Heid, F. Effenberger and F. Effenberger, *Langmuir*, 1997, **13**, 445–454.

[56] H. L. Cabibil, V. Pham, J. Lozano, H. Celio, R. M. Winter and J. M. White, *Langmuir*, 2000, **16**, 10471–10481.

[57] A. K. Chauhan, D. K. Aswal, S. P. Koiry, S. K. Gupta, J. V. Yakhmi, C. Sürgers, D. Guerin, S. Lenfant and D. Vuillaume, *Appl. Phys. A Mater. Sci. Process.*, 2008, **90**, 581–589.

[58] K. Vasilev, L. Britcher, A. Casanal and H. J. Griesser, *J. Phys. Chem. B*, 2008, **112**, 10915–

10921.

[59] M. Sprik, E. Delamarche, B. Michel, U. Röthlisberger, M. L. Klein, H. Wolf and H. Ringsdorf, *Langmuir*, 1994, **10**, 4116–4130.

[60] H. J. Lee, A. C. Jamison and T. R. Lee, *Langmuir*, 2015, **31**, 2136–2146.

[61] A. Shaporenko, A. Terfort, M. Grunze and M. Zharnikov, *J. Electron Spectros. Relat. Phenomena*, 2006, **151**, 45–51.

[62] C. D. Bain, J. Evall and G. M. Whitesides, *J. Am. Chem. Soc.*, 1989, **111**, 7155–7164.

[63] A. Ulman, *An introduction to ULTRATHIN ORGANIC FILMS From Langmuir-Blodgett to Self-Assembly, Part-2: Langmuir-Blodgett Films*, Academic Press (San Diego), 1991, pp. 101–132.

Chapter 4

Characterisation and Deposition of Gold Nanoparticles on Aliphatic and Aromatic Amine Terminated SAMs as Function of pH on a MicroElectroMechanical System Micropaddle

Abstract

Aliphatic and aromatic amine-terminated SAMs deposited on Au surface are used as protonatable functional groups for the self-assembly, through electrostatic interactions, of citrate passivated gold nanoparticles (G-NPs) as a function of pH. The challenge here is to determine the optimum conditions required for G-NPs deposition on 11-amino-1-undecanthiolate (Alk-amine) and 4-amino benzenethiolate (Ar-amine) SAM, for the purpose of developing microelectromechanical systems (MEMS) that can detect the attachment of nanoscale particulates such as G-NPs, anti-bodies, and other biological analytes. Thus, herein, the self-assembly of GNPs at pHs ranging from 3–7 at ambient conditions to both amine SAMs is investigated *via* Atomic Force Microscopy (AFM) and a Quartz Crystal Microbalance (QCM). After determining the optimum condition, these conditions were replicated on an Alk-amine functionalized micro paddle (MEMS device) and with the aid of a laser vibrometer the attachment of G-NPs on the surface was monitored. Prior to these MEMS experiments the G-NPs were characterised by UV-Vis Spectrophotometer and Transmission Electron Microscopy (TEM). Moreover, the stability of the G-NPs over the pH range as a function time (6 h) were studied using the Dynamic Light Scattering (DLS), Zeta Potential (ZP) and UV-Vis spectrometry, in order to evaluate the conditions (pH and time) over which the particles could be used in the later sensing experiments.

4.1. Introduction

The self-assembly of citrate passivated gold nanoparticles (G-NPs) on a functionalized surface is of interest due to the potential applications of this model system. For example, in the field of dyes,[1] detection of DNA strands (single or double),[2–5] drug delivery,[6,7] improvement of surfaces for enhancing of Raman scattering[8–11] and MEMS devices.[12]

Several studies[12–16] have been performed to investigate the optimum conditions required for the surface self-assembly of G-NPs onto aliphatic or aromatic amine-terminated SAMs. The self-assembly of G-NPs depends upon the adhesion force between the carboxylate groups on the G-NPs and the degree of protonation of the amine functionalized surface. This adhesion force is found to be dependent upon the pK_a of the two functional groups; COOH and NH_2. There are two methods to determine the pK_a of ionizable groups (-COOH/-COO^- and -NH_2/-NH_3^+), which are contact angle (CA) titration[17–19] and chemical force titration (Adhesion Force titration) by AFM.[20–25] For example, CA titration is known to be used to characterize the wetting properties of the surfaces with milliliter droplets of buffered water. A major drawback of this method is the difficulty of measuring the pK_a for very hydrophilic surfaces, as no droplet will be formed, as buffered water will spread on the surface leading to very low contact angles.[20,26] With AFM the wetting properties are determined on the nanoscale and it is as effective on both hydrophobic and hydrophilic surfaces, because the technique depends upon the adhesion force between the tip and a substrate that are functionalized with the same or opposing functional different groups.[21,25]

From the literature[20–25,27] there is an argument about the calculated pK_a of these two functional groups by AFM (adhesion force titration), because it depends upon the conditions of the experiment such as the ionic strength of the buffered solution and on the chain length of the organosulfur or organosilane, which is deposited on the Au or SiO_2 surface, respectively. For example, AFM (adhesion force) was used by Van der Vegte and Hadziioannou[21,22] to calculate the pK_a to be ~5 for a COOH-terminated SAM which was deposited on the two surfaces (AFM tip and Au substrate), while the pK_a for the NH_2-termintated SAM, which was deposited on the two surfaces, was ~7.5.[19–22]

The pK_a of a functional moiety such as -COOH and -NH_2 bound in the monolayer will be different to what it is in the solution due to the constraints of the surface, which will mean neighbouring groups will have an effect on protonation/deprotonation events. For example, as a surface becomes increasing protonated, the next protonation event becomes more difficult due to electrostatic repulsion of the cationic surface with the approaching proton, whilst in solution the already formed cations are free to move apart from each other, and 'free' protons.

Furthermore, at pHs below 4 the -COOH functionalized tip and the Au surface are known to be fully protonated and the adhesion force is at a maximum due to H-bonding between the COOH groups on the two surfaces.[22] In comparison, there is a lower adhesion force between the -NH_2 functionalised tip and surface at acidic pHs, due to the electrostatic repulsive forces between the protonated amine groups (NH_3^+).[20] At pHs above 7 the COOH groups are expected to be fully

deprotonated as carboxylate groups (-ve) and the adhesion force is weaker (due to the presence of electrostatic repulsive forces between the two surfaces).[22] Conversely, in the case of NH_2 functionalized surfaces, the surfaces will be neutral, and the dominating attractive interaction, will be hydrogen bonding between the NH_2 functionalised surfaces.[20]

Moreover, when the surface and the tip were coated with different functional groups, either -COOH and -NH_2, the adhesive behavior as a function of pH is different. Wang *et al*.[25] reported the adhesion force determined by AFM between a -COOH and NH_2 surfaces. The tip was coated with a COOH functionalized monolayer and the substrate was coated with a NH_2 functionalized monolayer in a 1 mM ionic strength solution whose pH was adjusted to between 2–12 by adding NaOH and HCl. The results revealed that the maximum adhesion force between the two surfaces was at pH 5.7, which is in good agreement with a previous study that was reported by Marti *et al.*,[28] where the pH was determined to be 5.5 for the maximum adhesion. The two studies imply that this pH represents the optimum value to achieve a good interaction between these two groups. The prominent intermolecular interaction is electrostatic. At pH ~5.5, COOH groups are largely deprotonated (COO^-) whilst the -NH_2 is protonated (NH_3^+). Thus, the interaction between the two surfaces will be dominated by the electrostatic interaction.

Accordingly, the pK_a obtained by the above study can be used to follow the attachment between Alk-amine and Ar-amine SAMs that are deposited on a Au substrate and citrate passivated gold nanoparticles.

4.2. Aim of the study in this chapter

In this chapter, the conditions for optimum deposition of G-NPs on Alk-amine or Ar-amine functionalized Au SAM will be determined and then used to coat a MEMS micro-paddle, which will be used to detect the deposition of G-NPs at optimum (Figure 4.1), hopefully at much lower limits of detection than currently possible. Atomic force microscopy (AFM) and a quartz crystal microbalance (QCM) will be used to evaluate the optimum conditions required for G-NPs deposition on the Alk and Ar-amine terminated SAMs, prior to the micro-paddle being used. Additionally, to ensure that individual citrate passivated G-NPs are deposited on the surface and not agglomerated of G-NPs, the colloidal stability of the particles will be investigated over the pH range 3–7 using DLS, Zeta potential and UV-Vis measurements, as a function of time.

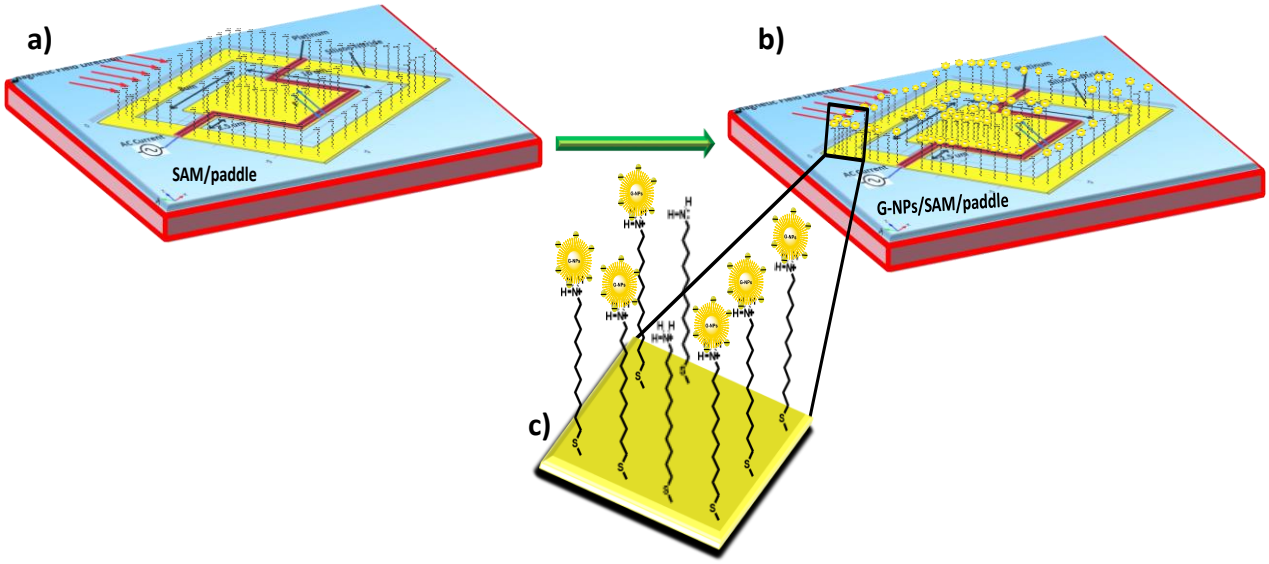

Figure 4.1: Cartoon representation of a) Alk-amine SAM deposited on the Au surface of a micro paddle, b) G-NPs deposited on an Alk-amine SAM/Au-micro paddle, and c) magnification of the deposited G-NPs on an Alk-amine SAM/Au-paddle

4.3. Results and Discussion

4.3.1. Synthesis of G-NPs colloidal solution

4.3.1.1. Synthesis of G-NPs

G-NPs were synthesized using the Frens[29] procedure (diluted method) with slight modifications. Applying this procedure to the synthesis G-NPs passivated with citrate is expected to produce G-NPs with an average diameter of ~15 nm in size and as follows. The overall scheme of synthesis is shown in Figure 4.2, and relies upon the aqueous reduction of a Au^{III} salt by sodium citrate to form gold nanoparticles, followed by purification by centrifugation.

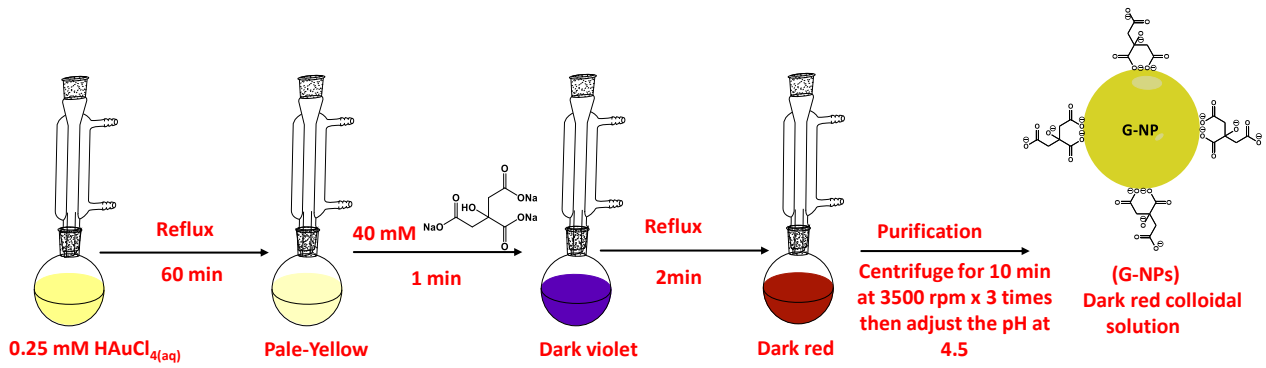

Figure 4.2: Schematic procedure of 14.5 ± 0.95 nm G-NPs synthesis and purification

4.3.2. Characterisation of G-NPs colloidal solution

4.3.2.1. UV-Vis Spectrophotometer measurements

The UV-Vis spectrum (Figure 4.3) for the G-NP colloidal solution reveals a surface plasmon resonance band (SPR) with a λ_{max} at 520 nm, which is indicative of ˜15nm diameter G-Nps.[30–33]

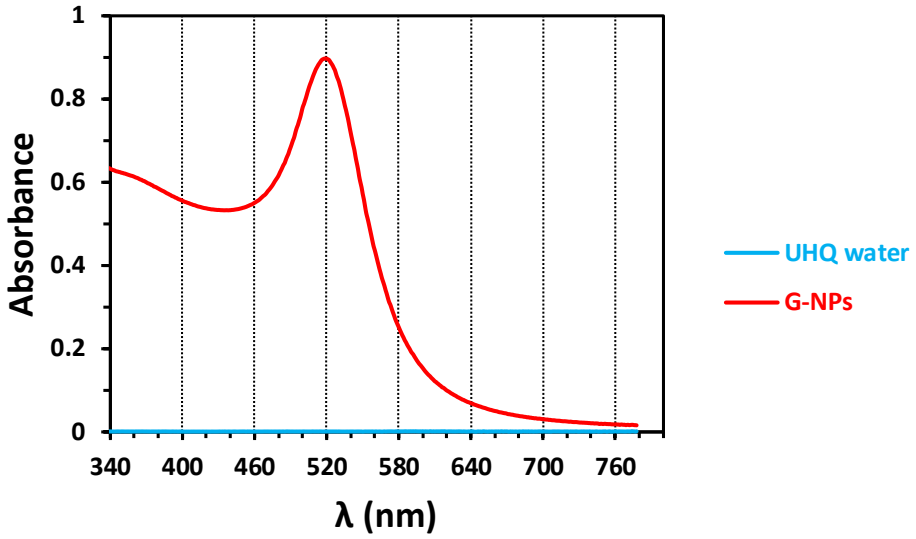

Figure 4.3: UV-Vis spectra of G-NPs colloidal solution at R.T.

4.3.2.2. Transmission Electron Microscopy (TEM)

TEM was used to directly determine the mean diameter of the G-NPs, using ImageJ (version 1.51r) to process the TEM images (Figure 4.4) to plot a histogram using OriginPro 2017. The histogram shows that the mean size distribution of G-NPs passivated with citrate is 14.50 ± 0.95 nm,[29,30,34] in good agreement with the surface plasmon.

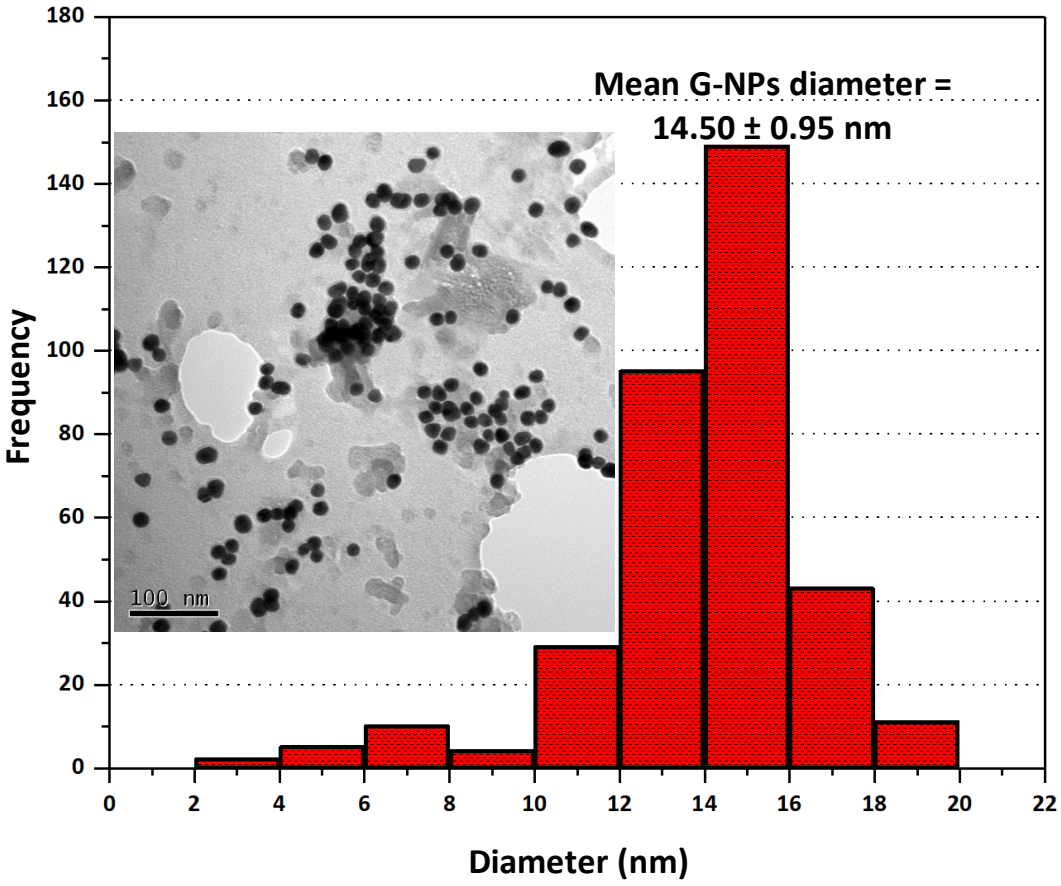

Figure 4.4: A TEM image of the G-NPs passivated with citrate and the histogram showing the size distribution of G-NPs passivated with citrate at pH 4.5

4.3.2.3. Investigation of Room Temperature G-NP Stability as a Function of pH and time: A Dynamic Light Scattering (DLS), Zeta Potentiometry (ZP) and UV-Vis Study on the Colloidal G-NPs Solution

The particle size and the charge of the G-NPs was observed, at room temperature, by dynamic light scattering (DLS) and zeta potentiometry, (ZP) respectively, over a pH range of 3–7 over 6 hours. By way of example Figure 4.5 displays the graphical raw data for the DLS and ZP data at pH 4.5 at t = 0 h, revealing an average diameter of 16 ± 2 nm with a surface charge of −43

± 2 mV.[34] Thus, one can infer that in a colloidal solution at pH 4.5 the particles are supporting a sufficient surface charge to prevent aggregation due to electrostatic repulsion between the particles.[31,32,35]

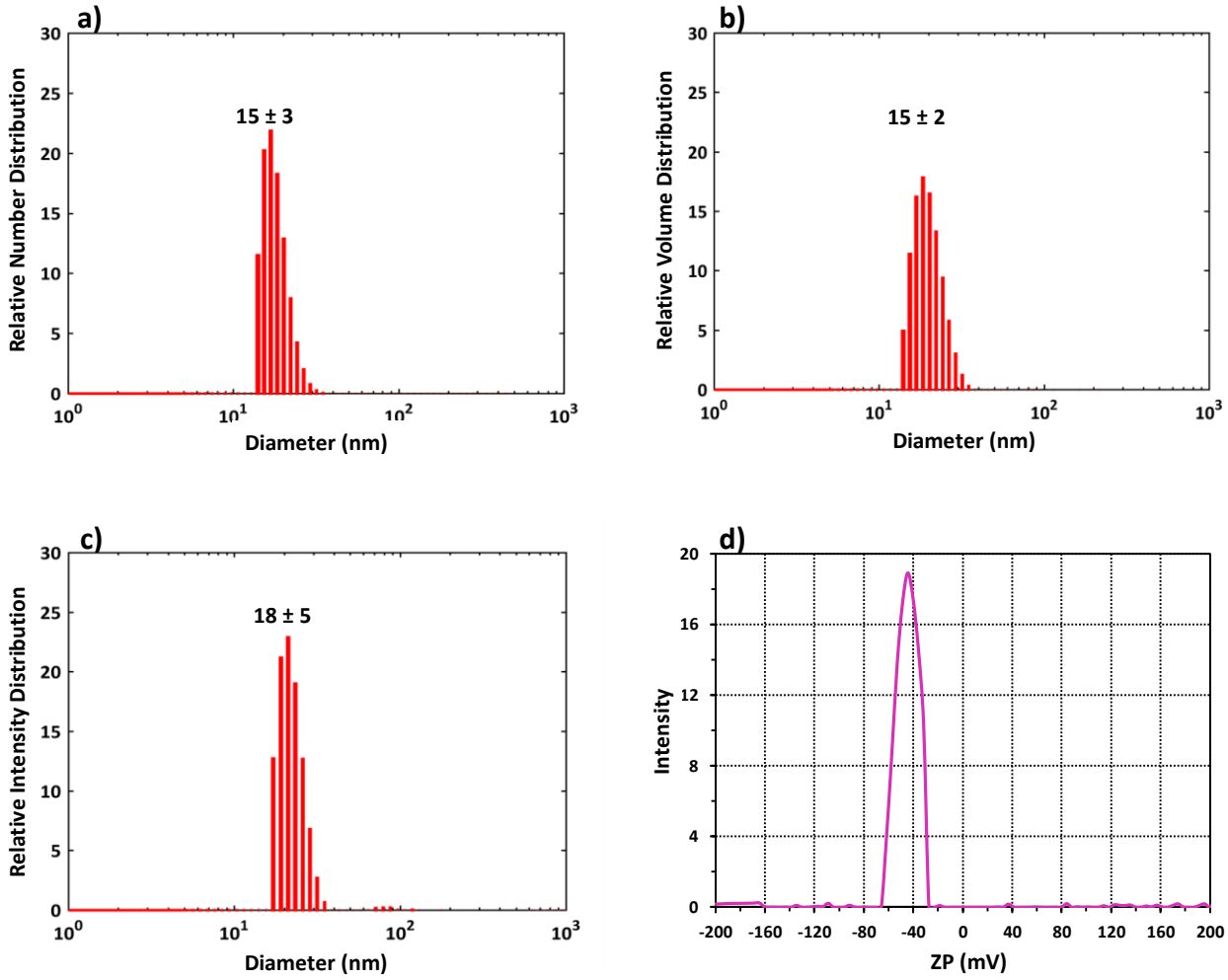

Figure 4.5: DLS of relative a) number, b) volume, c) intensity distribution, and d) Zeta Potential of synthesised G-NPs at pH 4.5 and room temperature

The G-NPs are stabilized by the citrate anions, resulting from the conjugate bases of the carboxylic acids. Thus, the carboxylate groups (conjugate bases of the carboxylic acids) on the G-NPs,[31,36] are providing the electrostatic repulsion between the G-NPs[37] (Figure 4.6). Therefore, the degree

of surface anionic charge on the G-NPs will controlled by (i) the pH of colloidal the G-NPs solution, and (ii) the pK_a of the carboxylic/carboxylate groups.[12,14,15,34,38] Thus, at low pH (below the pK_a of the carboxylic acids groups) of the colloidal solution, the surface charge on the G-NPs (Figure 4.6a, top structure) will be depleted leading to aggregation in solution. Whereas at high pH (above the pK_a of the carboxylic acids groups) (Figure 4.6c, top structure), there will be sufficient deprotonation of the carboxylic acid moieties to enable a surface anionic charge to electrostatically stabilise the G-NPs.

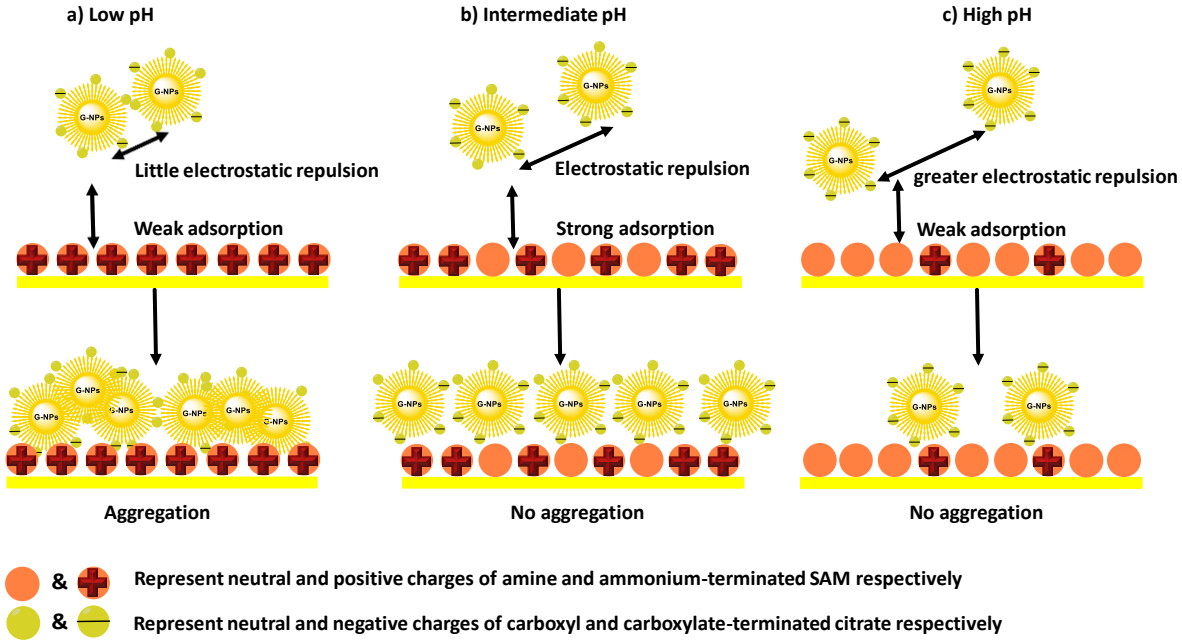

Figure 4.6: Schematic showing the charges present on citrate-passivated G-NPs deposition on the amine and ammonium-terminated SAM surfaces at five different pHs (low, intermediate and high pH) at room temperature

Thus, zeta potential (ZP), dynamic light scattering (DLS) and UV-Vis were used to study the impact of pH and time on the G-NPs colloidal solution stability over six hours. Figure 4.7a-c show the time dependent response (over six hours) of the zeta potential, diameter and polydispersity of the G-NP colloidal solutions as the pH was varied from 3–7.

pH < 4.5: At pHs 3 and 4 the negative colloidal G-NPs zeta potential is reduced sigificantly[14,36,39] (Figure 4.7a) to below or just at ~−30 mV, relative to pH 4.5 where the zeta potential was ~−43 mV. Concomitantly, it can be seen that at pHs below 4.5 the average particle size (Figure 4.7b) increases as pH is lowered and time increases, and has not plateaued at both pHs even at six hours, reaching up to ~50 nm. This behavior suggests time-dependent particle aggregation.[14,15,40] This behavior is congruent with the model proposed in Figure 4.6 as protonation of the carboxylate groups manifests itself in a reduction of the surface anionic charge, followed by the citric acid molecules detaching from the surface at pH 2,[13,41,42] leading to the G-NPs no longer being electrostatically stabilized, and as such then will begin to aggregate, displaying a growth in particle size as a function of time. Figure 4.7a shows that the zeta potential is reduced at pH 3[14,39] and pH 4 between time 0–4 h, after which there is a ZP increase, which is somewhat surprising, but the literature suggests this is due to the free citrates anions[42] and/or the chloride ions from adding HCl solution.[43] Also, it can be seen that the aggregation at pH 4 is lower than at pH 3 due the lower amount of HCl added.[36,38,44] The UV-Vis data supports this model of aggregation, (see below).

pH 4.5 and greater: pH 4.5 appears to give the most stable colloidal solution, despite the all the higher pHs maintaining a significantly negative zeta potential of approximately −43 mV or greater.[14,39] Thus, at pHs 5–7, in contrast to pH 4.5, the particulate size appears to increase as function of increasing time, up to 30 nm, but is still significantly less than at pHs 3 and 4. In addition, these particulates stabilise over six hours as shown by the plateauing of size as a function of time, unlike at pHs of 3 and 4 where the particulate size increases significantly over the 6 h.

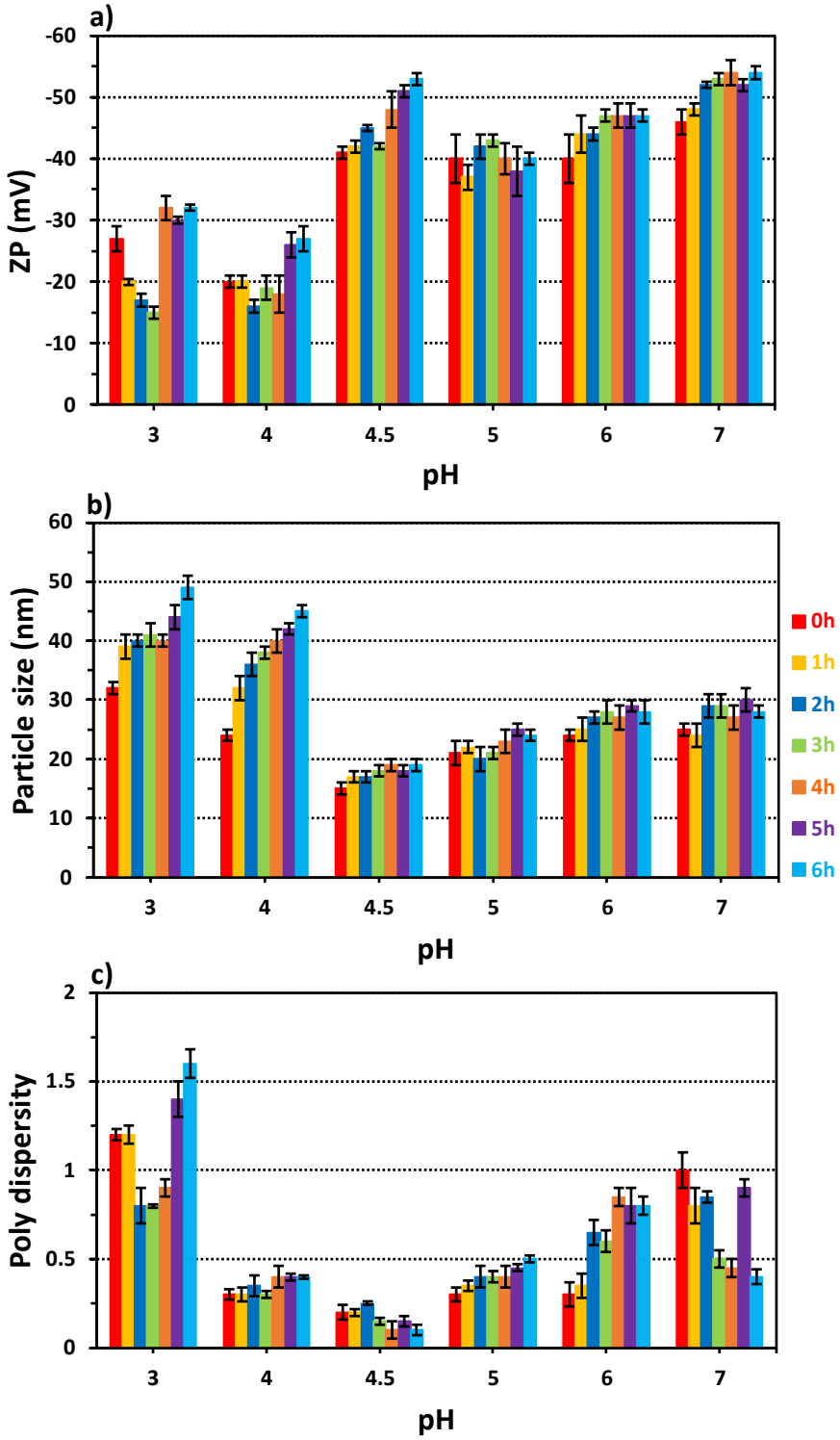

Figure 4.7: a) Zeta Potential, b) Dynamic Light Scattering and c) poly dispersity for G-NPs solution at different pHs and time

The time dependent UV-Vis spectral analysis is congruent with the zeta potential and particle size analysis (Figure 4.8). One can observe at pH 3 (and 4, though less so) a drop off in the absorption of the surface plasmon band at 520 nm, and a maintenance of it at pH 4.5 and above (Figure 4.8a).

The reduction in the maximum adsorption at pH 3 sees a concomitant rise of a new broad absorption band at λ_{max} = ~680 nm (Figure 4.8d,e), which is related to the aggregation and fusing of the of G-NPs cores.[45–47]

Interestingly, it should be noted that although at pHs 5–7 a relatively small increase in particle size was noted by DLS, there is no reduction of the surface plasmon band (520 nm), or any absorption band forming at 680 nm. Thus, one might conclude that these particles are stable at higher pHs, and the 'apparent' small increase in particle size by DLS is not due to aggregation, but some other physical parameter.[39,47,48]

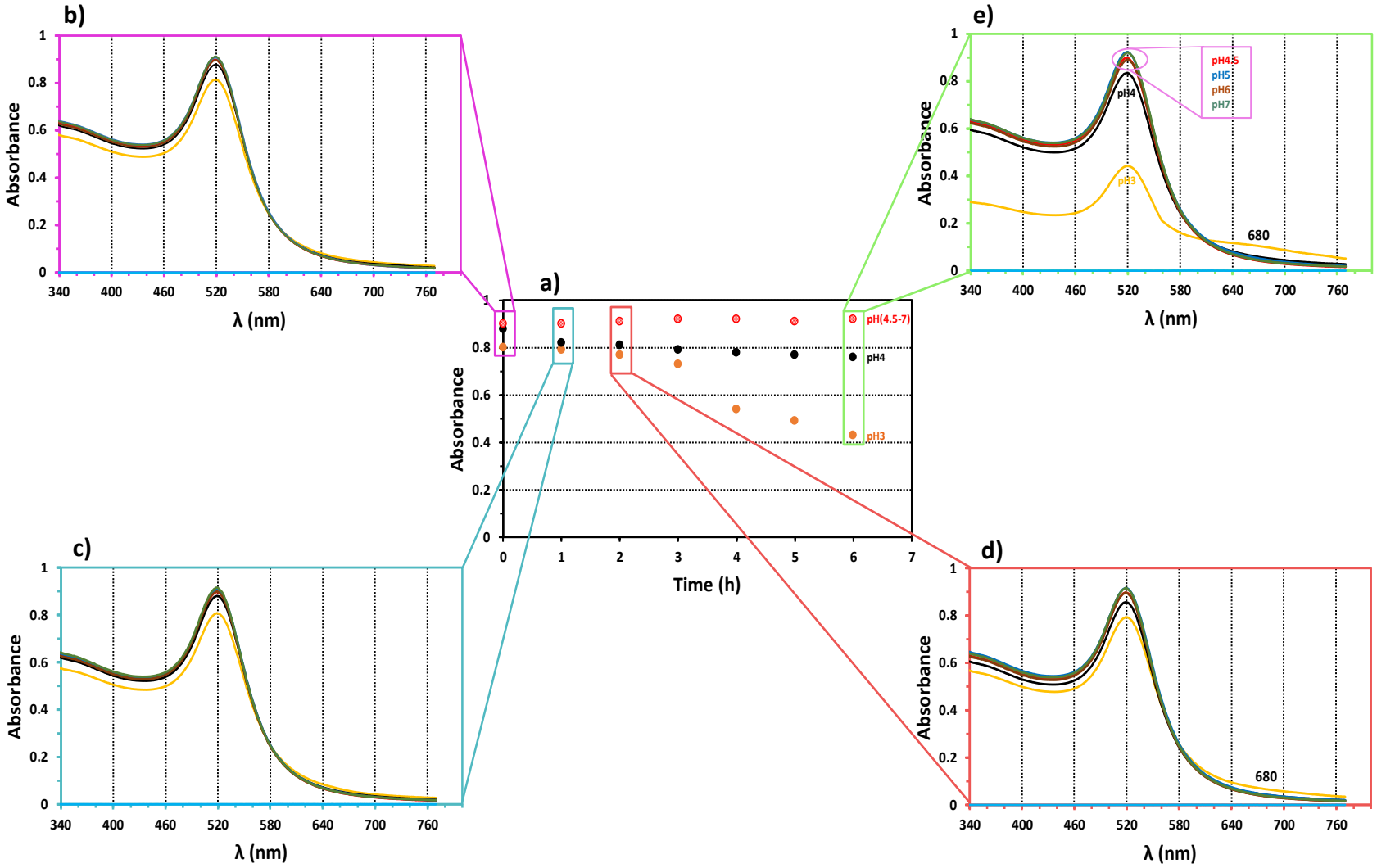

Figure 4.8: a) Absorption maximum change of surface plasmon band (~520 nm) of the G-NPs as a function of pH and time, and b) UV-Vis at pHs 3, 4, 4.5, 5, 6 & 7, at t = 0 h, c) t = 1 h, d) t = 2 h and, e) t = 6 h

In the G-NP/surface self-assembling experiments reported later the total immersion time for G-NPs to self-assemble on the Alk and Ar-amine SAM was 2 (Figure 4.8d). Thus, the results obtained from ZP and DLS at 2 h are plotted in Figure 4.9Error! Reference source not found.. Clearly, any departure from pH ~4.5 leads to some form of particle aggregation (DLS), which is most marked at lower pHs where the ZP also reduces markedly. This behavior is in good agreement with the UV-Vis data, where only at pHs 3 and 4 do you see a decrease in the surface plasmon at 2 hours, and indeed the tell-tale emergence of the surface plasmon at 680 nm at 6 h (Figure 4.8e) for the particles at pH 3 suggesting G-NPs fusing.

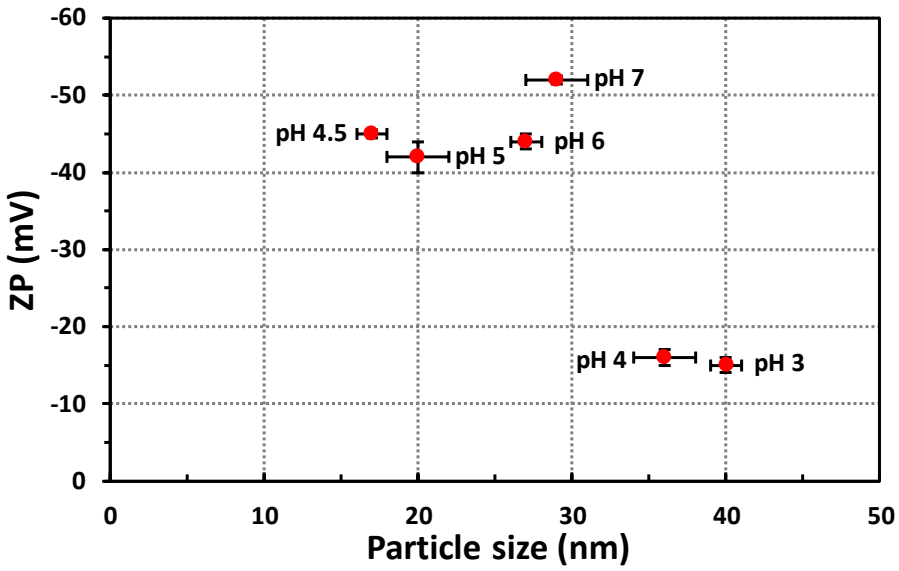

Figure 4.9: The Zeta Potential and Particle Size measurements for G-NPs solution after 2 h of changing the pH at different values

4.3.3. Characterization of the deposition of G-NPs on Alk and Ar-amine SAM at different pHs: Atomic Force Microscopy and QCM Analysis

Figure 4.6 highlights not only how the electrostatic interactions between the G-NPs will be modulated by the pH of the colloidal solution, but also how their adsorption onto an $-NH_2$/$-NH_3^+$ terminated surface will be modulated. At lower pHs the surface will be cationically charged, as result of protonation of the amine (Figure 4.6 a, lower structure) and, at higher pHs the surface will be neutral (Figure 4.6c, lower structure). Clearly, the adsorption between the G-NPs and the surface will be dependent on (i) the pK_a of the surface, (ii) the pK_a of the absorbing species, and the pH of the subphase. As such the absorption will be maximized at some intermediate pH where their electrostatic attraction between the anionic charge on the G-NPs is matched by the cationic charge of the surface.

In order to investigate this phenomenon atomic force microscopy (AFM) and a quartz crystal microbalance were used to investigate the adsorption behavior of the G-NPs to the Alk-amine and the Ar-amine SAM, as a function of the pH of the G-NPs colloid solution. Clearly the two amines have different pK_as (Alk-amine = ~7.5,[21,22,25,49–52] Ar-amine = ~5.9[19,53,54]), and as such will have different G-NPs adsorption profiles.

4.3.3.1. Atomic Force Microscopy (AFM) Analysis

In this section the Alk-amine and Ar-amine SAMs surfaces, as well as a bare Au surface, before and after immersion in the G-NPs dispersion for 2 h, at pHs between 3 and 7, were

studied.[12,14,15] The surfaces were imaged by AFM to investigate the final coverage. For all surfaces, 3–4 samples were analysed. A 2 h immersion time was chosen based on the fact that for all pHs the divergence in the change of the surface plasmon absorbance from t=0 to t=2h was minimal (Figure 4.8a,d), though clearly at pHs 3 and 4 the ZP has dropped considerably at 2 h (Figure 4.9) relative to the higher pHs studied. Therefore, certainly beyond 2 h aggregation was occurring, and upto 2 h further examination was needed, in order to determine a time frame in which to sense the G-NPs as function of time with the QCM and then via the MEMS sensor.

Initially bare gold substrates were immersed in the G-NP solution at pHs 3, 4 and 5 (Figure 4.10) for 2 h. Clearly, there is no noticeable deposition of G-NPs at pH 4 and pH 5, whilst at pH 3 there is considerable deposition. As observed in Section 4.3.2.3, at pH 3 the G-NPs are aggregating considerably within the dispersion over 2 hours, and therefore this deposition at pH 3 is related to the aggregation of G-NPs, whilst at pHs 4 and 5 this is not the case, and very little non-specific deposition is observed.[55] As noted earlier in Figure 4.6a the lowering of the pH protonates the carboxylate moieties, and as a result the negative charge is reduced leading to the G-NP aggregation.[41,56,57] Therefore, deposition of G-NPs at pH 3 is due to the agglomerates of G-NPs settling at the bottom of the vial and on top of the Au substrate. The aggregation of the G-NPs in the colloidal solution also happens at pH 4, but the impact is much reduced over 2 h, than it is at pH 3 (Figure 4.8).

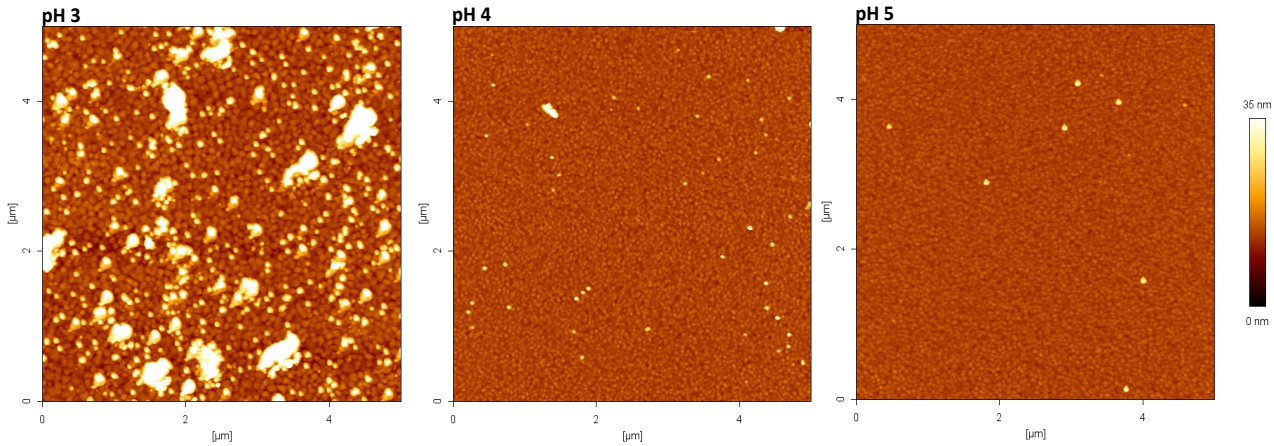

Figure 4.10: Deposition of G-NPs on bare Au at pH 3, pH 4 and pH 5, and 2 h immersion (control experiments)

4.3.3.1.1 Deposition of G-NPs on Alk-amine and Ar-amine SAM at pHs 3–7 (2 h Immersion)

The AFM images in Figure 4.11 show the self-assembled G-NPs on the Alk-amine SAM after 2 h immersion at pHs 3 through to 7.

The number of particles per unit area is tabulated in Table 4.1 as function of pH.

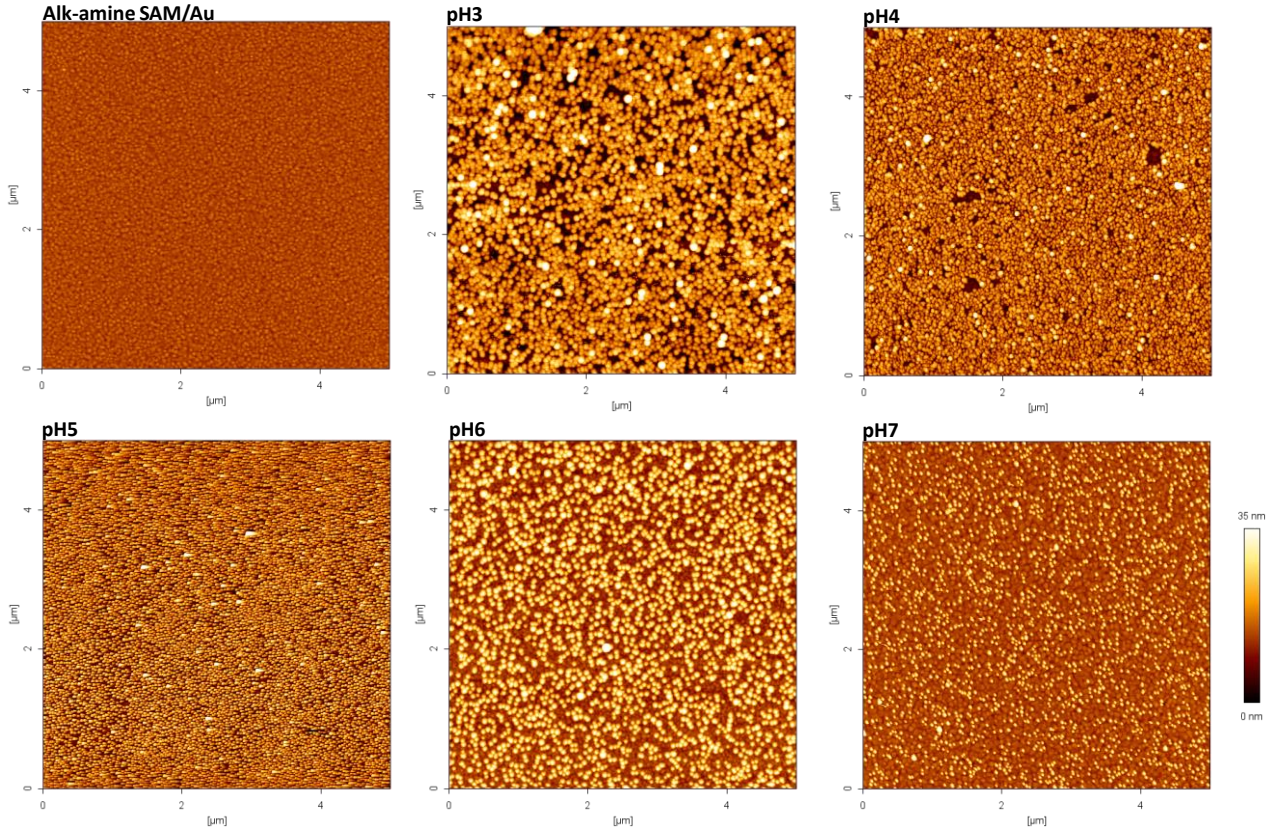

Figure 4.11: 5 × 5 µm AFM images for G-NPs deposited onto Alk-amine SAM at different pHs (2 h)

Table 4.1: The number of G-NPs deposited on Alk-amine and Ar-amine SAM at pH 3–7 obtained by AFM (Figure 4.11 and Figure 4.13)

	No. of G-NPs/25 µm^2	
pH	Alk-amine SAM	Ar-amine SAM
3	2820 ± 220[a]	3685 ± 127[a]
4	3631 ± 350 [a]	1960 ± 129[a]
5	5800 ± 250	2650 ± 140
6	2300 ± 63	610 ± 105
7	2103 ± 55	100 ± 12

[a] Multilayer structure, see Figure 4.11 and Figure 4.13

Clearly, Figure 4.11 shows a qualitative higher density of particles at pH 3–4 than pH 5, yet the quantitative analysis in Table 4.1 implies the density at pHs 3 and 4 is lower than pH 5. To

rationalize this anomalous result, one needs to examine the images in at high resolution, as shown in Figure 4.12. At this higher magnification one can see that at pHs 3 and 4 the particle density is indeed high, not because of a full monolayer formation, but because of multilayer formation, and particles are overlayed on each other. Thus, the image capture software was only capturing the top layer of nanoparticles, resulting in an apparent low particle density for pHs 3 and 4 in Table 4.1.[58]

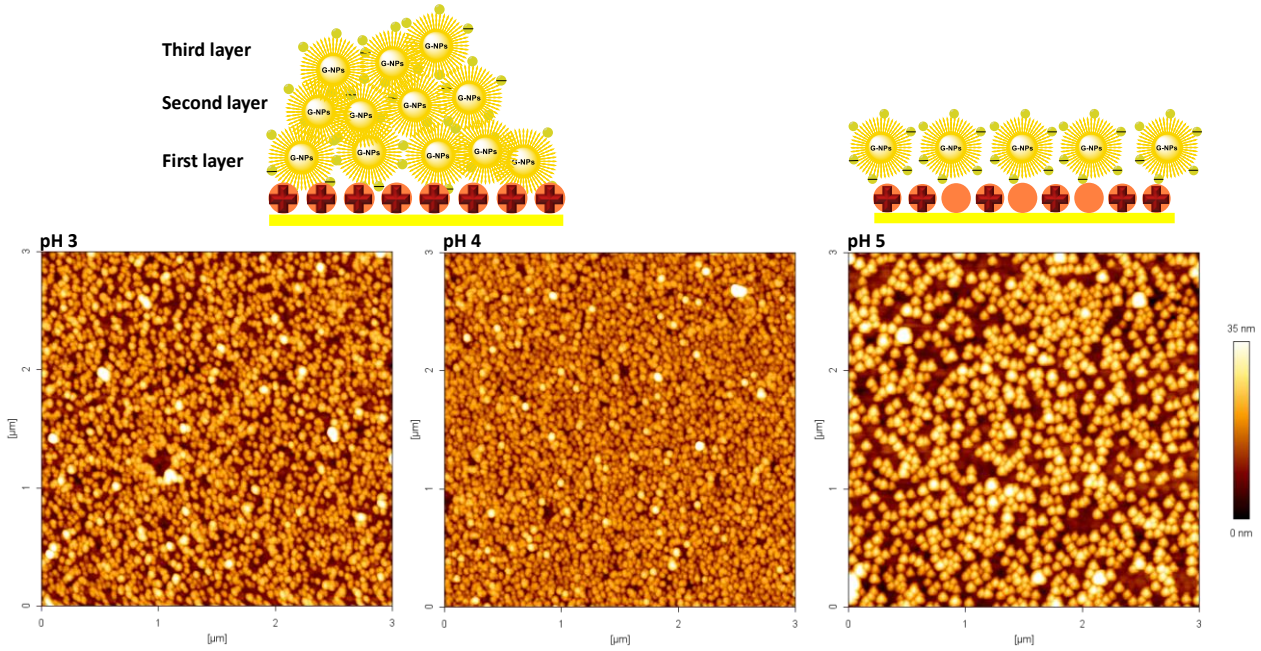

Figure 4.12: Expanded AFM images from Figure 4.11 at pH 3, 4, and 5 on Alk-amine SAM. At pHs 3 and 4 one can observe G-NPs on top of each other, presumably because of particle aggregation in the dispersion prior to deposition/self-assembly on the surface, whereas at pH 5 the particles are not aggregated

The same conditions were used to self-assemble G-NPs on Ar-amine SAM (Figure 4.13), and the particle density for each pH is also tabulated in Table 4.1.

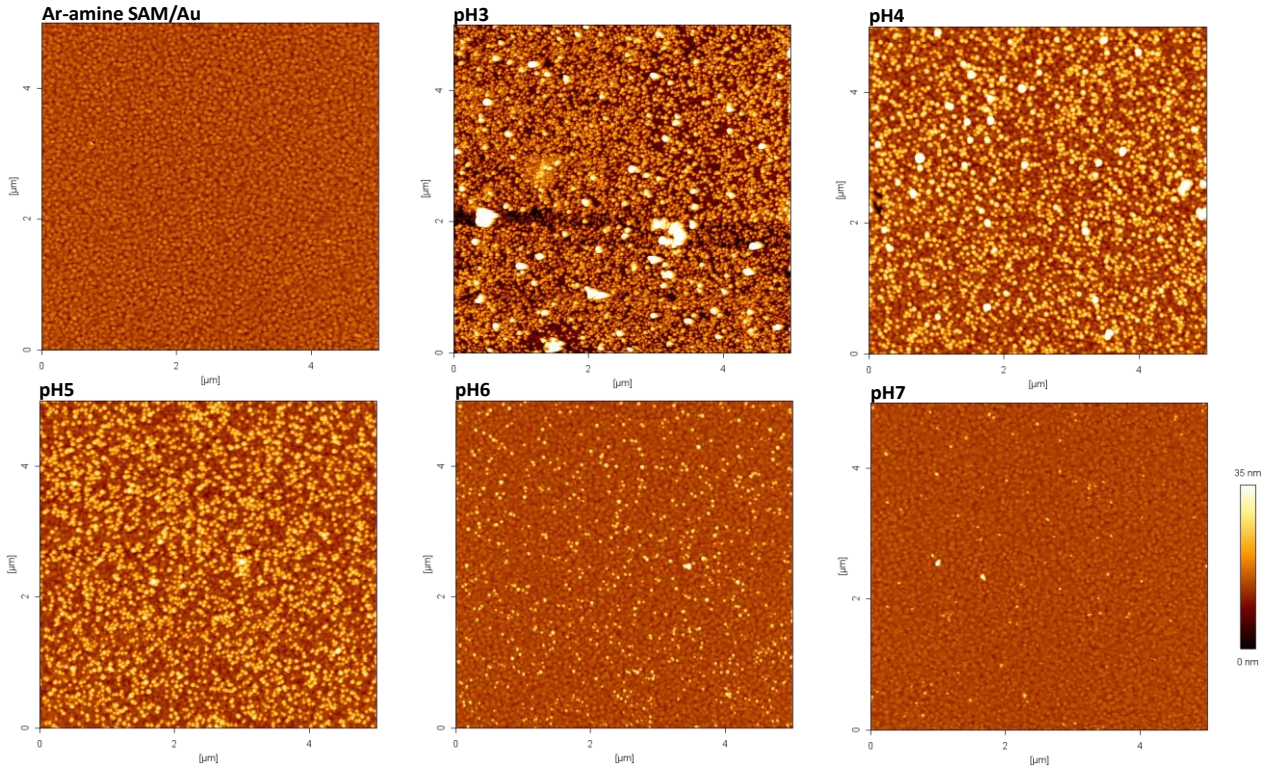

Figure 4.13: 5 × 5µm AFM images for G-NPs deposited onto Ar-amine SAM at different pHs (2 h)

Once again it can clearly be seen that at pHs 3 and 4 there are larger aggregates depositing on the surface, whilst at pHs 5 and above discrete particles can be observed. Thus, it could not be rely on the data at pHs 3 and 4, in terms of using it to determine the number of particles being deposited on the SAM at 2 h.

The data displayed in Figure 4.14, shows the number of particles per unit area as a function of pH. Bearing in mind that at pHs 3 and 4 at extended immersion times the mechanism of deposition is not the same as at higher pHs (aggregation followed by deposition), then one can see that at pH 5 and above where only (sub)monolayer G-NPs are depositing:

1. the number of particles self-assembled decreases for both amino terminated SAMs as pH increases, and

2. The number of particles per unit area is greater for the Alk-amine SAM at corresponding pHs.

From the pK_as of Alk-amine = ~7.5,[21,22,25,49–52] Ar-amine = ~5.9[19,53,54] one can deduce the cause of the decreasing amount of attachment of G-NPs on the amine SAMs with increasing pH (pH 5-7). The degree of SAM deprotonation will increase with increasing pH, subsequently leading to less favourable attachment conditions. In fact by applying Henderson-Hasselbalch equation,[59,60] one can calculate that 99% of the amine SAMs will be deprotonated at pH = ~9.5 and ~7.9 respectively. Although, this explains the decrease in G-NPs attachment between pH 5 to 6. However, as the G-NPs attachment remains similar between pH 6 and 7, this suggests there must be another interaction involved in the self-assembly of the G-NPs to the surface.

In relation to the Ar-amine SAM the situation is similar in that the number of particles decreases with increasing pH, but there is a reduction over rang pH 5 to pH 7, where it almost falls to zero. This behavior tells us that in contrast to the Alk-amine SAM there is no significant other interaction holding the G-NPs to the surface. Clearly this difference in behavior must be a result of the pK_a difference of the Alk-amine SAM relative to the Ar-amine SAM. Indeed, one would expect the Alk-amine SAM to be more protonated than the Ar-amine SAM, and therefore have greater number of particles self-assemble per unit area. However, it is not clear why the Alk-amine SAM would have G-NPs adhered to it after full deprotonation, relative to the Ar-amine SAM. Factors that will play into this differential behavior could potentially be differences in hydrogen bonding capacity of the Alk-amine relative to the Ar-amine, and the more hydrophobic nature of the Ar-amine SAM, relative to the Alk-amine SAM (Table 3.1, Chapter 3).

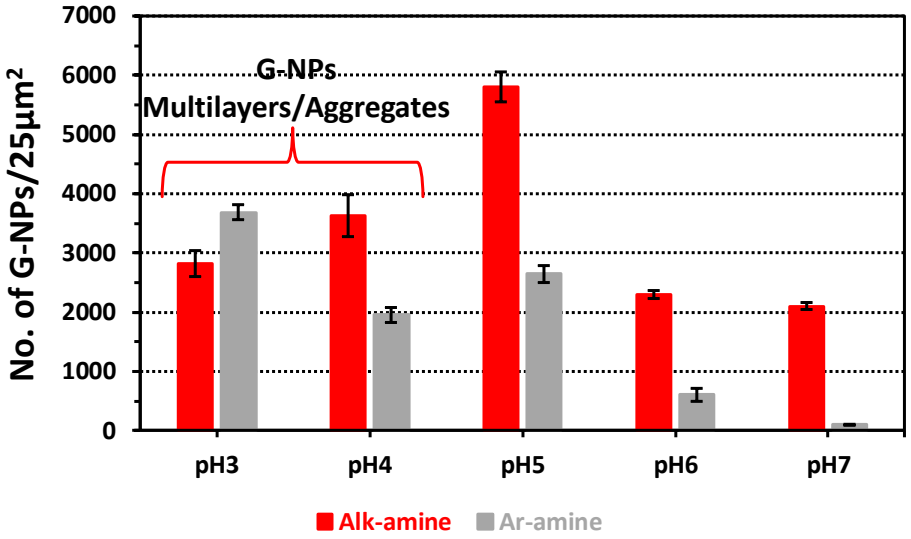

Figure 4.14: A histogram showing the difference between the number of G-NPs deposited on Alk and Ar-amine at different pHs (using AFM), 2 h)

Further analysis into the forces present between the charges of the G-NP and the SAM and using a combination of Coulomb's law (equation 4.1) and Henderson-Hasslebach equation,[61,62] it is possible to predict the attraction between the two surfaces. Assuming a pK_a value of the Alk-amine of ~7.5,[21,22,25,49–52]and a pK_a value of the citrate as 3.13, 4.76 and 6.40. An estimation of the magnitude of the attractive or repulsive interaction between them in solution at various pH is shown in Table 4.2.[58,62,63]

$$F = K_e\, q_1 q_2 / r^2 \qquad \textit{(Equation 4.1)}$$

Where k_e represents the Coulomb's constant (~9.0×10^9 N.m^2/C^2), q_1 and q_2 represent the signed magnitude of the charges, and r (5 nm, estimated) represents the distance between the charges, and F represents the force of the interaction between the charges. F is negative (attractive) when the q_1 and q_2 have opposite signs and it will be positive (repulsive) when q_1 and q_2 signs are the same.

Table 4.2: Electrostatic force between citrate passivated G-NPs and Alk-amine SAM deposited on Au surface (5 nm as separated distance) in solution at various pH ranging from 3-7 and at room temperature. Assuming pK_a values of citrate (3.13, 4.76 and 6.40), and pK_a = ~7.5 for Alk-amine SAM

	Alk-amine SAM/Au[a]	Citrate passivated G-NPs[b]	
pH	q_1 (C) × 10^{-2}	q_2 (C) × 10^{-2}	F (N) × 10^{-12}
3	99.997	44.320	4.095
4	99.968	103.316	9.542
5	99.685	165.972	15.286
6	96.935	222.899	19.963
7	75.975	279.338	19.608

[a] It is assumed that the concentration of Alk-amine SAM is 0.1 mM of thiol solution which was used to prepare this SAM.

[b] It is assumed that the concentration of citrate passivated G-NPs is 0.78 mM which was used to prepare G-NP colloidal solution.

The largest charge value is seen at pH 6. At this point most of the citrate is triply deprotonated. As pH increases above this point it approaches the pK_a value of the ammonium Alk-amine, thus the ammonium moieties are deprotonated and hence the number of amine moieties (no charge) present on the surface increases. Therefore, the overall charge of the system decreases, and thus the force decreases.

4.3.3.1.2 Recyclability of the Alk-amine and the Ar-Amine SAMs

As the deposition of the G-NPs on Alk-amine and Ar-amine SAMs relies upon protonation states to induce electrostatic interactions, in principle it should be possible to have a recyclable process, whereby the G-NPs adhered to the surface can be removed by raising the pH, and then re-adhered by lowering the pH.

To investigate whether the surface could be reused, a set of G-NPs deposited on the Alk-amine functionalized surfaces (deposited at the optimum pH 5) were immersed in aqueous NaOH (200 mM) solution for 2 h. After immersion the SAM surface was washed with copious amounts

of UHQ water then the Alk-amine was reactivated again by immersion in aqueous HCl (500 mM, pH~1) for 2 h to reprotonate the amine groups. After immersion, the SAM surface was washed with copious amount of UHQ water modified to pH 5 and then immersed in fresh G-NPs solution for 2 h at pH 5. AFM was used to image the surface after each step and the results are shown in **Figure 4.15**. It can be seen clearly that the deposited G-NPs can be removed, and the SAM surface can be reactivated.

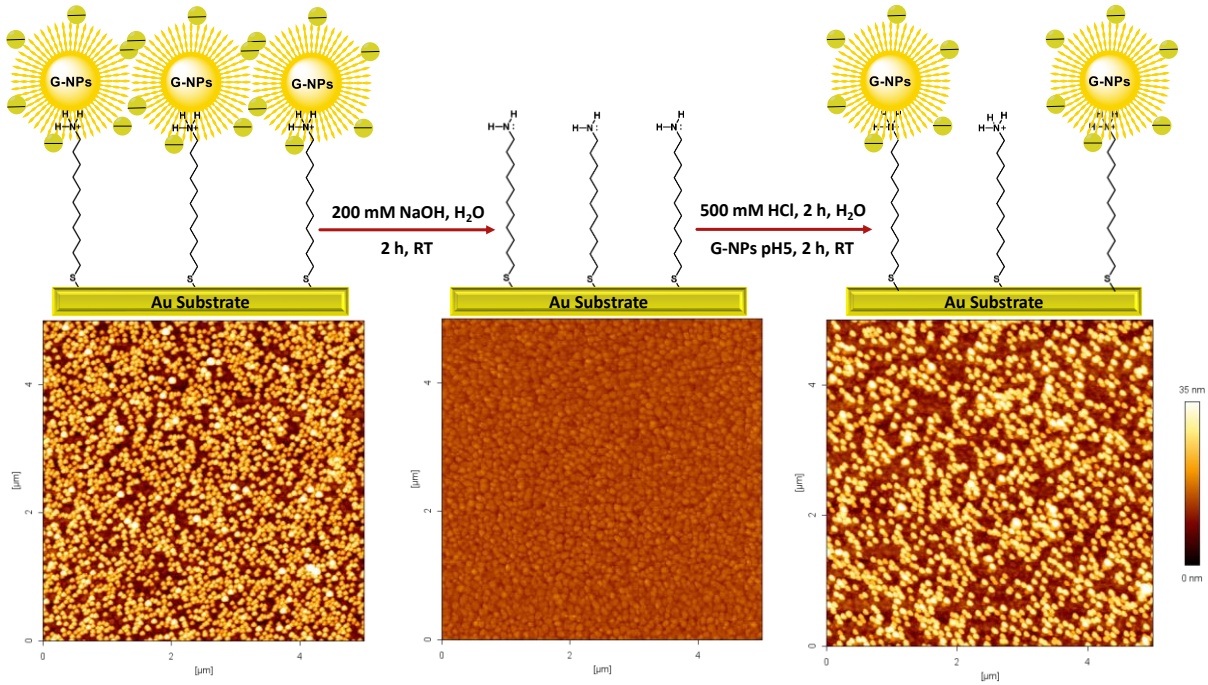

Figure 4.15: 5 × 5 µm AFM images of deactivation of Alk-amine SAM for new deposition of G-NPs at pH 5

Similar behavior was observed for Ar-amine SAM at pH 5 (Figure 4.16). However, on both SAMs the coverage of the deposited G-NPs after activation was (Alk-amine 2870 ± 200 NPs/25 μm^2 and Ar-amine 1230 ± 95 NPs/25 μm^2) lower than the first time (Alk-amine 5800 ± 250 NPs/25 μm^2 and Ar-amine 2650 ± 140 NPs/25 μm^2). This finding confirms that the amine-functionalized

SAMs can be reused and hence provide a promising system for sensing nanoparticles.

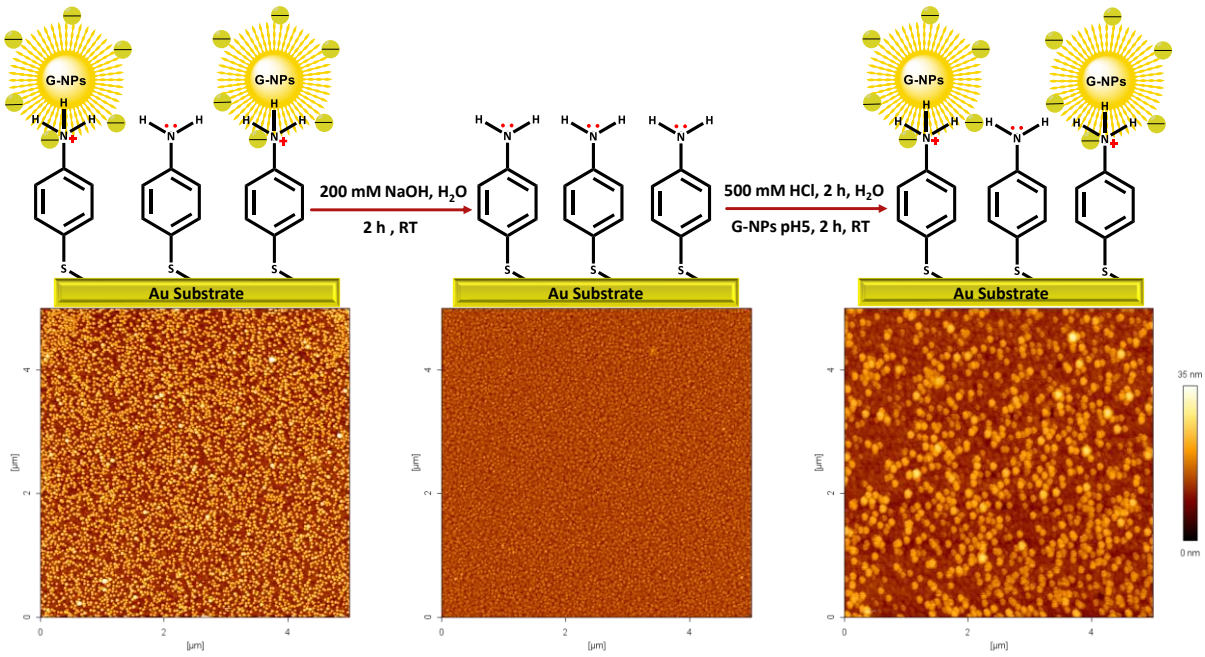

Figure 4.16: 5 × 5 µm AFM images of deactivation of Ar-amine SAM for new deposition of G-NPs at pH 5

4.3.3.2. Quartz Crystal Microbalance (QCM) measurements

QCM was used to measure the absorption of G-NPs deposited on Alk-amine and Ar-amine SAM at different pHs (4, 4.5, 5, 5.5, 6) as function of time. It should be noted that:

1. initial experiments at pH 3 resulted in the deposition of G-NPs aggregates inside the plastic tubing [Pump Tubing (ICP), Yellow/Blue/Yellow, Heat treated, temperature range (−50° to +74°C), medical grade PVC, and High chemical resistance (particularly milk acids, alkalis and salt solutions), and is highly recommended for concentrated and diluted solutions of HCl and NaOH], that was

being used to deliver the particles to the QCM chip, backing up the results in section 4.3.2.3 where aggregation was observed in the AFM experiments. Thus, no further experiments at pH 3 were carried out.

2. at pH 7 there was little evidence of G-NPs deposition on the QCM (see Appendix B2, Figure B2.1).

Therefore, pH 4.5 and pH 5.5 were added to the values of pHs studied in the QCM analysis presented in this section to follow the effect of pH on G-NPs deposition.

Figure 4.17 presents the G-NPs deposition on the Alk-amine and Ar-amine SAM at pH 5 on the QCM sensor (fundamental frequency of 10 MHz). The method on deposition and sensing was:

1. UHQ water at pH 5 was injected (60 µL/min) for 20 mins to obtain a stabilized baseline signal,
2. Followed by the injection (60 µL/min) of the G-NP dispersion at pH 5 for 1 h, by which time the QCM response had plateaued, and taken as maximum deposition of the G-NPs,
3. Followed by the injection (60 µL/min) of UHQ water at pH 5 to remove any physisorbed layer from the surface for 40 mins.

The final QCM response was a drop in resonant frequency of Δf = -944 Hz. Using the Sauerbrey[64] equation (Equation 4.2) the mass of G-NPs deposited on the two amine can be calculated.

$$\Delta m = -C\Delta f \qquad \textit{(Equation 4.2)}$$

Where C represents the mass sensitivity constant of quartz crystal sensor (4.5 ng/Hz.cm^2), f_0 is the fundamental frequency (10 MHz), and Δf represents the frequency change ($f_a - f_0$), where f_a

represents the frequency upon analyte binding.

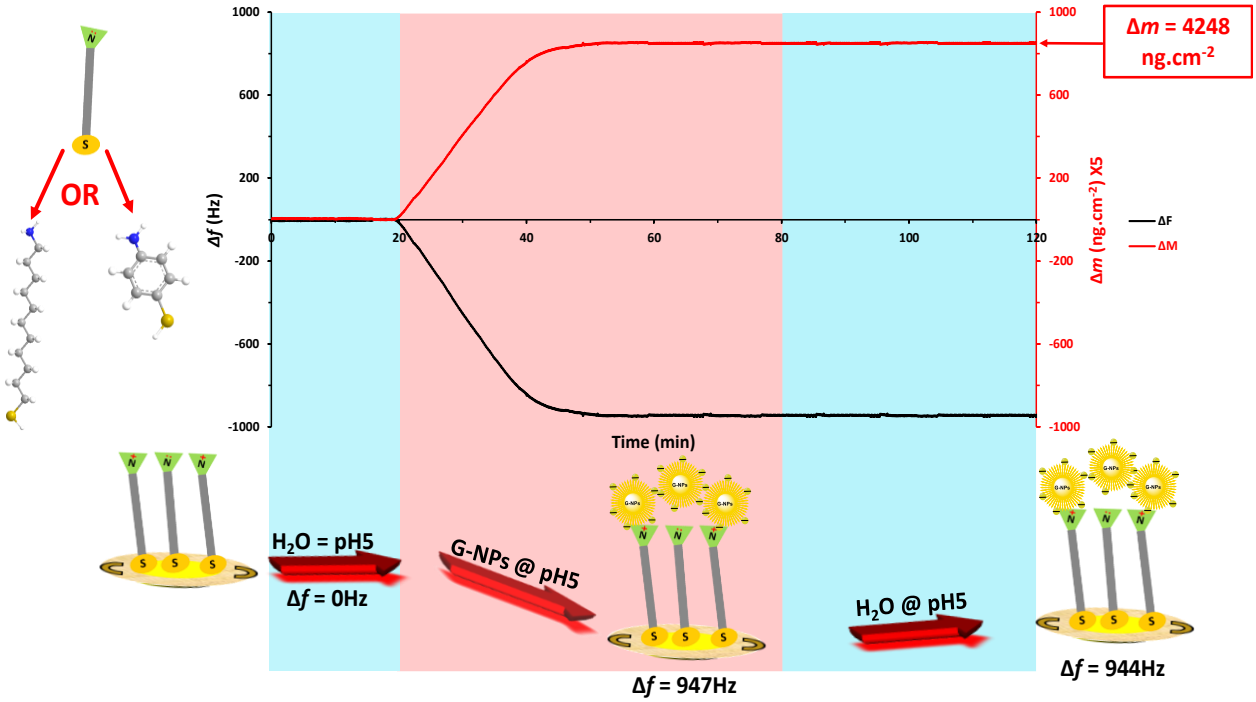

Figure 4.17: QCM Response of G-NPs adsorption on Alk--amine SAM by QCM at pH 5 and room temperature, together with a schematic highlighting the methodology

A control experiment was performed to investigate the deposition of G-NPs at pH 5 on bare Au (pH 5 was chosen due to this pH represents the optimum pH for G-NPs deposition). Figure 4.18 confirms that very few particles attached to bare Au and the number of these particles can be neglected.

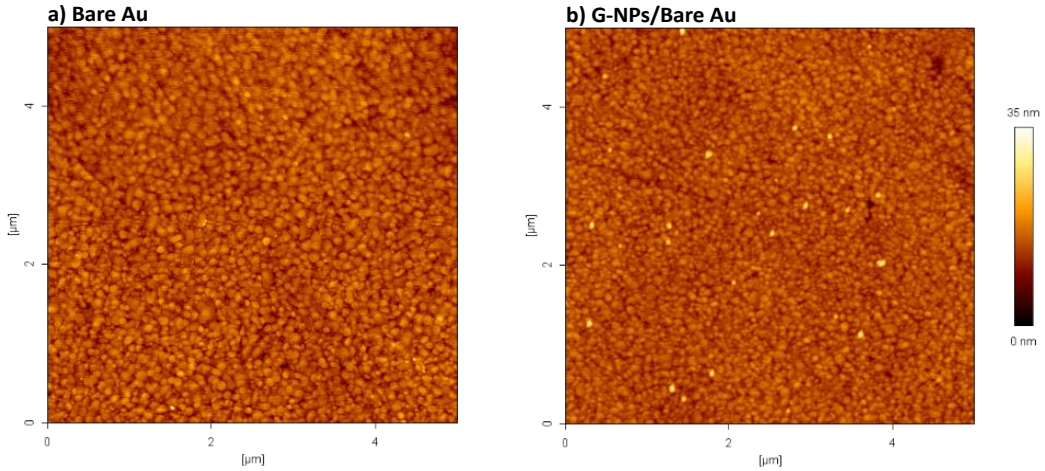

Figure 4.18: 5 × 5 µm AFM images of a control experiment a) bear Au, and b) of depositing G-NPs at pH 5 on bare Au of a QCM-sensor

4.3.3.2.2 QCM frequencies of G-NPs deposited on Alk-amine and Ar-amine SAM at different pHs

The deposition of G-NPs at different values of pHs (4, 4.5, 5, 5.5 and 6) on both Alk-amine and Ar-amine SAMs were followed by the reduction in resonant frequency of the QCM as function of time, and in addition the QCM sensor surfaces were imaged using AFM (Figure 4.19 and Figure 4.20, respectively**)** at the end of each experiment.[65]

For the Alk-amine SAM the largest response was observed at pH 5[66] (Figure 4.21), with a waning frequency increase either side of pH 5, with the exception of pH 4, in line with the conclusions found earlier with respect to particle aggregation at pH 4 and 3.

It is noteworthy to see that

(i) the time required for a complete binding between citrate passivated G-NPs and amine groups-terminated SAM is ˜20 min (Figure 4.19a and Figure 4.20a), which is shorter than the time

(2 h) published from previous studies, and which was used for the AFM experiments earlier in this chapter.[12,14,15]

(ii) it can be seen in the static deposition AFM images (Figure 4.12, pH 4) compared to these dynamic QCM deposition AFM images (Figure 4.19b, pH 4) that the G-NPs deposition and degree of aggregation on the Alk-amine SAM is much less and presumably due to both the reduced contact time between the G-NPs dispersion and the Alk-amine SAM functionalized in the QCM experiment, and the dynamic nature of the flow of the G-NP dispersion across the QCM sensor chip, which will inhibit the sedimentation of any aggregated G-NPs.

The same procedure for deposition of G-NPs on the Alk-amine SAM using QCM was followed to investigate the changes in the frequencies of QCM-sensor after deposition of G-NPs on the Ar-amine SAM and these surfaces were also analyzed using AFM (Figure 4.20).

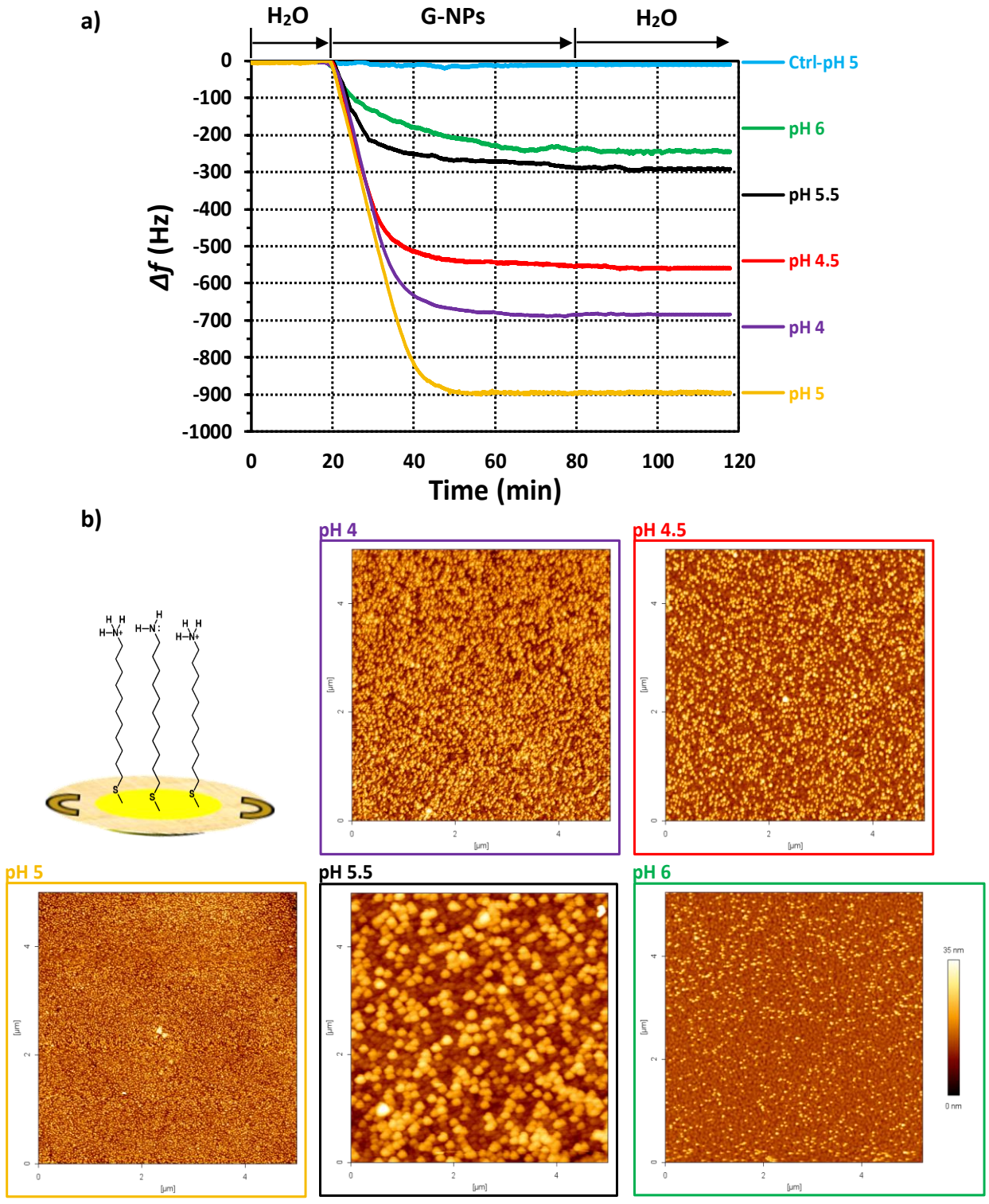

Figure 4.19: a) Measured frequencies by QCM, and b) combined 5 × 5 µm AFM images of G-NPs deposition on Alk-amine SAM at different pHs

The analysis of the Ar-amine SAM system is consistent with the Alk-Amine SAM, with one clear difference being the change of frequency at pH 4 is slightly greater than pH 5, which is related to a greater degree of G-NP aggregation (Figure 4.20b), on pH 4, Ar-amine SAM compared to Figure 4.19b, pH 4, Alk-amine SAM, which may have resulted from a slightly lower pH than 4 being used in the Ar-amine SAM experiment. Moreover, interestingly a kink is observed for the Ar-amine SAM at pH 4 after 25 min of G-NPs deposition (Figure 4.20). This kink is not observed at other pHs as well as for the Alk-amine SAM at all pHs. From Figure 4.20, the presents of aggregates can be observed which are not observed in the other AFM images corresponding to the different pHs for both Ar-amine and Alk-amine SAMs.

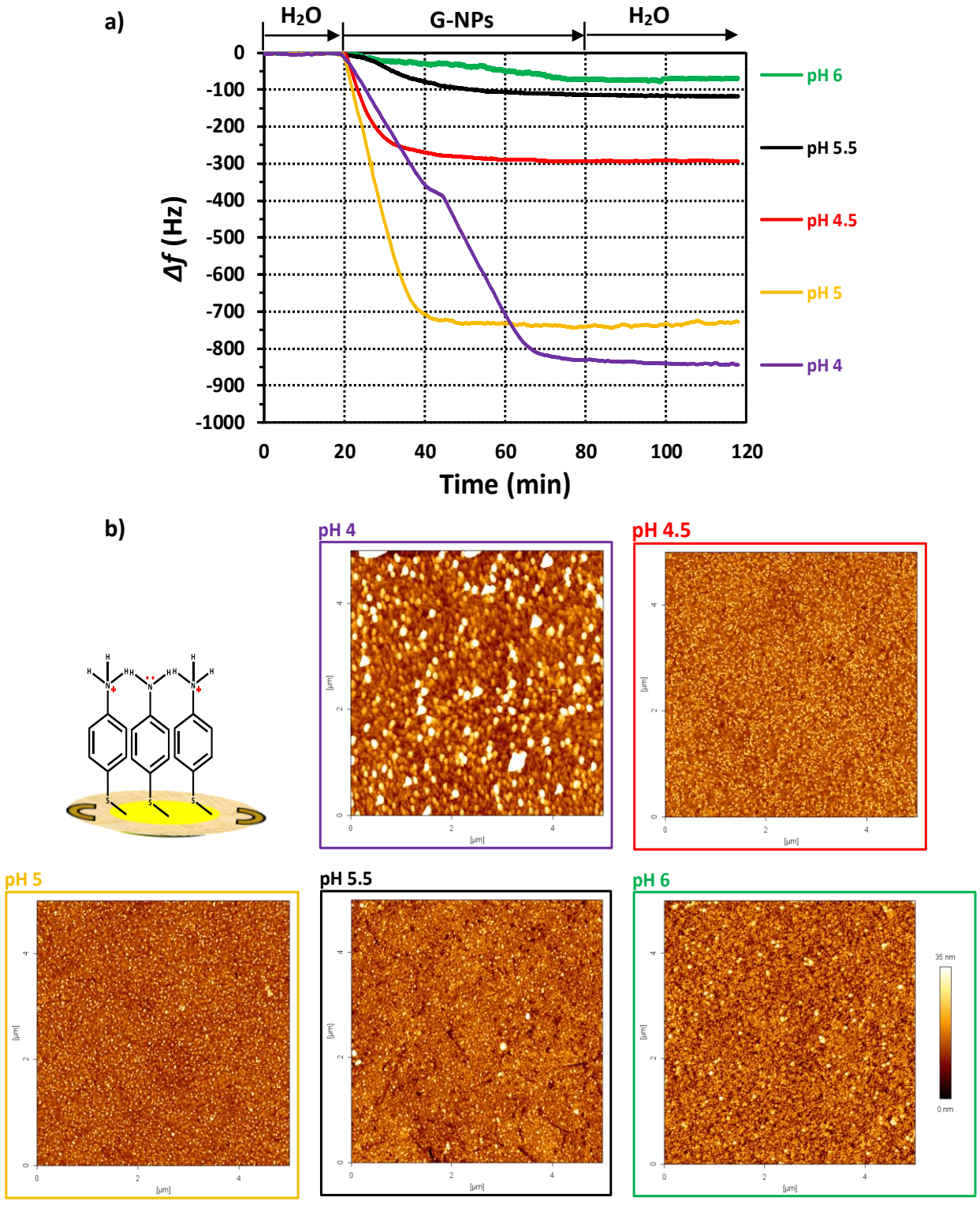

Figure 4.20: a) Measured frequencies by QCM, and b) combined 5 × 5 µm AFM images of G-NPs deposition on Ar-amine SAM at different pHs

Figure 4.21a, shows the changes in the frequencies of G-NPs deposited on both amine SAMs as a function of pH and it confirms that pH 5 represents the optimum condition for G-NPs deposition, if it is assumed that the pH 4 systems are voided due to particle aggregation.

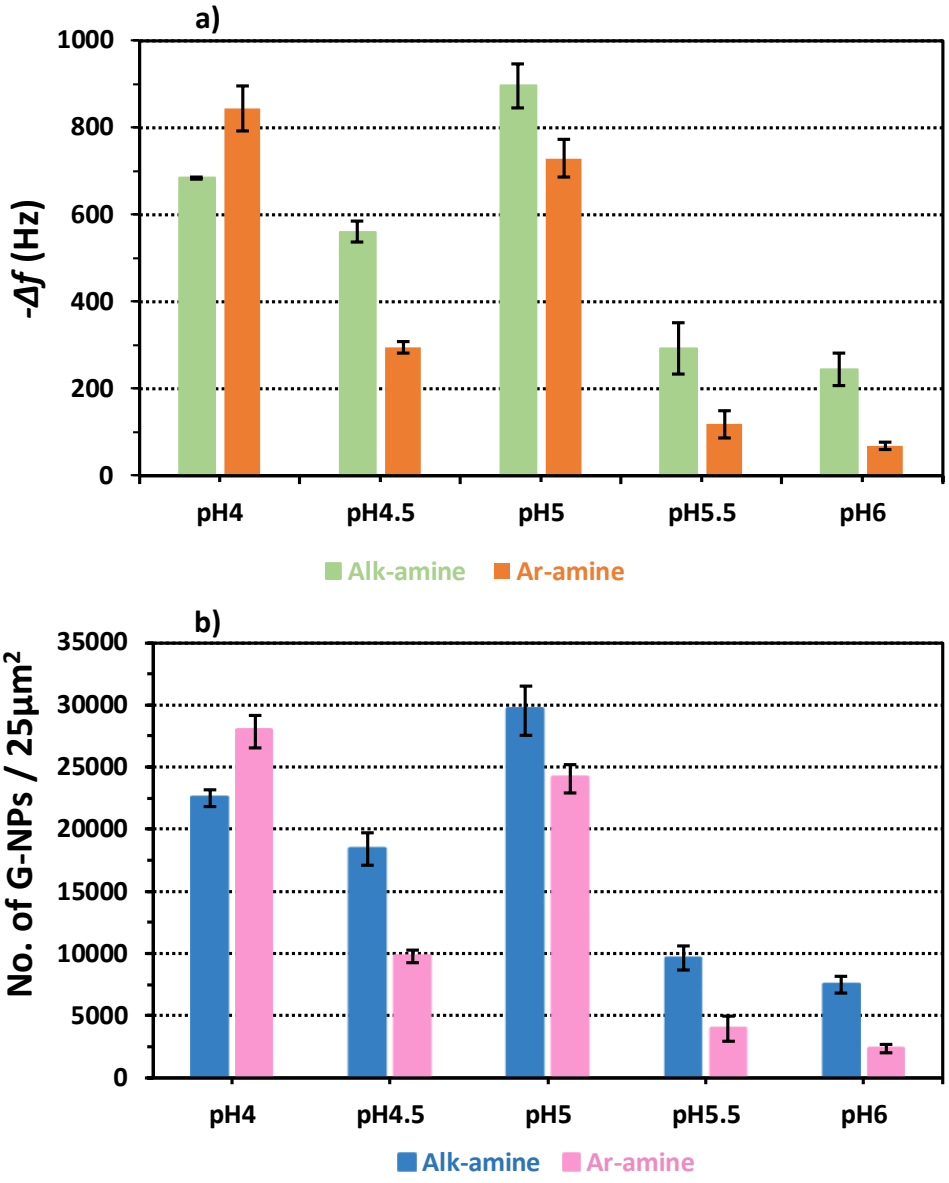

Figure 4.21: (a) Change in frequencies upon G-NPs deposition on the Alk and Ar-amine SAM (1 cm^2) as function of pH on the QCM, and (b) number of G-NPs deposited on the Alk and Ar-amine SAM (25 μm^2) as function of pH on the QCM (calculated via the Sauerbrey equation and scaled from 1cm^2 to 25 μm^2)

4.3.3.3. Translating the SAMs Technology to the MEMS Micro-Paddle: Laser Vibrometer measurements

As the maximum adsorption of G-NPs passivated with citrate was observed at pH 5, by both AFM and QCM techniques, on the two SAMs, as well observing that the adsorption of G-NPs at pH 5 on the Alk-amine SAM was higher than the Ar-amine SAM, it was decided to use pH 5 conditions on only the Alk-amine SAM when employing the MEMS micro-paddle.

The micro-paddles were fabricated using Focused Ion Beam (FIB) and one is shown in Figure 4.22a. The micro paddle consists of a Silicon Nitride (Si_3N_4, 500 μm^2) membrane with a thickness of ˜500 nm, and a ˜30 nm of Au ad-layer.[67] The dimensions of the micro paddle are shown in Figure 4.22a. The Alk-amine SAM was formed under the conditions highlighted earlier in this thesis.

Mass of Particles Adsorbed Via Laser Vibrometry: A single experiment was performed to measure the resonance frequency of the micro-paddle covered with the Alk-amine SAM prior to and after the deposition of G-NPs at pH 5, and the difference in the resonance frequency was related to the mass of G-NPs.[12,68] For the frequency measurements purposes, the micro-paddle was mounted in a glass vacuum chamber (0.001 mbar) and it was excited using an external piezoelectric disc. The vibration was recorded using a laser vibrometer. Figure 4.22b plots the change in resonant frequency before and after G-NP self-assembly to the Alk-amine surface, showing a change resonance frequency (Δf) for the micro-paddle of 6.5 kHz. The mass of deposited G-NPs on Alk-amine SAM at pH 5 was calculated to be 10.46 pg and according to the

Equation 2.8, where the mass sensitivity (*S*) of the micro paddle is determined to be 1.61 fg/Hz.[69,70]

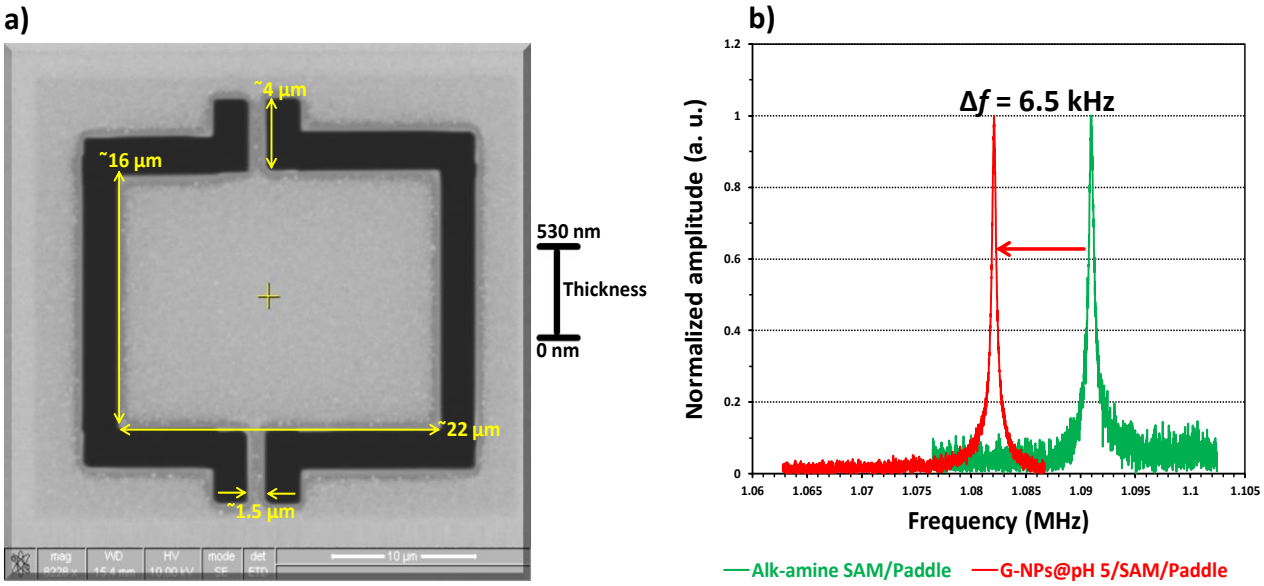

Figure 4.22: a) SEM image of micro paddle, and b) laser vibrometer signals of a micro paddle before and after G-NPs deposition on Alk-amine SAM at pH 5

Mass of Particles Adsorbed Via SEM Image: The deposition of G-NPs on the micro-paddle covered with the Alk-amine SAM before and after the self-assembly of the G-NPs was captured using Scanning Electron Microscopy (SEM). The SEM image in Figure 4.23a represents the surface of micro paddle before the G-NPs deposition, and Figure 4.23b after G-NPs deposition at pH 5, and from which the number of G-NPs was calculated to be 840 ± 42 NP/µm^2 (calculated from three different areas). Based on the total area of micro paddle which is ~352 µm^2 (~16 × ~22 µm), the total number of G-NPs deposited on the Alk-amine SAM is 2.957 × 10^5 NPs, which is equivalent to 10.08 ± 0.50 pg, assuming the mass of a single 14.50 nm diameter G-NP is 3.41 × 10^{-17} g, which is very similar to the mass calculated by laser vibrometry (10.46 pg).[70]

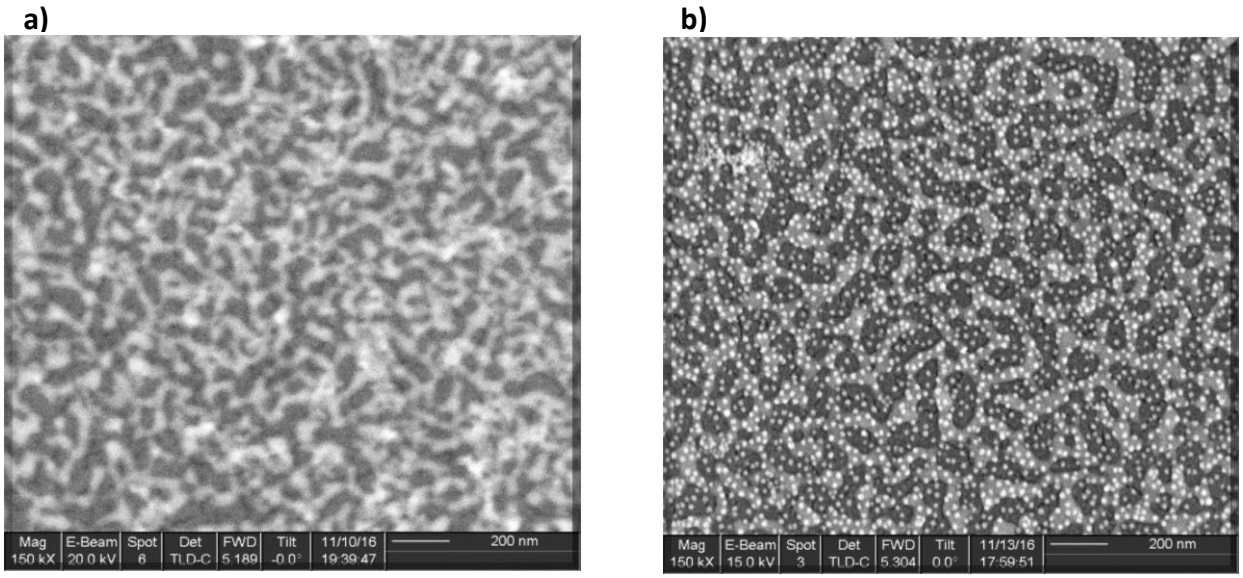

Figure 4.23: SEM image of a) before, and b) after G-NPs deposited on an Alk-amine SAM functionalized surface of a micro paddle

4.4. Conclusion

Using a modified Frens procedure, a diluted dispersion of citrate passivated G-NPs has been prepared, and the results from UV-Vis, DLS and TEM confirm that the G-NPs have a pseudo-spherical shape with an average diameter of ˜15 nm and a narrow SPR spectra at λ_{max} = 520 nm. A study of particle stability as a function of pH for the G-NPs solution has been performed using ZP, DLS and UV-Vis to observe the degree of G-NPs aggregation in reveal that G-NPs aggregate at pH 3 and pH 4 relative to pH 5 and greater.

Using AFM and QCM, the optimum conditions of G-NPs deposition on the Alk-amine and Ar-amine SAM have been investigated, and the maximum coverage of G-NPs has been found to be at pH 5. The coverage of G-NPs on the two amine SAMs at pH 3 and pH 4 is related to the aggregation of particles in the dispersion prior to deposition on the surface, due to the reduction in the

electrostatic repulsion between the particles, as a result of the reduction in the negative charge of carboxylate groups of the citrate anions (protonation).

G-NPs passivated with citrate have been deposited at pH 5 on Alk-amine SAM functionalized micro paddle (MEMS resonator) and the resonance frequencies before and after deposition of the paddle in the solution of G-NPs at pH 5 were measured and the mass of the deposited G-NPs was calculated. The results obtained from this study revealed that this system is an excellent model for use as resonators in the field of MEMS devices for sensing nanoparticles.

4.5. Future work

The prepared system in chapter 4 successfully detected the mass of G-NPs and the future work will be to increase the sensitivity of the micro paddle by reducing the thickness, changing the dimensions of a micro paddle[68,70,71] or increasing the mechanical Q factors (increase the quality of the resonance signal from the background noise)[72,73] in order to detect the masses of analytes which are lighter than G-NPs. For example, the micro paddle with mass sensitivity of 1.61 fg/Hz and dimensions ~352 μm^2 (~16 × ~22 µm)[70] which was successful to detect G-NPs and was not able to detect the deposited mass of NeutrAvidin on binary SAM (chapter 2) with laser vibrometer setup even though the sensitivity is close to predicted sensitivity of 1.25 fg/Hz.[70] Therefore, another micro paddle with mass sensitivity of 55 ag/Hz and dimensions ~80 μm^2 (~8 × ~10 µm)[68,71] was used to predict the minimum and maximum deposited mass of NeutrAvidin; and the number of NeutrAvidin molecules deposited on this micro paddle were calculated to be 6.90×10^7 Neutravidin/cm^2 and 3.99×10^{12} Neutravidin/cm^2 respectively.

4.6. Experimental

4.6.1. a. Chemicals Supplied

- Gold (III) chloride trihydrate was purchased from Sigma-Aldrich with purity 99.9%.
- Sodium citrate tribasic dihydrate was purchased from Sigma with purity 99.0%.
- HNO_3 99% (w/w) was purchased from Sigma-Aldrich.

The rest of chemicals which were used in this study for cleaning Au substrates or for preparing the two amine SAMs, are stated in chapter 2 (Section 2.10.1) and chapter 3 (3.7.1).

4.6.2. b. Au Substrates Supplied

1. ***The polycrystalline Au substrates for AFM*** are the same type of Au which were used in chapter 2 (Section 2.10.2). This type of Au substrate was used to deposit the two amine SAMs on and after to deposit G-NPs on the two SAMs. The deposited G-NPs on the two amine SAMs were characterised by AFM.
2. ***The Au substrate for QCM-***sensor is the same which is used in chapter 2 (Section 2.10.2). This type of Au substrate was used to deposit the two amine SAMs on, thereafter to deposit G-NPs on the two SAMs. The deposited G-NPs on the two amine SAMs were characterised by AFM.
3. The Au substrate for micro paddle was *prepared by a PhD student from Mechanical Engineering, University of Birmingham.* This Au substrate consists of a ˜30 nm of Au layer, on top of a ˜500 nm Si_3N_4 membrane, and had lateral dimensions of 7 × 7 mm. This type

of Au substrate was used to characterize the SAM and G-NPs by laser vibrometer.

4.6.3. SAM formation

4.6.3.1. Cleaning Au substrate for AFM and QCM Prior to SAM formation of the two amines

The same procedure was followed to clean the Au substrate for AFM and QCM which was described in chapter 3 (Section 3.7.3.1). The Au coated paddle was cleaned via exposure to UV plasma (USA, Model No. 342-220) for 1.5 h, and not piranha solution due to the possibility of damaging the membrane of Si_3N_4 of the paddle. After cleaning, the Au surface was washed with copious amount of HPLC EtOH, and immediately immersed in 0.1 mM of degassed HPLC ethanolic solution of Alk-amine thiol.

4.6.3.2. Preparation of Alk and Ar-amine Self-Assembled Monolayers

The same procedure was used to prepare a monolayer of the two amine SAMs on the two types of Au substrates (AFM, QCM and Laser Vibrometer) as was described in chapter 3, Section 3.7.3.2.

4.6.3.3. Preparation of gold Nanoparticles passivated with citrate

All the glassware before usage was immersed in Aqua regia solution[30] (3:1, concentrated 37% HCl: 99% HNO_3) for ~1 h at room temperature, (Caution: Aqua regia solution is an extremely corrosive), followed by rinsing with a copious amount of UHQW and finally dried in an oven at 150 ^oC. The gold nanoparticles passivated with citrate (G-NPs) colloidal solution were synthesised by a modified method to the one described by Frens[29] (diluted method). Gold(III) chloride

trihydrate (ChloroAuric acid) (10 mg, 0.025 mmol) was dissolved in UHQW (100 mL) and forming a pale-yellow solution which was heated under reflux for 1 h, with stirring. Sodium citrate tribasic dihydrate, $HOC(COONa)(CH_2COONa)_2 \cdot 2H_2O$, (23.5 mg, 0.08 mmol) was dissolved in UHQW (2 mL) and added rapidly to the vortex of the refluxing solution. Within 1 min the pale-yellow mixture converted first to a colorless solution, then to dark violet, and then finally to burgundy after 2 min. The dispersion was left heating and rapidly stirring under reflux for 5 mins and then rapidly stirred until the dispersion had cooled to room temperature. A purification step was performed after cooling the solution using a centrifuge (at 3500 rpm for 10 min) to remove larger sedimented material and recovering the supernatant with the dispersed G-NPs. The centrifugation was repeated three times and the supernatant retained. The purified G-NPs solution was stored for further characterisation and application in the refrigerator (2 ^{o}C) at pH 4.5.[14,74,75] The particle diameter was 14.50 ± 0.95 nm (TEM).

4.6.3.4. Deposition of G-NPs on Alk and Ar-amine SAMs at different pH

After completing the steps in the section 4.6.3.3, the Au substrate then was immersed for 2h in (3 mL) G-NPs solution which was modified with range of different pHs (3–7), (Figure 4.24) by adding 10–50 µL of stock solution (50 mM HCl or 50 mM NaOH). The change in the pH values of G-NPs solution were monitored with a digital pH meter (IQ 150 Scientific Instrument). After immersion, the Au substrate was removed from the vial and was rinsed with UHQW which was modified to the above range of pHs, dried under a stream of N_2 gas, and then stored, for characterisation by AFM, for 24 h in the freezer (-20 ^{o}C) in a clean dry vial, which was capped and sealed with parafilm and covered in foil.

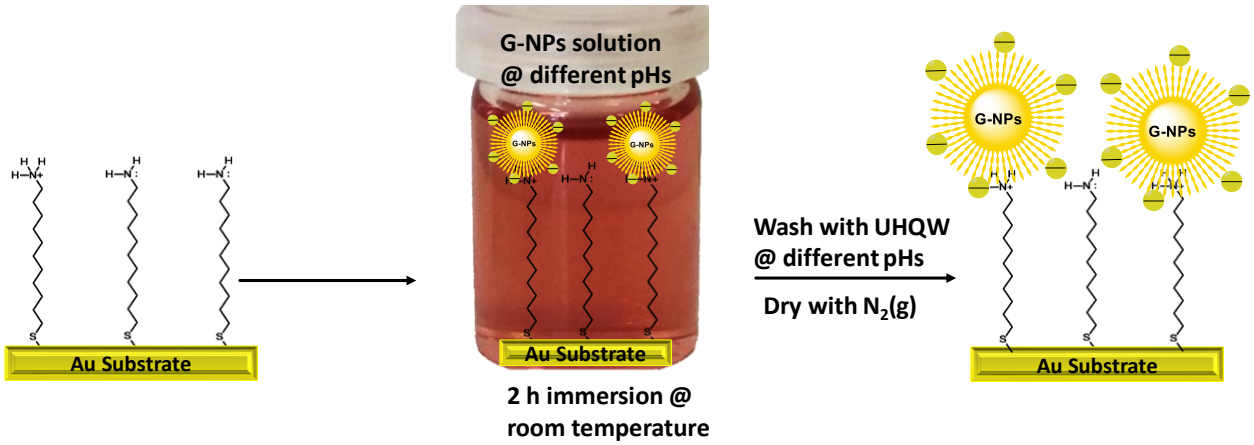

Figure 4.24: Deposition of G-NPs on Alk-amine SAM for 2 h at room temperature

4.7. Surface characterisation

4.7.1. Atomic Force Microscopy (AFM) measurements

A NanoWizard II AFM (JPK Instruments, UK) was used to image the topography of the surfaces before and after deposition of G-NPs onto one of the two amine SAMs, using non-contact or tapping mode in air, using an uncoated Si cantilever (PPP-NCL, Windsor Scientific, UK, nominal length 225 ± 10 µm, width 38 ± 7.5 µm, thickness 7 ± 1 µm, tip height 10–15 µm, tip radius <10 nm and spring constant 21–98 N/m. The scan size was 5 × 5 µm, employing a pixel density of 512 × 512. Three to four Au substrates were analysed, with and without G-NP deposition, scanning six areas on each, in order to observe the uniformity of the distribution of the deposited G-NPs.

4.7.2. Quartz Crystal Microbalance (QCM) measurements

All QCM were performed on OpenQCM (Novaetech, Italy) Figure 4.2. A one flow cell with two independent parallel flow channels were used to carry out the G-NPs binding experiments. A gold-coated AT-cut QCM-sensor, covered with one of the two amine SAMs was installed on the QCM holder (HC-48/u). All the experiments were performed at a flow rate of 60 µl/min. The UHQW and was modified with different pHs (4, 4.5, 5, 5.5 and 6), by adding 50 mM of HCl or 50 mM of NaOH, was flowed (60 µl/min) over the SAM for 20 min to obtain a baseline, followed by G-NP solution (60 µl/min) for 60 min, followed finally by the UHQW was modified with different pHs (60 µl/min) for ~40 min to wash any physisorbed G-NPs from the surface. This experiment was repeated 3–4 times for reproducibility of the QCM measurements.

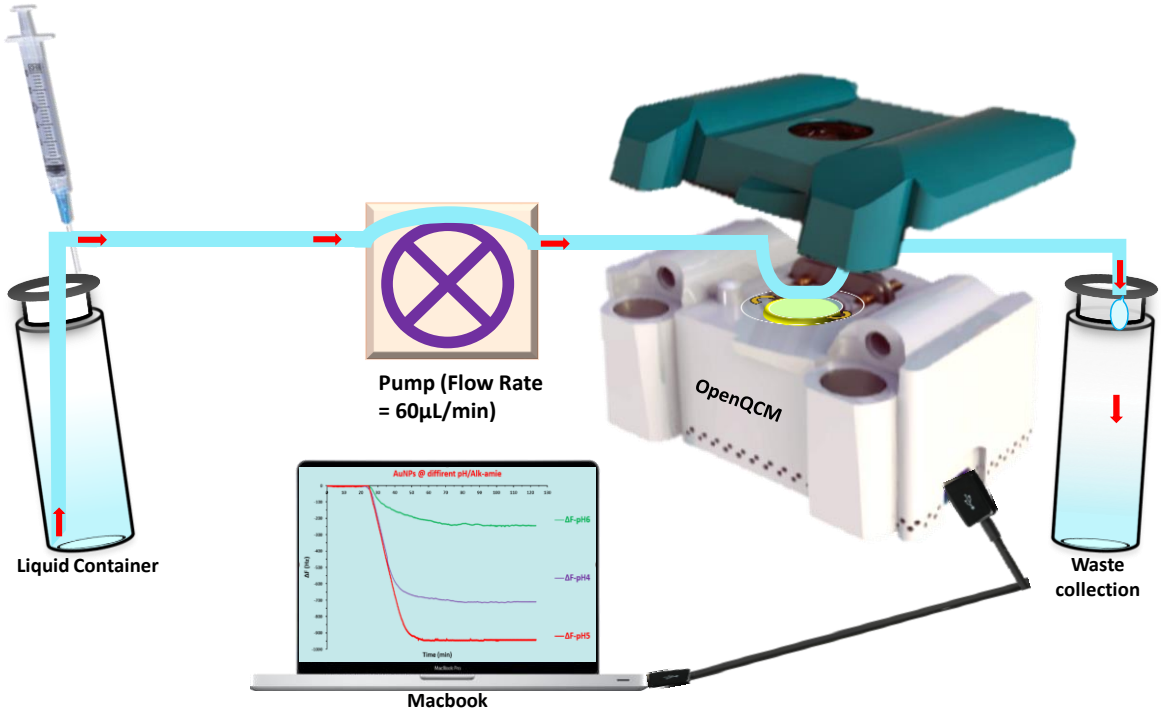

Figure 4.25: Schematic of QCM system for G-NPs deposition on Alk and Ar-amine SAM at different pHs

4.8. G-NPs colloidal solution characterization

4.8.1. Transmission Electron Microscopy (TEM)

The obtained images from transmission electron microscopy (TEM) for G-NPs passivated with citrate were observed using an electron microscope (JEOL JEM-1200EX and a JEOL JEM-2100) fitted with a Gatan camera. Two samples of TEM Formvar/carbon film-coated Cu-grids with 200 mesh (Ager Scientific) were prepared by applying one drop (10 µL) of synthesised G-NPs solution, which was stabilized at pH 4.5[14,74] *(at this pH G-NPs colloidal solution is stabilized for around one year without any sing of aggregation)* (see Appendix B, Figure B1.1), on each grid and they were left to be dried under vacuum for 24 h.

4.8.2. UV-Vis spectrophotometer measurements

The obtained spectra of UV-Vis were observed from a Varian Cary 50 UV0902M053 UV-Visible spectrophotometer, which was operated for all samples G-NPs passivated with citrate at wavelengths 340–800 nm and using a 1 cm length of quartz cuvette.

4.8.3. Dynamic Light Scattering (DLC) measurements

DLS measurements were performed using a Particle Analyzer (Delsa™ Nano Submicron Particle Size and Zeta Potential) equipped with a laser He-Ne (3.0 mW, 633 nm) and photodiode detector. After the laser hits the particles, the intensity distribution of the light scattered by these particles will be detected by the detector and the particle sizes will be generated, and these results were monitored using Delsa™ Nano UI software version 3.73. The setting of experimental

conditions was performed manually and UHQ water was used as a solvent due to the UHQ water being used to prepare the G-NP colloidal solution. All the measurements were achieved in a 1 cm path length quartz cell and temperature set at 25 ^{o}C. The temperature was controlled by a thermo-electric Peltier heater/cooler element. The DLS machine was allowed to settle for 1 min between the sample being placed in the sample chamber and the measurements being taken, to allow the sample to equilibrate at 25 ^{o}C. The cell was cleaned by using of Aqua regia solution, washed with UHQW followed by HPLC ethanol and dried with N_2 gas. After cleaning, the G-NPs solution at the required pH was injected immediately and slowly in the cleaned cell to prevent the formation of air bubbles, which would interfere with the measurements. After each measurement, the procedure of cleaning the quartz cell was repeated for each pH.

4.8.4. Zeta Potential (ZP) measurements

ZP was measured in the same machine as DLS, and same conditions to the DLS experiments were used to measure the ZP for each pH of the G-NP solution. Also, the same procedure of cleaning the quartz cell was followed. The only difference is the principle of the required measurement for each technique. For ZP no laser is used, and instead positive and negative electrodes are used to measure the charge of the G-NPs surfaces after changing the pH of the G-NPs solution.

4.9. References

[1] S. Sun, X. Ning, G. Zhang, Y. C. Wang, C. Peng and J. Zheng, *Angew. Chemie - Int. Ed.*, 2016, **55**, 2421–2424.

[2] E. Hutter and M.-P. Pileni, *J. Phys. Chem. B*, 2003, **107**, 6497–6499.

[3] J. Zhang, S. Song, L. Wang, D. Pan and C. Fan, *Nat. Protoc.*, 2007, **2**, 2888–2895.

[4] B. Manning, S. J. Leigh, R. Ramos, J. A. Preece and R. Eritja, *J. Exp. Nanosci.*, 2010, **5**, 26–39.

[5] X. Zhang, M. R. Servos and J. Liu, *Langmuir*, 2012, **28**, 3896–3902.

[6] G. Ajnai, A. Chiu, T. Kan, C. C. Cheng, T. H. Tsai and J. Chang, *J. Exp. Clin. Med.*, 2014, **6**, 172–178.

[7] E. C. Dreaden, L. A. Austin, M. A. Mackey and M. A. El-Sayed, *Ther. Deliv.*, 2012, **3**, 457–478.

[8] G. Chumanov, K. Sokolov, B. W. Gregory and T. M. Cotton, *J. Phys. Chem.*, 1995, **99**, 9466–9471.

[9] K. Kim and J. K. Yoon, *J. Phys. Chem. B*, 2005, **109**, 20731–20736.

[10] S. Hong and X. Li, *J. Nanomater.*, 2013, **2013**.

[11] T. Zhu, H. Z. Yu, J. Wang, Y. Q. Wang, S. M. Cai and Z. F. Liu, *Chem. Phys. Lett.*, 1997, **265**, 334–340.

[12] C. A. E. Hamlett, P. T. Docker, M. C. L. Ward, P. D. Prewett, K. Critchley, S. D. Evans and J. A. Preece, *J. Exp. Nanosci.*, 2009, **4**, 147–157.

[13] T. Zhu, X. Fu, T. Mu, J. Wang and Z. Liu, *Langmuir*, 1999, **15**, 5197–5199.

[14] S. Diegoli, P. M. Mendes, E. R. Baguley, S. J. Leigh, P. Iqbal, Y. R. Garcia Diaz, S. Begum, K. Critchley, G. D. Hammond, S. D. Evans, D. Attwood, I. P. Jones and J. A. Preece, *J. Exp.*

Nanosci., 2006, **1**, 333–353.

[15] J. Bowen, M. Manickam, S. D. Evans, K. Critchley, K. Kendall and J. A. Preece, *Thin Solid Films*, 2008, **516**, 2987–2999.

[16] M. Ben Haddada, J. Blanchard, S. Casale, J. M. Krafft, A. Vallée, C. Méthivier and S. Boujday, *Gold Bull.*, 2013, **46**, 335–341.

[17] T. R. Lee, R. I. Carey, H. A. Biebuyck and G. M. Whitesides, *Langmuir*, 1994, **10**, 741–749.

[18] S. E. Creager and J. Clarke, *Langmuir*, 1994, **10**, 3675–3683.

[19] H. Zhang, H. X. He, J. Wang, T. Mu and Z. F. Liu, *Appl. Phys. A Mater. Sci. Process.*, 1998, **66**, 269–271.

[20] D. V Vezenov, A. Noy, L. F. Rozsnyai and C. M. Lieber, *J. Am. Chem. Soc.*, 1997, **119**, 2006–2015.

[21] E. W. van der Vegte and G. Hadziioannou, *Langmuir*, 1997, **13**, 4357–4368.

[22] E. W. van der Vegte and G. Hadziioannou, *J. Phys. Chem. B*, 1997, **101**, 9563–9569.

[23] D. A. Smith, M. L. Wallwork, J. Zhang, J. Kirkham, C. Robinson, A. Marsh and M. Wong, *J. Phys. Chem. B*, 2000, **104**, 8862–8870.

[24] M. L. Wallwork, D. A. Smith, J. Zhang, J. Kirkham and C. Robinson, *Langmuir*, 2001, **17**, 1126–1131.

[25] B. Wang, R. D. Oleschuk and J. H. Horton, *Langmuir*, 2005, **21**, 1290–1298.

[26] L.-B. Zhao, M. Zhang, B. Ren, Z.-Q. Tian and D.-Y. Wu, *J. Phys. Chem. C*, 2014, **118**, 27113–27122.

[27] J. J. Shyue, M. R. De Guire, T. Nakanishi, Y. Masuda, K. Koumoto and C. N. Sukenik,

Langmuir, 2004, **20**, 8693–8698.

[28] A. Marti, G. Haehner and N. D. Spencer, *Langmuir*, 1995, **11**, 4632–4635.

[29] G. FRENS, *Nat. Phys. Sci.*, 1973, **241**, 20–22.

[30] K. C. Grabar, M. B. Hommer, M. J. Natan and R. G. Freeman, *Anal. Chem.*, 1995, **67**, 735–743.

[31] H. N. Verma, P. Singh and R. M. Chavan, *Vet. World*, 2014, **7**, 72–77.

[32] D. Kumar, B. J. Meenan, I. Mutreja, R. D'SA and D. DIXON, *Int. J. Nanosci.*, 2012, **11**, 1250023.

[33] J. Kimling, M. Maier, B. Okenve, V. Kotaidis, H. Ballot and A. Plech, *J. Phys. Chem. B*, 2006, **110**, 15700–15707.

[34] I. Ojea-Jimenez, F. M. Romero, N. G. Bastus and V. Puntes, *J. Phys. Chem. C*, 2010, **114**, 1800–1804.

[35] S. Link and M. A. El-Sayed, *J. Phys. Chem. B*, 1999, **103**, 4212.

[36] X. Ji, X. Song, J. Li, Y. Bai, W. Yang and X. Peng, *J. Am. Chem. Soc.*, 2007, **129**, 13939–13948.

[37] R. Kanjanawarut, B. Yuan and S. XiaoDi, *Nucleic Acid Ther.*, 2013, **23**, 273–280.

[38] T. Zhu, K. Vasilev, M. Kreiter, S. Mittler and W. Knoll, *Langmuir*, 2003, **19**, 9518–9525.

[39] S. E. Park, M. Y. Park, P. K. Han and S. W. Lee, *Bull. Korean Chem. Soc.*, 2006, **27**, 1341–1345.

[40] S. K. Ghosh and T. Pal, *Chem. Rev.*, 2007, **107**, 4797–4862.

[41] D. W. Thompson and I. a N. R. Collinst, *J. Colloid Interface Sci.*, 1992, **152**, 197–204.

[42] S. H. Brewer, W. R. Glomm, M. C. Johnson, M. K. Knag and S. Franzen, *Langmuir*, 2005, **21**,

9303–9307.

[43] S. Praharaj, S. Panigrahi, S. Basu, S. Pande, S. Jana, S. K. Ghosh and T. Pal, *J. Photochem. Photobiol. A Chem.*, 2007, **187**, 196–201.

[44] G. T. Wei, *Anal. Chem.*, 1999, **71**, 2085–2091.

[45] J. Lim, N. E. Lee, E. Lee and S. Yoon, *Bull. Korean Chem. Soc.*, 2014, **35**, 2567–2569.

[46] S. Lee, J. H. Yoon and S. Yoon, *J. Phys. Chem. C*, 2011, **115**, 12501–12507.

[47] J. Nam, N. Won, H. Jin, H. Chung and S. Kim, *J. Am. Chem. Soc.*, 2009, **131**, 13639–13645.

[48] K. Zabetakis, W. E. Ghann, S. Kumar and M. C. Daniel, *Gold Bull.*, 2012, **45**, 203–211.

[49] H. Zhang, H.-X. He, T. Mu and Z.-F. Liu, *Thin Solid Films*, 1998, **327**–**329**, 778–780.

[50] J. M. Campiña, A. Martins and F. Silva, *J. Phys. Chem. C*, 2007, **111**, 5351–5362.

[51] D. J. Garrett, B. S. Fiavel, J. G. Shapter, K. H. R. Baronian and A. J. Downard, *Langmuir*, 2010, **26**, 1848–1854.

[52] T. H. Degefa, P. Schön, D. Bongard and L. Walder, *J. Electroanal. Chem.*, 2004, **574**, 49–62.

[53] M. A. Bryant and R. M. Crooks, *Langmuir*, 1993, **9**, 385–387.

[54] P. M. Dietrich, N. Graf, T. Gross, A. Lippitz, S. Krakert, B. Schüpbach, A. Terfort and W. E. S. Unger, *Surf. Interface Anal.*, 2010, **42**, 1184–1187.

[55] K. Greben, P. Li, D. Mayer, A. Offenhäusser and R. Wördenweber, *J. Phys. Chem. B*, 2015, **119**, 5988–5994.

[56] K. C. Grabar, P. C. Smith, M. D. Musick, J. A. Davis, D. G. Walter, M. A. Jackson, A. P. Guthrie and M. J. Natan, *J. Am. Chem. Soc.*, 1996, **118**, 1148–1153.

[57] A. Cheng, San José State University, 2010.

[58] E. Palleau, N. M. Sangeetha, G. Viau, J. D. Marty and L. Ressier, *ACS Nano*, 2011, **5**, 4228–4235.

[59] V. Oommen, G. Ganesh and P. Kanthakumar, *j. physiol pharmacol*, 2016, **60**, 70–75.

[60] S. H. Yalkowsky, R. B. Patel and D. Alantary, *ADMET DMPK*, 2015, **3**, 359–362.

[61] J. S. Zhang, X. Zhang, Z. L. Zhang and Z. J. Tan, *Sci. Rep.*, 2017, **7**, 1–11.

[62] X. Shi, *J. Vac. Sci. Technol. B Microelectron. Nanom. Struct.*, 1999, **17**, 350.

[63] H. K. Lin, P. Van Der Schoot and R. Zandi, *Phys. Biol.*, 2012, **9**, 1–11.

[64] G. Sauerbrey, *Zeitschrift für Phys.*, 1959, **155**, 206–222.

[65] B. L. T. Lau, R. Huang and A. S. Madden, *J. Nanoparticle Res.*, 2013, **15**.

[66] A. G. Hemmersam, K. Rechendorff, F. Besenbacher, B. Kasemo and D. S. Sutherland, *J. Phys. Chem. C*, 2008, **112**, 4180–4186.

[67] N. Mahmoodi, A. I. Rushdi, J. Bowen, A. Sabouri, C. J. Anthony, P. M. Mendes and J. A. Preece, *J. Vac. Sci. Technol. A Vacuum, Surfaces, Film.*, 2017, **35**, 041514.

[68] S. C. Charandabi, P. D. Prewett, C. A. Hamlett, C. J. Anthony and J. A. Preece, *Microelectron. Eng.*, 2011, **88**, 2229–2232.

[69] A. Boisen, S. Dohn, S. S. Keller, S. Schmid and M. Tenje, *Reports Prog. Phys.*, 2011, **74**.

[70] N. Mahmoodi, University of Birmingham, PhD thesis, 2017.

[71] B. Boonliang, P. D. Prewett, J. Hedley, J. Preece and C. A. Hamlett, *J. Micromechanics Microengineering*, 2008, **18**, 1–4.

[72] P. Mohanty, D. A. Harrington, K. L. Ekinci, Y. T. Yang, M. J. Murphy and M. L. Roukes, *Phys. Rev. B - Condens. Matter Mater. Phys.*, 2002, **66**, 854161–8541615.

[73] T. Ono, D. F. Wang and M. Esashi, *Appl. Phys. Lett.*, 2003, **83**, 1950–1952.

[74] P. M. Mendes and J. A. Preece, *Curr. Opin. Colloid Interface Sci.*, 2004, **9**, 236–248.

[75] S. Begum, I. P. Jones, D. E. Lynch and J. A. Preece, *J. Exp. Nanosci.*, 2012, **7**, 1–16.

Chapter 5

Appendices

APPENDIX A

Appendix A1: Shows the calculated XPS data of N 1s/Au 4f ratio of TEG and BUT SAMs (pure and 8 mixed) deposited on Au surface at R.T and mole fraction of $X^{\%BUT}$ on the Au surface.

Table A1.1: Shows the calculated XPS data of N 1s/Au 4f ratio of TEG and BUT SAMs (pure and 8 mixed) deposited on Au surfaces at R.T. and mole fraction of $X^{\%BUT}$ on the Au surface.

$X^{\%BUT}$ Surface	N 1s/Au 4f x 10^{-2}
0	0
27.0 ± 2.0	0.273 ± 0.024
29.0 ± 0.6	0.321 ± 0.036
47.0 ± 2.0	0.521 ± 0.090
58.6 ± 1.0	0.591 ± 0.084
62.9 ± 1.0	0.883 ± 0.057
66.0 ± 0.5	1.045 ± 0.034
74.7 ± 3.0	1.037 ± 0.073
84.6 ± 2.0	1.090 ± 0.038
100	0.679 ± 0.079

Appendix A2: SPR response of NeutrAvidin deposition on 66 $X^{\%BUT}$ for 2h.

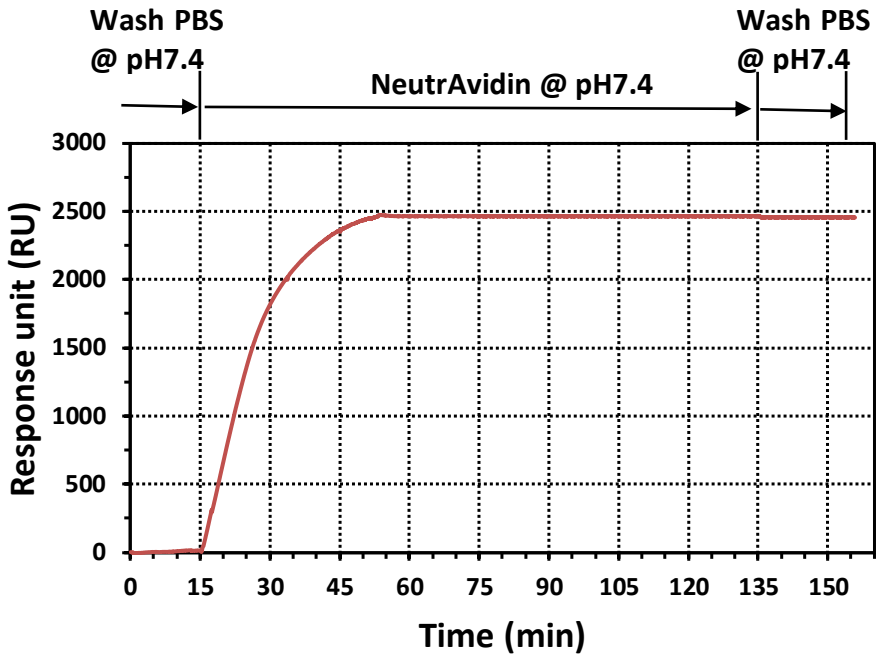

Figure A2.1: Shows the SPR response for 66 $X^{\%BUT}$ SAM on Au surface at room temperature

Appendix A3: Calculate the coverage of pure or mixed BUT and TEG SAM on Au surface, and the number of biotin required to immobilize NeutrAvidin on pure or mixed BUT and TEG SAM.

Coverage of pure BUT and TEG SAM

The coverage of the pure BUT (Θ_{BUT}) and TEG (Θ_{TEG}) on Au surface were calculated according to the following equation A3.1

$$\Theta_{BUT} = M/T \qquad \textit{(Equation A3.1)}$$

M: represents the average thickness which was measured by ellipsometry for each SAM

T: estimated thickness of each SAM and can be calculated by using equation A3.2.

$$T = L*cos30 \qquad \textit{(Equation A3.2)}$$

T: Estimated thickness of the BUT and TEG

L: Theoretical thickness of each SAM (BUT and TEG) which was calculated using ChemBio Draw

30: where 30 is in degrees, and assuming this is an appropriate angle for the SAM molecules if present in a well-formed monolayer.

For the Au (111) surface, it is assumed that the packing density is four SAM molecules per nm^2. Based on these information, and by applying equation A3.1 then A3.2, the Θ_{BUT} and Θ_{TEG} on Au surface is shown in table A3.1.

Table A3.1: shows the calculated Θ_{BUT} and Θ_{TEG} SAMs on Au surface

SAM	L (nm)	Cos(30)	T (nm)	M (nm)	Θ_{SAM} = (M/T)	Θ_{SAM} x 4 (nm^2)
BUT	4.50	0.87	3.92	2.92 ± 0.20	0.748 ± 0.05	2.99 ± 0.10
TEG	3.10	0.87	2.69	2.21 ± 0.10	0.83 ± 0.06	3.30 ± 0.04

Coverage of mixed BUT and TEG SAM

The coverage for mixed SAMs was calculated by using the ratios of the mixed SAMs which was calculated by using the results from contact angle after applying the Cassie equation 2.2 (see table 2.3). Accordingly, multiply these ratios with the coverage of pure SAMs which was calculated according to equation A3.2 and was reported in table A3.1, and the results are reported in table A3.2.

Table A3.2: Shows the calculation of the coverage of the mixed BUT and TEG SAMs

X^{BUT} Surface	$\Theta_{BUT} \times 4$ (nm^2)	X^{BUT} Surface × ($\Theta_{BUT} \times 4$)
0	2.99 ± 0.10	0
0.27 ± 0.02	2.99 ± 0.10	0.807 ± 0.059
0.29 ± 0.006	2.99 ± 0.10	0.867 ± 0.018
0.47 ± 0.02	2.99 ± 0.10	1.405 ± 0.059
0.585 ± 0.02	2.99 ± 0.10	1.749 ± 0.030
0.629 ± 0.01	2.99 ± 0.10	1.884 ± 0.030
0.66 ± 0.005	2.99 ± 0.10	1.973 ± 0.015
0.747 ± 0.03	2.99 ± 0.10	2.234 ± 0.089
0.846 ± 0.02	2.99 ± 0.10	2.533 ± 0.059
1	2.99 ± 0.10	2.990 ± 0.024

Table A3.3: Shows the calculation of the coverage of the mixed TEG and BUT SAMs

X^{TEG} Surface	Θ_{TEG} x 4 (nm^2)	X^{BUT} Surface × [$\Theta_{TEG} \times 4$]
1	3.300 ± 0.04	3.300 ± 0.023
0.73 ± 0.02	3.300 ± 0.04	2.409 ± 0.066
0.71 ± 0.006	3.300 ± 0.04	2.34 ± 0.02
0.53 ± 0.02	3.300 ± 0.04	1.749 ± 0.066
0.415 ± 0.02	3.300 ± 0.04	1.369 ± 0.033
0.371 ± 0.01	3.300 ± 0.04	1.224 ± 0.033
0.34 ± 0.005	3.300 ± 0.04	1.122 ± 0.017
0.253 ± 0.03	3.300 ± 0.04	0.8349 ± 0.099
0.154 ± 0.02	3.300 ± 0.04	0.508 ± 0.066
0	3.300 ± 0.04	0

Table A3.4: Shows the ratio of BUT required to immobilize NeutrAvidin

(BUT/cm^2) × 10^{14}	(Neu/cm^2) × 10^{12}	BUT/Neu
0	0.103 ± 0.025	0
0.807 ± 0.059	0.702 ± 0.064	115.000 ± 13.538
0.867 ± 0.018	0.853 ± 0.089	101.653 ± 10.850
1.405 ± 0.059	2.030 ± 0.158	69.227 ± 6.128
1.749 ± 0.030	2.160 ± 0.123	80.979 ± 4.830
1.884 ± 0.030	2.310 ± 0.141	81.416 ± 5.118
1.973 ± 0.015	2.560 ± 0.152	77.086 ± 4.600
2.234 ± 0.089	2.800 ± 0.164	79.768 ± 5.655
2.533 ± 0.059	2.840 ± 0.172	89.173 ± 5.779
2.990 ± 0.024	2.670 ± 0.226	111.985 ± 9.512

Table A3.5: Shows the ratio of BUT and TEG on the Au surface

(BUT/cm^2) x 10^{14}	(TEG/cm^2) x 10^{14}	BUT/TEG
0	3.300 ± 0.023	0
0.807 ± 0.059	2.409 ± 0.066	0.335 ± 0.026
0.867 ± 0.018	2.34 ± 0.02	0.370 ± 0.008
1.405 ± 0.059	1.749 ± 0.066	0.803 ± 0.044
1.749 ± 0.030	1.369 ± 0.033	1.277 ± 0.035
1.884 ± 0.030	1.224 ± 0.033	1.542 ± 0.045
1.973 ± 0.015	1.122 ± 0.017	1.758 ± 0.027
2.234 ± 0.089	0.8349 ± 0.099	2.675 ± 0.308
2.533 ± 0.059	0.508 ± 0.066	5.016 ± 0.600
2.990 ± 0.024	0	0

Appendix A4: Synthesis of TEG which is used in chapter two as spacer

Chemicals and Materials. Commercially available chemicals and solvents were purchased from Aldrich Chemicals and Fisher Chemicals and were used as received. Thin-layer chromatography (TLC) was carried out on aluminum plates coated with silica gel 60 F254 (Merck 5554). The TLC plates were dipped in potassium manganate dip and dried with a heat gun. Column chromatographic separations were performed on silica gel 120 (ICN Chrom 32–63, 60 Å).

NMR. 1H Nuclear Magnetic Resonance (NMR) spectra were recorded on a Bruker AC 300 (300.13 MHz) spectrometer. 13C NMR spectra were recorded on a Bruker AV 300 (75.5 MHz) using Pendent pulse sequences. All chemical shifts are quoted in ppm to higher frequency from Me4Si using either deuterated chloroform ($CDCl_3$) as the lock, and the residual solvent as the internal standard. The coupling constants are expressed in Hertz (Hz) with multiplicities abbreviated as follows; s = singlet, d = doublet, dd = double doublet, t = triplet, q = quartet and m = multiplet.

Mass Spectrometry (MS). Low and high resolution Electrospray Mass Spectrometry was performed on a micromass Time of Flight (TOF) instrument using methanol as the mobile phase.

Infrared Spectroscopy (IR). The IR spectra were recorded as thin solid films on NaCl discs using a Perkin Elmer 1600 FT-IR.

Elemental Analysis. Elemental analysis was carried out on a Carlo Erba EA 1110 (C H N) instrument.

Synthetic Procedures

TEG was synthesised through a multistep synthetic route (Scheme 1). The commercially available tetraethylene glycol was alkylated with allyl bromide at reflux in basic conditions to obtain **1**. Compound **1** was converted to **2** in the presence of thioacetic acid and AIBN heated at reflux for 1 h. Deprotection of **2** was performed in mild acidic condition at reflux for 4 h to obtain **TEGT**.

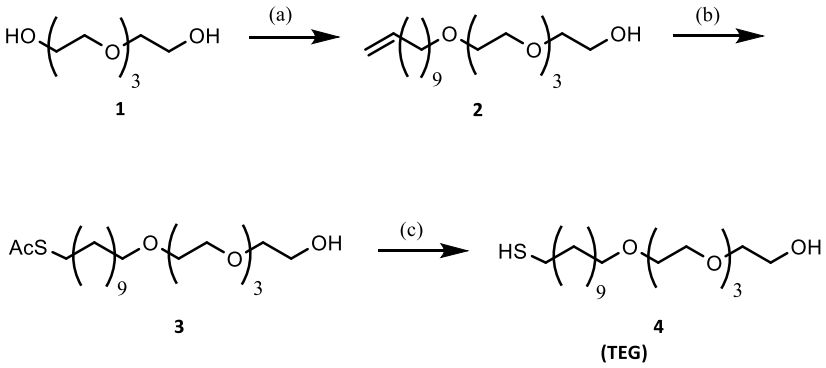

Scheme 1. Synthesis of **TEG;** (a) 11-Bromoundec-1-ene, $NaOH_{(aq)}$, reflux, 20 h, 79%, (b) Thioacetic acid, AIBN, PhMe, reflux, 20 h, 80% and (c) 0.1 M HCl, MeOH, reflux, 4h, N_2 atm, 90%.

Synthesis of TEG

*1-Allylundec-11-oxy tetraethylene glycol (1)***.** A mixture of tetraethylene glycol (16.30 g, 84.02 mmol) and 50% aqueous NaOH (0.64 g, 16.00 mmol) was heated under reflux under an N_2 atmosphere for 0.5 h. Followed by the addition of 11-bromoundec-1-ene (1.95 g, 8.37 mmol), the reaction mixture was heated for a further 20 h. The organic layer was extracted with Et_2O (3 × 50 ml), dried ($MgSO_4$), filtered and concentrated *in vacuo*. The crude product was purified by column chromatography on silica gel (eluent: EtOAc) and solvent removed *in vacuo* to give a colourless oil (2.30 g, 79%). ν_{max}/cm^{-1} (film): 3436brm, 3075m, 2926s, 2853s, 1640m; ^{1}H NMR (300 MHz; $CDCl_3$; Me_4Si) δ_H 6.91–5.74 (m, 1H, -OC_9H_{18}*CH*CH_2), 5.09–4.89 (m, 2H, -$OC_9H_{18}CH$*CH*$_2$), 3.76–3.58 (m, 16H, -O*CH*$_2$*CH*$_2$O-), 3.42 (t*, J*= 6.20 Hz, 2H, -O*CH*$_2C_{10}H_{19}$), 2.56 (s, 1H, *OH*), 2.02–1.96 (m, 2H, -$O(CH_2)_8$*CH*$_2C_2H_3$), 1.62–1.50 (m, 2H, -OCH_2*CH*$_2(CH_2)_7C_2H_3$), 1.40–1.25 (m, 12H, -$O(CH_2)_2$*(CH*$_2)_6CH_2CHCH_2$) ; ^{13}C NMR (75 MHz; $CDCl_3$; Me_4Si) δ_C 140.0, 114.9, 73.3, 72.4, 71.2, 70.9; 62.6, 30.4, 30.3, 30.2, 29.9, 29.7, 26.9 (ESMS): 369 ([M + Na]$^+$, 100%); HRMS: found 369.2611. Calc. mass for $C_{19}H_{38}O_5Na$: 369.2617.

1-Thioacetylundec-11-oxy tetraethylene glycol (2). To a solution of **1** (2.67 g, 7.72 mmol) in PhMe (25 ml), thioacetic acid (1.17 g, 15.39 mmol) and AIBN (catalytic amount) were added. The solution was heated under reflux for 1 h. The reaction mixture was quenched by addition of 1M $NaHCO_3$ (50 ml) and the organic layer extracted with EtOAc (3 × 25 ml). The combined organic layers were washed with 1 M $NaHCO_3$ (3 × 25 ml) and brine (25 ml). The organic layer was dried

($MgSO_4$), filtered and solvent removed *in vacuo* to yield a colourless oil (2.61 g, 80%). ν_{max}/cm^{-1} (film): 3464 brs, 2925s, 2855s, 1692s; 1H NMR (300 MHz; $CDCl_3$; Me_4Si) δ_H 3.74–3.55 (m, 16H, -O*CH*$_2$*CH*$_2$O-), 3.45 (t, *J* = 6.20 Hz, 2H, -O*CH*$_2$(CH_2)$_{10}$SAc), 2.81 (t, *J* = 7.20 Hz, 2H, -O(CH_2)$_{10}$*CH*$_2$SAc), 2.31 (s, 3H, -*SAc*), 1.62–1.50 (m, 4H, -OCH$_2$ *CH*$_2$(CH_2)$_6$*CH*$_2$$CH_2$SAc), 1.33–1.23 (m, 14H, -O(CH_2)$_2$*(CH*$_2$*)*$_7$(CH_2)$_2$SAc); ^{13}C NMR (75 MHz; $CDCl_3$; Me_4Si) δ_C 196.0, 72.7, 71.7, 70.8, 70.5, 70.2, 61.9, 30.8, 29.6, 29.3, 29.0, 26.2; (ESMS): 445 ([M + Na]$^+$, 100%); HRMS: found 445.2613. Calc. mass for $C_{21}H_{42}O_6SNa$: 445.2600.

1-Mercaptoundec-11-oxy tetraethylene glycol (TEG). A solution of 2 (2.27 g, 5.38 mmol) in 0.1 M HCl methanolic solution (100 ml) was heated under reflux under N_2 atmosphere for 4 h. The reaction was concentrated in vacuo. The crude product was purified by column chromatography on silica gel (eluent: EtOAc) to yield a colourless oil (1.84 g, 90%). Elemental analysis found: C, 59.86%; H, 10.72%. Calc. for $C_{19}H_{40}O_5S$: C, 59.96%; H, 10.59%; ν_{max}/cm-1 (film): 3464brs, 2925s, 2854s; 1H NMR (300 MHz; $CDCl_3$; Me4Si) δH 3.75–3.56 (m, 16H, -OCH2CH2O-), 3.50–3.42 (m, 2H, -OCH$_2$(CH_2)$_{10}$SH), 2.52 (q, J = 7.50 Hz, 2H, -O(CH_2)$_2$$CH_2$SH), 1.68–1.50 (m, 4H, -OCH$_2$$CH_2$($CH_2$)$_7$$CH_2$$CH_2$$_S$H), 1.4–1.23 (m, 15H, -O(CH_2)$_2$ (CH_2)$_7$(CH_2)$_2$SH) ; 13C NMR (75 MHz; $CDCl_3$; Me_4Si) δC 74.4, 74.0, 72.5, 72.2, 71.9, 63.6, 35.9, 31.3, 30.9, 30.2, 27.9, 26.5; (EIMS): 403 ([M+ Na]+, 100%); HRMS: found 403.2492. Calc. mass for $C_{19}H_{40}O_5SNa$: 403.2494.

APPENDIX B

Appendix B1: Checking the stability of G-NP colloidal solution by UV-Vis

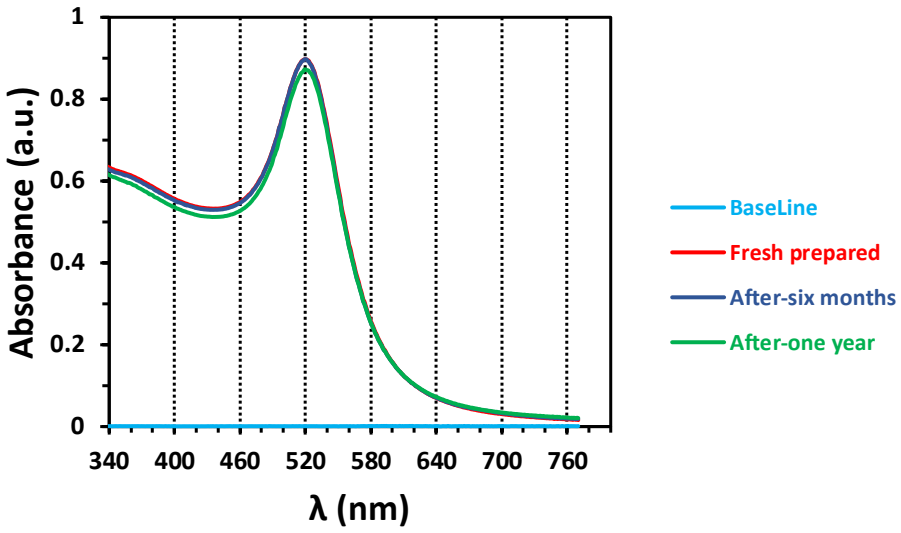

Figure B1.1: Shows the UV-Vis for synthesised G-NPs @ pH 4.5, fresh prepared, after-six months and after-one year

Appendix B2: Frequency measurement by QCM of G-NPs deposition on AlK-amine SAM at pH 7.

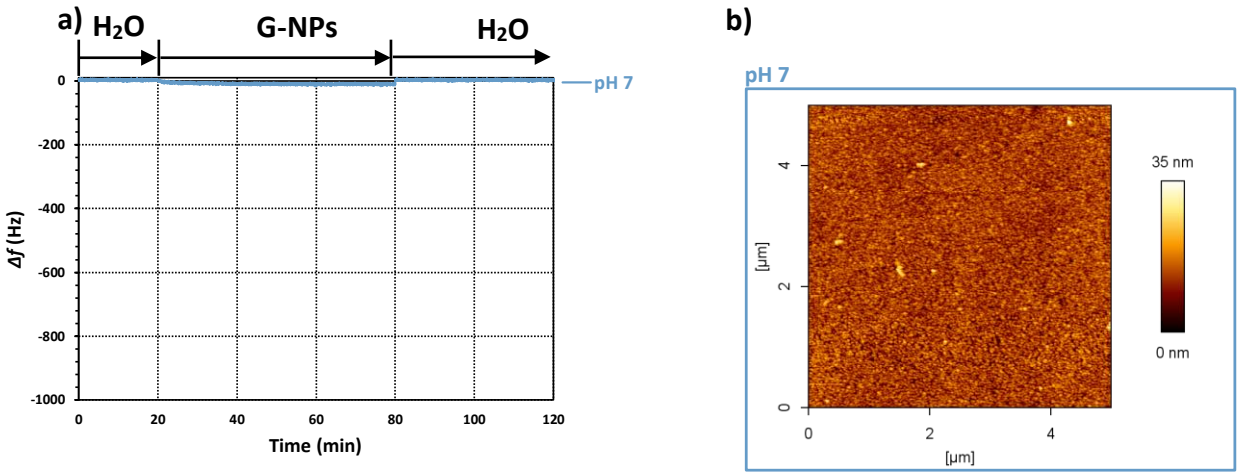

Figure B2.1: a) Measured frequency by QCM and b) combined 5 × 5 µm AFM images of G-NPs deposition on Alk-amine SAM at different pH 7

Appendix B3: Calculate the concentration of G-NPs

Based on TEM results, the diameter of synthesised G-NPs, herein is ~15 nm and the assumption is that the G-NPs have a spherical shape and have the same diameter. Thus, the average number of gold atoms (N_{ave}) for a single G-NP was calculated according to the following equation B.1.[60]

$$N_{ave} = \prod \rho N_A D^3/6M \qquad \textit{(Equation B3.1)}$$

N_{ave}: represents the average number of gold atoms

ρ: density of gold (19.3 g/cm^3)

N_A: Avogadro number (6.022×10^{23} atom)

D: the average diameter of the G-NPs

M: Atomic weight of Au (A_w = 197 g/mol)

N_{ave} = 10.4258×10^4 represents the number of gold atoms per a single G-NP

To calculate the conc. of G-NPs, it is assumed that the reduction of gold atom to G(III) a 100% occurs and the following steps should be applied:

$$Mol_{Gold} = wt/A_w \qquad \textit{(Equation B3.2)}$$

Number of moles of gold only which were used to synthesis G-NPs passivated with citrate herein

= weight of gold only (0.005 g)/A_w of gold (197 g/mol)

= 2.54×10^{-5} mol

Conc. of G-NPs (diameter 15 nm) = No. of mol of gold only / (Number of gold atoms x V ml),

V: Represents the volume of UHQW which was used for synthesising G-NPs (0.102 L).

= 2.54×10^{-5} mol/(104258 × 0.102 L)

= 2.38 nM